Antenna Design Solutions for Radio Frequency Identification (RFID) Tags based on Metamaterial-inspired Resonators and other Resonant Structures

Ph.D. Thesis written by

Simone Zuffanelli

Under the supervision of

Jordi Bonache Albacete

and

Ferran Martín Antolín

Bellaterra (Cerdanyola del Vallès), July 2015

Universitat Autònoma de Barcelona

UAB CEI CAMPUS OF INTERNATIONAL EXCELLENCE

The undersigned, Dr. **Jordi Bonache Albacete** and Prof. **Ferran Martín Antolín**,

Professors of the Electronic Engineering Department (Engineering School) of the *Universitat Autònoma de Barcelona*,

CERTIFY:

That the thesis entitled "Antenna design solutions for radio frequency identification (RFID) tags based on metamaterial-inspired resonators and other resonant structures" has been written by **Simone Zuffanelli** under their supervision, in fulfillment of the requirements for the PhD degree of Electronic Engineering.

And hereby to acknowledge the above, sign the present.

Signature: Jordi Bonache Albacete

Signature: Ferran Martín Antolín

Bellaterra, July 27th 2015.

Contents

Acknowledgements

This work would have never been possible without the help of the many people supporting me during these last years, and hence this thesis is partially their merit.

In particular, I would like to express my deep gratitude to my supervisors, Jordi Bonache and Ferran Martín, for their constant encouragement and useful critiques of this research work. Thank you Ferran for giving me the opportunity of joining the group as a researcher, and for introducing me to the world of metamaterials with invaluable enthusiasm and clearness. Jordi, I would like to express my very great appreciation for your inspiring support, which greatly expanded my knowledge in antennas and RFID, guided the development of this work and contributed to my formation as a researcher.

I would like to extend my thanks to the people in my research group, Gerard Zamora, Ferran Paredes and Pau Aguilà, for actively participating at discussing and patiently revising my work. Special mention to Gerard Zamora, who deeply contributed to the mathematical expressions presented in this work, and dedicated long hours to the inspiring discussions over the subjects of this thesis.

I also wish to thank all the people from GEMMA/CIMITEC, the Electronic Engineering Department and the Engineering School, for their assistance and the good times we spent together. A special thanks to Jordi Selga for his patient help and precious advices throughout my PhD.

This work is also a tribute to my family, who gave me the possibility of beginning my adventure in the world of science and technology, and supported me during these years in spite of the long distance separating us.

Finally, a very special “thank you” goes to a very special person, who encouraged me throughout the good and the bad moments: thank you Anna.

Summary

Nowadays, the automatic and univocal identification of items all around the world is becoming a growing necessity, as a consequence of the rapid increase of the global production and trade. In this regard, radio frequency identification (RFID) technology has been emerging as a suitable and more evolved alternative to barcodes, being already used in a multitude of applications in everyday life, such as items tracking through the supply chain, smart inventory, access control and contactless payment. However, although RFID has achieved entering into the mainstream of technology, already providing a cost-effective solution in many scenarios, several challenges are still waiting response. Among these, the identification of small metallic objects still requires further efforts for obtaining thinner and smaller RFID tags, being the current on-metal tagging solutions thicker and much more expensive than conventional RFID tags. Also, the design of miniaturized RFID tags presenting uniform (or quasi-uniform) reading pattern, which would allow identification of small objects independently from their orientation, is still troublesome. On the other hand, some applications require maximizing the reading distance, even at the expense of the tag dimensions, so that the design of RFID tags with optimized reading distance is another interesting research subject within the frame of RFID technology.

The main objective of this thesis is to explore solutions to the aforementioned problems, thus contributing to the advance of RFID technology, and to its further extension to everyday life applications. To this end, this work is focused on the antenna design for passive RFID tags working at the UHF frequency band (passive UHF-RFID tags), exploring the use of metamaterial-inspired resonators (i.e., the split-ring resonator and its derived structures) as radiating elements, and also considering alternative solutions based on other kinds of resonant structures.

1

Motivation and objectives

In modern societies, the production and trade of goods all around the world is constantly increasing. The latest technological achievements allow the mass-production of millions of items of every kind, which are being exchanged all around the globe with unprecedented rapidity. At the same time, the problem of identifying, classifying and tracking such a growing multitude of objects is consequently arising.

In the last decade, Radio Frequency Identification (RFID) technology has been emerging as a promising solution to these problems. The cost of RFID devices is becoming more and more competitive, making such technology affordable even for the identification of low-value consumable items. In particular, passive RFID systems have been experimenting fast growth over the last decade, being currently used for hundreds of applications, and further expansion is predicted for the near future. Nevertheless, to fully develop its potentiality as a worldwide leading solution for identification, passive RFID technology still has to deal with a set of challenges, which strongly depend on the specific application scenario. Concretely, the tagging of small metallic items remains troublesome, even after extensive research in the past years. Also, the development of miniaturized tags readable from any direction, as required by many applications, is still critical. In other applications, the tag design must be focused at maximizing the reading distance, even at the expense of the tag size. In any of these cases, and, to a more general extent, the tag antenna plays a fundamental role in passive RFID tag design. Moreover, as a result of the extensive integration of RFID transponders, the antenna size is currently the limiting factor of passive UHF-RFID tags dimensions. For these reasons, the future advance of RFID technology is still dependent upon the research efforts and accomplishments in the field of antenna design.

This work is aimed at exploring new antenna design solutions for passive RFID tags working at the UHF band, in order to overcome the aforementioned problems, thus contributing to the progress of RFID technology. To this end, we appealed to the world of metamaterials, which has been recently impulsed by the wide practical outcome obtained within the microwave community. Specifically, some resonating structures commonly used in metamaterial devices will be analyzed as radiating elements at the base of passive UHF-RFID tags, and their benefits and limitations will be discussed. This work was in part inspired by the lack of research on the radiation properties of the abovementioned resonators, from now on metamaterial-inspired resonators, when used as standalone elements, these being typically reported to be used in periodic arrangements to form metamaterial devices. However, to maintain an open approach to the problem, we also considered adopting other kinds of solutions, not related to metamaterials, when these demonstrated to be advantageous. In this regard, special mention must be done to the approach proposed in this work for the tagging of optical discs, which represent a special case of item-level identification of small metallic objects.

The outline of the presented thesis is as follows:

- In chapter two, a brief introduction to the RFID technology will be provided, including an overview of the development history and an analysis of the recent market predictions. The different types of RFID systems are then described, highlighting their functional benefits and limitations, and defining the typical applications of each typology.

- In the third chapter, the description is focused on passive UHF-RFID tags. The tag structure is explained in detail, and the most important tag performance indicators, i.e., the read range and the bandwidth, are introduced. Some common examples of tag antenna designs are then provided, discussing the design requirements and tradeoffs which are typically encountered. The last part of the chapter is devoted to outline the state of the art of passive tag design, with special attention to all those designs which included some kind of metamaterial-inspired resonators. Finally, the problem of tagging small metallic object is introduced, and the most relevant contributions from the literature to overcome this problem are detailed.

- The fourth chapter analyzes the radiation properties of some of the most common metamaterial-inspired resonators. These include the split-ring resonator (SRR) working around its first and second resonances, the non-bianisotropic split-ring resonator (NB-SRR), as well as their complementary counterparts. In the latter case, special attention is dedicated to the radiation of those particles in close vicinity of a metallic surface.

- In chapter five, the results obtained in the previous chapter are applied to the design of UHF-RFID tags, as a means to meet the challenging requirements mentioned above. Specifically, a miniaturized tag with reduced sensitivity to orientation and a low-profile tag for on-metal applications are presented. Moreover, an SRR antenna working at the 900 MHz ISM band is proposed as an alternative to half-wave dipole antennas. The design process is detailed, and the manufactured prototypes are subjected to experimental validation.

- In chapter six, a novel approach to the UHF-RFID tagging of optical discs is presented. The chapter opens with a description of the structure of the most common optical disc types, introducing the issues encountered in the tagging of such items, along with the solutions proposed in the literature and in commercial tags. Then, the suggested approach is presented, and an exhaustive design methodology is defined. On that basis, several examples of tag prototypes are proposed, detailing their design, fabrication and measurements.

- Chapter seven is devoted to explore the design of passive UHF-RFID tags with maximized reading distance. To this end, the stringent size constraints, which typically characterize passive UHF-RFID tag design, are relaxed, though maintaining practical suitability. As a proof of concept, a tag prototype is designed, fabricated and subjected to experimental measurements.

- Lastly, in chapter eight, the main conclusions and future research arising from this thesis, are outlined.

The work conducted during the realization of this thesis was carried out between 2011 and 2015, within the Group GEMMA/CIMITEC, which is part of the Electronics Engineering Department of the *Universitat Autònoma de Barcelona*. GEMMA/CIMITEC has been part of the European Network of Excellence NoE 500252-2 METAMORPHOSE (Metamaterials organized for radio, millimeter wave and photonic super lattice engineering), the main objective of which was to research, study and promote artificial electromagnetic materials and metamaterials within the European Union. It has recently given rise to the Virtual Institute for Artificial Electromagnetic Materials and Metamaterials (METAMORPHOSE VI AISBL). Furthermore, CIMITEC is one of the centers of the Technological Innovation Network of TECNIO (ACC1Ó) of the Catalan Government, created with the objective of promoting the transference of technology to industry in the field of Information and Communication Technology and has been recognized as a Consolidated Group by the Catalan Government (AGAUR). This work was, thus, supported by the European, Spanish and Catalan Governments by means of several projects and contracts. The *Universitat Autònoma de Barcelona* contributes through the *Vicerectorat de Projectes Estrategics - Parc de Recerca*.

Among the projects and contracts with the different institutions and companies that have given support to the developed research activities, we would like to highlight:

- Project CSD2008-00066 CONSOLIDER INGENIO 2010, granted to a consortium composed of eight research groups from different Spanish universities and funded by the Spanish Government. Title: *Ingeniería de Metamateriales (EMET)*. Period: 2008-2013.
- Award number 2009SGR-421 from the "Agencia de Gestión y Ayudas Universitarias y de Investigación (AGAUR)" of the Catalan Government. Period: 2009-2013.
- Project TEC2010-17512, funded by the Spanish Governement. Title: *Nuevas estrategias de diseño y síntesis de componentes de microondas basados en conceptos de METAmateriales con orientación a la TRANSFERencia tecnológica (METATRANSFER)*. Period: 2010-2013.
- Award number 2014SGR-157 from the "Agencia de Gestión y Ayudas Universitarias y de Investigación (AGAUR)" of the Catalan Government. Period: 2014-2016.
- Project TEC2013-40600-R, funded by the Spanish Government. Title: *Diseño y sintesis de componentes de RF/microondas basados en conceptos avanzados y su aplicacion a circuitos de comunicaciones, sensores y RFID*. Period: 2013-2016.

2

Introduction to RFID

In this chapter, an overview of RFID technology will be provided. The description begins with a brief history of the birth and development of RFID systems, and then focuses on the actual situation and future trajectory of the global RFID market. Then, the classification of the several RFID types is discussed. Due to the complexity of modern RFID systems, which encompass several aspects of the technological breakdown of the last century, such as wireless communication, antenna optimization, energy harvesting, integrated circuit design and mass production, an exhaustive description is not possible within the context of this work. Instead, we highlight the main characteristics distinguishing the several types of RFID systems, discussing the benefits, limitations and most common applications of each family.

2.1 Introduction to RFID technology

Radio frequency identification (RFID) is a widespread technology that allows identification of objects by using electromagnetic waves. Nowadays, RFID technology is being extended to many aspects of everyday life, such as regulating the access to buildings and public transportation, facilitating the inventory and shipping of any kind of goods in the supply chain, identifying and tracking animals, procuring additional information in assembly lines and even providing assistance for the visually impaired persons, among others. As it will be detailed in the next sections, further development, and further penetration into market, is expected for the next years, mainly due to the reduction of the tag cost, which is already in the order of tens of cents of US dollars.

The identification mechanisms relies on the wireless communication between a simple device, called RFID tag, which is attached to the item, and a more complex device, called RFID reader, which can receive the information from several tags placed nearby (see Figure 2.1). Specifically, the reader generates a query signal, which is radiated to the surrounding space by means of an antenna. Such signal hits the tag, which is attached to the object, and is composed of an antenna connected to an application specific integrated circuit (RFID ASIC), containing the information about the tagged item in a reserved memory area. As a response to the query signal, the RFID tag generates a response signal containing the item information, which is radiated back and received by the RFID reader. The reader is usually connected to a microcontroller, a host computer, or a computer network, in order to process and share the data. A functional scheme of a typical RFID system is depicted in Figure 2.2.

The key advantage of RFID over other existing technologies, such as optical barcodes, is the capability of identifying items without the need of line-of-sight operation, thus making unnecessary the human intervention in the reading process. In addition, due to the increased amount of data stored in the tag, RFID technology allows identifying each object univocally, rather than identifying the class of product or the lot number, and, unlike barcodes, allows read/write operation with advanced security by means of data

Figure 2.1. Illustration of an RFID system.

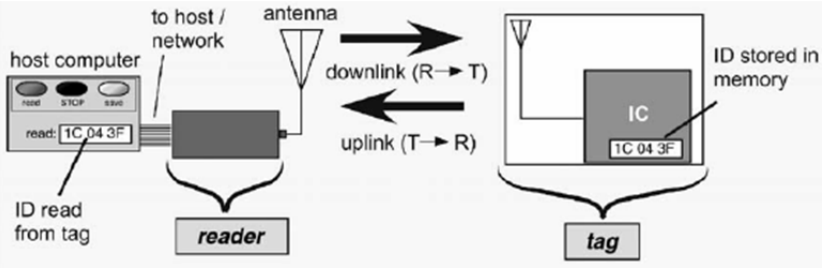

Figure 2.2. Scheme of a typical RFID system.

encryption. For these reasons, RFID is currently supplementing, or even replacing, optical barcodes for many applications.

Among the different kinds of RFID tags, passive tags working at the UHF-RFID frequency band are especially promising in many fields of application, due to the significant achievable read ranges, low cost, small dimensions, and because such tags do not need batteries. Moreover, the sophisticated anti-collision protocols implemented in UHF-RFID transponders allow reading a great number of tags simultaneously, from distances exceeding ten meters. All the tags presented throughout this work belong to the category of passive UHF-RFID tags, and the efforts were directed to the antenna optimization in response to specific market requirements and challenges.

2.1.1 Brief history of RFID technology

Although RFID technology is recently experiencing an unprecedented growth, its basic principles, such as the modulated backscatter, originated many decades ago. In fact, modern RFID systems are based on the military research developed during World War II, aimed at solving the problem of identifying incoming friendly aircrafts, which led to the introduction of the "Identification, Friend or Foe" (IFF) system in the late 30s of the 20th century. The first versions of the system, tested and put into operation in 1939, used a transponder (Mark I) mounted on the aircraft, which replied to the incoming radar pulse of a specific frequency with a distinctive echo signal characterized by a progressive amplitude increase over time [1]. The technology early evolved into more complex systems, such as the transponder Mark III, which was successfully used by the Allies during great part of the war, and incorporated a large number of improvements over the initial prototypes [2].

Shortly after the conclusion of World War II, the interest on civil and commercial applications of radio frequency identification progressively increased. In 1948, the first landmark work on the subject, entitled "Communication by means of reflected power" and written by Harris Stockman, was published. In that paper, the basic theory of

Figure 2.3. Cover of an aviation journal from the early 40s.

backscatter communication was discussed, and several modulations techniques were proposed, concluding that "considerable research and development work has to be done before the remaining basic problems in reflected-power communication are solved, and before the field of useful applications is explored" [3].

During the decades of the 50s and 60s, the development proceeded relatively slowly. In this period, ideas and patents related to the radio frequency identification were released (e.g., the patent entitled "Radio transmission systems with modulatable passive responder" by D.B. Harris), and further theoretical research was carried out (e.g., "Theory of Loaded Scatterers", written in 1964 by R.F. Harrington). However, it was not until the invention and development of integrated circuits in the late 60s that RFID technology eventually could be implemented to a large number of applications in everyday life. In fact, as a result of the exponential reduction of the price and size of electronic devices, microwave transponders eventually fulfilled the requirements of being very small and cheap, setting the technological base to the RFID explosion of the following decades. An important contribution to the RFID ASIC development came in 1975, with the work entitled "Short-Range Radio-Telemetry for Electronic Identification Using Modulated Backscatter", by Alfred Koelle, Steven Depp, and Robert Freyman, which introduced practical solutions in the modulation of the backscattered signal, and was at the base of the first practical passive tags with acceptable read range. Nevertheless, RFID was still highly developmental by that time, and the research efforts involved a large number of companies, such as Raytag and RCA in USA, Alfa Laval and Nedap in Europe, government laboratories and academic institutions.

Eventually, at the second half of the 80s, RFID technology accomplished its first worldwide commercial success, with its introduction for automatic toll collection at the end of the decade. By that time, RFID transponders were already using low-power CMOS digital circuitry and EEPROM nonvolatile memory, although the size of the circuitry was still a limiting factor, accounting for half the tag area (See Figure 2.4a-b). Throughout the decade of the 90s, tolling and rail application of RFID spread over the

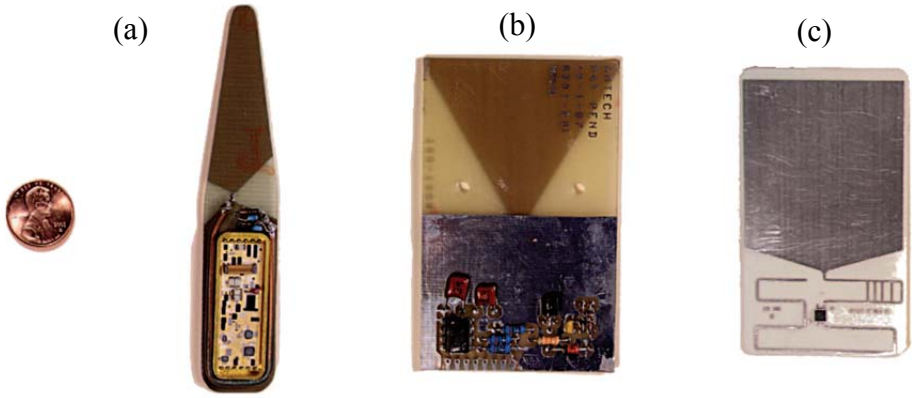

Figure 2.4. Evolution of RFID tags, compared in size to a penny. (a) A 12-b read-only tag from 1976, (b) a 128-b read-only tag from 1987 and (c) a 1024-b read-write tag featuring a single CMOS integrated circuit (black square on the lower side) from 1999. Extracted and adapted from [4].

world, involving many countries including Australia, China, Hong Kong, Philippines, Argentina, Brazil, Mexico, Canada, Japan, Malaysia, Singapore, Thailand, South Korea, South Africa, and Europe. New applications were successfully introduced, such as fuel dispensing, ski pass systems and vehicle access.

The development of RFID transponders found a key advancement when the first microwave Schottky diodes could be integrated in the CMOS technology, at the end of the 90s. This breakthrough allowed the transponder circuitry to be entirely contained inside a single integrated circuit (RFID ASIC), covering an insignificant portion of the tag area (See Figure 2.4c). Modern passive RFID tags were born. For the first time, the antenna size was the limiting factor of passive RFID tags, which still happens nowadays. Tags were manufactured in the form of thin sticky labels (inlays), equipped with planar antennas, which could be easily attached to the object to be managed.

By early 2000, RFID had successfully entered in everyday life. As the technology was spreading worldwide with increasing market penetration, many efforts were directed to develop standards and guidelines to regulate the communication protocols in the different countries. The work of organizations like GS1, the European Conference of Postal and Telecommunications (CEPT) and the International Standards Organization (ISO), led to many protocols still in use nowadays. Among them, the Electronic Product Code (EPC), defined in the EPCglobal Tag Data Standard, is currently the reference choice for supply chain and retail, and is expected to guide the future development of RFID standardization. In the last years, the tag performance has been rapidly improving, and costs dropped down. With a total market size exceeding $5 Billion in 2009 [5], RFID has entered in the mainstream of business and technology. Nevertheless, many experts believe that the RFID revolution is just at its beginnings. The Auto-ID Labs network, successor of the MIT Auto-ID Center, is currently working to the “Internet of

Things" (IoT) project, which aims at creating an intelligent network of objects equipped with electronics, software, or sensors, able to exchange data with the manufacturer, the owner or with other networks. With an expected number of many billion inter-connected objects by 2020, the actual scenario reveals only a small part of the future impact of RFID technology in our everyday life.

2.1.2 Market trend for the near future

Nowadays (2015), the total RFID market is already worth $9 billion [6], and predictions suggest a value exceeding $27 billion in 2024. The current market is almost entirely covered by High-Frequency (HF) and Ultra-High-Frequency (UHF) RFID systems (which will be detailed in the next section), with similar market share [7]. However, UHF-RFID market has been rapidly increasing in the last years, due to is global standardization and to the promising performance of passive UHF-RFID tags in the retail sector.

The limiting factor to the expansion of the RFID technology is the cost of the tag. In fact, since tags are intended to label virtually any kind of object, including everyday consumables, their cost must be fairly lower than the cost of the labeled item. Specifically, the cost of the tag is mainly determined by the cost of the RFID ASIC, which is currently in the order of few cents of dollar. A prediction of the RFID label cost for the near future, depicted in Figure 2.5, reveals that the number of tags globally sold by year will rapidly increase as the tag price drops down [5]. A global market trend prediction [7] for the different commercial applications of RFID is depicted in Figure 2.6. The financial, security and safety sector is currently leading the market, exceeding $1.5 billion in 2015, followed by transportation and automotive, animal tracking, military and retail. It is worth mentioning that, whereas some applications (e.g.,

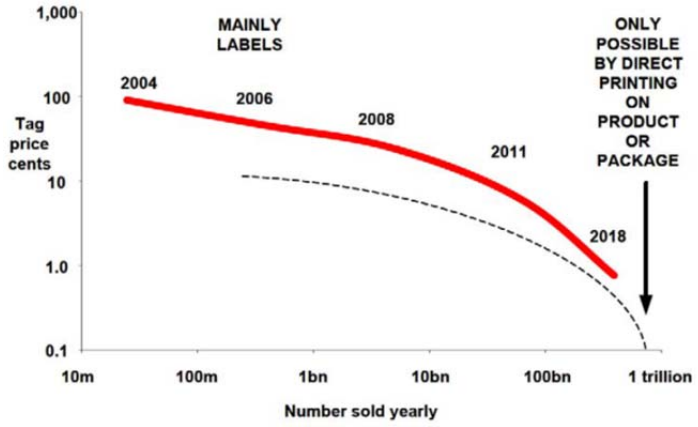

Figure 2.5. Prediction of chip (solid line) and chipless (dash line) tag price versus global sells for the next years. Extracted from [5].

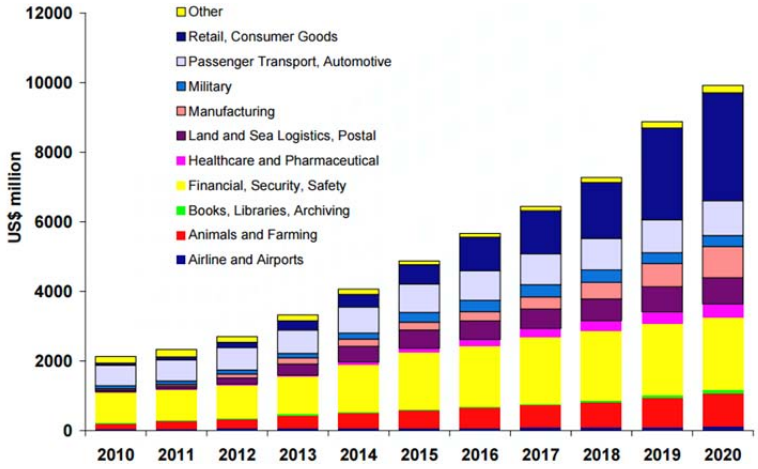

Figure 2.6. Global RFID market trend prediction divided by sector. Extracted from [7].

transportation and automotive) seem to have already reached a stable position on the market, a fast growth of other sectors is predicted for the very near future. Specifically, the retail and consumables sector is expected to become the market leader before the end of the current decade. Many companies are already introducing RFID to manage supplies, inventory, losses/thefts and even payment in different kind of stores. Since the retail market sector mainly relies on tags working at UHF frequencies, UHF-RFID technology is being triggered to a very important growth for the near future.

2.1.3 RFID types and operation frequencies

RFID systems evolved through the years with a large variety of solutions, each responding to specific design requirements. A first classification of RFID systems can be done on the basis of the tag power supply, as follows (see Figure 2.7 Figure 2.8).

Passive tags are not provided with any independent source of power to activate the integrated circuitry of the transponder. Instead, the power necessary to the transponder operation is delivered by the interrogation signal coming from the reader. The communication between the reader and passive tags is based on the modulated signal backscatter principle, which can be described as follows. The transponder is initially in a condition of good impedance matching with the antenna of the tag, so that it can absorb all the power received from the antenna. Once the transponder is provided with enough energy upon an incoming query signal, it changes its input impedance so that the electromagnetic power is reflected to the antenna and radiated back to the reader. The impedance states are alternated to generate a codified series of reflections, which contains the information requested in the query signal.

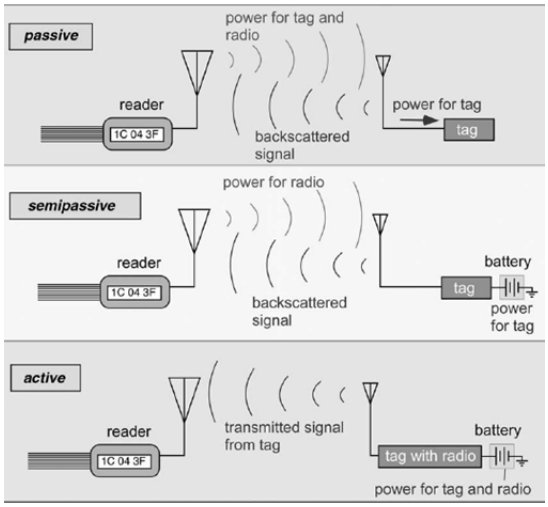

Figure 2.7. Overview of the different RFID types on the basis of the tag power source. Extracted from [8].

The absence of batteries, or any other kind of power supply, determines a tremendous advantage in terms of dimensions, simplicity, and cost. Passive tags can be machined in flexible adhesive inlays, with a thickness of few micrometers and a cost of few cents.

Active tags are equipped with an embedded power source, usually a battery, in order to provide energy to the tag circuitry and to communicate with the reader. Relying on a dedicated energy source, active tags can perform complex tasks and communicate to very large distances, in the order of hundreds of meters, by means of sophisticated and noise-robust phase-shift modulations. Contrarily to passive tags, which can only respond to a request, active tags can start a communication to the reader, as may be requested in specific applications.

However, active tags suffer from the increased complexity, dimensions and cost, which is in the order of tens of dollars. The presence of a fully-equipped radio, a battery and, in some cases, two separate antennas, makes impracticable the manufacturing of thin, flexible labels. The expected lifetime of active tags depends upon the battery duration, and in many cases the whole tag must be replaced once the battery is exhausted. Moreover, being provided with a fully-equipped transmitting radio, active tags must be subjected to certification according to the regulatory standards of each country.

Semi-passive tags, also known as *battery-assisted passive* (BAP) tags, are provided with a power source, usually a small battery, to feed the local tag circuitry, but use the backscatter principle for communication with the reader. This solution is widely employed in tags equipped with sensors, which need energy to continuously collect and store data, but are designed to minimize their complexity and required power, so that an active radio transmitter is not included.

Figure 2.8. Some examples of commercial RFID tags: (a) passive, (b) semi-passive and (c) active tags.

A further distinction of RFID technology can be done on the basis of the coupling mechanism (Figure 2.9) between the reader and the tag, which is determined by the tag antenna size in terms of wavelength. In fact, while RFID systems use frequencies varying by a factor of 50 000 or more, from around 100 kHz to over 5 GHz, the tag antenna size encounters a relatively small variation, ranging from one to ten centimeters in most cases. Therefore, whereas tag antennas of low frequency systems are much smaller than the wavelength, tag antennas of high frequency systems are comparable in size to a wavelength. In the first case, the tag antenna is essentially a small coil interacting with the magnetic field stored in the vicinity of the reader antenna, a mechanism often referred as *inductive coupling*. Rather than modeling the tag-reader interaction by means of incident and reflected waves, the system can be thought as a magnetic transformer, where the current flowing in one element induces a voltage across the other element. To provide intense magnetic fields in the surroundings of the reader antenna, large loop structures are usually employed.

On the other hand, when the antenna size is comparable with the wavelength, the coupling mechanism is *radiative coupling*. Under this condition, the tag and reader antennas communicate by means of traveling electromagnetic waves, being one antenna located in the far-field zone of the other antenna.

A clear advantage of radiative coupling over inductive coupling is the distance of operation. While the near fields stored in the vicinity of the antenna decay with the cube of the distance, providing a detection zone whose dimensions are comparable to the antenna size, the radiated fields attenuate with the square of the distance, so that systems relying on radiative coupling can operate to much larger distances. Contrarily, inductive coupling allows much smaller antenna sizes, which is categorically required by many applications (e.g., animal tracking, where tags are usually implanted subcutaneously).

As exposed above, RFID systems use a wide range of frequency bands. The choice of a frequency band involves a series of advantages and drawbacks, mainly related to the physical behavior of the electromagnetic fields (e.g., coupling mechanism, wave

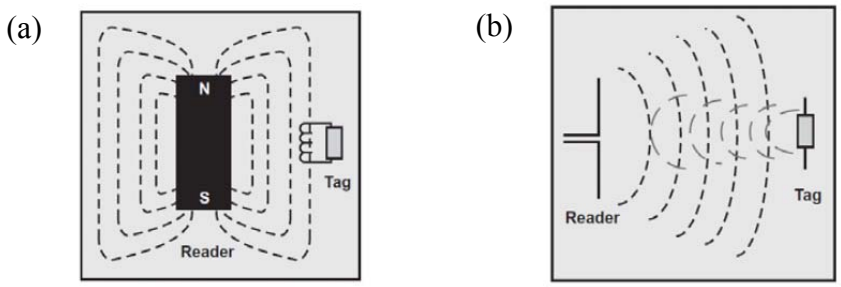

Figure 2.9. Scheme of inductive coupling vs. radiative coupling.

propagation characteristics and interaction with materials, required size of the tag antenna, among others) at a specific wavelength. On the basis of the frequency of operation, RFID systems are often classified as follows.

Low Frequency (LF) systems can operate from 30 kHz to 300 kHz, but most of them work at 125 kHz and 134.2 kHz. LF-RFID systems are usually passive and rely on inductive coupling, so that LF tag antennas are typically coils, often with tens of turns arranged around a ferrite core. Since magnetic fields at low frequencies suffer relatively low interaction with materials, LF tags can operate when attached, or even embedded, to objects containing water and other high-permittivity materials. A wide range of metal-mount LF tags is available, with performance comparable to the general-purpose tags. However, LF tags can be read from very short distances, in the order of few centimeters, the reading speed is relatively slow and multiple readings are impractical. The construction of the coil antenna requires a winding machine, which makes LF tags relatively expensive.

Typical applications include animal tracking, access control and item level identification of pharmaceutical products.

High Frequency (HF) band ranges from 3 MHz to 30 MHz, but most of HF-RFID systems operate at 13.56 MHz. Similarly to LF systems, HF systems use passive tags working on the basis of inductive coupling by means of coil antennas. However, being the operation frequency much higher, a smaller number of turns is required to produce sufficient voltage across the tag, generally in the order of only 5 or 6 turns. For this reason, HF tags can be manufactured in very thin and relatively inexpensive labels, and provide a read range of tens of centimeters, up to a meter in some cases. They are relatively insensitive to objects, but to a much lower degree compared to LF tags. While a HF tag can still be read when surrounded by a human hand, or attached to wood, liquids and tissues, it cannot operate when mounted on metallic surfaces, or when placed beyond metallic screens or films.

Typical applications of HF systems are near field communication (NFC), electronic ticketing, smart cards, library books and airline baggage tagging, among others.

Ultra High Frequency (UHF) systems work in the frequency bands centered around 433 MHz (active tags) and from 840 MHz to 960 MHz (passive and semi-passive tags). Although UHF-RFID systems all around the world have been operating at different frequency bands in the past (see Figure 2.10), most of the countries are currently converging to use the European (865-858 MHz) and the North-American (902-928 MHz) UHF-RFID bands [9], and many efforts are being directed to homogenize the regional regulations in order to ensure the worldwide operation of the tags.

Unlike in the case of LF and HF systems, passive UHF tags typically use radiative coupling to communicate with the reader. The tags are usually provided with a planar dipole antenna, tuned to resonate with the RFID ASIC, which is able to produce a backscattered wave travelling back to the reader antenna. The nature of radiative coupling allows passive UHF-RFID systems to operate to large distances, in the order of several meters, with many tags reaching distances up to 15 m in optimal conditions. Moreover, passive UHF-RFID tags can be manufactured in thin and inexpensive labels (inlays), whose dimensions can be easily adjusted to fit with a large variety of small items. The modern communication protocols of UHF-RFID systems (e.g., EPC Gen2 standard) are provided with sophisticated anti-collision mechanisms, enabling very fast multiple readings of nearby tags, and support anti-counterfeiting cryptography, electronic article surveillance (EAS) functionality and privacy settings. However, due to the behavior of electromagnetic waves at higher frequencies, systems working at UHF are much more sensitive to the composition of the tagged item, and to environmental conditions, with respect to LF and HF systems. The performance of passive UHF-RFID tags is negatively affected by the presence of water, body-tissue and metals. Although many efforts have led to several tag designs optimized to operate in proximity of liquids, or to be attached on metallic surfaces, such solutions suffer from increased dimensions and cost with respect to the general-purpose tags. As a consequence, item level tagging of small metallic object by means of passive UHF-RFID tags is still challenging.

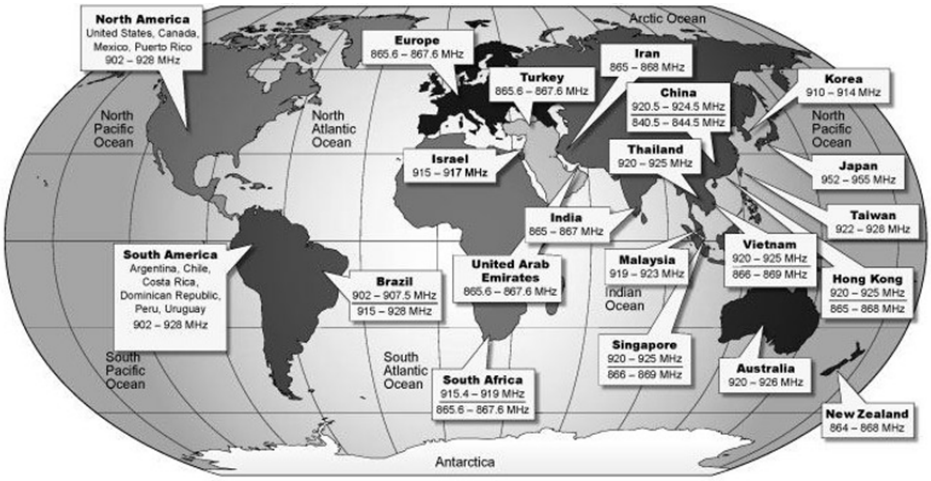

Figure 2.10. World map of traditional frequency allocations of passive UHF-RFID. Both Japan and China are currently migrating to the 902-928 MHz band.

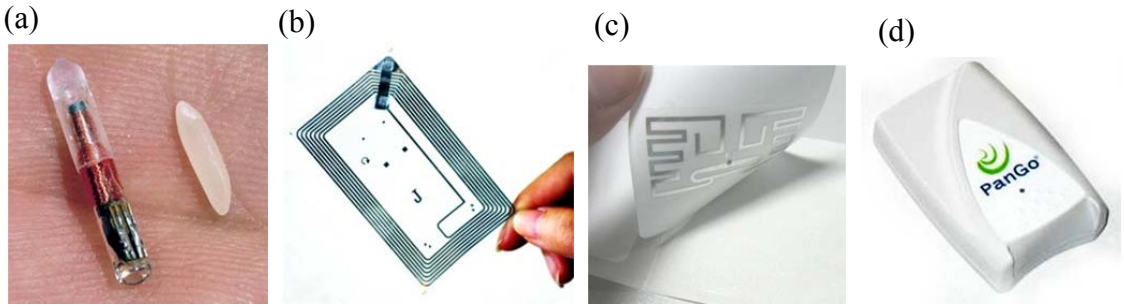

Figure 2.11. Examples of commercial RFID tags: (a) LF tag encapsulated for subcutaneous implantation, (b) HF tag based on plastic substrate, (c) UHF tag label, (d) microwave active tag compatible with 802.11 standards (Wi-Fi).

Due to the benefits of low cost and long operational distance, UHF-RFID tags are currently used for a multitude of applications. These include supply chain and inventory management, parking access control, baggage tracking and asset tracking, among others. Planned applications include smart-shelves and fitting rooms, fast payment and anti-theft systems in retail stores, and significant contribution to the abovementioned Internet of Things.

Many aspects regarding passive UHF-RFID tags, such as the transponder characteristics and the antenna design principles, will be illustrated in the next section.

Lastly, *Microwave* RFID systems operate at frequencies centered around 2.4 GHz and 5.8 GHz, according to the restrictions of the respective ISM bands. Several communication standards and regulations are available, and sometimes the tags are designed to be compatible with other existing standards (e.g., IEEE 802.11 family). Microwave RFID systems, which mostly always based upon active tags, are aimed at tagging relatively expensive items at large distances, or to provide additional features made possible by the circuital complexity of active tags. Being the first RFID systems to be successfully adopted for commercial applications worldwide (i.e., highway toll collection at the end of 80s), microwave RFID devices are a relatively mature technology, which is still widely used nowadays. Transportation, access control and real-time location systems (RTLS) are among the typical applications of microwave RFID systems.

The RFID systems introduced up to now use active tag circuitry in order to provide the required information to the reader. However, many efforts are being currently done in order to avoid the use of any electronic component in RFID tags, to further reduce the tag dimensions and especially its cost. The tags belonging to this category are named *chipless* RFID tags, and are constituted exclusively of dielectrics and conductors, although any other material with useful properties may be used in the future. At present, chipless RFID technology is still highly developmental. In the future, it may provide extremely low cost tags directly printable on the objects, replacing barcodes with drastically improved functionality.

3

Passive UHF-RFID tags: Overview and State of the Art

In this introductory chapter, the discussion is focused on the design requirements and state of the art solutions regarding passive UHF-RFID tags.

A brief description of the integrated transponder (UHF-RFID ASIC) technology, including an introduction to the most commonly used communication protocol (EPC Gen2), is firstly provided. The exposition continues with an introduction to passive tag antenna design, detailing the application requirements and providing an overview of the most common solutions employed in commercial tags. The main performance indicators of passive tags are then introduced, along with the measurement setups which have been used for obtaining the experimental data presented throughout this work.

Next, the concepts of metamaterial and metamaterial-inspired resonator are introduced, and the most relevant examples of passive UHF-RFID tags employing metamaterial-inspired resonators are reported from the literature.

Finally, the state of the art of on-metal passive tag design is discussed, specially focusing on the solutions aimed at reducing the tag thickness (low-profile tags) and dimensions.

3.1 Passive UHF-RFID tags: an overview

As stated in the previous chapter, passive tags are mainly composed of two elements: the transponder and the antenna. Usually, an impedance matching network is cascaded between the ASIC and the antenna, although the system antenna-matching network is often referred to as *antenna* in passive tag design. A third component, often necessary as a structural support, is the dielectric substrate.

Due to the large number of application fields of RFID technology, each presenting specific requirements, passive RFID tags have been evolving to a number of different application-optimized types. The current market offers a variety of tags optimized for being mounted on glass, or attached onto object containing liquids, or worn by persons. Special tags designed to be mounted on metallic surfaces, or to be attached to objects containing metallic parts, are available today. However, an important part of the actual market is owned by *general-purpose* tags. These are cost-effective tags which, rather than being optimized for a specific application, are designed to operate in a wide number of applications. One clear advantage of general-purpose tags is that the user can buy a large number of the same tag model, and use it for tagging different items. Obviously, these tags may suffer from severe performance degradation when attached to some objects containing liquids or metals [10], so that prior information about each tagged items is required to ensure good results.

3.1.1 UHF-RFID ASICs

The transponders currently used in passive RFID tags are characterized by being entirely implemented in a single monolithic chip. The enormous progress of low-cost CMOS technology in the last years allowed obtaining tiny transponders, gradually reducing their cost and power consumption. At present, RFID ASICs cover a die area in the order of a quarter mm^2, and requires few tens of μW of electric power.

3.1.1.1 Packaging

Several solutions exist for the packaging of RFIS ASICs (Figure 3.1), each optimized for a specific mounting process on the final tag. When the tag is manufactured as a label in highly productive assembling lines, the unpackaged chip is directly attached to the antenna, usually by means of flip chip techniques. This solution allows fast, efficient and reel-to-reel production of very thin and reliable inlays, but also needs a high initial investment. For this reason, the manufacturers also offer an alternative solution, which consists of pre-mounting the ASIC on a small polymer strap provided with metal pads connected to the ASIC input pads. The straps are thus mounted on the tag by using less

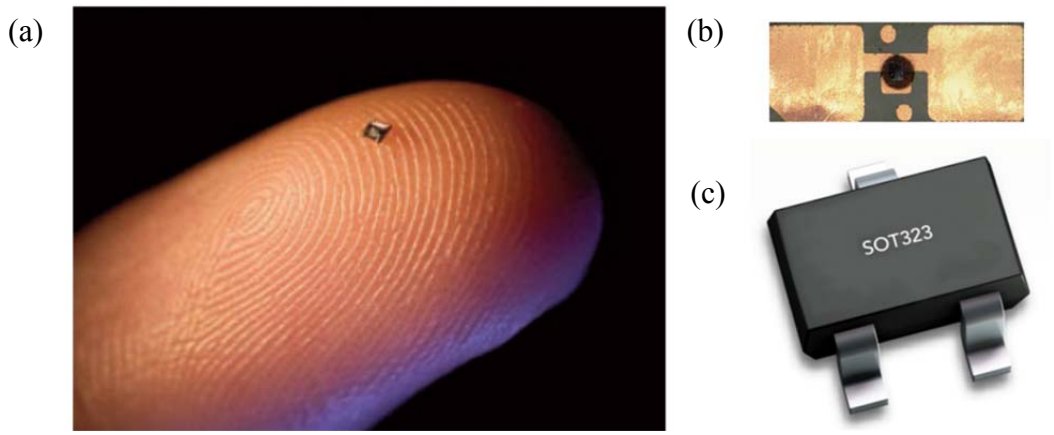

Figure 3.1. Modern UHF-RFID integrated circuits in different packaging. (a) Unpackaged chip, (b) strap and (c) SOT-323 packaged.

expensive assembly lines, but the reliability and durability of the final product is lower, due to the presence of a more complex process and a double connection. A third solution, mainly directed to tag prototyping, employs conventional SMD chip packaging to allow easy mount on experimental, PCB board-based tags.

3.1.1.2 EPC Gen2 Standard

Most of the modern RFID ASICs are designed to comply with the EPC Class 1 Generation 2 protocol, firstly published by EPCglobal in 2004. The standard is based on the concept of *Electronic Product Code* (EPC), which can be considered as an evolution of the UPC code traditionally used in barcodes. In fact, with the global commerce and mass production constantly increasing each year, the problem of uniquely identifying each physical item anywhere in the world, for all time, is increasingly challenging. To this end, the EPC code is designed as a flexible framework that can support many existing coding schemes, and whose length can be expanded according to future requirements. In their basic form, EPC codes are divided into 4 segments, which provide identification of the protocol version, the product manufacturer, type and serial number, respectively, for a total length of 96 bits (see Figure 3.2). This version of the code allows identifying 268 million different companies, each disposing of 16 million product types with 68 billion serial numbers available for each type. Moreover, EPC based tags are further divided in 5 classes (from EPC Class 0 to EPC Class 4), depending on the read and write abilities and other functionalities. Each class provides a set of functions optimized to perform activities related to a certain application field.

Figure 3.2. Exampe of EPC code contained in a passive Gen2 tag.

Besides integrating the EPC coding system, the *Gen2* standard defines all the physical and logical requirements necessary for UHF-RFID tags and readers. The internal architecture of RFID ASICs is designed to implement the different layers of the Gen2 protocol, which regulate a multitude of parameters, such as the signal modulation and channel allocation, the encryption and authentication mechanisms, the data transfer rate, the required memory size, among others. Advanced functions, often related to the privacy of consumers, allow for example to disable or "kill" the tags after their functional cycle has been complied. To provide all the required functionality, the internal circuitry of RFID ASICs integrates a radiofrequency block (including voltage rectifiers, modulator and demodulator), digital control logic and a non-volatile memory area containing the tagging information.

3.1.1.3 Input impedance and sensitivity

Passive tags are required to collect the RF power contained in the incoming query signal from the reader, in order to energize the active circuitry of the transponder. To this end, the first stage of RFID ASICs is a voltage multiplier, which provides the rectified DC voltage necessary for the operation of the subsequent blocks. Traditionally implemented by means of Schottky diodes and capacitors, the rectifying stage is now completely integrated with CMOS technology (an example is depicted in Figure 3.3a), which allowed a significant reduction of the transceiver dimensions and cost. As can be expected, the design strategy and optimization of the input stage is of primary importance for the ASIC performance, being strongly related to its sensitivity and input impedance, which affect the final tag read range and bandwidth, respectively.

The read sensitivity P_{th} of an RFID ASIC is defined as the minimum power that must be delivered to the ASIC in order to obtain a successful response upon a data read request. The advances in the design of high-efficiency voltage multipliers, along with the reduction of the power consumption of integrated CMOS circuitry, made possible a significant improvement of the transponder sensitivity. In the last 15 years, the typical power sensitivity of RFID ASICs passed from −8 dBm to about −20 dBm [11], which means that the power required by the latest ASICs has decreased by a factor 16. Further advance in this direction is expected for the near future, and part of the research is focused on the use of optimized-shaped carriers in the query signals from the reader, as

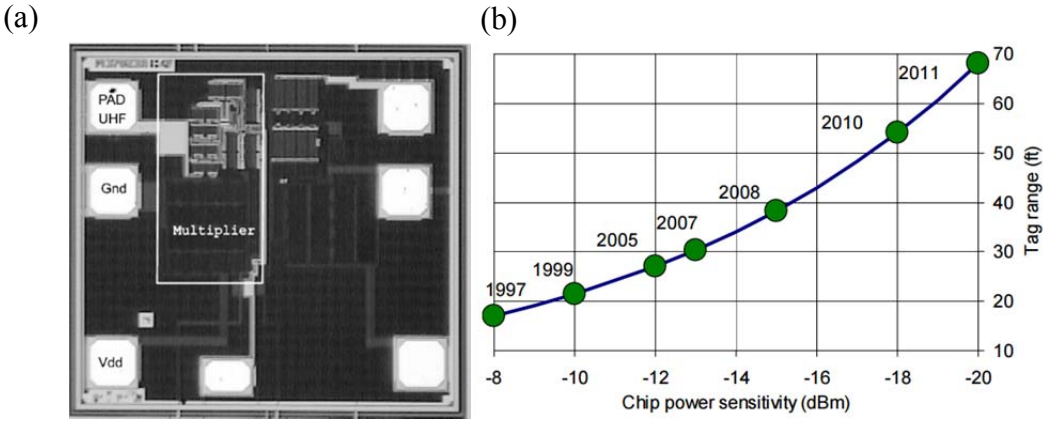

Figure 3.3. (a) Photograph of an RFID integrated circuit using a CMOS-based voltage multiplier, (b) evolution of the power sensitivity of RFID ASICs over the years. Extracted from[12] and [11], respectively.

in the case of the power-optimized waveform (POW) technique reported in [12], allowing to further increase the power efficiency of the charge pump-based RFID ASICs.

The input stage of RFID ASICs also determines their input impedance Z_C, as seen from the tag antenna, when the transponder is in the state of "waiting" an incoming signal. A good characterization of this parameter is crucial in RFID tag design, since the ASIC impedance is supposed to be matched to the antenna impedance, so that the incoming electromagnetic energy can be effectively delivered to the ASIC. Unfortunately, being the transceiver a non-linear load with a strong reactive component, its input impedance varies upon frequency, and also depends on the bias point of the device, i.e., on the input power level. As a result, since RFID tags are designed to obtain good impedance matching at the minimum power level required by the ASIC to operate, significant mismatch may occur when the incoming power level is strongly increased (e.g., when the tag is very near to the reader) [13]. Although in most cases passive tags continue operating even in close proximity of the reader, some special tags with very narrow bandwidth may lose their functionality in this situation. For this reason, many efforts are done by the designers in order to reduce the power dependence of the ASIC input impedance.

To simplify the tag antenna design, the ASIC input impedance Z_C is usually modeled by a parallel combination of a resistance R_c and a capacitance C_c, whose values (for an input power in the vicinity of P_{th}) are provided by the manufacturer. Although this is a simplified model, it is considered as a useful approximation inside the operational bandwidth of a typical passive UHF-RFID tag, which is in the order of few tens of MHz. While the resistance R_c accounts for the power dissipated by the active load, the capacitance C_c includes all the capacitive effects associated to the rectifying diodes and to the energy-storing capacitors of the charge pump. In order to facilitate the impedance

TABLE 1 INPUT CHARACTERISTICS OF SOME COMMERCIAL UHF-RFID CHIPS.

	P_{th} (dBm), typical	R_c (Ω)	C_c (pF)	τ_c (ns)	Z_C (Ω) at 915 MHz
Alien Higgs 4	−18.5	1800	0.85	1.53	$23 - j202$
Alien Higgs 3	−18	1500	0.85	1.27	$27 - j201$
Alien Higgs 3 (SOT-323)	−17	1500	0.9	1.35	$25 - j190$
Impinj Monza 5	−17.8	1800	0.825	1.48	$24 - j208$
Impinj Monza 4	−17.4	1650	1.21	2	$12 - j142$
Impinj Monza X-2K Dura	−17	1600	1	1.6	$19 - j172$
NXP UCODE G2XM	−15	1385	1.16	1.61	$16 - j148$

matching to the tag antenna, and to obtain reasonable bandwidth, the ASIC input capacitance should be maintained as low as possible. However, design considerations impose a tradeoff between the input capacitance and the energy harvesting efficiency of the charge pump, so that the input capacitance cannot be decreased indefinitely. As a result, the input impedance of UHF-RFID ASICs typically present strongly capacitive input impedance, with a reactance in the order of hundreds of ohms, and a resistance of few tens of ohms. As it will be detailed at Section 3.2.2, the product $\tau_C = R_c C_c$ is an important design parameter, since it is inversely proportional to the maximum bandwidth that can be accomplished by the tag under optimal conditions. The main input characteristics of some commercial RFID ASICs are resumed in Table 1.

3.1.2 Passive UHF-RFID tag antenna

In this section, an overview of the antenna characteristics in the frame of passive RFID tag is provided. Firstly, the main radiation parameters of tag antennas, and their relation with the tag performance, are discussed. The exposition is then focused on reporting the most common design solutions and tips employed in commercial tags, discussing the limitations and tradeoffs typically encountered in each case.

3.1.2.1 Tag antenna parameters

The *radiation efficiency*, η_{rad}, of an antenna is the ratio between the power radiated by the antenna and the power accepted by the antenna, which includes the ohmic losses within the antenna conductors and dielectrics. Obtaining high radiation efficiency is one of the most important goals in passive tag antenna design. In fact, it is easy to understand that higher radiation efficiency leads to better performance in terms of read range, because a larger part of the energy coming from the reader can be delivered to the ASIC. Whereas in many cases obtaining high radiation efficiency is not a problem, things become challenging when dealing with very small tags, or when the tags are attached to items made of high-loss materials.

The *radiation pattern* is also very important for the tag performance, since it describes how the tag antenna is able to collect (or radiate) energy from different directions. Usually, but not always, an isotropic-like pattern is the optimal pattern of passive tag antennas. This is especially true for general-purpose tags, or in any case the tag orientation in the application scenario is unknown a priori. When the tag orientation is known, however, a more directive pattern may be preferred, since it allows increasing the tag read range in the desired direction, sacrificing the tag performance in other directions.

The quality of the communication link between the tag and the reader is also dependent upon the *polarization* of the tag antenna. It is well known that, in order to obtain efficient coupling between two antennas, their polarization must be matched. However, in general, the polarization mismatch depends upon the relative orientation between antennas, which is not known in advance in many RFID applications. Generally, tag antennas are provided with single linear polarization, to contain the tag size and cost. Therefore, the task of managing the polarization mismatch is charged to the reader, which, by its nature, is a more complex and costly device. A typical approach is to provide the reader antenna with circular polarization. As a drawback, the read distance is reduced because the tag receives only half of the incoming energy, which is spread in two orthogonal polarizations. Due to its simplicity, this solution is commonly used when the read range reduction is acceptable. Otherwise, in order to reduce the sensitivity to orientation while maintaining unaltered the potential read range, readers using alternate polarization have been recently commercialized (e.g., *Impinj Speedway xPortal*). In this case, the reader continuously switches between two linear orthogonal polarizations, so that all the power is received when the tag is properly aligned, and half of the power is received in the worst scenario, that is, when the tag angle with respect to each reader polarization is 45º. However, this solution requires additional circuitry in the reader, increasing its cost and complexity. As an alternative, the tags are properly arranged so that their orientation is known in advance. Obviously, this solution is only possible in some applications (e.g., library management, pallet tracking, assembly lines) provided that a certain control over the item arrangement is obtained. In this case, it is preferable to use simple linear polarized reader antennas, which allows maximizing the tag read range.

Being related to the energy transfer with the ASIC, the antenna *input impedance* is also a fundamental parameter in passive tag antenna design. As explained above, the impedance of the ASIC is typically capacitive, so that, for conjugate matching, an inductive behavior of the load is required. However, in few cases an antenna provides suitable matching when directly connected to the transponder, so that a matching network is usually introduced to improve the energy transfer. Nevertheless, when the antenna impedance is particularly different from the required value, matching can be difficult even using a dedicated matching network. This is because, to reduce the tag cost and to maintain a planar geometry, distribute matching elements are used, rather

than lumped elements, so that the reactance values which can be obtained in practice are penalized.

The frequency variation of the antenna input impedance is strictly related with antenna *bandwidth*. In passive tags, a wider bandwidth has a series of advantages over a narrow bandwidth. First, although a very small bandwidth (in the order of few MHz) is required for a tag to operate in one region, a noticeably wider bandwidth is necessary to ensure uniform performance worldwide. As stated in the previous chapter, the UHF-RFID band currently spans from 840 MHz to 960 MHz all over the world, so that it is actually troublesome to obtain a tag which offers the same performance in different locations. Another advantage of wideband antennas is that they are less sensitive to detuning, which may occur in response to the permittivity of the tagged item. Consequently, tags with a wider bandwidth are more likely to work efficiently over a higher range of materials.

The relationship between the abovementioned parameters will be further detailed at Section 3.2, where analytical expressions for the tag read range and bandwidth will be provided. An overview of the most common tag antenna designs is provided at the next section.

3.1.2.2 Common tag antenna designs

Most general-purpose UHF-RFID tags are based on planar *dipole* antennas. In fact, this kind of antenna is simple, efficient and versatile. Its geometry can be adjusted to a great number of shapes, and its lateral dimensions can be tailored to fit even relatively small items. The most commonly known type of dipole antenna is the half-wave dipole, consisting of two linear wires whose overall length is approximately equal to half the wavelength at the working frequency. However, since a half-wavelength at the UHF RFID band exceeds 15 cm, unmodified half-wave dipole antennas are rarely used for general-purpose tags. Instead, size-reduction techniques are usually employed to obtain smaller versions of the half-wave dipole antenna. Among them, the most commonly used is meandering, which involves folding the radiating body by a certain number of times, reducing its lateral dimensions while maintaining its total length substantially unaltered [14]. When designing a dipole antenna, meandering can be applied to a certain degree, so that the resulting tag size can be adjusted according to the application constraints. In Figure 3.4a, examples of commercial passive tags with increasing degree of meandering, from left to right, are shown. Whereas the final dimensions of most general-purpose tags using meandering are in the range of 7-10 cm, strong meandering allows obtaining tags whose size is reduced to few centimeters. However, the size reduction provided by dipole meandering is always paid with a reduction of the tag performance. In fact, while all the current elements in a straight dipole contribute positively to radiation, the currents in neighboring arms of a meander flow in opposite directions, so that their contributions to radiation are almost totally cancelled. In a

heavily-meandered dipole, only a small part of the current contributes to radiation, while the rest merely produces energy loss due to ohmic heating inside the non-perfect conductors. As a result, the antenna resistance acquires very small values, encumbering the impedance matching to the ASIC, and its radiation efficiency decreases, involving significant degradation of the tag performance. Moreover, belonging to the category of electrically small antennas, heavily meandered dipoles are characterized by significant reductions of bandwidth, according to very well-known physical limitations [15, 16].

For these reasons, a tradeoff between the degree of meandering and the antenna performance exists, and the antenna size is rarely reduced below 3 cm for commercial tags (as one of the few exceptions, the smallest dipole-based label currently offered by Alien Technology, covers 2.25cm x 2.25cm, but the read range is not declared).

Another very common size-reduction method applied to tag dipole antennas, often combined to meandering, is capacitive tip loading [8]. In this case, the final part of each arm is significantly widened, in order to increase the antenna series capacitance, and, consequently, to lower the self-resonant frequency. This allows obtaining shorter antennas which are still relatively easy to match with the ASIC for proper energy transfer. Moreover, since the resistance of a conductive path is inversely proportional to its width, capacitive tip loading also allows limiting the ohmic losses, which is specially critical when working with reduced-conductivity materials, such as the conductive inks occasionally used for printed tag antennas. The commercial tags shown in Figure 3.4b are examples of dipole design emphasizing tip loading, while the tags represented in Figure 3.4c exhibit a tradeoff between meandering and tip loading.

Other variations of the dipole structure are often aimed at increasing the antenna bandwidth. In particular, passive tags characterized by fat dipole antennas encountered wide commercial deployment in the last years. It is well known that, by increasing the dipole width, the antenna inductance is reduced, while its capacitance rises [17]. Consequently, the antenna quality factor of a fat dipole is lower as compared with a thin dipole of the same dimensions, thus it can operate over a wider frequency range. Provided that the width dependence of the antenna quality factor is relatively weak, a substantial broadening of the dipole is necessary in order to obtain an appreciable bandwidth improvement. Therefore, combining this technique with meandering is unpractical. Moreover, very fat dipoles may increase the tag manufacturing cost, depending on the antenna fabrication process. Application examples of this technique are provided by the tags of Figure 3.4d.

An important limitation of dipole antennas for RFID tags results from their radiation pattern. In fact, there exist two directions in which the radiated (or received) power is zero, so that a blind spot in the tag reading pattern appears around each of these zones.

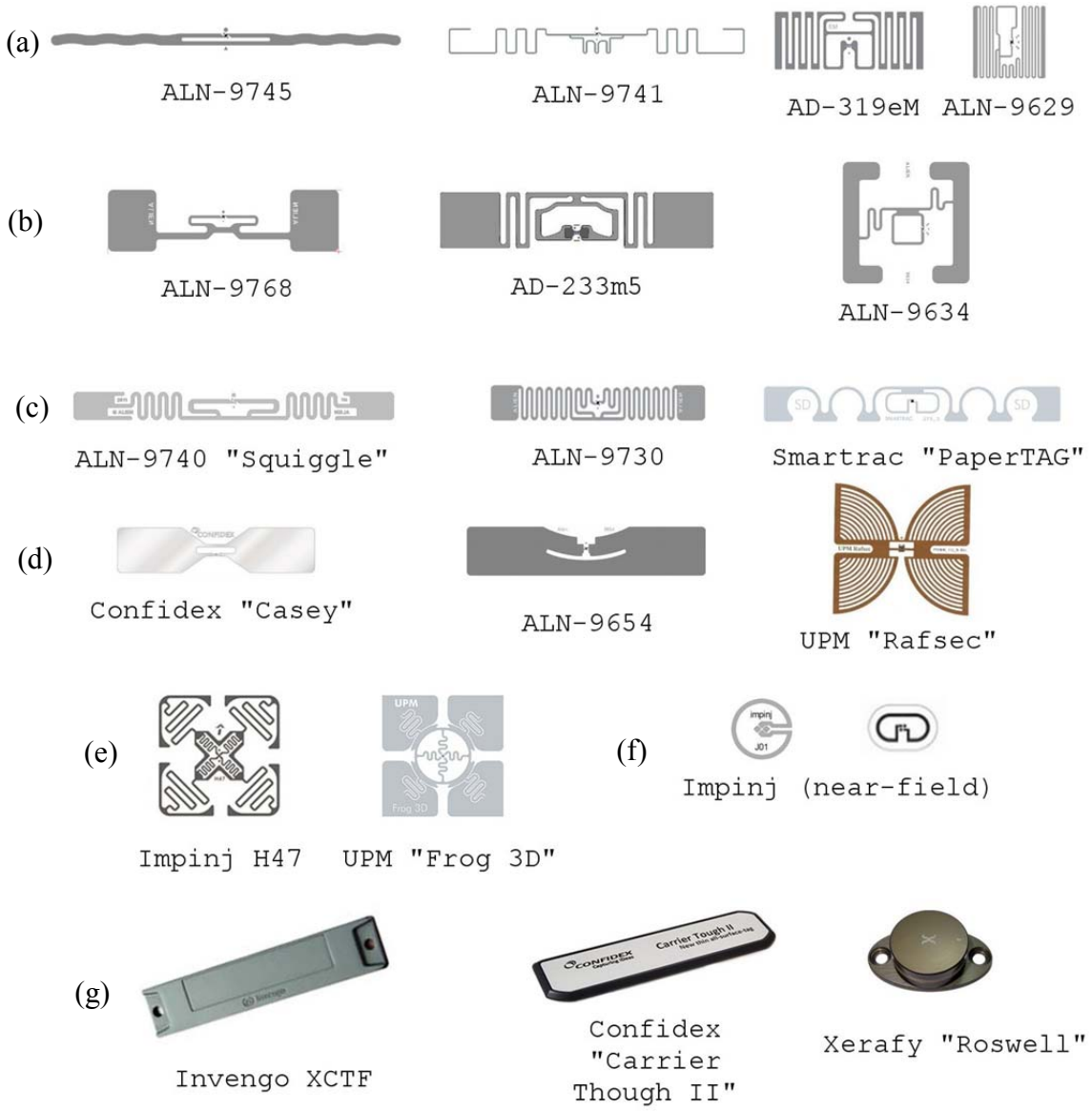

Figure 3.4. Examples of commercial passive UHF-RFID tags (not drawn to scale), classified by antenna type: (a)-(e) dipole, (f) small loop and (g) metal-friendly antennas. Design solutions, such as (a) meandering, (b) tip loading and (c) a combination of both, (d) dipole widening and (e) orthogonal radiators can be seen for the dipole-based tags.

In many RFID applications, the orientation of the tag is not known a priori, so that reading failures of relatively near tags may occur due to bad orientation. The most common solution to this problem is to provide the tag with two orthogonal dipole antennas (see Figure 3.4e), which entirely cover the tridimensional space in an isotropic-like pattern. However, more complex ASICs are required in this case, because each antenna requires an independent input, equipped with a dedicated RF frontend. Also, the tag area is increased, and its shape is constrained to a square, which can be unsuitable in some cases.

Although the electric dipole antenna, and its derived structures, is the most commonly used in passive tag antenna design, there exist some alternative solutions. When the tag dimensions are required to be extremely small, in the order of 1 cm, a commonly used design is the *loop* antenna. Being much smaller than the wavelength at the working frequency, this behaves as a homogeneous current loop, generating a voltage on the ASIC as a response of an oscillating magnetic field across the loop surface. However, since the radiation of a small loop is dependent upon the fourth power of its dimensions in terms of wavelength, the radiation resistance associated to loops of such dimensions is extremely small. Hence, rather than working as an antenna, the tag loop behaves as an inductor, so that the communication with the reader is dominated by inductive coupling. For this reason, tags based on small loops are typically constrained to near-field applications, with reading distances in the order of few tens of centimeters. In Figure 3.4f, some commercial loop-based tags oriented to near-field applications in the UHF-RFID band are illustrated.

Small loop antennas are sometimes combined to electric dipole to form *hybrid* tags. This tag typology is able to work in far-field, by using radiative coupling, and also takes advantage of the reliability of inductive coupling for near-field applications. Since a loop structure is often introduced as a matching network for dipole tag antennas (see next section), many general-purpose tags can be classified as hybrid tags, though not specifically designed for near-field operation.

To conclude this brief description of the most commonly used antenna types in passive UHF-RFID tags, special mention must be done to *patch* antennas. In fact, this kind of radiator, along with its derived structures, is the most common solution for on-metal operation. For their nature, patches operate on ground planes. Unlike electric dipoles, whose radiation is cancelled when attached on conductive surfaces, patches benefit from the field reflection on the metal plane, resulting in a significant increase of directivity. Hence, provided that good radiation efficiency is obtained, the reading performance of tags mounted on metallic surfaces can be even better as compared to general-purpose tags, with some designs exceeding 20 m of reading distance [18, 19]. However, a challenging aspect of on-metal passive tag design, which still represents a significant limitation with respect to general-purpose tagging, is related to the tag thickness and cost. In fact, in order to properly operate, patch antennas require a certain thickness of dielectric material between the upper patch and the underlying ground plane. The height of a patch antenna for optimal operation in the UHF-RFID band is in the order of the centimeter, which make it suitable only when a relatively thick tag is acceptable. The patch height can be reduced to the order of a millimeter or smaller, as currently done by many commercial on-metal tags, but this improvement is hardly paid with a drastic reduction of the operating bandwidth and radiation efficiency. Moreover, native patches require interconnection of the input port between the upper layer and the ground plane. Although this can be accomplished by several methods (e.g., via hole in the substrate, wraparound connection on the side of the dielectric), the tag

manufacturing cost is relatively high in any case [8]. For these reasons, even after extensive effort and research, on-metal tags based on patch antennas are still more expensive and bulky as compared to general-purpose tags. Commercial examples of on-metal tags, which are likely to be based on patch-type antennas, are shown in Figure 3.4g.

The alternative solutions reported in the literature will be detailed in Section 3.4, where the state of the art of low-profile on-metal passive tag design will be treated.

3.1.2.3 Impedance matching methods

Due to the highly capacitive ASIC input impedance, passive tag antennas often require the aid of a matching network to maximize the energy transfer. Although, as a result of the intensive antenna research of the last years, several matching methods are known, two solutions in particular have seen wide implementation in the context of passive UHF-RFID tag design.

The first and most common method is based on the use of a *T-match* network. Although many variations exists, the structure is characterized by connecting the ASIC to a short stub, oriented parallel to the main dipole and separated from it by a certain distance, whose ends are connected to the radiating dipole by means of shorts circuits (Figure 3.5a). The T-match was first proposed by S. Uda and Y. Mushiake [20], who also provided a transmission line model to explain its behavior. Initially proposed as an impedance transformer for cylindrical-wire dipole antennas, the structure was then applied to planar structures, and eventually to passive UHF-RFID tags [14, 21, 22]. However, the lack of a systematic design flow, resulting from the poor accuracy of the analytic equations describing the structure, caused the design of a T-match network to be complex. Partly motivated by the wide employment of the T-match network in RFID tag antenna design, many efforts have been directed at obtaining simpler circuit models, thus simplifying the design and synthesis process [8, 10, 21, 23].

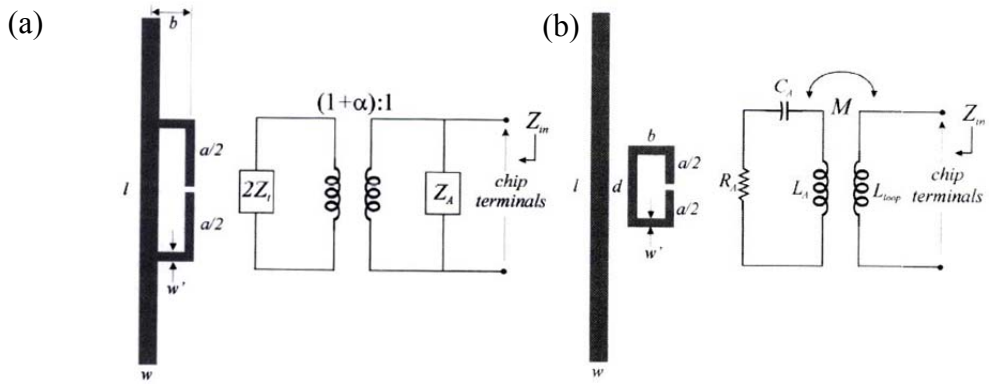

Figure 3.5. Schematic representation of impedance matching to a dipole antenna by means of (a) T-match network and (b) inductively coupled feed. Extracted from [14].

Examples of T-match networks, applied in different variations to commercial passive tags, can be observed in all the dipole-based inlays presented in Figure 3.4.

An alternative to the T-match network, which has been used in passive tag antenna design working at the UHF band, is the *inductively coupled feed.* In this case, the ASIC is connected to a small loop which is placed nearby to the dipole antenna, in the vicinity of its current maximum (which, in the case of a symmetric structure, is also its geometrical center) (Figure 3.5b). Due to the mutual inductance between the loop and the dipole wire, the magnetic field associated to the small loop induces an electric current on the dipole, feeding it for radiation. Moreover, the antenna impedance seen from the ASIC can be adjusted by varying the magnitude of the mutual inductance, which depends upon the loop area and its distance from the dipole, until obtaining proper impedance matching. One advantage of this method is that the system admits a relatively simple circuit model, and therefore the equations used in the design process are also relatively simple. This technique is especially effective when working with highly reactive ASICs [14].

In any case, the introduction of a matching network results in additional ohmic losses, worsened by the fact that inductive paths are often required being narrow. While this is not a problem for relatively large antennas, it may introduce a significant degradation of the radiation efficiency when the antenna dimensions are reduced to challenging values. Thus, direct matching to the ASIC should be attempted in these cases, making the impedance matching a special design concern in the context of tag miniaturization.

3.2 Passive tag performance

In this section, the main performance indicators of passive UHF-RFID tags will be discussed. In particular, the tag read range and bandwidth will be treated, being the most commonly used parameters for quantifying the tag performance. At the end of this section, the measurement setup for obtaining the experimental data exposed throughout this work is detailed.

3.2.1 The read range

For most applications, the most important tag performance indicator is the read range. The read range is the maximum distance, between the reader antenna and the tag, allowing a successful reading of the tag content. Usually, the reader sensitivity is much smaller than the tag sensitivity, so that the limiting factor is the tag performance, i.e., whether or not the tag collects enough energy to activate is transponder.

As mentioned before, the read range of a passive tag not only depends on the characteristics of the tag itself. Its orientation, the materials where the tag is attached, the presence of obstacles towards the reader, nearby objects and even nearby tags, may degrade the read range [24]. For these reasons, the read range is measured under optimal conditions, which can be obtained in a controlled environment. In this case, a simple expression for the maximum read range *RR* can be found, on the basis of the Friis transmission equation, as follows [25]:

$$RR = \frac{\lambda_0}{4\pi}\sqrt{\frac{EIRP \cdot G_0 \cdot \tau}{P_{th}}}, \tag{3.1}$$

where λ_0 is the free-space wavelength at the working frequency, *EIRP* is the equivalent isotropically radiated power from the reader, G_0 is the maximum tag antenna gain, τ is the power transmission coefficient between the tag antenna and the ASIC (which is related to the power reflection coefficient, $|s_{11}|^2$, by $\tau = 1-|s_{11}|^2$) and P_{th} is the ASIC threshold power.

It can be deduced from (3.1) that the theoretical read range of a tag is determined by the antenna (G_0, τ) and the ASIC (P_{th}) characteristics, but also depends on the regional regulations on EM emissions at the UHF band, which limit the *EIRP* associated to the reader to a certain value. A very common value, used in most countries including United States, China, Japan, Australia and South America, is *EIRP* = 4 W, while a value of *EIRP* = 3.3 W is used in other countries, including Europe and Singapore [9].

For a given region (i.e., fixing the value of EIRP and the operation frequency), the predicted read range can be represented as a function of the antenna realized gain G_r (that is, the factor $G_0 \cdot \tau$) and the ASIC sensitivity P_{th}, as depicted in Figure 3.6a. For example, in case the realized gain is 0 dB and the ASIC sensitivity is −18 dBm, the predicted read range is around 13 m. For the same ASIC, an antenna gain of −10 dB

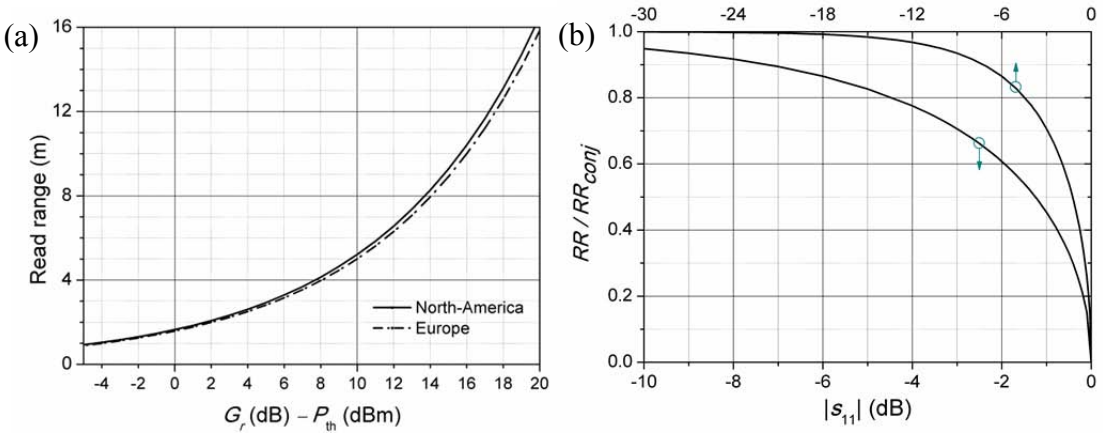

Figure 3.6. Theoretical (a) read range as a function of the antenna realized gain and the ASIC sensitivity, and (b) normalized read range as a function of the power reflection coefficient.

would provide a read range of 4 m, suggesting that even relatively poor antennas can provide useful performance in UHF-RFID tags. Let us now examine the influence of the impedance mismatch over the tag read range. Again, this can be done on the basis of (3.1). In Figure 3.6b, the read range, normalized to the value obtained in conjugate matching conditions, is plotted as a function of the power reflection coefficient between the antenna and the ASIC. It is worth mentioning that a value of $|s_{11}| = -10$ dB, which is considered inappropriate or poor in many microwave applications, still provides 95% of the maximum read range of passive RFID tags. Even smaller values may result acceptable when the read range reduction is acceptable, at the expense of tag dimensions or complexity.

Expression (3.1) predicts the read range when both reader antenna and tag antenna are oriented towards each other in the direction of maximum gain and their polarizations are matched. When the tag is oriented at a different direction towards the reader, (4.15) can still be used by replacing G_0 by the tag antenna gain G in that specific direction. In the case of polarization mismatch, the gain must be multiplied by the polarization loss factor, *PLF*, which can be defined as the squared module of the dot product between the polarization vectors of each antenna [17].

3.2.2 Tag bandwidth

Due to the physical limitations regarding the behavior of both the tag antenna and the ASIC, RFID tags can properly operate only in a limited range of frequencies. Normally, the most restrictive limitation comes from the antenna, since electrically small antennas are generally used for UHF-RFID tags. According to the classical definition, introduced by H. Wheeler in 1947 [16], an electrically small antenna is any antenna whose maximum dimension is less than the "radianlength", corresponding to $1/(2\pi)$ wavelengths. Derived from such definition, electrically small antennas must satisfy the the condition $ka < 0.5$, where a is the radius of the smallest sphere enclosing the antenna and $k = 2\pi/\lambda_0$ is the wavenumber in free-space at the working frequency. Consequently, the boundary for an electrically small antenna at the UHF band is a total length of around 5 cm, which is comparable to the size of most the passive tags available on the market. As it was demonstrated in many works, firstly by H. Wheeler [16] and Chu [15] at the end of the 40s, small antennas are subjected to significant limitations. Specifically, the radiation quality factor Q_{rad}, defined as the ratio between the reactive power stored in the fields around the antenna and the power radiated by the antenna, encounters a lower bound, expressed by Chu as $Q_{\text{rad}} \geq (1/ka)^3 + (1/ka)$. For very small antennas, the expression can be simplified, since the second term on the right side is much smaller than the first term. Recently, W. A. Davis *et al.* presented a new version of the limit, which definitely simplifies the lower bound to $Q_{\text{rad}} \geq (1/ka)^3$ [26] for any antenna dimension. However, the presented limit applies to the general case of tridimensional

antennas, that is, those structures who take advantage of the whole volume contained in the minimum sphere closing the antenna. The limitations of antennas confined to planar geometry were first studied by M. Gustafsson [27], as an extension of the work of Harrington and Chu. It was found that the minimum radiation quality factor Q_{rad} for a planar antenna enclosed in a sphere of a radius a is at least $9\pi/8$ times higher than the lower bound for any antenna enclosed in the same sphere [27, 28]. Therefore, taking into account that the total quality factor accounting for losses is $Q = Q_{rad} \cdot \eta_{rad}$, it follows that

$$Q \geq \frac{9}{8}\pi\eta_{rad}\left(k_0 a\right)^{-3}. \tag{3.2}$$

As it is well known, the quality factor of a system is inversely proportional to its bandwidth, so that very small values of a lead to significant bandwidth degradation. The antenna half-power fractional bandwidth, assuming conjugate matching, can be expressed as [29]

$$FBW \approx \frac{2}{Q} \leq \frac{128}{9}\pi^2\eta_{rad}^{-1}\left(\frac{a}{\lambda_0}\right)^3. \tag{3.3}$$

Expression (3.3) is valid for $Q >> 1$, a condition normally satisfied for an electrically small antenna with acceptable radiation efficiency. According to (3.3), a tag length of 5 cm limits the half-power bandwidth to about 50 MHz at the UHF band, a poor value to ensure uniform operation worldwide. The situation gets worse for tag length in the order of 3 cm, where a bandwidth of 10 MHz can be obtained in the best case.

The frequency behavior of the antenna and ASIC impedance, and the consequent read range, for a typical dipole antenna-base tag, is represented depicted in Figure 3.7. It can be seen that the read range usually peaks when the impedance of the antenna matches

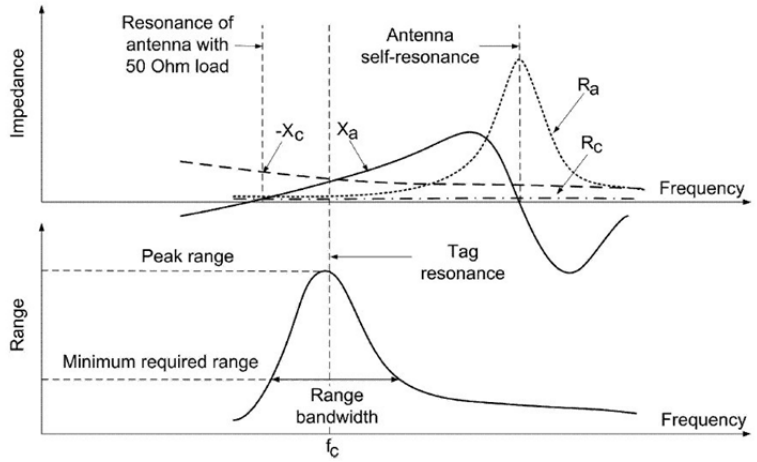

Figure 3.7. Qualitative behavior of the antenna impedance, ASIC impedance, and read range as functions of frequency for a typical RFID tag. Extracted from [25].

the ASIC impedance, because the power transmission coefficient τ is the dominant factor in (3.3), in terms of frequency dependence.

Up to now, we discussed about the tag bandwidth limitations imposed by the antenna. Even though the tag bandwidth is typically limited by the antenna, this is not necessarily true. In fact, in case the antenna is sufficiently large, the tag bandwidth is eventually limited by the ASIC quality factor. On the basis of the Bode limit [30], the maximum half-power bandwidth achievable by a tag can be expressed as [31]

$$BW \leq \frac{1}{\pi R_c C_c}, \tag{3.4}$$

where R_c and C_c are the resistance and capacitance of the ASIC shunt circuit model, respectively. However, the typical values of R_c and C_c of modern ASICs (see Table 1) allow very high bandwidth values, in the range of 150-250 MHz.

3.2.3 Measurement setups

There exist several methods to measure the read range of passive tags. In any case, a controlled environment must be created, where the link between the reader and the tag is free from reflections, and far-field conditions between antennas are accomplished. The most simple and direct method is to use a commercial UHF-RFID reader. The tag distance is increased until the communication is lost, i.e., when the tag stops responding. The measuring process can be carried out in an anechoic chamber, or, alternatively, in a TEM cell, which represents a much more economical solution. The most important limitation of this method is that commercial readers are usually designed to operate at just one region, making impossible a frequency characterization of the read range. Some readers are provided with multi-region functionality, but even in this case a continue curve of the read range over the whole UHF band cannot be obtained.

A suitable alternative to solve this problem, employed throughout this work, is to emulate the behavior of an RFID reader, by means of electronic test equipment (e.g., signal generators and analyzers) commonly found in RF laboratories, which allows a high degree of freedom in the operation frequency. The measuring setup available in our laboratory is detailed as follows.

An *Agilent N5182A* vector signal generator, capable of generating RFID interrogation frames, is connected to a TEM cell (*WaveControl WaveCell*) by means of a 50 Ω coaxial cable. To increase the output signal power, a solid state RF amplifier (*RFPA RF101000–10*) may be cascaded between the signal generator and the TEM cell, when required. The tag under test is placed inside the TEM cell and oriented along the maximum directivity axis, or, alternatively, along others directions of interest. A

circulator is used to send the backscattered signal from the TEM cell to an *Agilent N9020A* signal analyzer, which is equipped with a software allowing demodulation of RFID frames, and detects whether or not the tag is responding to the interrogation frame. To measure the tag read range, an RFID interrogation frame is sent to the TEM cell at different power levels, in order to determine the minimum power level $P_{\min}$ required to activate the tag, that is, to receive a backscattered response frame. An isotropic electric field probe *(WaveControl EFCube*) is then placed at the tag position in order to measure the root mean square of the electric field E_{rms} generated by the interrogation frame at the power $P_{\min}$. Being E_{rms} the minimum electric field required for the tag operation, is possible to calculate the read range directly from its value. In fact, the average power density S associated to a plane wave is determined from the value of the electric field E_{rms} according to

$$S = \frac{E_{\text{rms}}^2}{Z_0}, \tag{3.5}$$

where Z_0 is the impedance of free space. For a radiating antenna, the far-field Poynting vector module in a given direction is given by

$$S = \frac{EIRP}{4\pi r^2}, \tag{3.6}$$

where r is the distance from the antenna. Thus, the read range RR can be obtained by equating (3.5) and (3.6), resulting in

$$RR = \frac{\sqrt{30EIRP}}{E_{\text{rms}}}. \tag{3.7}$$

The method described above is then repeated for each frequency of interest (e.g., at 5 MHz steps) in order to obtain the read range in the whole UHF band, or in the band of interest of a specific tag. A scheme of the described setup, along with a photograph, is provided in Figure 3.8.

An approximate value of the tag half-power bandwidth can be extracted from the measured read range, on the basis of (3.1). This can be accomplished by considering that the frequency dependence of the read range is typically dominated by the power reflection coefficient, τ, so that the frequency dependence of the rest of parameters can be neglected. Under this assumption, and considering conjugate matching between the antenna and the ASIC, the tag half-power bandwidth is defined by the two frequency points where the read range is reduced by a factor $\sqrt{2}$ with respect to its peak value. Obviously, the narrower is the tag bandwidth, the more accurate is the method.

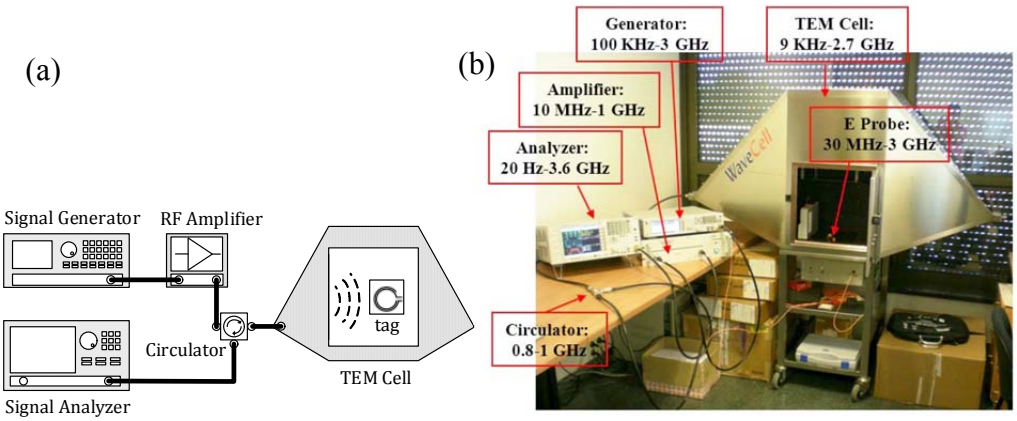

Figure 3.8. (a) Scheme and (b) photograph of the tag read range measurement used throughout this work.

The described technique can also be extended to measure the tag normalized radiation pattern at a given frequency. To this end, the tag orientation inside the cell was swept, with a step of 30º in our case, by means of a foam rotatable support. At each angle, the value of the power $P_{\min}$ required to activate the chip is measured. The normalized pattern was then obtained dividing the required power $P_{\min,0}$ at the maximum gain direction by the minimum required power $P_{\min,i}$ at the *i*-esim direction. This method allows measuring the radiation pattern of a tag antenna without connecting its input terminals to a measuring device by means of metallic cables. For very small antennas, this represents a clear advantage, because the presence of connectors and nearby coaxial cables may strongly affect the radiation and impedance behavior of the antenna.

A similar setup was also used to measure the gain of small antennas in a given direction. In this case, the prototype was placed inside a TEM cell, and oriented towards the direction of interest. The cell was excited with a pure tone at the operation frequency, generated by means of the vector signal generator and amplified through the RF amplifier. The signal received by the antenna was delivered, by means of a coaxial cable, to the input port of the signal analyzer, where the input power P_r was measured. Finally, the antenna was removed from the chamber, and replaced by the electric field probe, carefully placed at the same position. The electric field strength E_{rms} measured by the probe was used to evaluate the antenna gain G_0 as

$$G_0 = \frac{4\pi Z_0}{\lambda_0^2}\frac{P_r A}{E_{\text{rms}}^2} \quad , \tag{3.8}$$

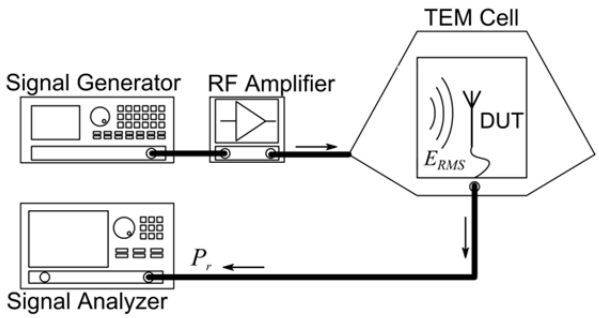

Figure 3.9. Scheme of the antenna gain measurement by means of the TEM Cell.

where the dimensionless parameter A accounts for the losses introduced by the cable and the balun used to feed the antenna. Equation (3.8) is based on the common definition of antenna effective area as the relation between the received power and the incident power density, and assumes a pure TEM propagation inside the cell. This configuration is outlined at Figure 3.9.

3.3 Metamaterial-inspired resonators: overview and application to passive UHF-RFID tag design

Since its first appearance by the end of the 60s, the concept of metamaterial has raised a lot of interest in the scientific community. The promising potentialities of metmaterials triggered a large number of research efforts in several fields, such as optics, microwave devices and acoustics, with several books have been written on the subject [32-36].

Metamaterials can be defined as "artificial media with unusual electromagnetic properties" [32, 33], or, to a more specific description, as "artificial effectively homogeneous electromagnetic structures with unusual properties not readily available in nature" [35]. Concretely, these unusual "properties" refer to exhibiting negative electric permittivity and negative magnetic permeability, at the same time, which has never been observed in any known ordinary matter. Wave propagation in negative parameters media was first studied by the V. G. Veselago in its seminal paper at the end of the 60s [37]. The research predicted that propagation in these hypothetical bodies is characterized by negative phase velocity, so that phenomena such as the Doppler effect, Cherenkov radiation, and even the Snell's law, are inverted. Due to the reverse orientation of the triad formed by the electric field, the magnetic field and the direction of propagation, these structures were named "left-handed" media. Although these exotic properties, and, more generally, the controllability of the electromagnetic properties of matter, opened the doors to a wide range of applications, the possibility of synthetizing

such artificial materials had to expect more than 30 years. In fact, while media exhibiting negative electric permittivity are relatively common in nature (e.g., low-loss plasmas, metals and semiconductors at optical and infrared frequencies), media exhibiting negative permeability are rare. Traditionally, only ferromagnetic materials near resonance were known to exhibit negative magnetic response.

In 1999, J. B. Pendry proposed the first structure exhibiting very small electrical size and strong negative permittivity above its resonance, the split-ring resonator (SRR) [38], as an evolution of the structures proposed by Schelkunoff [39] and Hardy [40]. One year later, based on a periodic arrangement of SRRs and short wires, the first effective "left-handed" medium working at microwave frequencies was obtained [41]. From that moment on, the split-ring resonator, along with derived structures, was extensively used to obtain one-dimensional effective media metamaterials [42], including metamaterial transmission lines. Negative permeability (or mu-negative −MNG) [43], left-handed (LH) [44] and composite right-/left-handed (CRLH) [45] transmission lines have been implemented by loading a host line with SRRs (and with other additional elements for LH and CRLH lines). These artificial lines and other artificial lines based on modifications of the SRR topology (including the complementary counterpart, i.e., the CSRR [46]) have been applied to improve the performance and/or the size of microwave components and to implement new functionalities. Compact wideband and ultra-wideband (UWB) filters [47], power dividers [48] and microwave sensors [49, 50] among other devices, have been implemented by means of SRR- or CSRR-loaded lines. The control of the phase constant and characteristic impedance (a unique feature of metamaterial transmission lines) in SRR- and CSRR-loaded lines has also been successfully applied to the design of leaky-wave antennas with broadside and backward-to-forward radiation capabilities [51-53]. Along with the SRR, several electrically small resonators with similar properties have been successfully used to implement the unit cell of metamaterial structures. We refer to all those resonators, including the SRR, with the term metamaterial-inspired resonators. In Figure 3.10, some of the most common metamaterial-inspired resonators implemented in planar technology are shown. These include the two-turn spiral resonator (2-SR), the non-bianisotropic split-ring resonator (NB-SRR) and the open split-ring resonator (OSRR), among others, as well as all their complementary counterparts. Such a variety of different solutions allowed obtaining interesting results in electrically small antenna

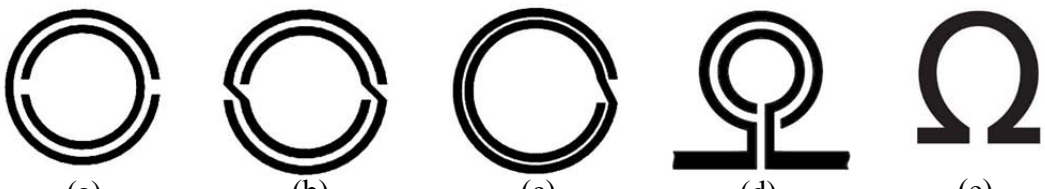

Figure 3.10. Some examples of metamaterial-inspired resonators in planar technology: (a) split-ring resonator (SRR), (b) non-bianisotropic SRR, (c) two-turns spiral resonator (2-SR), open SRR (OSRR), omega structure.

design, such as reducing dimensions [54, 55], obtain multiband and multi-frequency operation [56, 57], high radiation efficiency [58], and achieving tuning capability [59].

Over the years, the comprehension of the SRR behavior has been progressively extended. The resonance modes of SRRs have been extensively studied in [60], and the values of their resonance frequencies were analytically predicted in [61]. Nevertheless, since the particle is normally designed to work around its first (fundamental) resonance, all the theoretical studies have been focused on the properties of the SRR at that frequency. For instance, the first-order terms of the polarizability tensor of the particle have been quantified in [32, 62-64] by using the quasi-static analysis at the fundamental resonance. From such analysis, it follows that the SRR acts as a current loop at the fundamental resonance, thus suggesting the possibility of using it as a radiating element. However, since the particle size is in the order of 0.1 free-space wavelengths, and the radiation resistance of a current loop depends on the fourth power of the radius in terms of wavelengths, narrow bandwidth is expected, and impedance matching is troublesome. For these reasons, the SRR has been rarely used as stand-alone radiating element at the fundamental resonance [65]. Nevertheless, as it will be demonstrated in this work (at Sections 4.1 and 5.1), the SRR antenna working at around its first resonance is a suitable solution for obtaining small passive UHF-RFID tags with interesting performance. Moreover, the lack of research about the radiation properties of the SRR encouraged the study of the SRR behavior when operating around its second resonance, presented in Section 4.2.

3.3.1 Application to passive UHF-RFID tag design

The first applications of SRRs to passive RFID tag design are relatively recent. In 2008, S. Lim *et al.* presented a tag based on a split-ring resonator antenna [66]. In this work, however, the authors declare that the radiating part is only the external ring, being the internal ring much smaller and dedicated to the impedance matching functionality between the ASIC and the antenna (Figure 3.11a). Due to the significant difference between the internal and external radii, the SRR does not behave as its quasi-static analysis predicts, that is, the SRR electrical size in [66] is not reduced as compared to that of a single ring resonator [where $r_0 \approx \lambda_0/(4\pi)$, r_0 and λ_0 being the ring radius and the free-space wavelength, respectively]. The tag overall size is in the order of 5 cm, which is comparable to the size of many small tags obtained by means of meandering, or by other common techniques. Moreover, many important aspects relative to tag performance, e.g., radiation efficiency, bandwidth and read range are not treated in this work.

In 2010, B.D. Braaten *et al*. used a series combination of complementary open split-ring resonators (OCSRR) as a radiating element for a passive RFID tag working at the

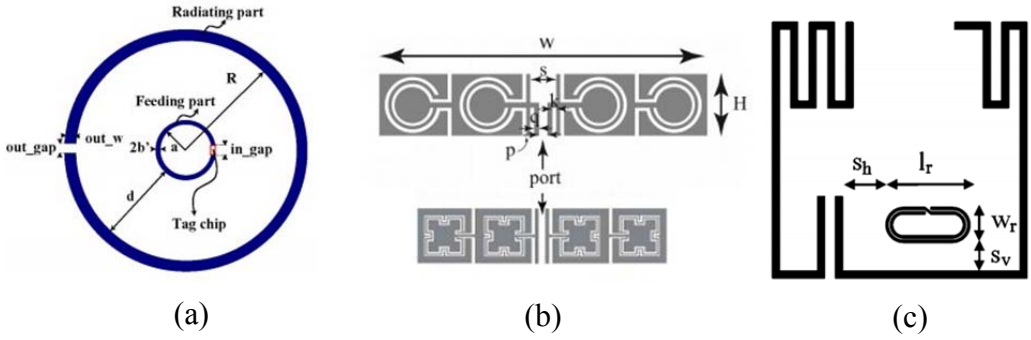

Figure 3.11. Application examples of metamaterial-inspired resonators to passive tag design. Works by (a) S. Lim *et al.* [66], (b) B.D. Braaten *et al.* [67, 68], (c) F. Paredes *et al*. [69].

UHF-RFID band [67]. As the authors claim, this solution is a valid alternative to meandering, and allows easily controlling the impedance matching to the ASIC. Nevertheless, although good performance in terms of gain was obtained (1.8-2 dB) by means of parametric optimization techniques, the lateral dimensions of the presented tag are still in the order of 5 cm, because four resonators were cascaded in series. Once again, the radiation properties of the resonator were not analyzed. Instead, the overall structure was modeled by a small electric dipole in terms of radiation, so that little control was achieved over the radiation properties of the tag. In the same year, the authors propose a meandered version of the complementary open split-ring resonators (MOCSRR), and applied it to reduce the dimension of their previous structure. Specifically, the lateral size was reduced to 3.6 mm, with an acceptable 25% loss in read range [68] (the abovementioned structures are depicted in Figure 3.11b). Comparable results were achieved by using deformed omega resonators in a similar manner [70]. As in the previous cases, however, the tag bandwidth was not declared, nor was a frequency-dependent read range measurement carried out.

Another important contribution came in 2010 by F. Paredes *et al.*, when split-ring resonators were employed for the first time to obtain dual-band functionality in passive UHF-RFID tags [71]. By loading a microstrip transmission line with an SRR, the authors achieved conjugate matching with the tag antenna at two arbitrary frequencies. In practice, very similar performance in different regions, such as Europe and North-America, could be obtained, which is troublesome to obtain by means of broadband tag approaches. The design process, based on equivalent circuit models and a perturbation method, was fully explained, and analytical expressions were provided. The same concept was then applied to obtain compact, dual-band tags based on meandered antennas and loaded with 2-SR resonators (Figure 3.11c) [69].

The suitability of a standalone SRR as antenna for UHF-RFID tags was explored again in 2013 by M. Polivka *et al*. [72]. Based on a set of parametric simulations of the SRR antenna in terms of impedance and efficiency, the authors concluded that the

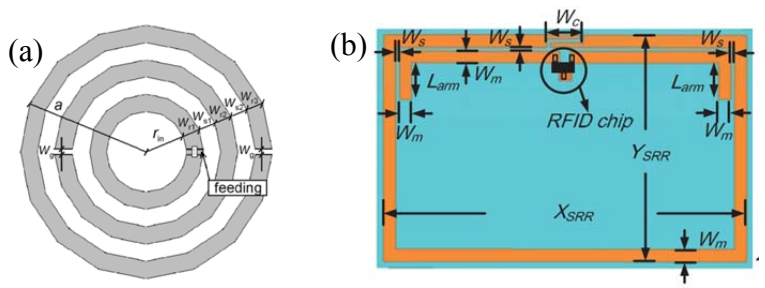

Figure 3.12. Modified SRRs proposed by (a) M. Polivka *et al*. [72] and (b) T.H. Cheng *et al*. [73].

minimum SRR external radius in order to obtain acceptable impedance matching to typical RFID chip impedances is in the order of 26 mm (λ/13). However, by adding a third split ring to the structure (Figure 3.12a), smaller overall size can be achieved (down to 16 mm in radius, corresponding to λ/21), while maintaining the possibility of proper impedance matching. The simulated radiation efficiencies ranged from around η_{rad} = 50% for the smaller structures, up to η_{rad} = 90% for an SRR antenna with a radius of 26 mm (the tags were manufactured on a thin *Taconic TLP-3* substrate of thickness h_s = 0.127 mm, relative permittivity ε_r = 2.33 and loss tangent tanδ = 0.0009). Based on the simulation results, a bandwidth comparison for different antenna sizes was also provided, suggesting that a 3% fractional bandwidth could be obtained in the best case.

More recently (2014), another SRR-based passive tag working at UHF was presented by T.H. Cheng *et al.* [73]. In this case, the authors loaded modified the split-ring resonator to a rectangular topology, and significantly shortened the internal ring (Figure 3.12b). The dimensions of the tag are 35 mm x 18 mm, but the radiation efficiency only reaches 25%, so that the tag read range is less than 2 meters (the tag was coupled to the *Alien Higgs-3* SOT-323).

The lack of analytical approach and design methodology in the reported state of the art inspired our contributions on this subject, which are described throughout chapters 4 and 5.

3.4 On-metal low-profile passive UHF-RFID tags: overview and state of the art

Since the beginnings of passive RFID tagging, great research effort was dedicated to find affordable solutions to the problem of metallic surfaces. As already mentioned, the performance of general-purpose passive UHF-RFID tags is severely degraded when they are attached to metallic surfaces [74-76]. This is because the metallic interface imposes a series of boundary conditions on the electric and magnetic fields, which are not compatible with the field distribution associated to electric dipole antennas placed parallel to the conducting surface. Such effect is also commonly explained in terms of image currents formed on the metal plane, which have opposite sign with respect to the antenna current, thus cancelling the radiation [17]. In terms of antenna properties, this involves a reduction of the radiation resistance and radiation efficiency, with consequent degradation of the impedance matching and gain. In Figure 3.13, the radiation efficiency of a typical T-matched folded dipole antenna placed at different distances over a metallic plane is depicted [77]. The plot suggests that the efficiency quickly falls towards zero when the thickness is in the order of the millimeter, and very small values (5%) are obtained even for distances of 3 mm.

The amount of challenges associated to the development of an on-metal UHF-RFID tag can vary a lot upon the application scenario of such tag. For example, applications related to industrial environments, such as railways, oil and gas, assembly lines, but also commercial applications such as access control and vehicle identification may not require the tag to be thin, small and cheap, or flexible. On the other hand, item-level identification of low-value small metallic items (e.g., tin cans, tools, spray bottles) may concentrate all the above mentioned requirements, thus resulting particularly troublesome. For these reasons, the research interest on low-profile small tags for on-metal operation remains high, and the following discussion will be limited on reporting the most relevant examples of size reduction in the context of on-metal passive UHF-RFID tags.

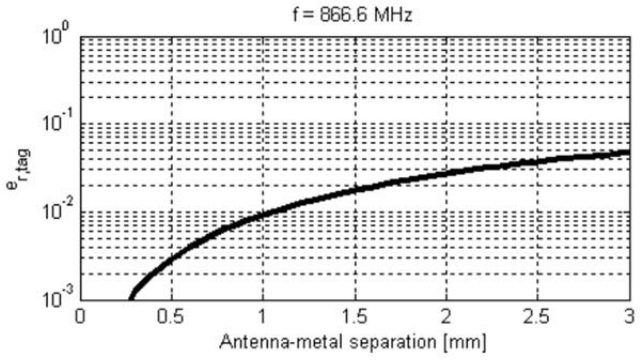

Figure 3.13. Radiation efficiency versus distance from metal of a folded T-matched dipole placed parallel to a metal plate. Extracted from [77].

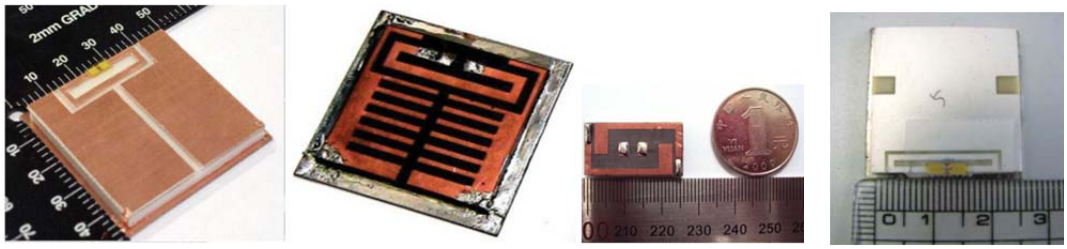

(a) (b) (c) (d)

Figure 3.14. Examples of patch-based low-profile small on-metal tags from the literature. Works from (a) B. Yu *et al.* [78], (b) T.V. Koskinen *et al.* [79], (c) J. Zhang *et al.* [80] and (d) J. Kim *et al.* [81].

Ever since the beginnings of passive tag design, a common approach for on-metal tags consisted of using patch-type antennas [82]. However, even the early tags exhibited some modifications to the conventional patch design, to reduce the antenna size, thickness and complexity to the constraints imposed by RFID tag design. In many cases, only one half of the patch is used, with a side shorted to ground, to form a PIFA antenna [83-85].

In 2007, B. Yu *et al.* proposed a tag based on two radiating patch elements, fed by means of inductive coupling (Figure 3.14a) [78]. The authors achieved small footprint (47.5 mm x 50 mm), and a thickness of 3 mm (obtained by sandwitching a 0.6 mm FR-4 layer with a 2.4 mm foam layer), while maintaining the read range in the order of 5 m. In 2008, the same research group proposed a more conventional design, consisting of a patch radiating element, matched by means of a feed line, with an overall thickness reduced to 1.6 mm [86]. However, the lateral dimensions of the tag were incremented to 40 mm x 80 mm, and the read range was reduced, ranging from 3.5 m to 4.2 m, as a function of the ground plane size.

In 2011, T.V. Koskinen *et al.* proposed a thinner version of the tag presented in [78], with similar lateral dimensions (Figure 3.14b) [79]. As a means to improve the tag bandwidth, the authors introduced a series of slots etched in the radiating patch, which allowed covering the whole 902–928 MHz band in spite of the very low profile of 1.6 mm over metal. Again, the thickness reduction was paid in radiation efficiency, with an antenna gain of −8 dB and a read range limited to 2 m.

Other attempts to further reduce the thickness of patch antennas also lead to a significant reduction of the radiation efficiency. In [87], trapezoid patch antennas of different sizes were designed, using a FR-4 substrate of thickness 0.8 mm. However, even the largest structure (60 mm x 90 mm) exhibited relatively low gain (−7 dB).

Recently (2014), J. Zhang *et al.* proposed a tag characterized by extreme miniaturization of the lateral dimensions [80]. The antenna design is based on two symmetric radiating patches, fed by means of inductive coupling, through an embedded

dual-element PIFA array (Figure 3.14c). In this case, the tag overall dimensions were reduced to just 26 mm x 14 mm x 2.4 mm. However, the structure requires two metal layers and two substrates (PTFE and FR-4, with thicknesses of 0.8 and 1.6 mm, respectively), which makes it complex for standard manufacturing. Moreover, good impedance matching was not fully accomplished, with a simulated power reflection coefficient limited to −4 dB.

Another reported approach to reduce the lateral dimensions of patch-based tags is the use of high-permittivity ceramic substrates. Early in 2008, J. Kim *et al.* combined the very high permittivity of the substrate ($\varepsilon_r = 48$) with the inductive coupling feed technique, obtaining a tag with extremely small footprint (25 mm x 25 mm) and relatively low-profile (3 mm) [81]. Despite its reduced size (Figure 3.14d), the antenna gain reached 0.5 dB, allowing read ranges exceeding 10 m when coupled to the recent ASIC available on the market. However, the use of ceramic makes the tags rigid and very expensive, and the thickness is greater compared to many other solutions.

Although they may be convenient for many applications, the solutions based on patch type antennas involve higher manufacturing cost and complexity as respect to the general-purpose labels, due to the presence of two or more conductor layers with interconnections. Moreover, rigid tags are obtained. For these reasons, research effort was also dedicated to mitigate the effect of metal on single-conductor label-type tags [88, 89]. In [88], the authors applied an optimization technique (the Pareto genetic algorithm) to a modified dipole antenna, to obtain similar performance in free-space and over metal. However, for acceptable performance, the label had to be spaced from the metal by means of a 3 mm thick foam substrate. Nevertheless, poor read range (2 m and 3 m, for free-space and on metal operation, respectively) was reported, in spite of the relatively large lateral dimensions of the tag (83.4 mm x 29.9 mm). In 2011, Koo *et al.* proposed the introduction of a loop-structure surrounding a folded dipole antenna, to mitigate the effect of the metal [89]. Although representing an improvement over an unmodified dipole antenna, the results suggested a severe degradation of the gain (−11 dB) when the tag was placed at 1 mm from the ground.

Other designs, also aimed at minimizing the tag complexity, focused on the reduction of the lateral dimensions. To this end, ceramic substrates have been used to obtain extremely small tags based on dipole antennas and slot antennas. In the first case, along with reducing dimensions, the high permittivity of the substrate was a means to obtain a greater effective distance from the metal plane, mitigating its negative effects. In 2012, T. Björninen *et al.* obtained a small (14 mm x 28 mm) and flexible tag by using a composite barium titanate ($BaTiO_3$) substrate with a thickness of 1.5 mm (Figure 3.15a) [90]. Due to its small footprint and flexibility, the tag can be attached to many everyday items such as spray bottles and tin cans. However, the gain is significantly degraded as compared to a full-sized dipole operating in free-space, with values ranging from −18 dB to −8 dB as a function of the labeled object size. Consequently, the read range is

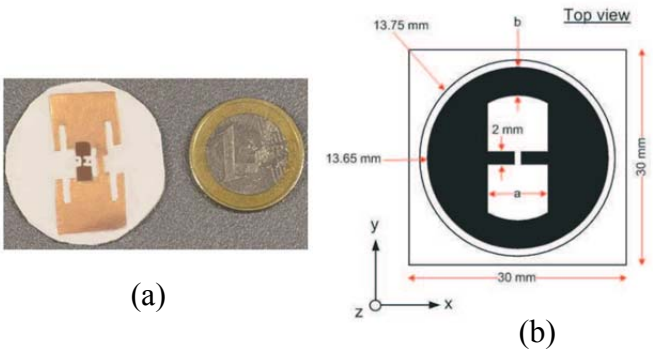

Figure 3.15. Examples of on-metal tags based on ceramic substrates from the literature.

in the order of 2-3 m, which limits the utility of the presented tag to less distance-demanding applications. In the same year, the authors used the same substrate for designing a tag employing a slot antenna (Figure 3.15b) [91]. In this case, the lateral size is 27.5 mm, and the thickness is 2.75 mm. Again, the antenna gain was degraded to −17 dB, and the read range reached less than 2 meters.

In the last decade, electromagnetic bandgap (EBG) structures have also been used to obtain low-profile tags for on-metal operation [92, 93]. In these cases, the controllable reflection from an EBG surface can be tailored to obtain in-phase response, even at small distances from the metal, thus isolating the tag from the negative effect of the underlying metallic surface. However, these antennas are still complex to fabricate, requiring multi-layer structures, and the EBG technology still requires further miniaturization to compete with the performance-to-size ratio obtained with patch antennas [77].

In this work, we explored for the first time the possibility of using metamaterial-inspired resonators as radiating particles for low-profile small on-metal UHF-RFID tags. Based on the study of the radiation properties of the SRR and some of its derived structures (NB-SRR and complementary particles), carried out in the next section, a tag design is proposed in Section 5.2.

4

Radiation Properties of Edge-coupled Split-ring Resonators (EC-SRRs) and Derived Structures

In this chapter, a study of the radiation properties of the SRR and other metamaterial-inspired resonators will be detailed. Due to its uniplanar geometry, which contributed to its widespread diffusion in the metamaterial community, the edge-coupled SRR (EC-SRR) is the topology considered throughout this work. Analytical approach was at the base of the presented results, and provided approximated expressions for the most relevant antenna parameters, such as the input resistance, the radiation efficiency and the cross-polarization of the radiated fields. The results have been validated by comparison with full-wave EM simulations in different cases, obtaining good agreement.

The expressions obtained in this chapter are at the base of the antenna designs presented in the next chapter, where experimental data provided additional validation of the analysis exposed below.

4.1 EC-SRR at its fundamental resonance

The topology of the EC-SRR is depicted in Figure 4.1 (cylindrical coordinate system r, z, φ is adopted for the analysis). The ring trace width, c, is assumed to be the same for both rings, a condition which is usually complied in most of the designs involving the EC-SRR. The width of the cuts in each ring is not critical for the SRR response, since the capacitance associated to the cut can be neglected [4]. Its value is set greater than the distance between rings d and, obviously, much smaller than the mean ring radius $r_0 = (r_A + r_B)/2$, where r_A and r_B are the mean radii of the external and internal rings, respectively.

The electric current distribution in each ring at the fundamental (first) resonance can be found from the quasi-static analysis presented in [62], which assumes that the particle length is small in terms of wavelengths. Such assumption is usually satisfied in practical SRR designs, where the coupling between the internal and external rings makes the resonant particle much smaller than the wavelength, typically in the order of $\lambda_0/10$ (in terms of diameter) [32], where λ_0 is the free-space wavelength. Strong coupling between rings involves a reasonably small distance d between rings, which ensure a high value of distributed capacitance between rings. From the quasi-static analysis, it was found that: i) the currents on the internal and external rings flow in the same direction, and present the same maximum amplitude i_0, ii) the current on each ring can be approximated to follow a linear dependence over the position angle φ, iii) the current at the ring cuts is approximately zero, since the capacitance associated to the cuts in each ring can be neglected. Due to the considerations above and the position of the cuts, the sum of the currents in the outer and inner rings is constant and equal to i_0 along the whole circumference (it does not depend on the position angle φ), as represented in Figure 4.1. Hence, it follows that the SRR can be treated like a constant current loop of radius r_0 in terms of magnetic polarizability. This has been usually done

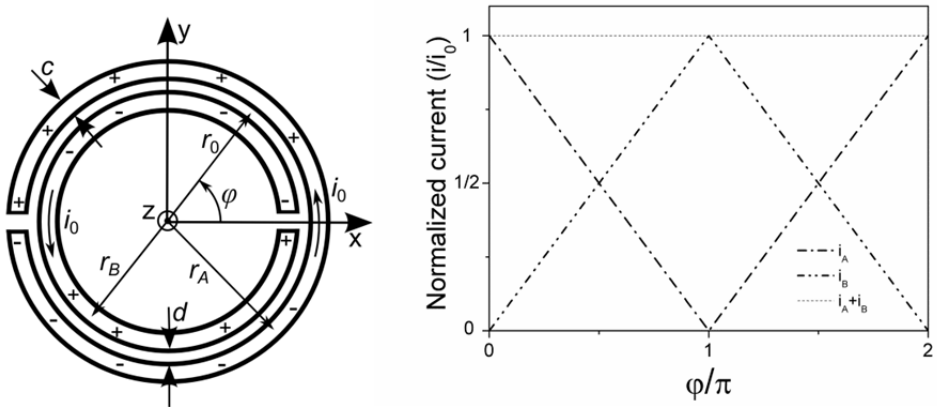

Figure 4.1. Topology and electric current/charge distribution of the EC-SRR at its fundamental resonance under the quasi-static approximation.

in the quasi-static analysis of the particle, in order to evaluate its magnetic polarizability around the resonance [32]. However, while this approach is a good approximation for typical EC-SRR designs (where $c << r_0$), SRR designs oriented to radiation require a more accurate analysis. This is because, in order to obtain high radiation efficiency, the rings of a radiating SRR are required to be somewhat wider (see Section 4.1.2), as compared to the rings of an SRR used in metamaterial design, and therefore the condition $c << r_0$ complies more weakly.

In the next section, such analysis is carried out in order to obtain an expression for the radiation resistance of the EC-SRR at its first resonance.

4.1.1 Radiation resistance

As mentioned before, the SRR working around its first resonance is much smaller than the wavelength. It is also well known that the radiation properties of small particles are mainly determined by its first-order electric and magnetic moments (dipole moments). Hence, the first step in our analysis is to evaluate both moments, individually, on the basis of the current distribution of the EC-SRR.

Let us now focus on the magnetic dipole moment $\boldsymbol{m}_A$ associated to the SRR external ring A. According the definition of dipole moment, this can be written as

$$\boldsymbol{m}_A = \frac{1}{2}\iiint_{V_A} \boldsymbol{r} \times \boldsymbol{J}_A dV_A , \tag{4.1}$$

where $\boldsymbol{J}_A$ is the current density on the ring cross-section and V_A is the volume occupied by ring A. The exact evaluation of (4.1) requires the current density dependence over the r coordinate (i.e., over the ring width) to be known and expressed analytically. Due to the proximity effect [94] between the internal and external rings, the current is not uniformly distributed along the ring width (see Figure 4.2), and at the first resonance it tends to accumulate far from the slot d because the currents in the rings flow in the same direction (Figure 4.2a). The magnitude of the effect depends upon the position angle φ, and is minimized at $\varphi = 0$ and at $\varphi = \pi$ for the external and internal rings, respectively, due to the positions of the current zeroes and maxima on the SRR. That is, the current distribution is approximately uniform where the maxima i_0 occur, because the current on the other ring is zero. Since the zones around the current maxima provide the main contribution to the magnetic dipole moment, expression (4.1) can be evaluated to a good approximation by assuming a uniform current distribution along the ring width at any position angle φ. Under this assumption, that is $\boldsymbol{J}_A = \boldsymbol{J}_A(z,\varphi,t)$, (4.1) leads to

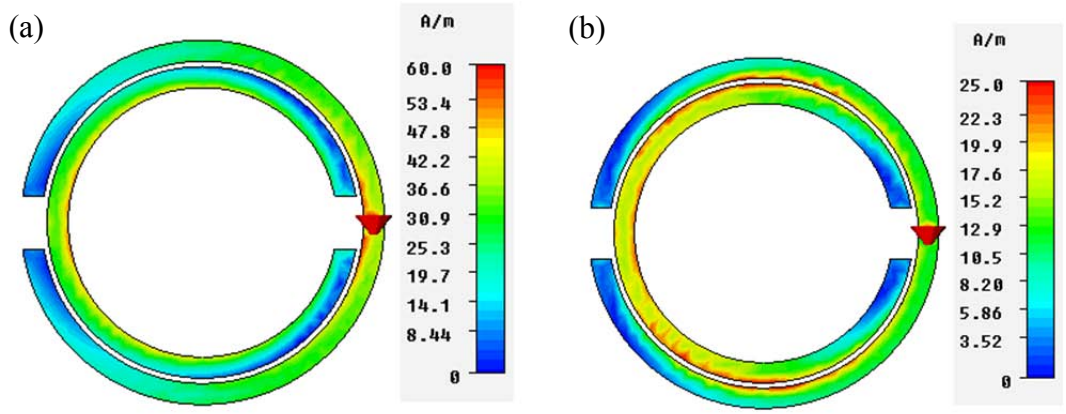

Figure 4.2. Amplitude of the electric current density on the EC-SRR at the (a) first and (b) second resonance, simulated with CST Microwave Studio [r_0 = 15 mm (λ_0/24), c = 2 mm, d = 0.5 mm]. The input port is represented as a red triangle.

$$\boldsymbol{m}_A = \frac{1}{2}\left(r_A^2 + \frac{c^2}{12}\right)\int_{-\pi}^{\pi} i_A(\varphi,t)d\varphi\,\hat{\boldsymbol{z}} \tag{4.2}$$

where c is the ring width and i_A is the current flowing on the external ring. Based on the quasi-static analysis, the current vector $\boldsymbol{i}_A$ on the external ring at the angular frequency ω_0 can be expressed as

$$\boldsymbol{i}_A(\varphi,t) = i_0\left(1-\frac{|\varphi|}{\pi}\right)\cos(\omega_0 t)\hat{\boldsymbol{\varphi}}\,, \tag{4.3}$$

as represented in Figure 4.1. Substitution of (4.3) into (4.2) and integration provide

$$\boldsymbol{m}_A = \frac{\pi}{2}\left(r_A^2 + \frac{c^2}{12}\right)i_0\cos(\omega_0 t)\hat{\boldsymbol{z}}\,. \tag{4.4}$$

The magnetic dipole moment $\boldsymbol{m}_B$ associated to the internal ring B can be evaluated by using the same method, and provides an expression analog to (4.4), with r_A changed for r_B. After some manipulation, the total magnetic dipole moment $\boldsymbol{m} = \boldsymbol{m}_A + \boldsymbol{m}_B$ can be written as

$$\boldsymbol{m} = \pi\left(r_0^2 + \frac{c^2}{3} + \frac{cd}{2} + \frac{d^2}{4}\right)i_0\cos(\omega_0 t)\hat{\boldsymbol{z}}\,. \tag{4.5}$$

Expression (4.5) provides a good approximation to the problem. It shows that the magnetic dipole moment generated by the SRR at resonance is actually somewhat higher than that of a current loop of mean radius r_0. However, even when the ring width c is increased up to r_0/2 (which could be taken as limit to ensure the correct operation of the resonator), all the terms depending from c and d in (4.5) can be neglected (note that

d is usually maintained small in order to obtain reasonable coupling between the resonators). Therefore, for practical cases, (4.5) can always be reduced to

$$\boldsymbol{m} = \pi r_0^2 i_0 \cos(\omega_0 t)\hat{\boldsymbol{z}}\,, \tag{4.6}$$

which is the expression of the magnetic dipole moment associated to an infinitely thin current loop of amplitude i_0 and radius r_0, and is the expression commonly used for the EC-SRR.

Let us now evaluate the resistance associated to the loop radiation. The power radiated by an electrically small magnetic moment of amplitude m_0 can be written as [95]:

$$P_{\text{rad}}^{\text{M}} = \frac{Z_0 k^4 m_0^2}{12\pi}\,, \tag{4.7}$$

where Z_0 is the free-space impedance and k is the free-space wavenumber. Therefore, by using (4.6), the radiation resistance associated to $\boldsymbol{m}$, referred to the current amplitude i_0, can be found to be

$$R_{\text{rad}}^{\text{M}} = \frac{8}{3}\pi^5 Z_0 \left(\frac{r_0}{\lambda_0}\right)^4. \tag{4.8}$$

Since the size of the SRR mean radius in terms of wavelength is in the order of 1/20, the radiation resistance associated to the axial magnetic dipolar moment $\boldsymbol{m}$ is in the order of 1-2 Ω, though it strongly depends on the particle size (i.e., on the substrate thickness and permittivity, and on the magnitude of the coupling between rings).

As it is well known, the EC-SRR at its fundamental resonance also exhibits an electric dipole moment $\boldsymbol{p}$ tangential to the plane of the particle, which arises from the bi-anisotropy of the structure. Such a dipole moment can be evaluated based on the electric charge distribution of the SRR, which can be inferred by applying the charge continuity law to the equation of the current profile (4.3) along the rings. As a result, the linear charge density λ_A on the external ring can be written as

$$\lambda_A(\varphi,t) = \frac{i_0}{\pi r_A \omega_0}\sin(\omega_0 t)\,\text{sgn}(\varphi)\,. \tag{4.9}$$

Since expression (4.9) is odd with respect to the position angle φ (as a result of the electric wall along the xz-plane), the total electric dipole moment associated to ring A is the sum of the infinitesimal dipole moments directed along the $\hat{\boldsymbol{y}}$ direction, namely:

$$\boldsymbol{p}_A = \int_0^{\pi} \lambda_A(\varphi,t) 2r_A^2 \sin\varphi d\varphi \hat{\boldsymbol{y}}\,. \tag{4.10}$$

Once again, for simplicity, $\boldsymbol{J}_A$ has been considered uniform through the ring width, so that the effective distance between charges is $2r_A\sin\varphi$. By integrating expression (4.10) we obtain

$$\boldsymbol{p}_A = \frac{4}{\pi}\frac{r_A}{\omega_0} i_0 \sin(\omega_0 t)\hat{\boldsymbol{y}} . \tag{4.11}$$

The internal ring B (with radius r_B) exhibits an electric dipole moment $\boldsymbol{p}_B$ with the same orientation, but presents opposite sign, due to the ring cut position. Therefore, the total electric dipole moment $\boldsymbol{p}$ is obtained by subtracting their amplitudes. By assuming the hypothesis of strong coupling between rings, which is normally satisfied at the first resonance, the current in the internal ring has roughly the same amplitude i_0 as the current in the outer ring. Taking into account that $r_A - r_B = c + d$, the total electric dipole moment is

$$\boldsymbol{p} = \frac{4}{\pi\omega_0}\left(c+d\right) i_0 \sin(\omega_0 t)\hat{\boldsymbol{y}} . \tag{4.12}$$

Then, by using the Larmor equation [96] for the radiated power by a given electric dipole moment of amplitude p_0, that is

$$P_{\text{rad}}^{\text{E}} = c_0^2 \frac{Z_0 k^4 p_0^2}{12\pi}, \tag{4.13}$$

where c_0 is the speed of light in vacuum, the radiation resistance associated to $\boldsymbol{p}$, and referred to the maximum current i_0 can be expressed as follows:

$$R_{\text{rad}}^{\text{E}} = \frac{32}{3\pi} Z_0 \left(\frac{c+d}{\lambda_0}\right)^2 . \tag{4.14}$$

Due to the proximity effect between rings, which was not taken into account in the analysis, the radiation resistance associated to the electric dipole moment is expected to be slightly higher than the value predicted by (4.14). This is because the effective distance between charges is actually higher than $c + d$, since the currents in the internal and external rings tend to separate each other.

Let us now compare (4.14) with (4.8). Since the typical values of $c + d$ in terms of wavelength are in the order of 1/100, that is, five or more times smaller than the mean radius r_0, the radiation resistance associated to the electric dipole moment is in the order of 0.1 Ω, which is an order of magnitude smaller than the radiation resistance related to the magnetic dipole moment of the SRR. Therefore, the radiation resistance of the particle can be approximated by the resistance associated to the axial magnetic moment, that is

$$R_{\text{rad}} \approx R_{\text{rad}}^{\text{M}}. \tag{4.15}$$

4.1.2 Loss resistance and radiation efficiency

As it is well known, the ohmic losses introduced by the metals in any structure strongly depend upon the current distribution $\boldsymbol{J}$ inside the conductors. Hence, in order to provide an accurate estimation of the loss resistance, the skin effect and the proximity effect have to be taken into account. Due to the skin effect, the current density distribution $\boldsymbol{J}$ within the ring cross section decays exponentially from the surfaces, with a penetration depth (skin depth) depending on the working frequency f_0 and the metal conductivity σ (among others). Since the conductor thickness h is usually much smaller than its width c, only the top and bottom faces are considered to carry current, neglecting the small contribution from the lateral faces.

The assumptions above lead to the following expression for $\boldsymbol{J}_A$ (the current density in the outer ring) in phasorial form:

$$\boldsymbol{J}_A(r,\varphi,z) = \begin{cases} J_0(r)e^{-\gamma\left(z+\frac{h}{2}\right)}\left(1-\dfrac{|\varphi|}{\pi}\right)\hat{\boldsymbol{\varphi}} & -\dfrac{h}{2} < z < 0 \\ J_0(r)e^{\gamma\left(z-\frac{h}{2}\right)}\left(1-\dfrac{|\varphi|}{\pi}\right)\hat{\boldsymbol{\varphi}} & 0 < z < \dfrac{h}{2} \end{cases} \tag{4.16}$$

where $\gamma = (1+j)/\delta$ is the complex propagation constant inside the conductor and δ is the skin depth, given by $\delta = (2/\omega\mu\sigma)^{1/2}$ [97], where μ and σ are the permeability and conductivity of the conductor material, respectively. The above expressions (for γ and δ) are valid for low-loss conductors, that is, for those satisfying $\sigma >> \omega\varepsilon$ (ε being the permittivity). As said in Section 4.1.1, the radial dependence of $\boldsymbol{J}_A$ [i.e., $J_0(r)$] is cumbersome to be expressed analytically. However, an effective width $c_{\text{eff}} < c$ can be defined to account for the proximity effect, so that the current density is assumed to be uniform and equal to J_0 inside the effective width c_{eff}, and zero elsewhere. In the EC-SRR, the value of such effective section always depends on the width c (this is not true, for example, for the effective thickness h_{eff} associated to the skin effect, which does not depend on the thickness h when $h >> \delta$) because there exist zones ($\varphi = 0$ and $\varphi = \pi$ for the external and the internal rings, respectively) of the rings where the current is distributed uniformly, and therefore all the cross-section is used. If the current is assumed to concentrate in an infinitely small area in the zones where the proximity effect is maximized (at $\varphi = \pi$ and $\varphi = 0$ for the external and the internal rings, respectively), and that a linear variation of the used section with the angle arises, the effective width can be approximated to $c_{\text{eff}} \approx \frac{1}{2}\, c$. As it will be shown at Section 4.2.2, this value works very well for the SRR at the second resonance, while a slightly higher

value $c_{\text{eff}} = 2/3\ c$ has been found to provide good results at the first resonance, and to agree with the expression proposed by Marques *et al.* in [63].

The power loss in the outer ring, inferred from the Ohm's law, is therefore

$$P_{\text{loss},A} = \frac{1}{2}\int_{-\pi}^{\pi}\int_{(-\frac{h}{2})}^{(\frac{h}{2})}\int_{(r_A-\frac{c_{\text{eff}}}{2})}^{(r_A+\frac{c_{\text{eff}}}{2})}\frac{\left|\boldsymbol{J}_A(z,\varphi)\right|^2}{\sigma} r\,dr\,dz\,d\varphi. \tag{4.17}$$

By solving (4.17) the power loss is found to be

$$P_{\text{loss},A} = \frac{\pi c_{\text{eff}} r_A \delta (1-e^{-\frac{h}{\delta}})}{3\sigma} J_0^2. \tag{4.18}$$

The power loss in the inner ring can be obtained by using the same procedure. Thus, the total power loss can be written as:

$$P_{\text{loss}} = \frac{2\pi c_{\text{eff}} r_0 \delta (1-e^{-\frac{h}{\delta}})}{3\sigma} J_0^2. \tag{4.19}$$

Let us now compute the total current i_0 flowing at the input section ($\varphi = 0$), in order to calculate the loss resistance. By integrating the current density over the effective cross-sectional area, namely

$$i_0 = \int_{(-\frac{h}{2})}^{(\frac{h}{2})}\int_{(r_A-\frac{c_{\text{eff}}}{2})}^{(r_A+\frac{c_{\text{eff}}}{2})} (\boldsymbol{J}_A(0,z)\cdot\hat{\boldsymbol{\varphi}})\,dr\,dz\,, \tag{4.20}$$

it can be found that the squared RMS (root mean square) current can be expressed as:

$$\frac{\left|i_0\right|^2}{2} = J_0^2 c_{\text{eff}}^2 \delta^2 \left[1 + \mathrm{e}^{-\frac{h}{\delta}} - 2\,\mathrm{e}^{-\frac{h}{2\delta}}\cos\left(\frac{h}{2\delta}\right)\right]. \tag{4.21}$$

Finally, the loss resistance is obtained by dividing the power loss (4.19) by the squared RMS current (4.21), obtaining

$$R_{\text{loss}} = \frac{2\pi r_0}{3\sigma c_{\text{eff}}\delta}\left[\coth\left(\frac{h}{2\delta}\right) - \operatorname{csch}\left(\frac{h}{2\delta}\right)\cos\left(\frac{h}{2\delta}\right)\right]^{-1}. \tag{4.22}$$

The hyperbolic function on the right side of (4.22) can be approximated by the hyperbolic cotangent with the same argument, that is

$$\left[\coth\left(\frac{h}{2\delta}\right) - \operatorname{csch}\left(\frac{h}{2\delta}\right)\cos\left(\frac{h}{2\delta}\right)\right]^{-1} \approx \coth\left(\frac{h}{2\delta}\right) \tag{4.23}$$

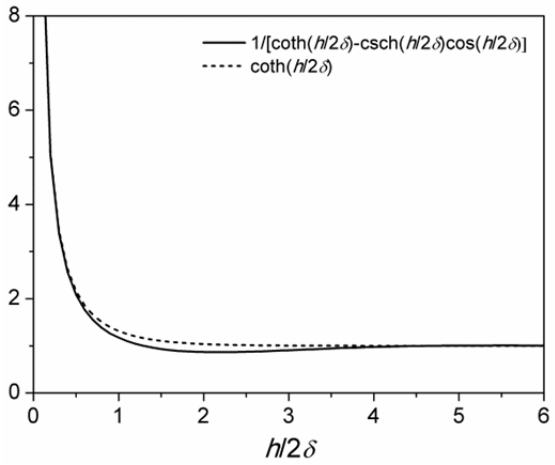

Figure 4.3. Comparison between the functions in the left (solid line) and right (dashed line) hand of equation (4.23).

with a maximum error of 20% for $h = 3.7\,\delta$ (see Figure 4.3). We will later show that, for practical cases, the error introduced by approximation (4.23) is reduced to a few percentage points in the expression of the radiation efficiency, so that (4.23) provides a substantial simplification of the formulas while maintaining good accuracy in the results. In fact, by combining (4.22) and (4.23), the loss resistance can be expressed in a very simple form, that is

$$\mathrm{R_{loss}} \approx \frac{2\pi r_0}{3\sigma c_{\mathrm{eff}}\delta}\coth\left(\frac{h}{2\delta}\right). \qquad (4.24)$$

As said above, the value of effective width providing good agreement with the simulated results is $c_{\mathrm{eff}} = 2/3\ c$. Therefore, the final expression for the loss resistance of the SRR around its fundamental resonance is found to be

$$\mathrm{R_{loss}} \approx \frac{\pi r_0}{\sigma c\delta}\coth\left(\frac{h}{2\delta}\right). \qquad (4.25)$$

It is worth mentioning that (4.25) converges to the values provided in [63] when the metal thickness approaches the values $h << 2\delta$ and $h >> 2\delta$, and additionally describes the behavior of the loss resistance for intermediate values of h.

Let us now discuss the radiation efficiency at resonance, η_{rad}. To this end, it is worth mentioning that the equivalent circuit model of the SRR at resonance, usually being reported to be a shunt LC circuit [32], becomes a series RLC circuit when the particle is excited through a cut opened in one ring, and both radiation and losses are considered (a simulated and experimental validation of this fact will be provided in Section 5.1.1). Therefore, the ohmic losses in the SRR can be modeled by a resistance placed in series with the radiation resistance, so that the radiation efficiency (neglecting dielectric losses)

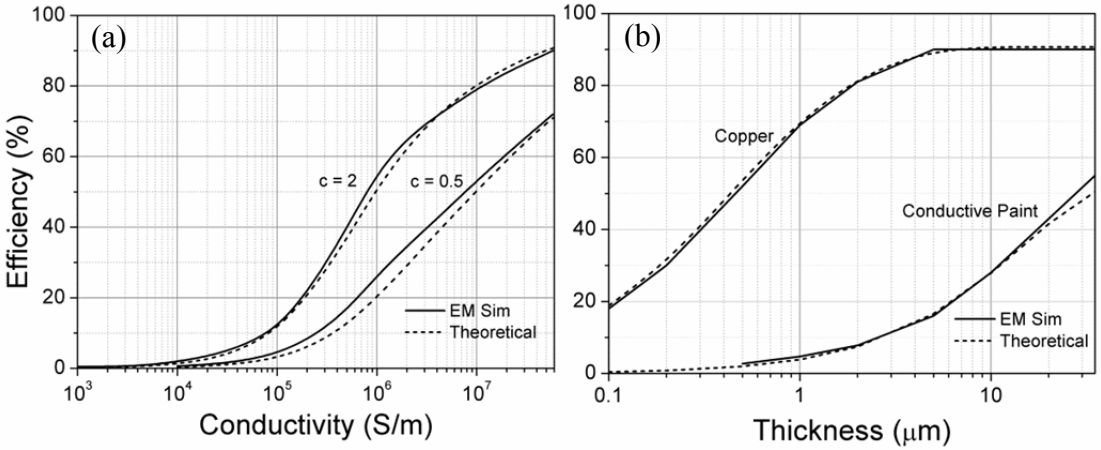

Figure 4.4. Theoretical and simulated results for the radiation efficiency of the EC-SRR at the first resonance, as a function (a) of the metal conductivity (for different values of trace width c, with metal thickness $h = 35$ μm) and (b) thickness (for trace width $c = 2$ mm). The conductivity of the conductive paint is set to 10^6 S/m [98, 99].

is also the ratio between the radiation resistance R_{rad} and the total resistance $R_{rad} + R_{loss}$. Based on this consideration, and on the previous analysis, it follows that

$$\eta_{rad} \approx \left[1+\frac{3}{8}\frac{c_0^4\sqrt{\pi\mu_0}}{\pi^4 Z_0}\left(cr_0^3\sqrt{f_0^7\sigma}\right)^{-1}\coth\left(\frac{h}{2\delta}\right)\right]^{-1}, \qquad (4.26)$$

where μ_0 is the permeability of free-space and f_0 is the working frequency. Expression (4.26) does not take into account dielectric losses, which strongly depend on the dielectric properties and the thickness of the substrate, and require integration of the fields over the substrate volume to be calculated.

In order to validate (4.26), and consequently, the expressions obtained above for the radiation (see previous section) and loss resistance, full-wave simulations of an EC-SRR without dielectric substrate were carried out by means of the commercial software *ADS Momentum*. The simulated structure was fed by a differential port placed across a cut (0.2 mm) opened in the external ring at the position $\varphi = 0$, and the dimensions of the SRR were adjusted to locate the resonance at $f_0 = 1$ GHz, obtaining $r_0 = 15$ mm ($\lambda_0/20$) and $d = 0.5$ mm. In the first set of simulations, the efficiency was found as a function of the metal conductivity σ for two different values of c (Figure 4.4a), setting the metal thickness to $h = 35$ μm. In the second set, the width was fixed to $c = 2$ mm, and the efficiency was depicted as a function of the metal thickness h for different materials (Figure 4.4b). In both cases, good agreement between (4.26) and EM simulation was obtained. As can be seen in Figure 4.4a, the antenna efficiency strongly depends on the ring width c, which is therefore one of the most important design parameters of the SRR antenna.

4.1.3 Far-field radiation pattern and quality factor

According to the analysis of the previous section, the main radiation mechanism of the EC-SRR at the first resonance is attributed to the electrically small current loop which results from the current distribution in the external and internal rings. Hence, in a first approximation, the SRR is expected to produce a linearly polarized omni-directional radiation, with maximum power density in the *xy*-plane (*E*-plane) and a theoretical directivity of 1.5 (1.76 dBi) [17]. However, the presence of the electric dipole moment introduces some changes in the fields radiated by the resonator. First, it generates a cross-polarization component. In fact, if the radiation produced by the magnetic dipole moment is defined as co-polar (being the main radiation mechanism), the contribution from the electric dipole moment is entirely cross-polar in the *yz*-plane ($\varphi = \pi/2$), due to the orthogonality and the 90º phase shift [see (4.6) and(4.12)] between the two radiators. Note that, in the *xz*-plane, the electric dipole radiation does not contribute to the formation of cross-polarization components, because the fields radiated by the loop and the dipole are oriented towards the same direction ($\hat{\boldsymbol{\varphi}}$ for the electric field). It is useful to define the quantity

$$XPOL_{\max} = \frac{R_{\text{rad}}^{E}}{R_{\text{rad}}^{M}} = \frac{4}{\pi^6}\left(\frac{c+d}{\lambda_0}\right)^2\left(\frac{r_0}{\lambda_0}\right)^{-4}, \tag{4.27}$$

which represents the maximum value of the cross-polar component (which occurs at $\theta = 0$), normalized to the maximum value of the co-polar (which occurs at $\theta = \pi/2$) in the *yz*-plane. This can be deduced by assuming that the radiation patterns of the magnetic and electric moments present the same shape (i.e., both are elemental radiators). The value of $XPOL_{\max}$ controls several characteristics of the far-field, in terms of gain and axial ratio (defined as the ratio between the major and minor axis of the ellipse described by the electric field of the radiated plane wave). In the *yz*-plane, the gain in the axial (*z*-axis) direction is found analytically to be $XPOL_{\max}$ times the gain in the endfire direction (*y*-axis). Furthermore, four zones where the axial ratio decays down to unity exist in the *yz*-plane. In fact, since the co-polar radiation is proportional to $\sin^2(\theta)$ and the cross-polar is proportional to $\cos^2(\theta)$, circular polarization is generated at the four angles

$$\theta_c = \left\{\pm tg^{-1}(\sqrt{XPOL_{\max}}), \pm tg^{-1}(\sqrt{XPOL_{\max}}) + \pi\right\}, \tag{4.28}$$

and the axial ratio maintains under an arbitrary level AR_0 (e.g., $AR_0 = 10$ dB can be considered for linear polarization) in each of the four regions centered in θ_c and subtending an angle equal to

$$\Delta\theta_{\text{ell}} = tg^{-1}(AR_0\sqrt{XPOL_{\max}}) - tg^{-1}(AR_0^{-1}\sqrt{XPOL_{\max}}), \tag{4.29}$$

where elliptical polarization is produced. It was verified by simulation that, for values of AR_0 in the order of 10 dB, each of these regions describes approximately a cone in the radiating sphere, thus enclosing a solid angle $\Omega_{ell} \approx 2\pi[1-\cos(\Delta\theta_{ell}/2)]$. This expression can be used to quantify the polarization purity across the radiating space of tags based on the SRR antenna, as in the case of the design presented in the next chapter.

In terms of radiation diagram, the presence of the electric dipole radiation distorts the omni-directional pattern of the current loop in the *xy*-plane to a bi-directional pattern, with maxima at $\varphi = \{0,\pi\}$. As reported in [100], this kind of pattern results from the 90º phase-shift between an electric and a magnetic radiator oriented orthogonally. It is interesting to relate the minimum antenna gain G_z, which occurs in the axial direction (or $\theta = 0$) to the maximum antenna gain G_x, occurring in the *xy*-plane at $\varphi = \{0,\pi\}$. It was found that

$$\frac{G_z}{G_x} \approx \frac{XPOL_{\max}}{1+XPOL_{\max}}. \tag{4.30}$$

Expression (4.30) assumes that the magnetic dipole moment produces a perfectly omni-directional pattern in the *xy*-plane. However, since the sum of the inner and outer currents in the SRR is only approximately a constant function of φ, the assumption made above is not strictly satisfied, so that expression (4.30) should be considered as an approximation. In the next chapter, the formula will be used in order to relate the minimum read range to the maximum read range of UHF-RFID tags based on the SRR antenna at its first resonance, and an experimental validation will be provided.

As it is expressed in (4.27), the value of $XPOL_{\max}$ is controlled by the SRR mean radius and the distance $c + d$ (which is also the radius difference $r_A - r_B$). For very small values of $c + d$, the cross-polarization level can be lowered to −20 dB/−25 dB (according to simulation results). However, this involves a reduction of the radiation efficiency, as predicted by (4.26), so that the the typical values of $XPOL_{\max}$ at the first resonance for efficient EC-SRR antenna designs are in the range of −8 dB/−10 dB. In any case, the value of $XPOL_{\max}$ is much smaller than unity, because the distance $c + d$ cannot be increased indefinitely. As a result, the solid angle Ω_{ell} is much smaller than 4π (which represents the solid angle of the sphere) in any case, and therefore the EC-SRR radiation can be considered linearly polarized on most of the radiating sphere.

The radiation pattern described above, along with the cross-polarization level predicted in (4.27), was validated by the far-field EM simulations (experimental validation of the SRR antenna radiation pattern will be provided at Section 5.1). To this end, two different lossless EC-SRR layouts with very different values of $c + d$ (2.5 mm and 0.7 mm) were simulated, and the far-field characteristics were compared. The results, in terms of radiation diagram and axial ratio, are depicted in Figure 4.5. As expected, the radiation of the SRR can be modeled by the sum of an axial magnetic moment (main radiator) and an electric moment oriented towards the *y*-axis (secondary

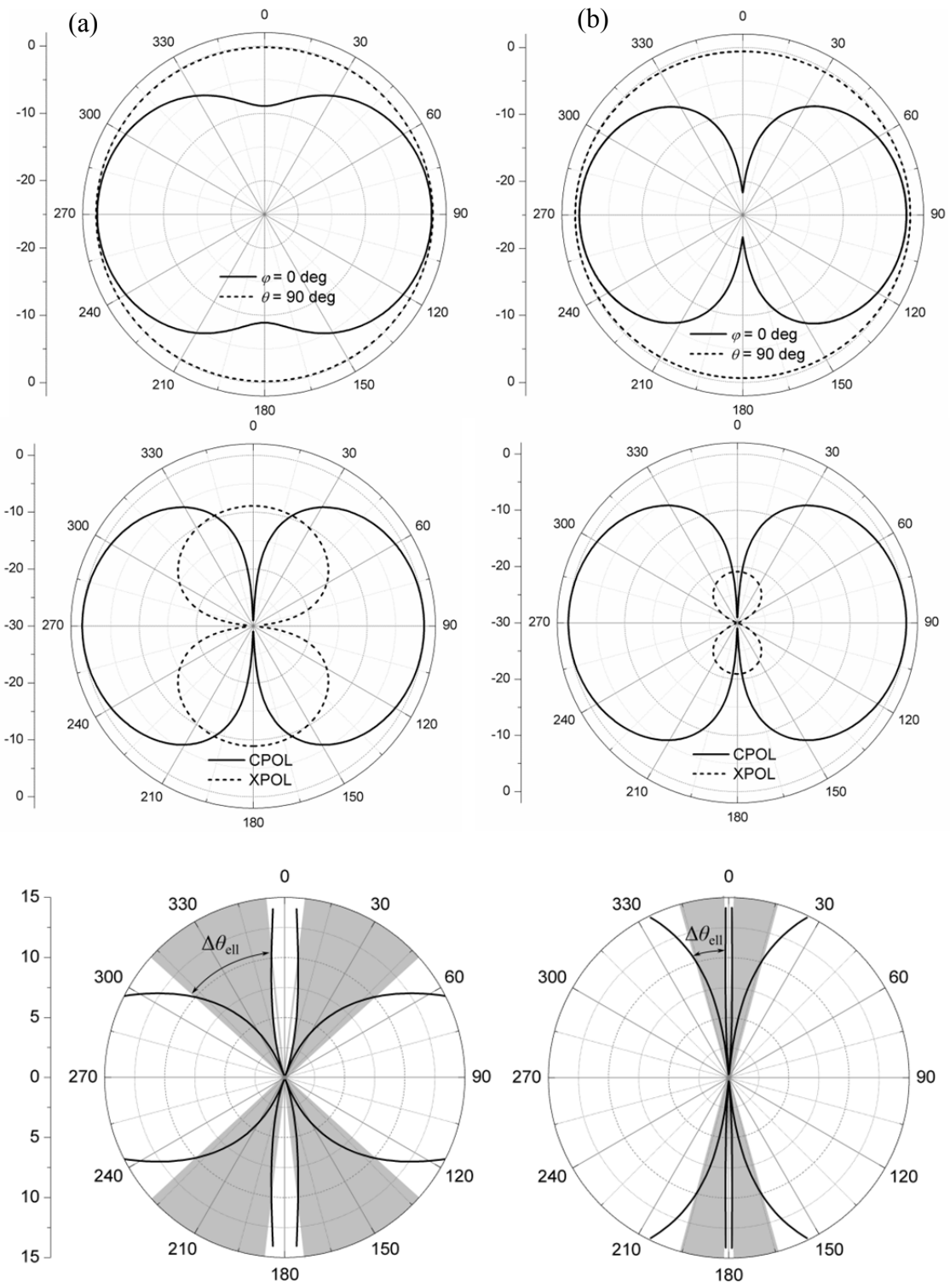

Figure 4.5. (top) Simulated normalized radiation pattern at $\varphi = 0º$ (*xz*-plane) and $\theta = 90º$ (*xy*-plane), (middle) co-polar and cross-polar components in the *yz*-plane and (bottom) axial ratio in the *yz*-plane, of a lossless EC-SRR at the first resonance for (a) $c + d = 2.5$ mm and (b) $c + d = 0.7$ mm. The value of r_0 is 15 mm. The low axial ratio (≤ 10 dB) region is depicted in grey.

TABLE 2 THEORETICAL AND SIMULATED VALUES OF *XPOL*MAX FOR THE EC-SRR AT THE FIRST RESONANCE.

	THEORETICAL	EM SIMULATION
***c* + *d* = 2.5 mm**	−13 dB	−9 dB
***c* + *d* = 0.7 mm**	−25 dB	−21 dB

radiator). Moreover, the levels of the cross-polar radiation rise when the value of $c + d$ is increased, and the elliptical region gradually narrows and orientates toward the radiation minima, as predicted by theory. However, the simulated values of $XPOL_{max}$ are higher than the predicted values (see Table 2 for a comparison). We attribute this disagreement to the second order effects (e.g., the proximity effect, which is expected to increment the electric dipole moment) which were not taken into account in the analysis. Hence, (4.27) should be taken as a first approximation which allows easily understanding the behavior of the EC-SRR cross-polarization as a function of its geometrical parameters. The simulated antenna directivity is $D_0 = 1.6$ dBi for $c + d = 2.5$ mm and $D_0 = 2$ dBi for $c + d = 0.7$ mm; both values are similar to the directivity of an elemental radiator (1.76 dBi).

Let us now discuss the EC-SRR antenna quality factor at the first resonance, which determines the maximum bandwidth that can be obtained with conjugate impedance matching. Due to the physical limitations affecting small planar antennas, discussed at Section 3.2.2, the quality factor and bandwidth are limited to the values provided by equations (3.2) and (3.3), respectively. Taking into account that, at the first resonance, the mean radius (and consequently the external radius) is in the order of 1/20 times the free-space wavelength and assuming that the radiation efficiency approaches unity, the half-power fractional bandwidth is expected to be $FBW \leq$ 1-2 %, corresponding to roughly 10-20 MHz at the UHF-RFID band. While this value could be considered poor for some communication applications, it is suitable for UHF-RFID tags, where the required bandwidth is limited to few megahertz.

The abovementioned equations set the lower bound for the quality factor of any small antenna confined to a planar geometry. In practice, the SRR antenna is expected to provide a higher quality factor, which can be predicted on the basis of its equivalent circuit model near the resonance, i.e., a series RLC resonator, which provides $Q_{rad} = \omega_0 L/R_{rad}$. The value of the EC-SRR self-inductance L can be computed as the average of the inductances of both rings [32], that is the inductance of a loop with radius r_0 and width c. A commonly used approximation for the inductance of a circular loop is $L \approx \mu_0 r_0[\ln(16r_0/c)-2]$, which assumes a circular section with radius $c/2$. Hence, by using (4.15) for the radiation resistance, the half-power fractional bandwidth of the SRR antenna, in the case of conjugate matching, can be approximated to

$$FBW \approx \frac{8}{3}\pi^4 \eta_{\text{rad}}^{-1} \left[\ln\left(16\frac{r_0}{c}\right) - 2 \right]^{-1} \left(\frac{r_0}{\lambda_0}\right)^3 . \quad (4.31)$$

Expression (4.31) assumes that the input resistance of the port driving the antenna does not vary in frequency. This condition is not strictly satisfied in the case of RFID ASICs, which are modeled by shunt RC circuits. However, the variation of the ASICs input resistance R_C is usually very small within the UHF-RFID band [31], so that (4.31) can be used for the tag bandwidth to a good degree of approximation. For practical cases, the values found by using (4.31) are in the order of $FBW \approx 0.8{-}1\%$, when radiation efficiency near unity is obtained. Although this value does not allow a worldwide operation of the tag, it is large enough for ensuring its correct operation in one of the UHF-RFID bands. It is worth to mention that ohmic and dielectric losses decrease the overall quality factor, thus increasing the bandwidth at the expense of a reduction of the tag peak read range. Equation (4.31) will be verified by means of EM simulation and measurements at Section 5.1.1, where an UHF-RFID tag based in the EC-SRR antenna will be presented.

4.2 EC-SRR at its second resonance

In this section, the study of the EC-SRR radiation resistance will be extended to the case of working around the second resonance of the structure, where the currents in the external and internal rings flow in opposite directions [60]. Due to the increased particle dimensions and the different current distribution, the quasi-static analysis presented at the previous section does not hold for the second resonance. However, the EC-SRR dimensions at its second resonance are still very near to the commonly accepted boundary of electrically small antennas ($ka = 0.5$), since its radius is typically in the order of 0.1 free-space wavelength, corresponding to $ka \approx 0.6$. Therefore, its radiation properties can still be predicted to a good degree of approximation by evaluating the first order (dipole) terms of the electric and magnetic moments generated by the current distribution, and treat such sources as elemental radiators.

4.2.1 Radiation resistance

At the second resonance, the currents in the outer and inner rings flow in opposite directions [60], and the current distribution approximately satisfies $\boldsymbol{i}_A(\varphi) = -\boldsymbol{i}_B(\varphi \pm \pi)$, where $\boldsymbol{i}_A$ and $\boldsymbol{i}_B$ is the current in the external (A) and internal (B) ring, respectively, and φ is the angular position with respect to the x-axis. This relation is valid if the distance between rings, d, is small as compared to the mean ring radius r_0 (strong coupling condition). Since the length of each ring is approximately half-wavelength, the current

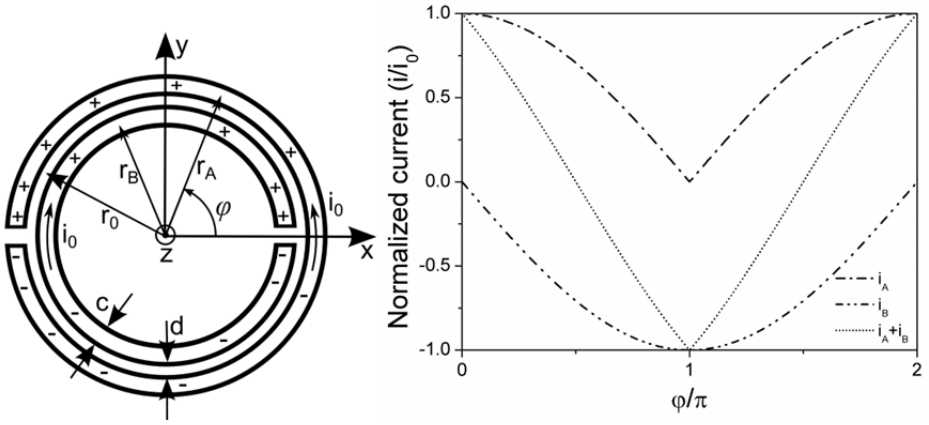

Figure 4.6. Topology and theoretical electric current/charge distribution of the EC-SRR at its second resonance.

along the ring circumference can be assumed to exhibit a sinusoidal profile (Figure 4.6), with a maximum value at the center ($\varphi = 0$ for ring *A* and $\varphi = \pm\pi$ for ring *B*), and null at the ring edges (approximated to $\varphi = \pm\pi$ for ring *A* and $\varphi = 0$ for ring *B*). However, as it is corroborated later (see Figure 4.7b), the current in each ring actually exhibits a slight discrepancy to this approximation, mainly because the length of each ring at the second SRR resonance is somewhat greater than the half-wavelength at the working frequency. Nevertheless, by means of this sinusoidal approximation to the rings currents, analytical expressions can be found, and good agreement between theory, simulation and experiment is obtained. Moreover, as in the previous section, the proximity effect will not be taken into account in the calculation of the radiation resistance, in order to maintain the expressions simple and to show that such effect does not substantially affect the result.

The current in the external ring, of mean radius r_A, can thus be written as:

$$\boldsymbol{i}_A(\varphi,t) = i_0 \cos\left(\frac{\varphi}{2}\right)\cos(\omega_0 t)\hat{\boldsymbol{\varphi}}\,. \tag{4.32}$$

By solving the well-known electric charge continuity equation, the linear charge density in the ring is found to be

$$\lambda_A(\varphi,t) = \frac{i_0 \sin\left(\frac{\varphi}{2}\right)\sin(\omega_0 t)}{2r_A\omega_0}. \tag{4.33}$$

As in the case of the analysis at the first resonance, expression (4.10) can be used to evaluate the electric dipole moment associated to the external ring, obtaining

$$\boldsymbol{p}_A = \frac{4}{3}\frac{r_A}{\omega_0} i_0 \sin(\omega_0 t)\hat{\boldsymbol{y}}. \tag{4.34}$$

The internal ring *B*, of mean radius r_B, exhibits an electric dipole moment with the same orientation and phase, so that the total dipole moment amplitude is the sum of the internal and external dipole moments amplitudes, leading to

$$\boldsymbol{p} = \frac{8}{3}\frac{r_0}{\omega_0} i_0 \sin(\omega_0 t)\hat{\boldsymbol{y}}. \tag{4.35}$$

Since the radiating particle is electrically small, it is still possible to consider the total moment given by (4.35) as an infinitesimal electric dipole moment located in the *y*-axis. Thus, by using the Larmor equation [96] for the radiated power by a given electric dipole moment of amplitude p_0, the total radiation resistance referred to the maximum current i_0 can be expressed as

$$R_{\text{rad}}^{\text{E}} = \frac{128}{27}\pi Z_0 \left(\frac{r_0}{\lambda_0}\right)^2 \approx 5600\left(\frac{r_0}{\lambda_0}\right)^2 \Omega\,. \tag{4.36}$$

It is interesting to compare the value found in (4.36) with the radiation resistance of a small dipole, which can be expressed by means of the well-known expression:

$$R_{\text{rad}0} = 20\pi^2 \left(\frac{l}{\lambda_0}\right)^2 \approx 790\left(\frac{r}{\lambda_0}\right)^2 \Omega \tag{4.37}$$

where *r* is the length of each dipole arm. As can be seen by comparing (4.36) and (4.37), for a given radiator size (r_0 for the SRR or *r* for the dipole), the SRR working at the second resonance exhibits a much higher radiation resistance as compared to a small electric dipole. This can be explained arguing that the SRR takes advantage of most of the area enclosed by its lateral dimensions, while the dipole only distributes its charges along a line.

Let us now compute the magnetic dipole moment associated to EC-SRR at the second resonance. By solving (4.1), the magnetic contribution associated to the external ring is found to be

$$\boldsymbol{m}_A = 2r_A^2 i_0 \cos(\omega_0 t)\hat{\boldsymbol{z}}. \tag{4.38}$$

As explained above, the current in the internal ring flows in the opposite direction, and generates an opposite axial magnetic dipole moment. Therefore, the total magnetic dipole moment can be written as:

$$\boldsymbol{m} = 4r_0\left(r_A - r_B\right) i_0 \cos(\omega_0 t)\hat{\boldsymbol{z}}. \tag{4.39}$$

As in the previous case (Section 4.1.1), the radiation resistance associated to the magnetic dipole moment, referred to the current maximum i_0, can be found by using (4.7). Taking into account that $r_A - r_B = c + d$, it is found that

$$R_{\text{rad}}^{\text{M}} = \frac{128}{3}\pi^3 Z_0 \left(\frac{r_0}{\lambda_0}\right)^2 \left(\frac{c+d}{\lambda_0}\right)^2. \tag{4.40}$$

It can be easily verified that, due to a nearly complete cancellation of the axial magnetic moments of the internal and external rings, the power radiated by the magnetic dipole at the second resonance is much smaller (two orders of magnitude) than the power associated to the electric dipole. Therefore, to a good approximation, the radiation resistance of the particle is dominated by the one associated to its electric dipole moment, that is,

$$R_{\text{rad}} \approx R_{\text{rad}}^{\text{E}}. \tag{4.41}$$

The potential of SRRs as radiating elements operating at their second resonance is demonstrated by evaluating (4.41) for typical values of r_0/λ_0, which are in the order of 0.1. The resulting radiation resistance values are very close to the radiation resistance of the commonly used, and very well-known, half-wave dipole antenna (73 Ω). This fact suggests that half-wave dipole antennas can be replaced with SRRs (operating at the second resonance) without the need of a matching network, thereby reducing the maximum dimension of the antenna (defined as the radius of the minimum sphere enclosing the antenna) by a factor 2.5, approximately.

In order to validate the analysis presented above, an EC-SRR was simulated by means of the commercial software *Agilent Advanced Design System (ADS)*. The geometry of the particle was adjusted to locate the second resonance at the frequency f_0 = 1 GHz (λ_0 = 300 mm) when no substrate is used. The values for the geometric parameters are r_0 = 35.25 mm (λ_0/8.5), c = 2 mm, d = 0.5 mm, and the cut width was set to 5 mm.

The discrete port was placed across a 0.4 mm gap opened at the center of the external ring (φ = 0º), where a current maximum i_0 is expected to occur. Therefore, in a lossless case, the input resistance R_{in} of the system corresponds to the radiation resistance R_{rad} of the particle. Hence, in the first set of simulations the metal is treated as a perfect conductor, in order to isolate the radiation resistance of the SRR and to verify (4.41).

The simulated input impedance of the SRR (without dielectric substrate), depicted in Figure 4.7a, clearly reveals the first (0.4 GHz) and second (1 GHz) resonant frequencies of the SRR, and the first anti-resonant frequency (0.66 GHz), which corresponds to the intrinsic resonance of the inner ring. Note also that the radiation resistance at the second resonance (73 Ω) is nearly two orders of magnitude greater than the radiation resistance at the first resonance (1 Ω), and is exactly equal to the radiation resistance of a canonical half-wave dipole. The simulated electric current density distribution at the

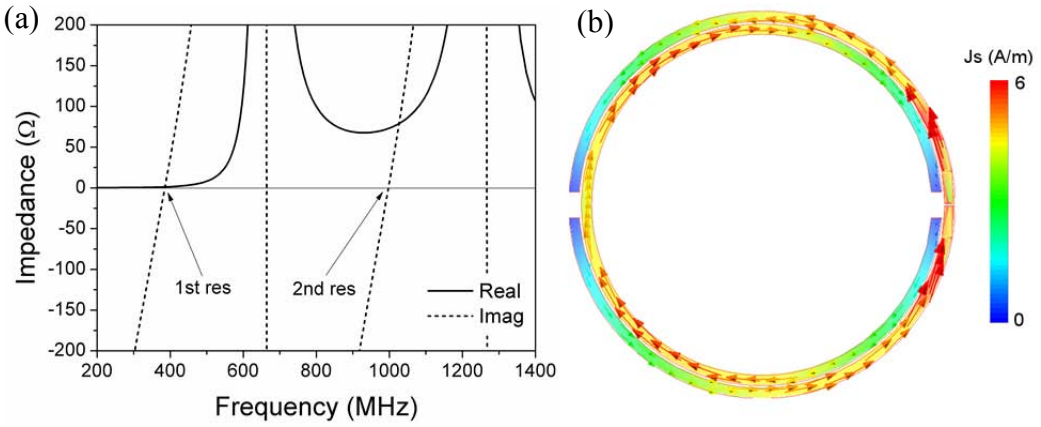

Figure 4.7. Simulated (a) input impedance and (b) electric current distribution at the second resonant frequency (1 GHz) of a lossless EC-SRR (no dielectric substrate is considered).

second resonance (Figure 4.7b) is in good agreement with the approximated theoretical distribution described at the beginning of this section, i.e., the current in the internal and external rings flow in opposite directions, and their amplitudes are similar. However, since the length of each ring is slightly greater than half-wavelength, the maximum at the center of the rings splits into two maxima symmetrically positioned around the center. Nevertheless, expression (4.32) is a useful approximation, as it allows simplifying the analytical treatment maintaining high accuracy in the results.

In order to validate (4.41), a lossless dielectric of thickness $h_s = 2.54$ mm was then added as substrate, allowing to control the value of the second resonance frequency f_0, and consequently the value of λ_0. By increasing the dielectric permittivity ε_r of the substrate, the value of r_0/λ_0 was gradually decreased, and the simulated input resistance of the particle was compared in each case to the radiation resistance calculated by (4.41). The results, depicted in Figure 4.8, reveal that there is very good agreement between theory and simulation.

It is worth to mention that, in order to modulate the electrical size of the particle without changing the substrate dielectric constant, it is also possible to vary the coupling between rings, mainly controlled by the slot width d. In fact, according to the theory of coupled resonators [101], decreasing the coupling (while fixing r_0) reduces the frequency split between first and second resonance. Therefore, the second resonance is lowered and the particle becomes electrically smaller, providing an additional degree of freedom at the design stage. However, only relatively small changes of r_0/λ_0 are possible by using this technique. Moreover, if the coupling between rings is very small, the assumptions for the derivation of equations (4.35) and (4.39) no longer hold. The reason is that the difference between the internal and external rings radii increases with the distance d, and the internal and external current amplitudes diverge as well.

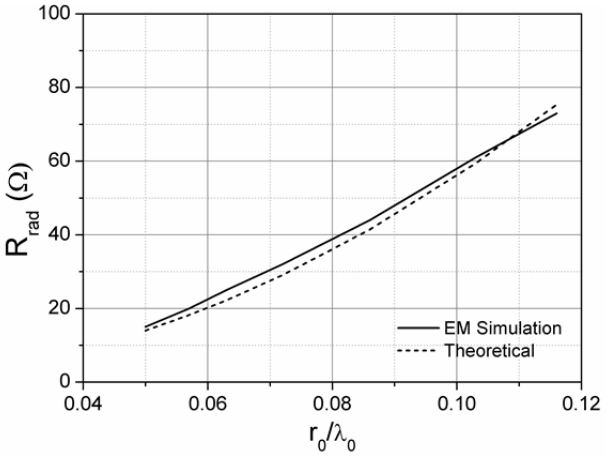

Figure 4.8. Radiation resistance at second resonance as a function of the EC-SRR mean radius relative to the wavelength. Note that the radiation resistance is roughly 73 Ω (i.e., the radiation resistance value of a half-wave dipole) for $r_0/\lambda_0 = 0.118$.

4.2.2 Loss resistance and radiation efficiency

The assumptions regarding the current density distribution along the EC-SRR cross-section (Section 4.1.2) still hold at the second resonance. In this case, however, the current dependency over the position angle φ is different, being imposed by (4.32). Therefore, the following expression for $\boldsymbol{J}_A$ (the current density in the outer ring) in phasorial form can be written as

$$\boldsymbol{J}_A(r,\varphi,z) = \begin{cases} J_0(r)e^{-\gamma\left(z+\frac{h}{2}\right)}\cos\left(\frac{\varphi}{2}\right)\hat{\boldsymbol{\varphi}} & -\frac{h}{2} < z < 0 \\ J_0(r)e^{\gamma\left(z-\frac{h}{2}\right)}\cos\left(\frac{\varphi}{2}\right)\hat{\boldsymbol{\varphi}} & 0 < z < \frac{h}{2} \end{cases} \tag{4.42}$$

As said in Section 4.1.2, an effective width $c_{\text{eff}} < c$ can be defined to account for the proximity effect, so that the current density $J_0(r)$ is taken to be uniform and equal to J_0 inside the effective width c_{eff}, and zero elsewhere. If the current is assumed to concentrate in an infinitely small area in the zones where the proximity effect is maximized ($\varphi = \pi$ and $\varphi = 0$ for the external and the internal rings, respectively), and that a linear variation of the used section with the angle arises, the effective width can be approximated to $c_{\text{eff}} \approx c/2$.

The power loss on the outer ring can be calculated by using (4.17), leading to

$$P_{\text{loss,A}} = \frac{\pi c_{\text{eff}} r_A \delta (1 - e^{-\frac{h}{\delta}})}{2\sigma} J_0^2, \tag{4.43}$$

so that the total power loss is found to be

$$P_{\text{loss}} = \frac{\pi c_{\text{eff}} r_0 \delta (1 - e^{-\frac{h}{\delta}})}{\sigma} J_0^2. \tag{4.44}$$

Starting from (4.44), the procedure described at Section 4.1.2 [involving expressions (4.21) and (4.23)] can be used to evaluate the loss resistance, obtaining

$$\mathrm{R}_{\text{loss}} \approx \frac{\pi r_0}{\sigma c_{\text{eff}} \delta} \coth\left(\frac{h}{2\delta}\right). \tag{4.45}$$

As mentioned above, the effective width can be approximated by $c_{\text{eff}} \approx c/2$, leading to the final expression for the loss resistance of the EC-SRR at the second resonance:

$$\mathrm{R}_{\text{loss}} \approx \frac{2\pi r_0}{\sigma c \delta} \coth\left(\frac{h}{2\delta}\right). \tag{4.46}$$

Let us now discuss the radiation efficiency of the EC-SRR at the second resonance. As it was found in the previous section, the ohmic losses can be modeled by a resistance placed in series with the radiation resistance. Therefore, the radiation efficiency η_{rad} can be expressed as

$$\eta_{rad} \approx \left[1 + \frac{27}{64} c_0 \sqrt{\frac{\pi}{\mu_0}} \left(c r_0 \sqrt{f_0^3 \sigma}\right)^{-1} \coth\left(\frac{h}{2\delta}\right)\right]^{-1}. \tag{4.47}$$

The expression above was validated by EM simulation. To this end, ohmic losses were added to the metal layer of the simulated structure presented in the previous section [f_0 = 1 GHz without dielectric substrate, r_A = 36.5 mm, r_B = 34 mm c = *2* mm, d = 0.5 mm, r_0 = 35.25 mm (λ_0/8.5), cut width 5 mm]. The simulated radiation efficiency as a function of the metal conductivity for different values of the strip width c, setting the value of the metal thickness to h = 35 μm, is shown in Figure 4.9a. The thickness dependence of the radiation efficiency for a strip width of c = 2 mm is simulated and depicted in Figure 4.9b for different materials. Very good agreement between electromagnetic simulations and theoretical predictions is observed for efficiency values greater than 15%, which is the region of interest in practical antennas.

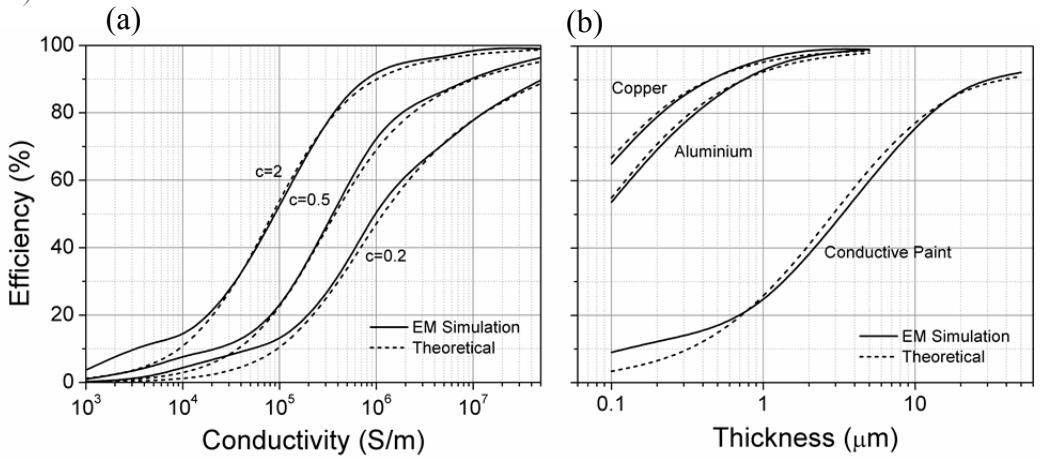

Figure 4.9. Simulated and theoretical radiation efficiency of the EC-SRR at the second resonance, (a) versus conductivity for $h = 35$ μm and (b) versus conductor thickness for $c = 2$ mm. The considered conductive paint has a conductivity $\sigma = 10^6$ S/m [98, 99].

4.2.3 Far-field radiation pattern and quality factor

Since the main radiation mechanism of the EC-SRR at the second resonance is the tangential electric dipole moment oriented along the *y*-axis (see Figure 4.6), the structure is expected to produce a linearly polarized omni-directional radiation, with maximum power density at $\theta = \{0,\pi\}$ and a theoretical directivity of 1.5 (1.76 dBi). However, due to the non-zero length of the particle in the *x* direction (the structure can be seen as an array of near elements radiating in phase), a slightly bi-directional pattern is expected over the *xz*-plane ($\varphi = 0$), thus resulting in a higher value of the directivity. Moreover, the presence of a magnetic dipole moment oriented along the *z*-axis generates radiation, which is entirely cross-polar in the *yz*-plane (*E*-plane), as in the case of the electric dipole radiation at the first resonance (Section 4.1.3). In this case, the cross-polar radiation is maximized at $\theta = \pi/2$. Hence, in this direction the value of the cross-polarization level is maximized, and it can be evaluated by dividing (4.40) by (4.36), obtaining:

$$XPOL_{\max} = 9\pi^2 \left(\frac{c+d}{\lambda_0} \right)^2 . \tag{4.48}$$

Notice that, unlike in the case of the first resonance [see Equation (4.27)], the value of $XPOL_{\max}$ does not depend on the SRR mean radius.

The considerations made at the previous Section, about the effect of $XPOL_{\max}$ over the radiation pattern and the axial ratio, still hold at the second resonance. However, in this case the low axial ratio zones are centered on the angles

$$\theta_c = \left\{ \pm tg^{-1}\left(\sqrt{XPOL_{\max}^{-1}}\right), \pm tg^{-1}\left(\sqrt{XPOL_{\max}^{-1}}\right) + \pi \right\}, \tag{4.49}$$

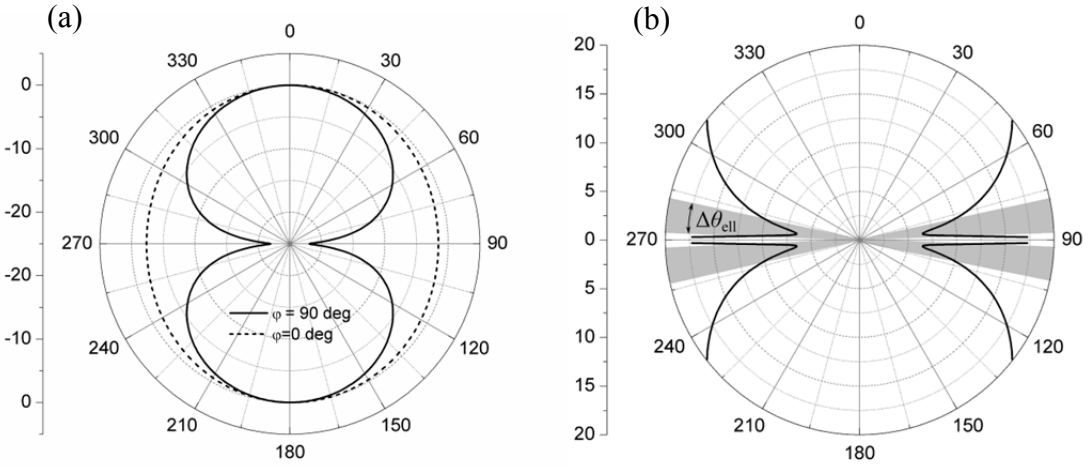

Figure 4.10. Simulated (a) normalized radiation pattern and (b) axial ratio in the *yz*-plane of a lossless EC-SRR at the second resonance (with $c + d = 2.5$ mm). The low axial ratio (≤ 10 dB) region is depicted in grey.

and the region with elliptical polarization is comprised in

$$\Delta\theta_{\text{ell}} = tg^{-1}(AR_0\sqrt{XPOL_{\text{max}}^{-1}}) - tg^{-1}(AR_0^{-1}\sqrt{XPOL_{\text{max}}^{-1}}). \qquad (4.50)$$

The simulated results for the radiation pattern and the axial ratio of a lossless EC-SRR at the second resonance are depicted in Figure 4.10 [$f_0 = 1$ GHz, $r_A = 36.5$ mm, $r_B = 34$ mm $c = 2$ mm, $d = 0.5$ mm, $r_0 = 35.25$ mm ($0.118\,\lambda_0$), cut width 5 mm]. The normalized radiation pattern in the *yz*-plane confirms that the main radiation mechanism is the electric dipole oriented along the *y*-axis, and the value of the cross-polarization level is $XPOL_{\text{max}} = -22$ dB, in perfect agreement with the theoretical value predicted by (4.48). As expected, such a small value of the cross-polarization level provides a very small elliptical radiation area ($\Delta\theta_{\text{ell}} = 10^{\text{o}}$), centered very near to the radiation minima, so that the radiation provided by the magnetic moment does not practically affect the polarization of the radiated fields. Regarding the *xz*-plane ($\varphi = 0$), the pattern is slightly bi-directional, due to the array effect associated to the non-zero length of the particle in the *x*-direction (notice that, at the first resonance, the lateral dimensions of the particle in terms of wavelengths are sensibly smaller, and therefore a quasi-circular pattern is obtained). As a result, the directivity is increased, and reaches $D_0 = 2.7$ dBi according to the simulations.

Let us now treat the quality factor of the EC-SRR at the second resonance. Due to the greater dimensions of the particle in terms of wavelength, the quality factor of the EC-SRR at the second resonance is expected to be much lower than the quality factor of the same particle at the fundamental resonance. Specifically, doubling the antenna size in terms of wavelengths involves an increase of 8 times in the minimum radiation quality factor, since it depends upon the third power of the electric length of the antenna. However, these values should be considered only as qualitative, since very few antennas actually approach the lower bound of the radiation quality factor calculated on the basis

of their size. Unfortunately, an analytical prediction of the EC-SRR quality factor at the second resonance is not straightforward. In fact, though a series RLC circuit model can be used to describe the particle behavior in terms of impedance (see Figure 4.7a), no closed expressions linking the values of L and C to the geometrical values (r_0, c, d) are known, unlike in the case of the first resonance. For this reason, the values presented in this work will be merely based on EM simulations, i.e., on the simulated half-power bandwidth $FBW = 2/Q$ when conjugate matching is obtained. For the lossless structure simulated in this section, the value of the fractional bandwidth is $FBW = 11.5\%$, corresponding to a radiation quality factor of $Q_{rad} = 17$. For comparison, equation (3.2) provides a lower bound of $Q_{rad} \geq 7.3$ (given that $r_{ext} = r_0 + c + d/2 = 37.5$ mm and $f_0 = 1$ GHz), which is sensibly smaller than the value found in our case. Even though the EC-SRR antenna does not approach the Gustafsson limit, its radiation quality factor is similar to that of a small planar rectangular (with a length-to-width ratio around unity) dipole antenna of the same size, and much better as compared to small thin dipole antennas [27, 28].

Unlike in the case of working at the first resonance, the EC-SRR antenna at the second resonance is capable of providing the bandwidth required for many applications, even outside the context of RFID, including wireless communication systems. A design example in the 900 MHz ISM band is described at Section 5.3, with the aim of providing experimental validation to the analysis carried out in this chapter, and to demonstrate the utility of the proposed antenna design.

4.3 Non-Bianisotropic Split Ring Resonator (NB-SRR)

The non-bianisotropic split ring resonator was first proposed in [102] in order to avoid cross-polarization effects, which affect the behavior of many resonators (e.g., the EC-SRR), while maintaining uniplanar geometry. The topology of the resonator, along with a sketch of the electric current and charge distribution at the first and second resonance, is represented in Figure 4.11. The non-bianisotropy in the particle response arises from the inversion symmetry with regard to its geometrical center, which ensures an exact cancellation of i) the tangential electric dipole generated at the first resonance and ii) the axial magnetic dipole generated at the second resonance, when uniform external excitations (such as plane waves) are considered. This is because both rings are identical, and the current/charge impressed in one ring presents the same amplitude of the current in the other ring. This is also true, though not formally exact, when the particle is excited as an antenna, i.e., through a differential port located in a cut opened in one of the rings, provided that the coupling between rings is strong, so that the current amplitudes in both rings are equal to i_0. The absence of the cross-polarization terms in

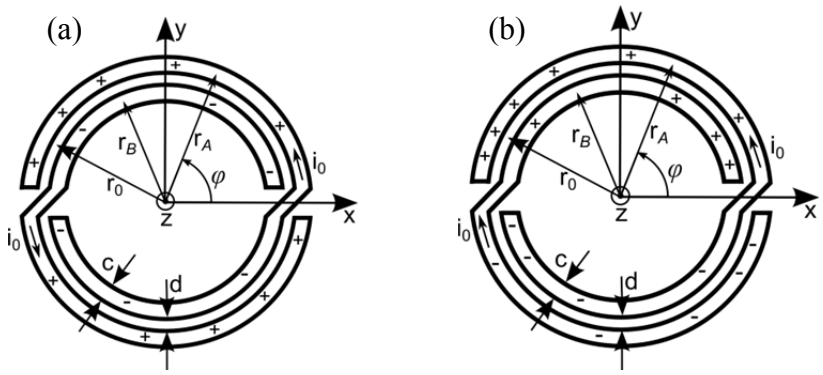

Figure 4.11. Topology and theoretical current/charge distribution of the NB-SRR at the (a) first and (b) second resonance.

the polarizability tensor represents the most important difference between NB-CSRR and EC-SRR behavior, being their electrical sizes and their equivalent circuit models fundamentally equal [32]. Hence, the radiation resistance R_{rad} of the NB-SRR at the first and second resonance can be approximated by (4.8) and (4.36), respectively. Similarly, expressions (4.25) and (4.46) can be used to evaluate the loss resistance R_{loss} at the first and second resonance, respectively, along with expressions (4.26) and (4.47) for the radiation efficiency. On the other hand, the cross-polarization level $XPOL_{max}$ of the radiated fields is expected to be much lower (ideally zero), at both resonances, as compared to the EC-SRR, due to the absence of cross-polarization. Another expected characteristic of the NB-SRR radiation pattern at the second resonance is that the electric dipole moment is not oriented along the y-axis, as it happens in the case of the EC-SRR. In fact, due to the NB-SRR topology, the ring center is not positioned at $\varphi = 0$, because the inner part of the ring is shorter than the outer part (the difference is increased when the $c + d$ is increased). Therefore, the ring center is shifted few degrees towards positive values of φ, and so the position of i_0, depending primarily on the relationship between r_B and r_A. The ring center angle φ_0 is well approximated by the expression $\varphi_0 \approx \pi/2 \cdot (1 - r_B/r_A)$, or, alternatively, $\varphi_0 \approx \pi(c + d)/(2r_0 + c + d)$, provided that the cut width is greater than the distance $c + d$. As a result, the electric dipole moment is also expected to be rotated anti-clockwise of the same angle φ_0 with respect to the y-axis.

In order to confirm the behavior detailed above, a lossless NB-CSRR without substrate was simulated by means of *Agilent Advanced Design System (ADS)*. The values of the geometrical parameters r_0, c and d are the same as in the case of the EC-SRR simulated in the previous section ($r_0 = 35.25$ mm, $c = 2$ mm, $d = 0.5$ mm, cut width 5 mm), so that the response of the structures can be compared. The differential port is placed at the position $\varphi_0 = 0.197$ (6º), which was calculated using the expression above, and corresponds to the ring center.

The simulated input impedance of the NB-SRR is depicted in Figure 4.12: the analogy with the EC-SRR impedance (Figure 4.7a) in all the frequency range is evident. The

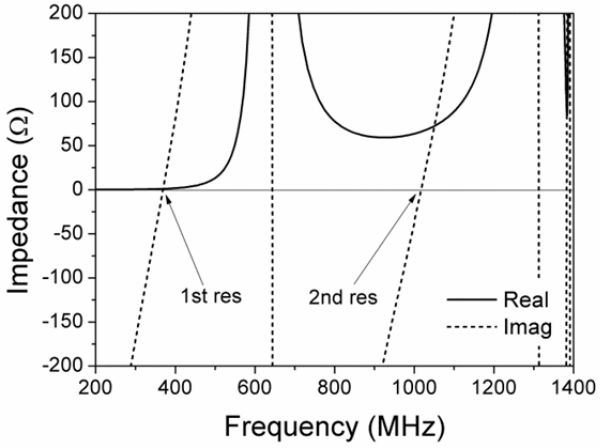

Figure 4.12. Simulated input impedance of a lossless NB-SRR. Notice the analogy with the behavior of a EC-SRR of the same dimensions (see Figure 4.7a)

most relevant difference is that the radiation resistance of the NB-SRR at the second resonance (63 Ω) is slightly smaller as compared to the EC-SRR (73 Ω), due to the slightly different charge distribution (which is not treated in this work).

The radiation diagrams at the first (0.362 GHz) and second (1.016 GHz) resonance are shown in Figure 4.13. The cut planes ($\theta = 90º$, $\varphi = 6º$) at the first resonance and ($\varphi = 96º$, $\varphi = 6º$) at the second resonance correspond to the *E*-plane and the *H*-plane, respectively. The simulated patterns confirm that the main difference between the patterns of the EC-SRR and the NB-CSRR is the absence of cross-polarization in the latter, while the directivity of the two particles are very similar (the NB-SRR provides $D_0 = 2$ dBi and $D_0 = 2.8$ dBi at the first and second resonance, respectively).

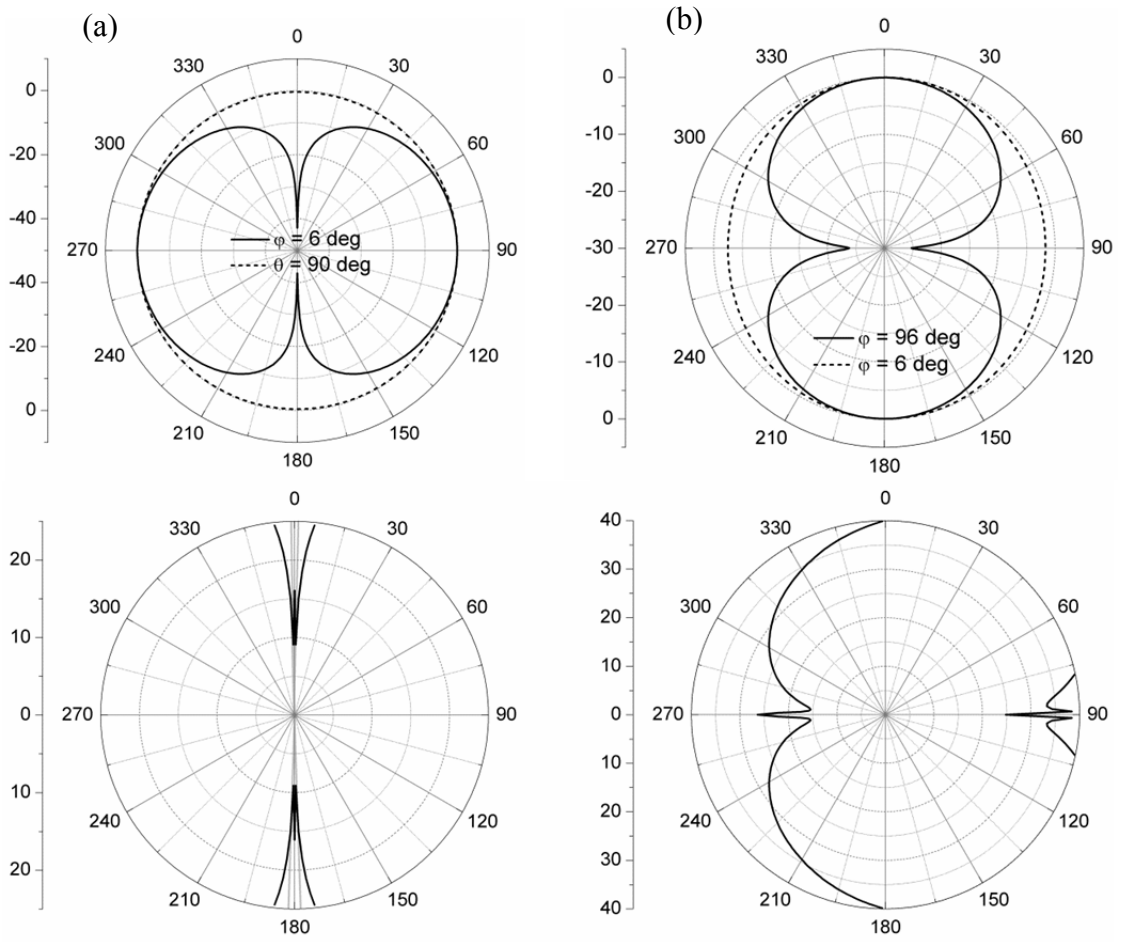

Figure 4.13. Simulated normalized radiation pattern (top) and axial ratio in the $\varphi = 96^{\circ}$ plane (bottom) of a lossless NB-SRR at the (a) first resonance and (b) second resonance. Notice that, due to the non-bianisotropy, the low-axial ratio (≤ 10 dB) region is practically inexistent.

4.4 Complementary particles (EC-CSRR, NB-CSRR): free-space and on-metal radiation

When a planar particle is replaced by its complementary screen, i.e., an unbounded, very thin and perfectly conductive sheet where the particle has been subtracted forming a slot, the complementary particle is obtained. For example, the complementary split ring resonator (CSRR), proposed in [103] as a means to obtain negative permittivity propagating structures, was obtained as the complementary screen of the EC-SRR (Figure 4.14). This transformation can be applied to any planar particle, and allows obtaining equivalent structures which may be, in certain situations (e.g., when radiating over metallic surfaces), more convenient than the initial particle. As it is well known from the concept of duality and complementarity in electromagnetism [104, 105], the fields associated to a planar particle and its complementary screen are directly related. Specifically, being $F = (E, H)$ the solution for the electromagnetic field generated by a

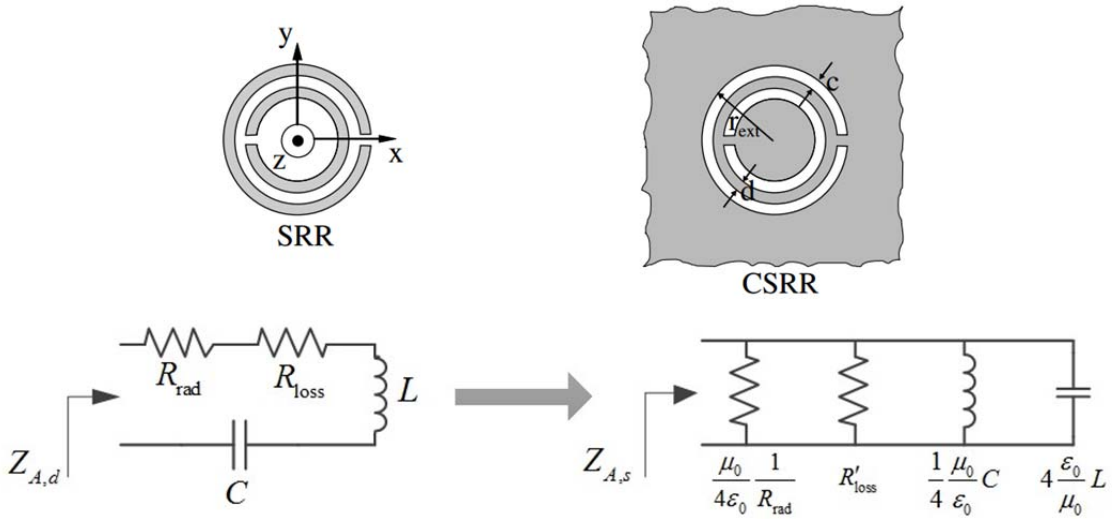

Figure 4.14. Construction of the CSRR as the complementary screen of the EC-SRR (metal is depicted in grey) (top). Extracted and adapted from [32]. Transformation of the equivalent circuit model, as seen from the center of the external ring (bottom).

particle, the field $F' = (E', H')$ associated to its complementary screen in one half-space (delimited by the screen) is defined by

$$F' = (E', H') = (-\sqrt{\mu/\varepsilon}\cdot H, \sqrt{\varepsilon/\mu}\cdot E), \tag{4.51}$$

while, due to the boundary conditions in the perfectly conductive screen and to the symmetry of the problem, the solution in the other half-space is $-F'$. It directly follows from duality that, in one side of the screen, the CSRR produces an axial electric dipole moment at the first resonance and a tangential magnetic dipole moment at the second resonance (of course, due to bi-anisotropy, each resonance actually generates both electric and magnetic moments). Equivalently, the CSRR can be seen as a magnetic current loop and a magnetic dipole at the first and second resonance, respectively. Another direct consequence of duality is that the radiation diagram of the complementary screen in an unbounded medium is the same as the radiation diagram of the particle, but the magnetic and electric field orientations are interchanged, and therefore the polarization is rotated [104]. Other far-field characteristics, such as the axial ratio, are maintained in the transformation.

As it was found by Booker in [104], duality also relates the driving impedance of a planar antenna to that of its complementary screen, namely:

$$Z_d Z_s = \frac{Z_0^2}{4} \tag{4.52}$$

where Z_d and Z_s are the impedances of the lossless particle and its complementary screen, respectively, and Z_0 is the impedance of free-space. From (4.52) it can be

deduced that the admittance of the complementary particle is proportional to the impedance of the original particle, thus suggesting that a trasformation from series to shunt occurs in the equivalent cirtuit model of the complementary particle around resonance. In fact, as it is well known in slot antenna theory, the radiated power is dependent upon the equivalent magnetic current, which corresponds to the voltage applied to the slot at a certain position. Equation (4.52) allows obtaining the radiation conductance G_{rad} of the CSRR (or the NB-CSRR) directly from the previous expressions of the EC-SRR radiation resistance (Sections 4.1 and 4.2), assuming that the particle is driven from the central position ($\varphi = 0$). At the first resonance, the radiation conductance of the ideal CSRR is found to be

$$G_{\text{rad}} = \frac{32}{3}\frac{\pi^5}{Z_0}\left(\frac{r_0}{\lambda_0}\right)^4, \tag{4.53}$$

while at the second resonance the value is

$$G_{\text{rad}} = \frac{512}{27}\frac{\pi}{Z_0}\left(\frac{r_0}{\lambda_0}\right)^2. \tag{4.54}$$

The values of the transformed shunt inductance and capacitance for the CSRR equivalent circuit model can be deduced by applying the Booker formula (4.52), obtaining the relations exposed in Figure 4.14. It is easy to show that the radiation quality factor maintains in the transformation.

As said above, the complementary screen is an ideal structure which cannot exist in practice, so that, in many cases, the principle represents an approximation. First, the Babinet's principle does not take into account losses. When finite conductivity materials (such as copper) are used, a certain amount of ohmic losses is introduced, which is in general different from the amount of losses introduced by the same material in the original particle. Several studies [106-109] shown that there is no principle relating the total losses introduced in a resonator to the losses introduced in its complementary counterpart, and only approximated expressions depending upon the slot geometry can be obtained [108]. Therefore, the antenna efficiency is in general not maintained when passing to the complementary screen of a lossy resonator (an analytical calculation of the losses associated to the CSRR is very complex, and will not be treated in this work). In addition, the Babinet's principle requires the complementary screen to be infinitely extended and to radiate in an unbounded medium. In practice, the complementary antenna is limited in size, and it often radiates over/near other bodies, such as dielectrics or ground planes. Nonetheless, in many practical cases, the principle can still be considered as a good approximation, and remains a very useful guideline to understand the impedance and far-field behavior of slot antennas. For example, when the size of the surrounding metal sheet approaches the value of $\lambda_0/2\pi$ [104], a further size increase has little influence on the impedance of the antenna.

Concerning ground planes, they are sometimes intentionally placed below the complementary structure to confine its radiation to one half-space. In these cases, their distance can be properly adjusted (ideally to the distance of $\lambda_0/4$) in order to minimize the reactive loading thrown across the center of the slot antenna, and therefore to maintain the resonant frequency and the radiation pattern virtually unaltered. However, in on-metal UHF-RFID tag design, the ground plane is represented by the metallic surface of the object, so that the distance from the radiating particle is equal to the tag thickness, which is supposed to be much smaller than $\lambda_0/4$ for obvious practical reasons. As a result, substantial changes in the particle response are expected due to the vicinity of the metal plane, such effect increasing as the distance h_s between the particle and the ground decreases. According to image theory, in one half-space (delimited by the ground plane) the system is equivalent to a set of two parallel complementary screens, separated from a distance $2h_s$, with currents flowing in opposite directions. Therefore, a system of two coupled CSRRs separated by en electric wall is obtained. According to coupled resonators theory [101], this situation leads to a decrease of the resonance frequency, with respect to the uncoupled CSRR, when the coupling between resonators is electric, and to an increase of the resonant frequency when the coupling is magnetic. As said above, the CSRR at first resonance produces a strong axial electric dipole moment, thus involving an electric coupling with the resonator image. For this reason, the first resonant frequency is lowered by the presence of a ground plane. On the other hand, it can be deduced that the second resonant frequency of the CSRR is raised by the presence of a ground plane, being basically a magnetic resonance. In both cases, the ground plane sensibly reduces the antenna radiation efficiency, due to several reasons. First, since the particle radiates only in one half-space, its radiation conductance G_{rad} is halved [104]. Moreover, the metal plane introduces an additional capacitance, as seen from antenna the input port (further increased when high-permittivity dielectric substrates are used), which involves an increase of the electric currents exciting the particle for a given applied port voltage, thus increasing the ohmic losses in the plane of the particle. Additional losses mechanisms include the ohmic losses on the metal plane, and dielectric losses (when a dielectric substrate is used). From the Poynting theorem, the latter can be evaluated according to

$$P_{\text{loss,diel}} = \omega_0 \varepsilon_0 \varepsilon_r \tan\delta \iiint_V |E|^2 dV \,, \tag{4.55}$$

where ε_r and $\tan\delta$ are the substrate relative permittivity and loss tangent, respectively, E is the electric field evaluated in the volume V between the particle and the ground plane. Dimensional analysis suggests that dielectric losses in (4.55) tend to increase as the distance h_s from the metal plane decreases, for a given voltage applied to the slot.

The radiation pattern of the CSRR in the radiating half-space is not substantially modified by the presence of the metal plane, provided that the electric field distribution along the slot (or, equivalently, the magnetic current distribution) maintains roughly

unaltered (of course, 3 dB are added to the directive gain because the power is radiated in one half-space). On the other hand, as it was deduced by Booker, important modifications of the radiation pattern of a complementary antenna come from the finite dimensions of its screen, especially in the directions of the screen plane ($\theta = 90º$), where, due to symmetry, no radiation is possible. However, short-circuiting the screen edges to the ground plane is an effective way to avoid this effect, even when the metal surroundings of the particle are small. In this case, the boundary conditions allow exciting the structure by a plane wave coming from the direction $\theta = 90º$, with electric field orientated in the z-direction, as in the case of an infinitely extended complementary screen. Technically, such antenna can be classified as a cavity-backed slot antenna, since the slot is boxed in a metallic cavity. It is known that the resonant modes in the cavity might affect the electric field distribution on the slot [110], and consequently the radiation pattern. We observed that the boxed CSRR antenna, excited with a voltage across the center of the outer ring slot (see Figure 4.15), maintains a radiation pattern similar (in one half-space) to that of the unbounded complementary screen, even for very small distances from the metal plane (Figure 4.17).

The behavior described above was verified by means of electromagnetic simulations, which also provided an estimation of the resonance split and the radiation efficiencies for different distances (5 mm, 2 mm, 1.27 mm, no metal plane) of the CSRR over the metal plane. To this end, the commercial software *CST Microwave Studio* was used. The CSRR was etched on an infinitely extended screen made of (a) perfectly conductive material (lossless case) and (b) copper (lossy case), with thickness $h = 35$ μm, and excited with a differential port placed across the slot at the position $\varphi = 0$. In order to compare the impedance response, the simulated CSRR has the same dimensions as the EC-SRR simulated at Section 4.2 ($r_0 = 35.25$ mm, $c = 2$ mm, $d = 0.5$ mm). In the cases which consider the presence of a ground plane below the resonator, the screen containing the CSRR was cut with lateral dimensions of 150 mm x 150 mm, and the four sides of the square were connected to ground by means of vertical copper walls

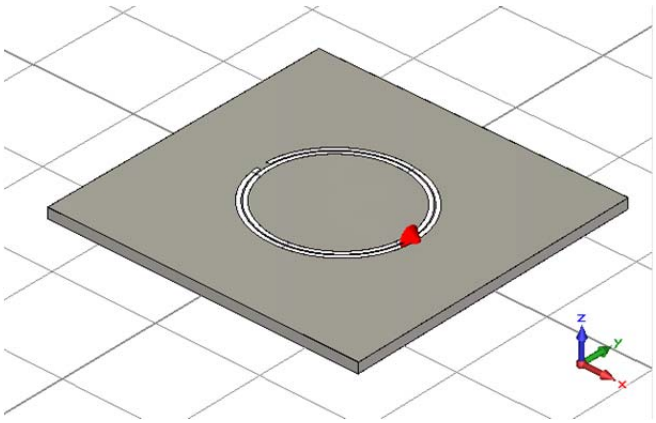

Figure 4.15. Finite size CSRR antenna short-circuited to the ground plane. Metal is depicted in grey; the ground plane is represented by the grid. The excitation port is represented by the red triangle.

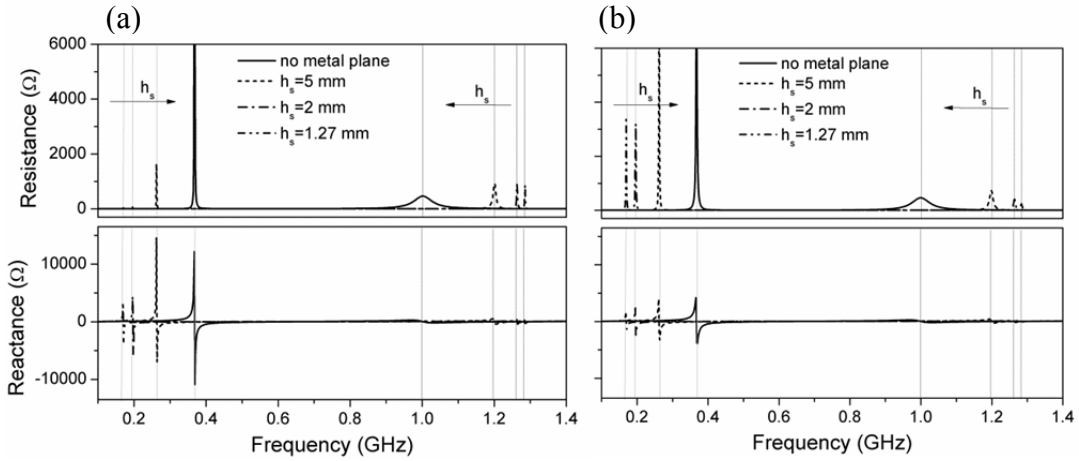

Figure 4.16. Simulated input impedance of a (a) lossless and (b) lossy (etched on a copper layer) CSRR at different distances over an infinitely extended ground plane (first resonances are marked in light grey, second resonances in dark grey).

(with thickness equal to h). The ground was defined by forcing the boundary condition $E_t = 0$ (where E_t is the electric field tangential to the plane), which describes a lossless and infinitely extended ground plane.

The simulated input antenna impedance for different cases is depicted in Figure 4.16. As expected, the frequency split associated to the presence of the ground plane is evident. It is interesting to note that, even for very small distances from the ground plane (h_s = 1.27 mm), the impedance response of the CSRR clearly shows its resonances, thus suggesting that the particle behavior is not strongly affected by the ground plane. In case no ground plane is present, the first (0.37 GHz) and second (0.99 GHz) resonances of the CSRR agree very well with the resonant frequencies of an EC-SRR of the same dimensions (see Figure 4.7). The radiation conductance G_{rad} calculated by using (4.53) and (4.54) for the first and second resonances, respectively, shows good agreement with the simulated values in the unbounded lossless case, as expected from duality. The theoretical/simulated values are $3.1 \cdot 10^{-5}$ S/$4.2 \cdot 10^{-5}$ S at the first resonance, and $2.2 \cdot 10^{-3}$ S/$2.1 \cdot 10^{-3}$ S at the second resonance.

Equation (4.53) and (4.54) were also applied to predict the radiation conductance when the radiation is confined by the ground plane, taking into account that the results must be halved, since radiation occurs only in one half-space. In this case, however, the theoretical prediction is not as accurate as in the unbounded case, and only provides a rough approximation.

As can be seen in Figure 4.16, ohmic losses associated to copper do not introduce changes in the resonant frequencies. In such a lossy case, one of the main concerns is the radiation efficiency, which can be severely affected as the distance from the ground plane is made very small. As illustrated in Table 3, the simulated values of the radiation

TABLE 3 SIMULATED VALUES FOR THE FIRST AND SECOND RESONANT FREQUENCIES OF THE BOXED CSRR OVER AN IDEAL GROUND PLANE.

	f_1 (GHz)	f_2 (GHz)	η_{rad1} (%)	η_{rad2} (%)
no ground	0.37	1	45	98
h_s = 5 mm	0.26	1.2	6	77
h_s = 2 mm	0.2	1.26	2	46
h_s = 1.27 mm	0.17	1.28	<1%	30

efficiency decrease as the value of h_s is reduced. At the first resonance, the efficiency quickly falls to very small values, due to the combined effect of the electrical size reduction (the first resonance is lowered down to half its value) and the additional losses arising from the vicinity of the ground plane. On the other hand, the results at the second resonance are encouraging even for the smallest value of h_s = 1.27 mm (λ/185), where η_{rad} = 30% is predicted. It is worth mentioning that no substrate has been considered so far. Obviously, a dielectric substrate may be necessary in many practical cases, due to its structural function. Moreover, when designing an UHF-RFID tag based on this resonance, one might want to reduce lateral dimensions, which have been increased by the presence of the metal plane (a 100 mm x 100 mm tag would result when working at 915 MHz without adding any substrate, so that the resulting tag area would be significantly larger than average), and this can be accomplished by properly choosing the permittivity of the substrate. However, as mentioned before, the substrate may cause an important reduction of the radiation efficiency, so that a careful tradeoff between tag dimensions and read range is necessary at the tag design stage.

Let us now check the electric field distribution and the radiation pattern of the CSRR (Figure 4.17) when boxed on a ground plane. The simulation results suggest that, even when the distance from the ground is small (1.27 mm), the field distribution on the slot is similar to that of the ideal CSRR. Notice that, due to duality, the proximity effects encountered in the EC-SRR are also replicated in the electric field distribution (or, equivalently, in the magnetic current density) on the slot. As a result, the radiation pattern (in the upper half space) is also very similar (Figure 4.7c).

In conclusion, although the ground plane lowers the radiation efficiency of the CSRR, it is actually interesting to explore this solution for the design of UHF-RFID tags with low-profile and acceptable read range, in light of the novelty that this kind of design represents over the state of the art. In the next chapter, an on-metal UHF-RFID tag based on a NB- CSRR working at the second resonance will be presented, along with the design concepts and the measured read range.

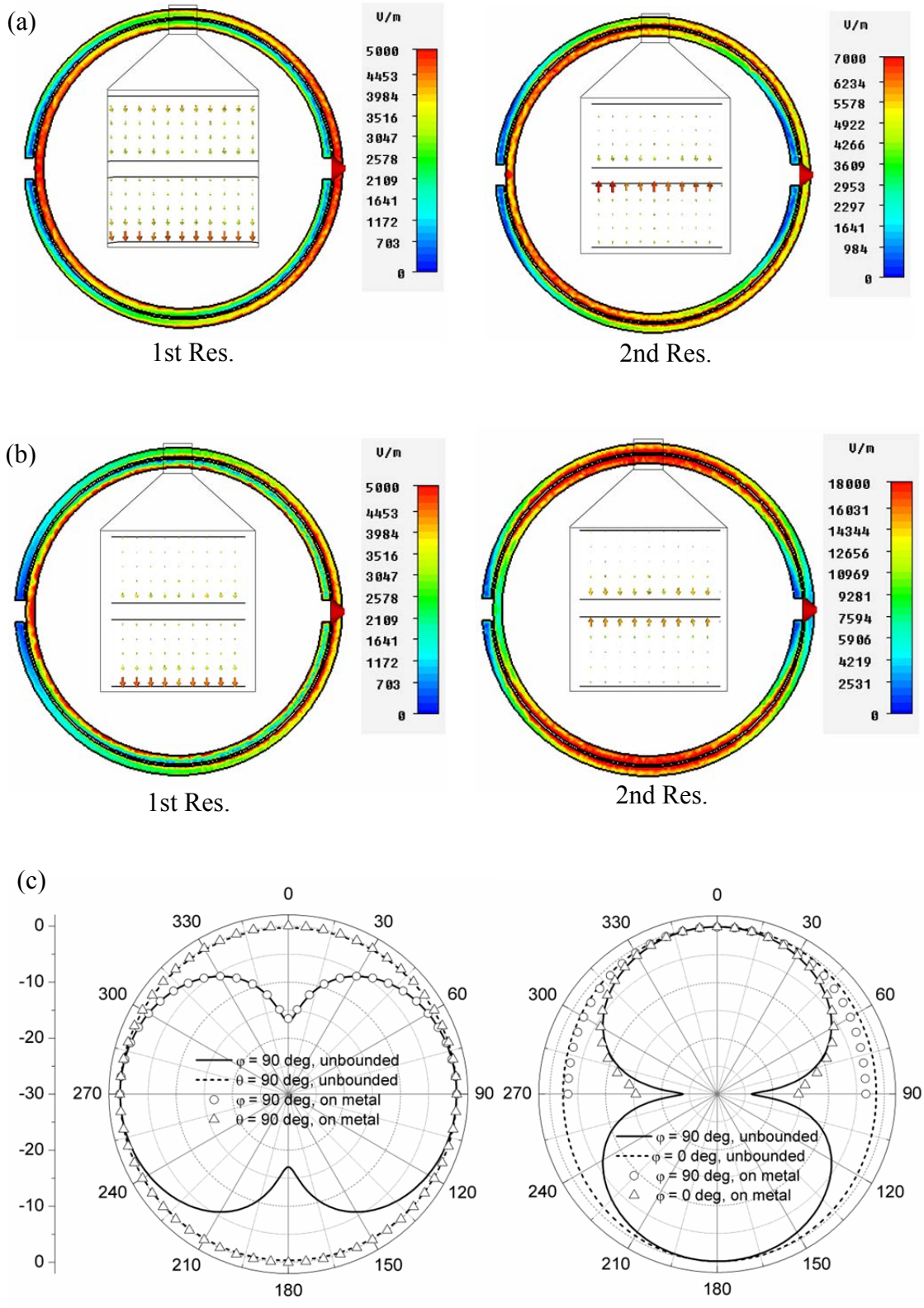

Figure 4.17. Amplitude of the electric field tangential to the slot of the (a) unbounded CSRR and (b) CSRR boxed on a ground plane (at a distance h_s = 1.27 mm). A zoom of the *E*-field vector in the slot at the position $\varphi = 90^{\circ}$ is also represented. (c) Radiation pattern at the first and second resonance (left and right, respectively).

5

Antenna and UHF-RFID Tag Design based on Split-ring Resonators and Derived Structures

In the previous chapter, an analysis of the radiation properties associated to the more commonly used electrically small resonators (EC-SRR, CSRR, NB-CSRR) was provided and validated by means of electromagnetic simulations. Such analysis is at the base of the antenna and UHF-RFID tag designs presented in this chapter. The main purposes of this chapter are i) to validate, by means of experimental data, the analysis from the previous chapter and ii) to demonstrate the practical utility of metamaterial-inspired resonators in antenna and UHF-RFID tag design. The design process, including antenna geometry adjustment and impedance matching strategy, is detailed in each case. Then, a prototype is fabricated and measured, and the results are compared with simulations and theory.

The presented devices include an electrically small UHF-RFID tag based on an EC-SRR at its fundamental resonance (Section 5.1), a low-profile on-metal UHF-RFID tag based on a NB-CSRR at its second resonance (Section 5.2), and a 50 Ω EC-SRR antenna working in the 900 MHz ISM band (Section 5.3).

5.1 UHF-RFID tag based on EC-SRR at its fundamental resonance

As shown at Section 4.1, the SRR at its fundamental resonance is capable of providing acceptable radiation efficiency when the trace width c is properly chosen. As mentioned above, an important limiting factor in this case is the operating bandwidth, which is severely restricted ($FBW \approx$ 1-2%) due to the very small electrical dimensions of the antenna ($\lambda_0/10$ in diameter). While this represents a serious problem for many applications, this is not the case of UHF-RFID, where the required bandwidth is very small. Moreover, the radiation pattern of the EC-SRR at its first resonance is interesting for UHF-RFID tags, since it does not present radiation zeros. As seen at Section 4.1.3, the parameter $XPOL_{\max}$ provides a relation $[XPOL_{\max}/(1+XPOL_{\max})]$ between the minimum and maximum antenna gain, which occur in the z-axis and x-axis directions, respectively. Therefore, on the basis of the read range equation (3.1), it can be found that:

$$RR_z = RR_x \sqrt{\frac{XPOL_{\max}}{1+XPOL_{\max}}} \,. \tag{5.1}$$

For a value of $XPOL_{\max} = -10$ dB, the tag read range in any direction is higher than the 30% of the maximum read range. This is a clear advantage over the conventional RFID tags, based on meandered electric dipoles, which present two blind spots in the direction of the tag axis. Another important advantage is represented by the significant reduction of the tag lateral dimensions, as compared to conventional tags, without the need of any size reduction technique (e.g., meandering). Furthermore, as it will be demonstrated below, proper impedance matching between the antenna and the RFID ASIC can be achieved without the need of a matching network. This represents a benefit in terms of tag size and performance. All these features encouraged us to propose an UHF-RFID tag prototype based on an EC-SRR antenna, as detailed below.

5.1.1 Tag design and simulation

In this section, the tag prototype design process, based on the analysis of the previous section and aided by means of EM simulations, is presented. The tag was designed to be used in the North-American UHF-RFID band (902-928 MHz), which is centered at $f_0 = 915$ MHz. The simulations were performed by means of the commercial software *Advanced Design System*. The RFID ASIC used for the prototype is the *Alien Higgs 3* with SOT-323 packaging, a nominal input impedance of $Z_C = R_C + jX_C = 25 - j190\ \Omega$ at f_0, and a minimum sensitivity of $P_{\text{th}} = -17$ dBm (as detailed in Table 1).

Let us first discuss the impedance matching between the RFID ASIC and the SRR antenna. Since the SRR presents a narrow-bandwidth (as it will be detailed later) series

resonance, it is expected that nearly beyond resonance the inductive reactance part will match the capacitive reactance of the chip. At this frequency, the reflection coefficient notch depth (and thus the value of τ) depends on the ratio between the input resistance R_{in} and the chip resistance R_C. If the port is placed in the external ring at $\varphi = 0^o$, where a current maximum i_0 occurs, the input resistance is equal to $R_0 = (R_{rad}+R_{loss})$, which is in general much lower than R_C, resulting in an important impedance mismatch. However, it is possible to change the port position in order to increase the input resistance $R_{in}(\varphi)$ until reaching a good impedance matching without the need of an external matching network. In fact, as reported in [17], the following expression provides the input resistance, as a function of the port position, for asymmetrically fed wire antennas:

$$R_{in}(\varphi) = \frac{i_0^2}{i_A^2(\varphi)} R_0 . \tag{5.2}$$

where i_A is the amplitude if the current on the external ring at the position φ. By combining (5.2) with the current profile i_A expression (4.3), the port angle providing $R_{in} = R_C$ is found to be:

$$\varphi_p = \pm\pi\left(1-\sqrt{\alpha}\right). \tag{5.3}$$

where α is a scaling factor, and is defined as $\alpha = R_0/R_C$. The proposed method allows overcoming the limitations reported in [111] on the impedance matching between an RFID ASIC and an SRR antenna.

As a first step of the design process, a dielectric substrate was chosen. To avoid further size reduction, with consequent radiation efficiency decrease, a thin and low permittivity substrate was chosen (as in the case of most commercial UHF-RFID inlays). The *Arlon CuClad 250LX* was selected, presenting a thickness $h_s = 0.49$ mm, a relative permittivity $\varepsilon_r = 2.42$, a loss tangent $\delta_{loss} = 0.0018$ and a copper layer with a thickness $h = 35$ μm. Thus, the SRR was designed as follows. A differential 50 Ω port was connected through a 1 mm wide cut opened on the external ring at the position $\varphi_p = 0$, where the input resistance R_{in} is equal to R_0 by definition. Based on the radiation efficiency expression (4.26), the ring width was set to $c = 2.2$ mm, in order to ensure an efficiency of about 90% (neglecting dielectric losses, and considering that $r_0 \approx \lambda_0/20$) (see Figure 4.4). Then, a combination of mean radius r_0 and distance d was chosen in order to locate the first resonance just below the working frequency f_0, according to the impedance matching considerations exposed above. The set of values $r_0 = 13.1$ mm ($\lambda_0/25$) and $d = 0.33$ mm (consequently, $r_{ext} = 15.46$ mm) provided resonance at $f_r = 900$ MHz, as can be observed on the basis of the simulated input impedance, depicted in Figure 5.1. The simulated value of the input resistance is $R_0 = 1.3$ Ω. [Note that, by combining the expressions of the radiation resistances associated to the SRR electric and magnetic dipole moments, i.e., expressions (4.15) and (4.25), respectively, a theoretical value (which neglects the dielectric losses) of $R_0 = 1$ Ω is obtained].

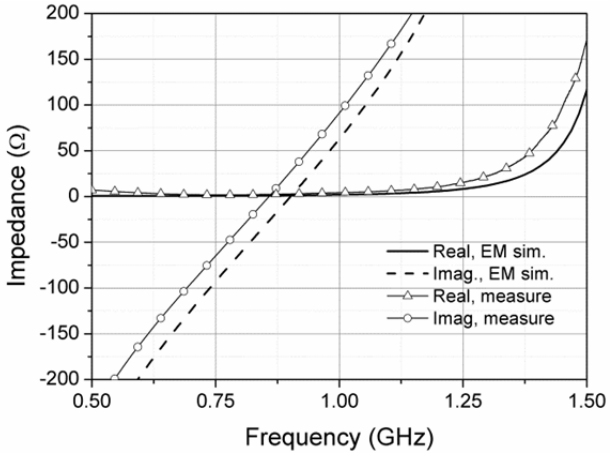

Figure 5.1. Input impedance of the SRR antenna fed at the center of the external ring. Dimensions are r_0 = 13.1 mm, c = 2.2 mm and d = 0.33 mm.

Therefore, the scaling factor was determined as $\alpha = R_0/R_C = 1.3/25 = 0.052$ and, by using (5.3), the port positions providing conjugate matching were found to be $\varphi_p = \pm 139º$. The following simulation was then performed by placing the port cut at the position $\varphi_p = -139º$, and modeling the port by the RFID ASIC equivalent circuit model, which is an RC shunt circuit, with values R_c = 1500 Ω, C_c = 0.9 pF (as mentioned above, it provides $Z_C = R_C + jX_C = 25 - j190\ \Omega$ at f_0). The final tag layout, along with the simulated current distribution at the working frequency, is depicted in Figure 5.2a.

The simulation results, in terms of power reflection coefficient, are depicted in Figure 5.2b. As expected, good impedance matching [−19 dB, which in RFID provides 99.4% of the read range obtained with conjugate matching, according to (3.1)] was obtained closely above the SRR resonant frequency, at 920 MHz, which is close to the central

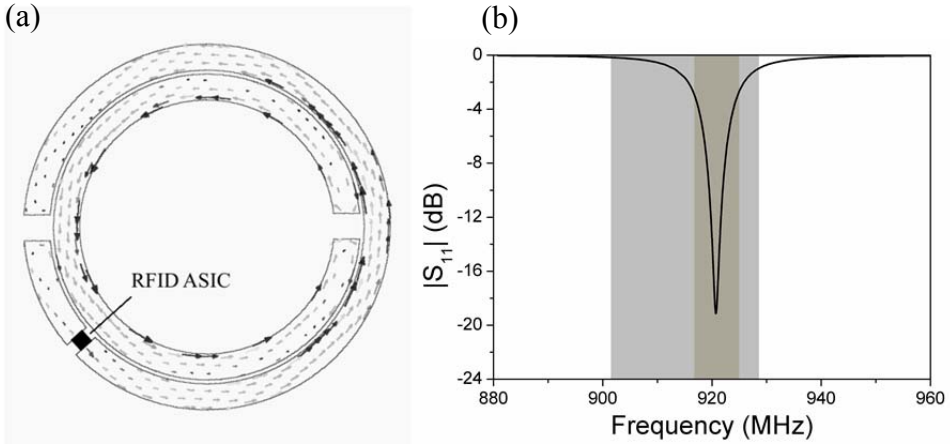

Figure 5.2. Simulated (a) current distribution in the SRR tag antenna and (b) power reflection coefficient of the proposed tag. The half-power bandwidth is depicted in dark grey, the North-American UHF RFID band is depicted in light grey.

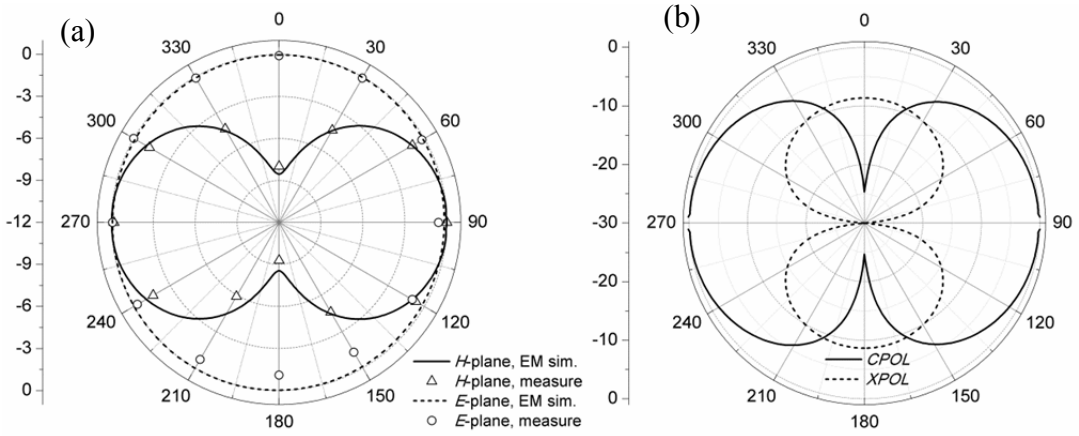

Figure 5.3. (a) Normalized radiation pattern in the *H*-plane (φ = 0º) and *E*-plane (θ = 90º), (b) co-polar and cross-polar pattern in the *yz*-plane

frequency of the North-American UHF-RFID band. The simulated half-power bandwidth of the tag (depicted in grey) is BW = 8 MHz.

The simulated radiation pattern, depicted in Figure 5.3, is very similar to that of the EC-SRR shown in Figure 4.5a, which has approximately the same dimensions of the design presented here. The realized gain provided by simulation is −0.1 dB. Therefore, the maximum read range, predicted by using (3.1), is RR_x = 11.5 m. Again, the tag read range in the axial direction can be predicted by using (3.1) with the simulated gain in the z-direction (−8.7 dB), resulting in RR_z = 4.3 m. The simulated value of $XPOL_{\max}$ can be directly read in the normalized pattern in the *yz*-plane (Figure 5.3b), where the radiation from the electric and magnetic moments is decoupled, as predicted in Section 4.1.3). Note that the simulated value (−9 dB) is very near to the theoretical value (−10 dB), obtained from (4.27). A validation of expression (5.1), and, consequently, of the SRR antenna modeling as a combination of two elemental radiators, can be done by evaluating the tag read range in the axial direction on the basis of $XPOL_{\max}$ and RR_x. The result is RR_z = 3.8 m, which is similar to the value predicted above (the discrepancy is around 15%). The simulated directivity is D_0 = 1.6 dB, and the radiation efficiency was found to be η_{rad} = 67%. In comparison, by using (4.26) with the given SRR dimensions, a theoretical efficiency of 84% is predicted. The difference is attributed to the presence of the substrate, which, as confirmed by means of simulations with lossless substrates, introduces significant amount of dielectric losses.

Figure 5.4. SRR antenna input impedance measurement assembly.

5.1.2 Fabrication and measurements

To validate the simulated results, the layout described in the previous section was fabricated by means of a PCB drilling machine (*LPKF-H100*). In order to measure the SRR antenna input impedance, a first prototype was fabricated with the input port placed at the center of the external ring ($\varphi = 0$) (Figure 5.4). The antenna impedance was measured by using the technique reported in [23], resumed as follows. The SRR antenna was connected to the signal analyzer through a test fixture based on two semi-rigid coaxial cables soldered together. Based on the measured single-ended scattering parameters, the differential input impedance was then obtained by analytical transformations. The results, depicted in Figure 5.1, exhibit good agreement with simulations. Nevertheless, the first resonance according to measurements is located at 857 MHz, which is 43 MHZ below the simulated value (900 MHz).

The final tag prototype (Figure 5.5a) was then fabricated by applying a scaling factor (0.97), in order to compensate the frequency shift detected in the measurements. The final tag dimensions are $r_0 = 12.7$ mm, $c = 2.1$ mm, $d = 0.32$ mm and consequently $r_{ext} = 15$ mm ($\lambda_0/22$). The ASIC was soldered across the cut opened at the position $\varphi_p = -139^o$ (see previous section). The substrate, which was considered infinite in the simulations, was cut round-shaped with a radius approaching r_{ext} in order to minimize the tag dimensions (Figure 5.5a).

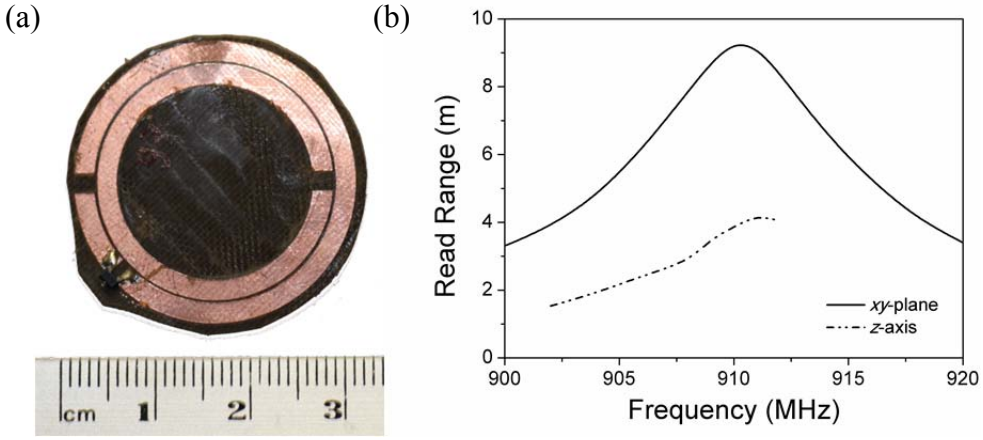

Figure 5.5. (a) Fabricated tag prototype (97% scaled) and (b) experimental read range.

The tag radiation pattern was then measured by using the method described at Section 3.2.3. The pattern in the *E*-plane and *H*-plane, depicted in Figure 5.3a, exhibits very good agreement with both theory and simulation. The experimental read range along the *x*-direction (also obtained according to the setup described at Section 3.2.3), depicted in Figure 5.5b, reaches $RR_x = 9.3$ m at 911 MHz, which is 20% lower than the predicted value (11.5 m, see previous section). However, this discrepancy is compatible with the tolerance of P_{th} declared by the ASIC manufacturer, which ensures a minimum value of $P_{th} = -15$ dBm (while $P_{th} = -17$ dBm is the "typical" value). By using this value, the predicted read range is 9.2 m, very similar to the measured value.

The measured axial read range reaches $RR_z = 4.2$ m, which is very close to the value predicted in the previous section (4.3 m). Nevertheless, if a new prediction is done by correcting the value of P_{th} to −15 dBm (as in the case of RR_x), the simulated value only reaches 3.4 m. As a result, measurements suggest a value of $XPOL_{max} = -6$ dB, i.e., nearly 3 dB higher than the simulated value and 4 dB higher than the theoretical value predicted by means of (4.27). Such a difference might be attributed to non-idealities in the measurement process, e.g., the non-perfect TEM propagation inside the cell. The tag half-power bandwidth, extracted from the read range curve, is $BW = 7$ MHz, which is in good agreement with the simulated bandwidth (8 MHz, previous section). It is interesting to compare the measured value to the value predicted in (4.31), taking into account the size of the scaled tag and considering $\eta_{rad} = 0.67$ (i.e., the simulated value). The result for the predicted half-power bandwidth is $BW = 8$ MHz, which is in perfect agreement with the simulated value, and very near to the measured one.

As confirmed by measurements, the proposed tag is very performing (relatively to its dimensions) in terms of read range. It is worth mentioning that with the latest ASICs available on the market (e.g., Alien Higgs 4, with $P_{th} = -18.5$ dBm [24]), the read range could be extended up to 13.7 m. Nevertheless, like any other electrically small UHF-RFID tag, performance degradation in terms of radiation efficiency and impedance matching may occur when the tag is attached to some objects, depending on the electromagnetic properties of the labeled item. In many cases this can be taken into account in the tag design stage (e.g., when the object is known a priori) in order to mitigate these effects.

5.1.3 Conclusions

In this section, a small passive UHF-RFID tag based on an SRR antenna working around its first resonance has been presented. The tag design, aided by means of EM simulations, was based on the theoretical analysis of the input impedance and the radiation properties of the SRR, described in the previous chapter. An impedance matching strategy has been introduced, suggesting that good impedance matching between the ASIC and the SRR antenna can be achieved without the need of an additional matching network. In order to validate the simulated results, a tag prototype

of size 30 mm × 30 mm ($\lambda_0/11 \times \lambda_0/11$) was manufactured. The SRR antenna input impedance, along with the tag radiation pattern and read range, were validated experimentally. The tag measured read range reaches 9.3 m at 911 MHz in the direction of maximum read range, and 4.2 m at the same frequency in the direction of minimum read range.

The main advantages of the presented tag are its small dimensions and the absence of radiation zeros, which are typically present in general-purpose UHF-RFID tags, and result in undesired blind spots in the read range.

5.2 On-metal UHF-RFID tags based on Non-bianisotropic Complementary Split Ring Resonator

The radiation properties of complementary split ring resonators (CSRRs) boxed over a ground plane were discussed in Section 4.4. The analysis, mainly based on electromagnetic simulations, showed that good performance can be obtained when the particle works around its second resonance, even at a very small distance over the metal plane (1.27 mm). However, such results have to be considered only a starting point, because no substrate was used in the simulations. The dimensions of the resonator are, in terms of area, greater than most of the commercial UHF-RFID tags, including many on-metal tags. Obviously, the introduction of a dielectric substrate reduces the electric size of the tag, but also its performance (as mentioned in the previous section, special concern is about radiation efficiency). For this reason, when choosing a substrate, the value of its permittivity should be properly chosen to obtain an acceptable tradeoff between dimensions and performance, mainly depending upon the final tag application. In the tag prototype design presented in this work, we wanted to explore the possibility of reducing lateral dimensions to a great extent, while maintaining a reasonable value of the tag read range. The non-bianisotropic version of the CSRR (NB-CSRR) was chosen for this preliminary design due to its simpler radiation diagram, which arises from a single radiating dipole moment, and presents very low values (ideally zero) of cross-polarization.

5.2.1 Tag design and simulation

As stated above, the presented tag design was aimed to reduce the lateral dimensions. Hence, a high permittivity substrate was chosen, namely the *Rogers RO3010*, with relative permittivity $\varepsilon_r = 10.2$, loss tangent $\tan\delta = 0.0023$ and thickness $h_s = 1.27$ mm

($\approx \lambda/260$ at 915 MHz). The ASIC used for the design is the *Alien Higgs 3* with SOT-323, which presents an input impedance of $Z_C = 25-j190\ \Omega$ at 915 MHz.

The impedance matching strategy adopted in this case is very similar to the one used for the tag of the previous section, where an EC-SRR was used as the radiating element. As a result of duality, a complementary resonator can be modeled as a shunt circuit around resonance (see Figure 4.14), and hence it presents inductive behavior below resonance. Due to the reduced dimensions of the particle in terms of wavelength, and the vicinity of the metal plane, the radiation quality factor of the particle is expected to be high, leading to high values of the reactance slope around resonance. As a result, the antenna reactance is expected to resonate with the ASIC capacitive reactance nearly below the NB-CSRR second resonance. The matching level at resonance is a function of the ratio between the ASIC conductance G_c and the antenna input conductance G_a (neither of the quantities depend on frequency, in a first order approximation, provided the bandwidth is small), which can be controlled by adjusting the position φ_p of the input port along the slot. Duality ensures that, similarly to the case of moving the input port along the SRR ring (see Section 5.1.1), the NB-CSRR input conductance is transformed to higher values, as respect to the input conductance at the center, when moving towards the ends of the slot. Therefore, provided that the input conductance at the center of the NB-CSRR is lower than the ASIC conductance, it is possible to obtain the required impedance matching at the working frequency without the need of a matching network, by properly choosing the port position along the slot. Unlike in the case of the SRR based tag, were the port position φ_p was evaluated on the basis of expression (5.3), a parameter sweep of the port position was performed here. This is because, as a result of the low radiation efficiency, in this case we do not have a precise knowledge of the antenna input conductance and its variation with the angle, being the loss conductance expected to overtake the radiation conductance.

It is worth mentioning that, due to the high quality factor of the proposed particle when operating over metal, the bandwidth of the tag is limited to a few MHz, which excludes the possibility of a worldwide functionality of the tag, though it is fully sufficient for the correct operation in one region. However, narrowband impedance matching is typical for low-profile on-metal UHF-RFID tags [112].

Based on the electromagnetic simulations, the values of the geometric al parameters were adjusted to $r_0 = 18.95$ mm, $c = 1$ mm, $d = 0.5$ mm, $w = 6$ mm, obtaining the second resonance at $f_2 = 925$ MHz. The port position which provided optimal impedance matching with the *Alien Higgs 3* ASIC at $f_0 \approx 915$ MHz was found to be $\varphi_p = -30º$. The overall lateral dimension of the simulated structure are L x L, with $L = 45$ mm (Figure 5.6a).

The simulated power reflection coefficient of the tag is depicted in Figure 5.6b. A good matching level (−16 dB) is obtained at 914 MHz, with a half-power bandwidth of 5 MHz.

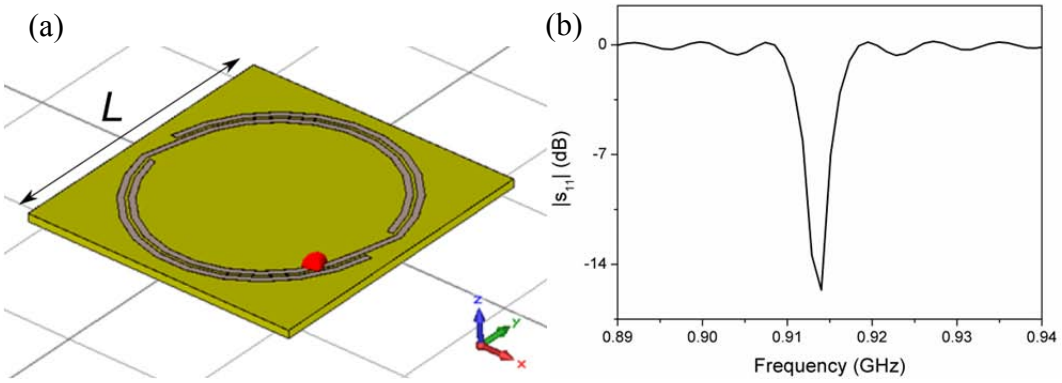

Figure 5.6. (a) Tag layout and (b) simulated power reflection coefficient.

Let us now focus on the simulated tag antenna parameters. As expected, the radiation pattern (Figure 5.7) at 915 MHz agrees very well with the pattern produced by the tangential magnetic dipolar moment of the NB-CSRR. The axis of the dipole is oriented at $\varphi = 107º$ *(H*-plane*)*, where a null in the far-field radiation occurs. The directivity of the antenna is D_0 =5 dBi (for an infinitely extended metallic plane), and the radiation efficiency is $\eta_{rad} = 10\%$, resulting in a gain of $G_0 = -4.7$ dB. Although, as expected, this value is considerably lower than the value obtained when no substrate was used ($\eta_{rad} = 30\%$ was obtained, see Table 3), it is still reasonable for an UHF-RFID tag. In fact, the predicted read range reaches $RR = 6.8$ m, which is in line with existing low-profile on-metal tags of similar dimensions (see Section 3.4). Moreover, as can be seen by observing the axial ratio depicted in Figure 5.8a, the non-bianisotropic nature of the resonator is maintained to a great extent in this configuration, despite the vicinity of the ground plane and the port position (which formally breaks symmetry in the excitation of the particle). The axial ratio is higher than 40 dB over the whole half-space ($z > 0$), and the Ω_{ell} zone is very small. For comparison, an alternative tag design based on a CSRR with the same dimension was simulated, and its axial ratio at the second resonance is

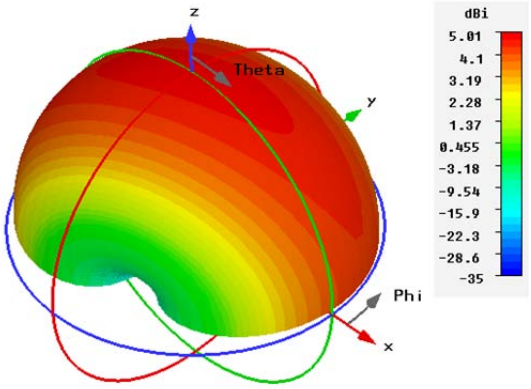

Figure 5.7. Simulated far-field radiation pattern of the NB-CSRR-based tag at 915 MHz.

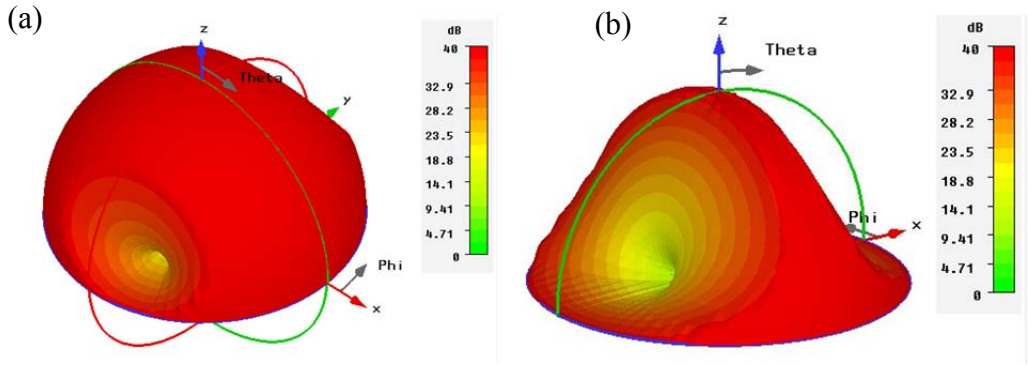

Figure 5.8. Comparision between the axial ratio of the (a) NB-CSRR-based and (b) CSRR-based tags working at their second resonance.

represented in Figure 5.8b. The difference is evident, and it consistent with the analysis presented at Chapter 4.

5.2.2 Fabrication and measurements

In this section, the manufactured tag prototype (Figure 5.9a) is presented, along with the experimental read range, in order to validate the simulated results. The layout, described in the previous section, was fabricated by means of a PCB drilling machine (*LPKF-H100*). For practical reasons, the short-circuit connections of the tag sides to the ground plane were implemented by using vias (8 each side, with radius 0.15 mm). Simulations suggested that, in this case, an increase of the lateral dimensions of the tag sides (the NB-CSRR dimensions are not changed) is necessary in order to maintain the resonant frequency at 915 MHz. The lateral dimensions of the fabricated tag are 60 mm x 60 mm.

The experimental read range is depicted in Figure 5.9b. The tag response is centered at the frequency $f_0 = 958$ MHz, exhibiting a frequency shift of about 40 MHz, which should be attributed to simulation and fabrication tolerances. The maximum measured read range (5.3 m) is roughly 20% smaller than the simulated value, while the measured half-power bandwidth (extracted from the read range, providing 12 MHz approximately) is wider than the simulated (5 MHz). Both of the effects mentioned above should be attributed to the additional ohmic losses introduced by: i) the connections to ground, which have been implemented in the prototype by using vias, instead of the vertical metallic walls considered in the simulation and ii) the losses on the copper metal plane, which were not considered in the simulations. The effect of these losses is to decrease the antenna quality factor, and therefore enhance its bandwidth. This behavior was confirmed by later simulations, which provided a bandwidth of 10 MHz and a gain of −10 dB, taking into account the presence of the vias and the losses in the metal plane. However, the read range resulting from simulations with vias is 3.5 m, which is lower

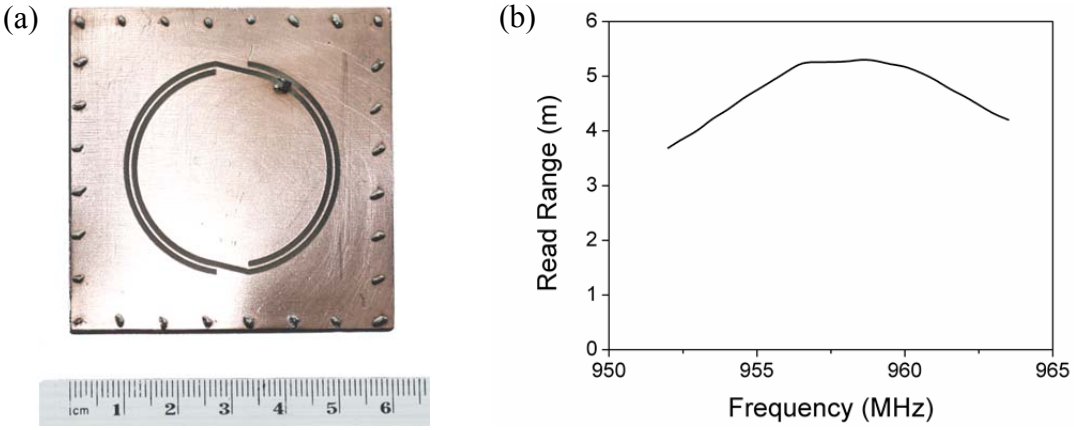

Figure 5.9. (a) Tag prototype and (b) experimental read range over a copper plane of 300x200 mm.

than the measured value. This fact, along with the 40 MHz frequency shift in the tag response, suggest that EM simulations of complementary particles working at a very small distance from a metallic surface are subjected to a certain degree of uncertainty, which increases as the distance from the metal decreases.

5.2.3 Conclusions

The behavior of the NB-CSRR antenna for UHF-RFID tags placed at very small distance (1.27 mm ≈ λ/260) from a metallic surface has been studied in this section. Due to the configuration of its intrinsic dipolar moments, the particle has been found by means of EM simulations to present acceptable radiation efficiency (10% with *RO3010* substrate) near its second resonant frequency. Furthermore, the non-bianisotropy of the NB-CSRR causes the polarization of the radiated fields to exhibit a very high linear axial ratio (> 40 dB in EM simulations). This property was emphasized when comparing the radiation of the presented particle and a complementary split ring resonator (CSRR) of the same dimensions.

Based on the NB-CSRR antenna, a very low-profile, on-metal passive UHF-RFID tag (dimensions are 45 mm × 45 mm ×1.27 mm) has been designed. The proposed impedance matching strategy allowed obtaining good impedance matching (−16 dB) between the antenna and the RFID ASIC (*Alien Higgs 3*) at 914 MHz (which is roughly the center of the North-American UHF-RFID band). The simulated overall antenna gain (−4.7 dB), suggested a read range of 6.8 m when placed over an infinitely-extended ground plane. In order to confirm the simulated results, a tag prototype was manufactured and tested. The experimental read range reached 5.3 m, validating the suitability of the NB-CSRR resonator as a radiating element for on-metal passive UHF-RFID tags with very low profile.

5.2.4 Other proposals

As discussed in Section (4.4), the use of high-permittivity dielectric substrates produces an increase of the ohmic losses in the conductors forming the slot antenna, reducing the radiation efficiency. In case of working over metal at the second resonance, however, high-permittivity substrates are necessary to contain the lateral size within acceptable values. On the other hand, when working at the first resonance, the particle is so small that the use of a high-permittivity substrate is not necessary, but at the same time, due to its reduced dimensions, its radiation efficiency is totally insufficient for practical use (Table 3). This situation is worsened as the thickness over metal is made smaller. However, the first resonant frequency of the SRR can be increased by using derived structures. In particular, the double-split SRR (2-SRR) resonates at twice the resonant frequency of an SRR of the same dimensions [102]. This structure is obtained by providing each ring with two cuts, separated by 180º (Figure 5.10a). At the fundamental resonance, the current in each ring section flows in the same direction, like in the native SRR, so that the structure still behaves as a uniform current loop in terms of radiation. Unlike the SRR, however, the 2-SRR presents inversion symmetry, which makes it a non-bianisotropic particle. It is clear that, being the tag oriented to on-metal applications, the complementary counterpart of the 2-SRR, i.e., the 2-CSRR, is much more suitable, since it generates an axial electric (equivalent) dipole moment, compatible with the boundary conditions imposed by the metallic surface. The geometric parameters (height over the metal plane, width and separation between rings, and port position across the slot) can be tailored to adjust the resonant frequency, or, equivalently, the electrical size of the antenna, until reaching acceptable radiation efficiency. In case, the number of slits can be even increased to obtain larger uniform current loops with controllable electrical size. Similarly to the case of the previous tag (based on the NB-CSRR), the impedance matching can be controlled by changing the port position along the slot. Again, the input conductance at the slot center must be lower than or similar to that of the ASIC, thus setting a limit to the maximum size of the loop suitable for the tag. On the basis of (4.52), and considering that radiation conductance is halved by the presence of the metal plane, the maximum loop radius for

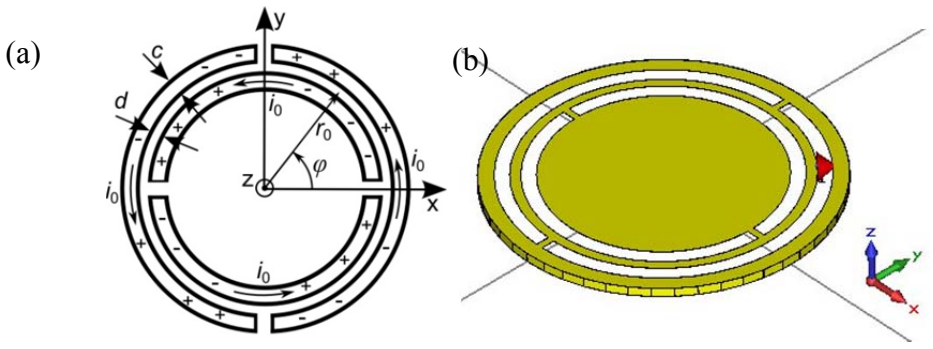

Figure 5.10. (a) Topology of the 2-SRR and electric current/charge distribution at its first resonance. (b) Layout of the proposed tag over metal (the input port is depuicted in red).

proper impedance matching to the *Alien Higgs 3* ASIC is in the order of 40 mm. This is a rough estimation, because, as already mentioned at Section 4.4, the prediction of the radiation conductance is not accurate when the particle is working over metal. Moreover, loss conductance was not taken into account.

By following the principles exposed above, a tag prototype was designed and simulated by means of *CST Microwave Studio*. The approach allowed obtaining a tag with lateral dimensions comparable to the tag based on the NB-CSRR at the second resonance, without using any substrate.

The tag layout is shown in Figure 5.10b. As in the previous case, the tag thickness over metal was fixed to $h_s = 1.27$ mm, and the thickness of the screen containing the particle was set to $h = 35\mu$m. In this case, the screen containing the particle was cut round-shaped, with a radius of 20.5 mm, and the boundary of the screen was connected to ground by means of a vertical copper wall (with thickness equal to h). To increase the accuracy of the simulation results, the ground was modeled by a conductive wall with the conductivity of copper ($\sigma = 5.96 \cdot 10^7$ S/m). The volume enclosed by the antenna was treated as air in the simulation, since no substrate was used.

The 2-CSRR mean radius was set to $r_0 = 18.6$ mm, the distance between rings to $d = 1.4$ mm and the ring width to $c = 2$ mm. The port position providing optimal impedance matching to the *Alien Higgs 3* SOT-323 ASIC was found to be $\varphi_p = 50º$.

The simulated power reflection coefficient, depicted in Figure 5.11a, exhibits good impedance matching at 915 MHz. The radiation pattern (Figure 5.11b) suggests that the 2-CSRR behaves as a loop antenna, with a quasi-omnidirectional pattern on the *xy*-plane, as expected from the current distribution of the 2-CSRR around its first resonance. Regarding the radiation efficiency, a significant improvement was obtained by avoiding the use of a dielectric substrate. The simulated value reaches $\eta_{rad} = 23\%$, with a maximum gain of $G_0 = -1.3$ dB towards the x-direction, thus allowing read ranges in the order of 10 m.

Obviously, due to the absence of a substrate, and the consequent lack of structural rigidity, the presented solution is not suitable for manufacturing without further modifications. One possible solution is to increase the thickness of the metal, and even the metal type, to obtain a self-supporting structure. For example, a stainless-steel edition of the tag would possess sufficient rigidity to withstand the environmental conditions in many applications. Due to the lower conductivity of this material, however, the radiation efficiency would be reduced. Simulation results predicted an efficiency of $\eta_{rad} = 11\%$, leading to a gain of $G_0 = -4.8$ dB and a read range of 6.7 m.

Alternatively, a very thin PET substrate with copper metallization may be used,

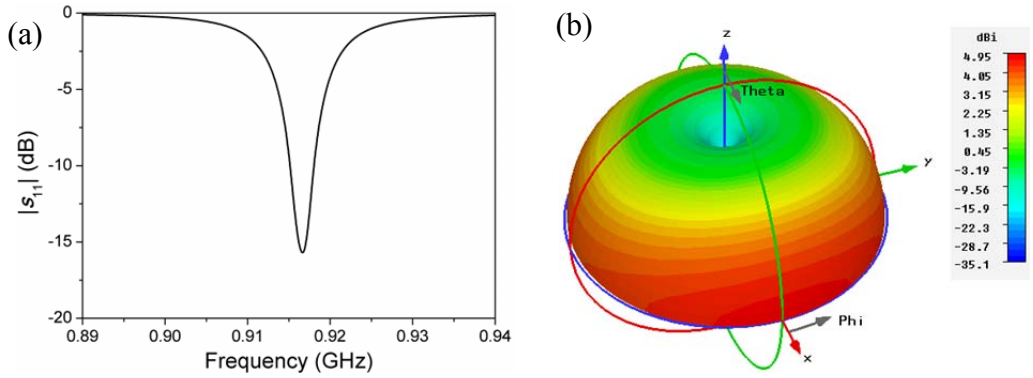

Figure 5.11. (a) Simulated power reflection coefficient and (b) far-field radiation pattern.

sustained by low-loss foam. In this case, the simulated results predicted smaller loss of performance, with the radiation efficiency reaching $\eta_{rad} = 18\%$ (with substrate characteristics: $h_s = 15\mu m$, and $\varepsilon_r = 3.3$, $\tan\delta = 0.015$), a gain of $G_0 = -2.6$ dB and a read range of 8.5 m. However, the metallization of the screen sides to the ground would still require special techniques, and may increase the tag complexity and cost.

5.3 EC-SRR antenna design: application to the 900 MHz ISM band

In this section, the theoretical analysis involving an EC-SRR working at the second resonance (Section 4.2) is applied to the design of an SRR antenna prototype, in order to validate its usefulness in the design stage, and to confirm the radiation properties of the SRR antenna introduced in this work. As a practical application example, the prototype was designed to operate at $f_0 = 915$ MHz, which is the center of the 900 MHz ISM band (902-928 MHz), matched to a 50 Ω port.

5.3.1 Design process and simulation results

The first step in the design process is to determine the SRR mean radius r_0, in order to adjust the antenna input resistance to the required value of $R_0 = 50\ \Omega$. In a general case, the antenna input resistance at resonance is $R_{in} = R_{rad} + R_{loss}$, i.e., it is obtained by summing (4.36) and (4.46). Therefore, its radius dependence is a second order polynomial of the form $R_{in} = ar_0^2 + br_0$, where a and b depend on the frequency f_0, the metal conductivity σ and the geometrical parameters c and h. As a result, the required mean radius r_0 is obtained by solving a second order equation (which provides a unique positive solution) after the parameters mentioned above (f_0, σ, c, h) have been set to a

given value. However, in case the radiation efficiency is expected to be sufficiently high (Figure 4.9), the loss resistance can be neglected, and by using (4.36) the required mean radius can be approximated to

$$r_0 \approx 4 \cdot 10^6 f_0^{-1} \sqrt{R_0} \ . \tag{5.4}$$

where all the quantities are expressed in SI units. Since the metal used for the prototype is copper with a thickness of h = 35 μm, setting the strip width to c = 2 mm allows using the expression above, because the expected efficiency is 98% (neglecting the substrate). The result is r_0 = 31 mm.

The second and final step in the design stage is to adjust, with the help of EM simulation software, the second resonance of the SRR (with radius r_0) at the desired frequency f_0. First, a dielectric substrate with the proper combination of relative permittivity ε_r and thickness h_s is chosen, obtaining a resonant frequency near to the desired value. Finally, by tailoring the distance d between rings, a fine adjustment of the frequency of resonance is done. In our case, we used a *Rogers R04003* substrate (ε_r = 3.55, h_s = 0.81 mm, tanδ = 0.0027) and the ring distance was found to be d = 1.6 mm. Consequently, the external radius of the SRR is r_{ext} = 33.8 mm (≈λ_0/10). The ring cut width and the port gap, which values are not relevant for the SRR response, were set to 5 mm and 0.8 mm, respectively.

The simulated power reflection coefficient of the SRR antenna prototype is depicted in Figure 5.12b. As expected, good impedance matching is achieved at the working frequency f_0 = 915 MHz. The simulated radiation efficiency and antenna gain are η_{rad} = 92% (lower to the predicted 98% due to the presence of dielectric losses) and G_0 = 2.2 dB, respectively, and the simulated bandwidth is 62 MHz (FBW = 7%).

5.3.2 Fabrication and experimental results

To validate the simulated results, the layout described in the previous section was fabricated (Figure 5.12a) by means of a PCB drilling machine (*LPKF-H100*). The layout was provided with soldering pads, in order to mount a SMD-packaged high frequency ceramic balun (*Johanson Technology* 0900BL15C050 [113]) across the SRR port gap, and a SMA connector to feed the balun and the antenna. The substrate was cut square-shaped with a side length of 80 mm.

The power reflection coefficient of the system was measured by means of an *Agilent N5221A* network analyzer, and the results (Figure 5.12b) are in good agreement with simulations, showing a small frequency shift (10 MHz) and a good impedance matching level (−18.5 dB). However, since the presence of the balun was not taken into account in the simulations, some differences between simulation and measurement arise. In

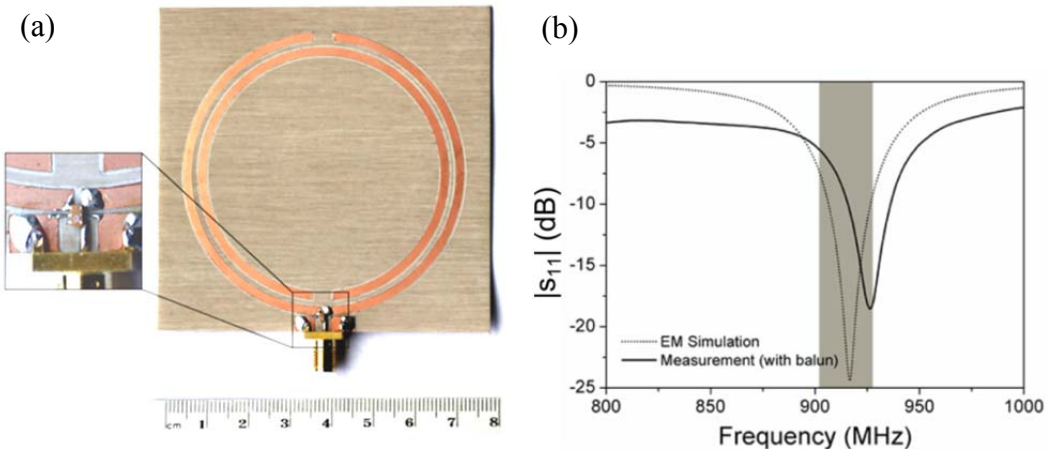

Figure 5.12. (a) Fabricated SRR antenna prototype. The SMD-packaged balun can be seen at the center of the close-up. (b) Simulated and measured power reflection coefficient of the prototype SRR antenna. The 900 MHz ISM band is depicted in grey.

particular, the measured notch depth and out-of-band response are limited by the return and insertion losses of the balun, respectively.

The antenna gain was evaluated by using the method reported at Section 3.2.3. The total losses in the antenna-analyzer link, accounted by the parameter A, where the sum of the coaxial losses (measured to be 0.9 dB) and the insertion losses of the balun (1.2 dB [113]). Therefore, by using (3.8), the experimental antenna gain was evaluated to be $G_0 = 2.05$ dB, which is very close to the predicted value (2.2 dB, previous section).

5.3.3 Conclusions

As a proof of concept, a prototype of the SRR antenna has been designed and fabricated to work at the 900 MHz ISM band, and the experimental data validated both the theoretical and simulated results (exposed at Section 4.2) in terms of impedance matching and antenna gain. Hence, further confirmation was provided indicating that the SRR antenna may be a valuable alternative to the commonly used half-wave dipole, especially when a reduction of the maximum antenna dimension is needed. It is worth mentioning here that, since the value of the radiation resistance is roughly the same, an SRR antenna operating at the second resonance can replace a half-wave dipole antenna without the need of any additional matching network. Its radiation pattern, which can provide a gain up to 2.7 dB, i.e., 0.5 dB higher than the one of the half-wave dipole, may also be preferred in some applications where a more directional pattern is needed.

6

UHF-RFID Tags for Optical Discs

This chapter is focused on the design of UHF-RFID tags to be mounted on optical discs (CDs, DVDs, Blu-ray discs). Due to the reflective layer buried under their surface, optical discs must be treated like metallic objects within the context of RFID tagging. The most challenging aspect is that the common solutions employed for metallic surfaces are not suitable in this case, and the solutions created ad hoc suffer from poor performance when compared to general-purpose UHF-RFID tags. In this work, a novel approach to the problem is proposed, which allows overcoming the abovementioned limitations and greatly reduces the performance gap with respect to general-purpose tags.

The chapter is organized as follows. Based on the study of the disc structure, the tag operation principle is proposed, and a working prototype is presented to confirm the validity of the presented solution. Then, the analysis is extended to solve the problem of impedance matching, defining a specific design method which allows the designer to optimize the performance for the several ASICs/discs types available on the market. As a practical example, such a method is then applied to the design of i) a tag for DVDs and ii) a tag for Blu-ray discs (BDs), both based on the *Alien Higgs 3* ASIC. It is worth mentioning that the impedance matching method developed in this work, namely the resistive scaling method, can be applied in a more general context of UHF-RFID tag design, providing a simple and intuitive alternative to other methods.

Due to its flexibility in the definition of three-dimensional geometries, the software *CST Microwave Studio* will be used for all the electromagnetic simulations related to optical discs.

6.1 Tag operation principle

In this introductive section, the operation principle of the proposed tag family will be explained. Since a study of the structure and electromagnetic properties of the different disc types was at the base of the presented solution, the disc structure will be first discussed as follows.

6.1.1 Structure of optical discs

Optical discs are composed of several layers bonded together; each layer is made of specific materials and is devoted to a specific function, as follows.

The *substrate* layer, made of polycarbonate plastic, provides structural rigidity and protects the internal layers from mechanical damage (scratches) and oxidation caused by atmospheric agents (humidity, oxygen, dust, etc.). In CDs and Blu-ray discs, the substrate is composed of a monolithic 120 mm (80 mm in the "Mini" versions) circular-shaped polycarbonate layer, with approximately 1.2 mm thickness (1.1 mm for Blu-ray discs). On the other hand, DVDs employ two identical polycarbonate layers (0.6 mm thickness each) bonded together, which opens to the possibility of reading the disc content, located in the middle, from both the top and bottom side (double-sided DVD discs). In every case, the substrate presents a central hole of 15 mm, in which the rotational head of the reader is inserted.

The *reflective* layer, which is found in all kind of optical storage devices, is necessary to reflect the laser beam during read and write operations of the data content. It is constituted by a very thin metal film (30-50 nm) grown on the polycarbonate by means of sputtering deposition. The sputtered material can be aluminum, gold, silver, or silver alloys, depending on the disc type [114]. The position of such layer varies with the disc type, according to the following configurations: i) top of the substrate in CDs (protected by an overlying lacquer layer, and sometimes an optional labeling layer), ii) middle of the substrate in DVDs and iii) bottom of the substrate in Blu-ray discs (protected by an underlying "protection layer" or "hard layer"). The reflective layer does not extend up to the disc center. Its inner diameter varies from 20-25 mm to 48mm (which is the beginning of the data zone), depending on the disc model. As it will be detailed later, the inner diameter of the metal layer is tightly related to the performance of the tags proposed in this work.

The *data* layer, which contains the information, is usually adjacent to the reflective layer, sometimes being the reflective layer itself (e.g., ROM discs). Data are stored in this layer in the form of nanometer scale pits and lands, which modulate the intensity of the reflected laser beam detected by the reader photodiode. Depending upon the disc type, different materials can be employed to form this layer. Molded polycarbonate, organic dye or phase-changing metal alloy film is commonly used for ROM

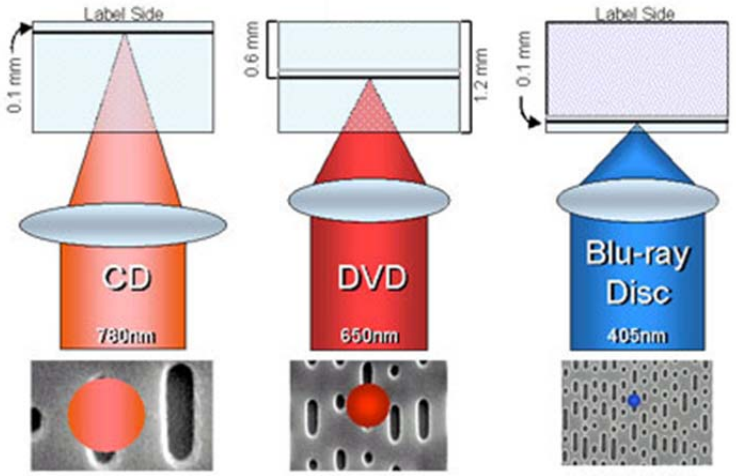

Figure 6.1. Basic structure of the different optical disc types.

(read only), R (recordable) and RW (rewritable), respectively [114]. Some kinds of DVDs and Blu-ray discs can include additional data layers, associated to additional semi-reflective layers (e.g., double data layer DVDs and BDs, triple and quadruple data layer BDs), so that the disc capacity is multiplied up to four times, without increasing the size (although the complexity of the disc is proportional to the number of layers).

Other layers, such as an optional labeling layer (thermal-printable, inkjet-printable, or silkscreen-printable [114]), a lacquer layer (found in CDs) and a protective layer (or "hard coating", at the bottom of Blu-ray discs) can be found on the disc.

When it comes to electromagnetic simulation, it is possible to simplify the problem by modeling the disc considering only the substrate layers and the metal layer. In fact, these are the most important layers in terms of electrical properties, as the other layers are very thin and do not present critical electrical properties (i.e., high permittivity or high conductance). This approximation can only be assumed in the case of single data layer discs only. Multiple layer discs should be modeled including additional metal layers.

As said above, the reflective layer is the responsible of the problems arising when tagging optical discs. This is because, although the film thickness is much smaller than the wavelength at the RFID band, its surface resistance is still much smaller than the free-space impedance, namely:

$$R_{\square} = \frac{\rho}{t} \approx 0.5\Omega \ll 377\Omega \tag{6.1}$$

where ρ is the metal resistivity and t is the film thickness (in the calculation above, a 50 nm silver film was considered). As it was demonstrated in [115], an incident plane

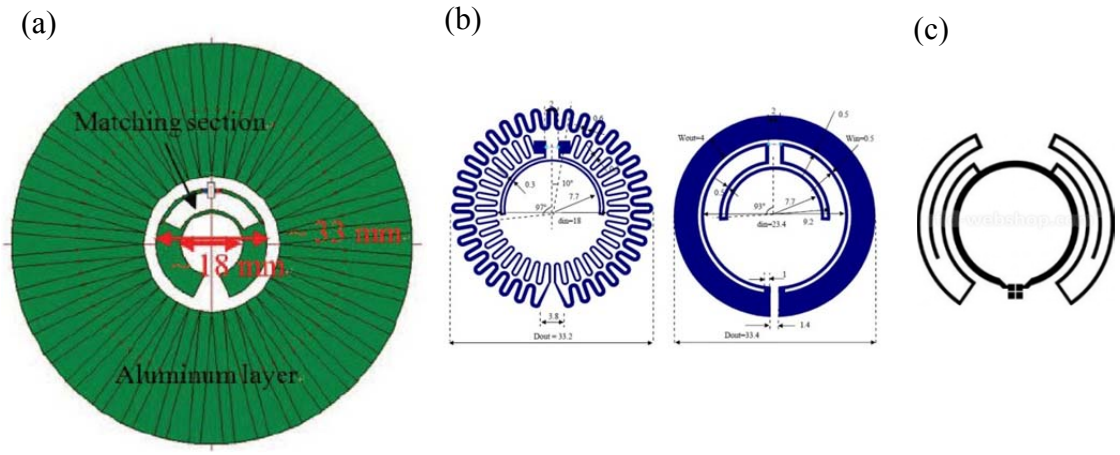

Figure 6.2. State of the art UHF-RFID tags for optical discs: (a) bending dipole (extracted from [116]) , (b) meandered and ring (extracted from [117]), (c) commercial meandered tag (*Impinji* corp.).

wave will be almost perfectly reflected by the thin film under this condition. This means that the film effectively behaves as a metal, forcing its boundary conditions which prevent the correct operation of any electric dipole-based tag (e.g., general-purpose tags) placed on the disc surface. This situation led to the development of specific tag designs, which will be detailed in the next section.

6.1.2 State of the art of UHF-RFID tags for optical discs

The unique solution proposed in the literature/market relies on bended [116] and meandered [117] dipole antennas (see Figure 6.2), to be placed in the small central area of the disc, which is metal-free [as said above, the reflective layer does not cover the central zone of the polycarbonate substrate, comprised between the inner hole (diameter 15 mm) and the beginning of the data zone (diameter 48 mm)]. However, this solution presents poor performance, mainly because of two factors: i) the proximity of the disc metallic layer, which generates image currents opposed to the dipole currents, and ii) the reduced tag size, which is a consequence of the small available area. Regarding the first point, preliminary simulations of a bended dipole (Figure 6.3), placed in the central zone of the disc, confirmed that image currents in the metal layer arise, so that the radiation resistance at resonance is reduced to only $R_{rad} = 2\ \Omega$ and the radiation efficiency drops to $\eta_{rad} = 2.5\%$. As a result, the achieved read ranges are sensibly reduced as compared to general-purpose tags. Declared read ranges are in the order of half a meter [116, 117], which is inadequate for many typical RFID applications. Moreover, this kind of tags typically presents complex layout geometries (as in the case of [117]), and the design process is not fully explained.

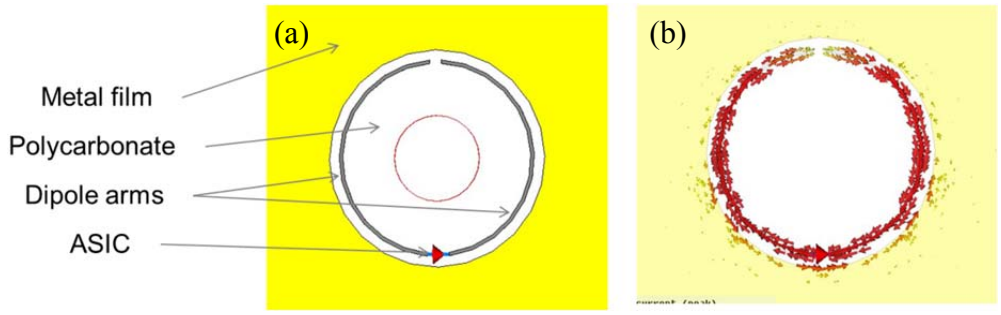

Figure 6.3. (a) Layout and (b) simulated electric current of a bended dipole placed in the central zone of an optical disc.

6.1.3 Optical disc-based tags

As an alternative to the designs presented above, where the tag was designed to avoid or minimize the effects of the metal layer, the tags proposed in this work use the disc reflective layer as the main radiating body. In fact, the physical disc dimensions (120 mm) are equal to $\lambda_0/2.7$, i.e., slightly smaller than half-wavelength at the UHF-RFID band, meaning that the disc behaves in a similar way to a half-wave dipole antenna. This can be seen in the simulated disc response, in terms of induced currents and electric fields, when illuminated by a plane wave (Figure 6.4). The tag proposed in this work is intended to excite a similar current distribution on the disc surface, so that an oscillating dipolar moment would be generated, acting as the main radiating element of the system. In this situation, the tag would take advantage of the whole dimensions of the disc, and no image currents would arise. We propose the term "optical disc-based tags" to the RFID tags which follow this operation principle, being their operation tightly based on the presence of the optical disc. Obviously, their radiation efficiency mainly depends on the losses in the radiating body, i.e., the reflective layer, so that its

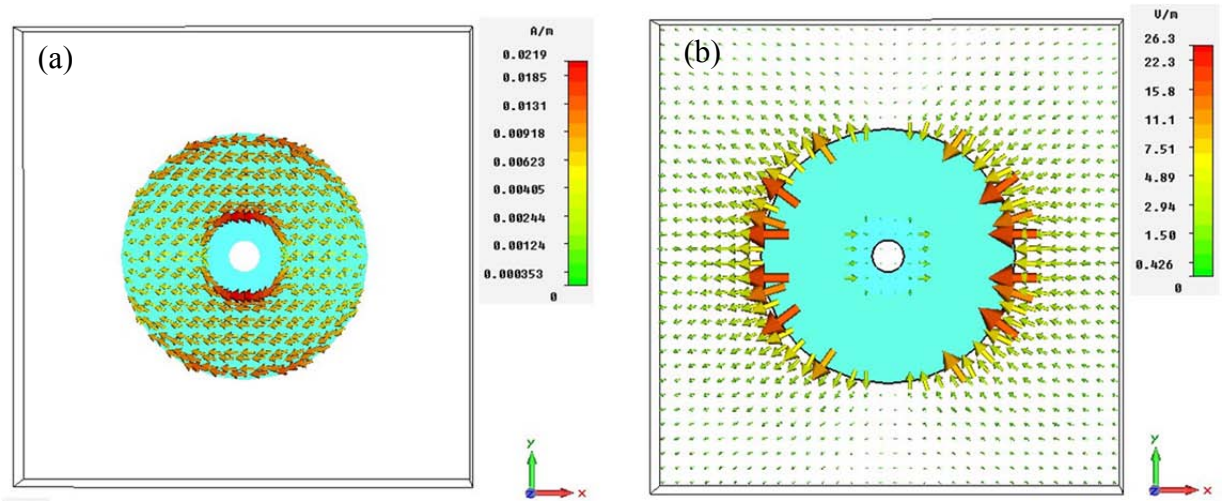

Figure 6.4. (a) Electric current density and (b) electric field induced on an optical disc illuminated by a plane wave (with E = 1 V/m oriented along x) travelling in the $-z$ direction.

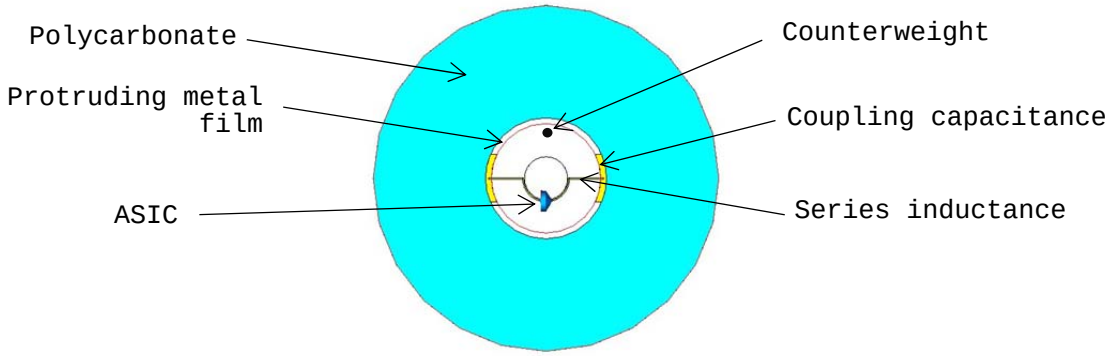

Figure 6.5. Scheme of an optical disc-based UHF-RFID tag.

square resistance is a fundamental parameter in this design approach. As it will be detailed in the next sections, the obtained efficiencies are sufficiently high to provide read ranges in the order of several meters, as a function of the disc type and the tag design. Since the metal layer is buried under the disc surface, it is not directly accessible by a tag attached to the disc. Therefore, the disc excitation must be based on electric/magnetic coupling between the tag and the reflective layer. This point, along with other important design aspects (e.g., impedance matching, mass balancing) will be detailed in the following sections, where practical examples will be presented. A scheme of an optical-disc based tag is represented in Figure 6.5.

6.2 UHF-RFID tag for DVDs

A first example of optical disc-based tag, intended to operate when attached to DVD discs, is presented in this section. The design process was based on the study of the radiation and impedance properties of a standalone DVD disc, and the generation of an equivalent circuit model, as explained below.

6.2.1 Circuit model of the DVD disc

Because electromagnetic (EM) coupling to the metal layer is required, the impedance matching between the antenna and the ASIC will directly depend on the input impedance of the disc metal layer. Therefore, in order to design the proposed tag, it is very useful to understand the electrical behavior of the disc in terms of its impedance. To analyze the frequency response of the disc, the *CST Microwave Studio* commercial software (the frequency domain solver) was used. The simulated structure, presented in

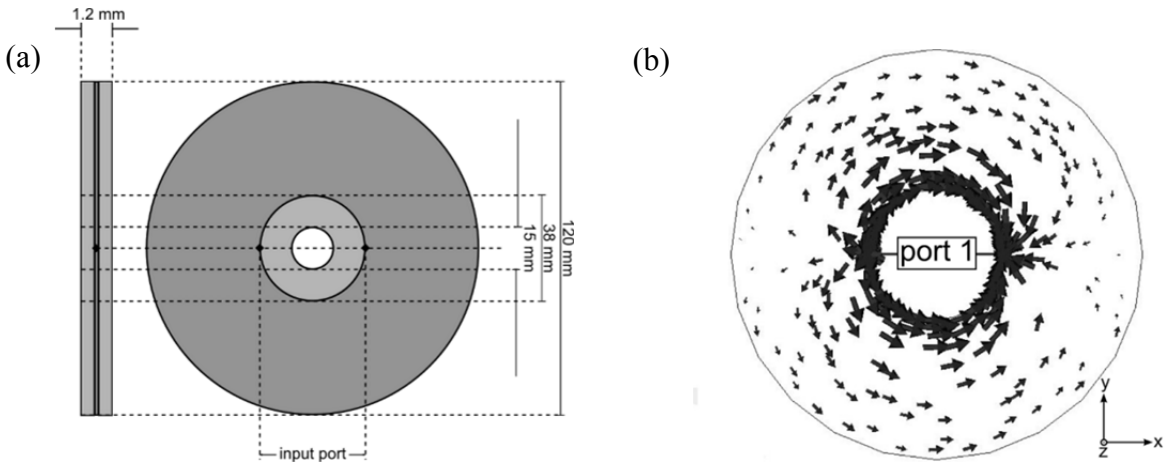

Figure 6.6. (a) Structure of the considered DVD disc: lateral view (left), top view (right). Dark grey represents silver, light grey represents polycarbonate. Layer thicknesses are not drawn to scale. (b) Simulated current profile on the metal layer at f_0 = 885 MHz.

Figure 6.6a, is a simplified model of a DVD+R disc, according to the approximations described in section 6.1.1. Silver was considered as the constitutive material of the reflective layer, which was modeled as an ohmic sheet with a square resistance given by (6.1). It is worth to mention that the value of the silver conductivity has been corrected to take into account the effects of the nanometric film thickness. In fact, it is known that that the effective electrical resistivity of thin metal films typically increases, with respect to the material bulk resistivity, as the film thickness decreases. This effect becomes very important when the thickness is in the order of the electron mean-free-path p of the conductive material [115, 118]. The value of p for silver is roughly 50 nm [119] at room temperature. Hence, for a reflecting layer thickness of 50 nm, the thickness to mean-free-path ratio t/p approaches unity. It is possible to predict the effective resistivity ρ' of a thin metal layer, given the values of the bulk resistivity ρ and the ratio t/p [115]. Based on [115], the value of ρ'_{Ag} for $t/p = 1$ can be found as $1.5\rho_{Ag}$ (where ρ_{Ag} = 16 nΩ·m is the bulk resistivity of silver [120]), leading to ρ'_{Ag} = 24 nΩ·m. Therefore, according to (6.1), the square resistance value is $R_{\square} = 0.5\Omega$. The relative permittivity and dielectric loss tangent values used for polycarbonate plastic are $\varepsilon_r = 2.88$ and $\tan\delta = 0.012$, respectively [121]. It is important to remark that the electrical properties of the polycarbonate plastic and silver layers may vary depending on many factors related to the fabrication process. In this regard, and considering the wide range of different DVD manufacturers, the choice of one set of electrical parameters for the structure is arbitrary and slight variations in the tag performance can result for different brands.

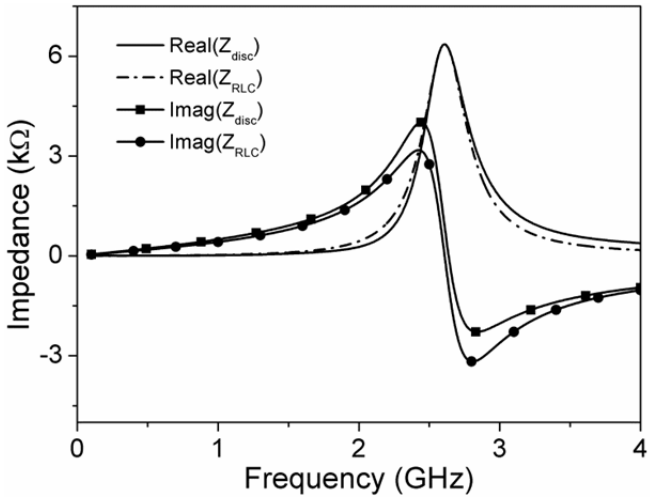

Figure 6.7. Comparison between the simulated input impedance of the DVD+R disc (Z_{disc}) and the input impedance inferred from the circuit model (Z_{RLC}).

In order to carry out the simulation, a differential input port is placed directly on the metal layer, and aligned to one of the infinite symmetry planes of the structure, as depicted in Figure 6.6a. The reason for choosing a symmetric position of the port is simple: the final structure (tag layout and DVD) should present (at least in a first order approximation) symmetry in order to prevent a displacement of the barycenter. Actually, unbalancing the rotating mass can cause read/write problems and physical damage of the disc and the reader.

The simulated input impedance Z_{disc} of the structure, depicted in Figure 6.7, shows a parallel-type resonance occurring at $f_0 = 2.61$ GHz, suggesting that a shunt RLC circuit model can be used to describe the disc impedance to a good approximation. Based on the resistive part of Z_{disc} and the reactance slope values at f_0, it is possible to perform a parameter extraction. The calculated values for the circuit parameters are $R_p = 6350\ \Omega$, $L_p = 57$ nH, $C_p = 65$ fF. Good agreement between the circuit model and EM simulation is observed in Figure 6.7.

Let us now discuss the expected radiation properties of the disc metallic plate. Since the excitation signal is applied over one of the symmetry planes of the structure (*x*-axis in Figure 6.6), a magnetic wall is expected to form along such axis. Moreover, the *y*-axis is also a symmetry plane of the structure, and a differential excitation is applied on its sides. Therefore, an electric wall is formed along the *y*-axis. Due to the symmetry walls generated in the structure, a first order cancellation of the fields radiated by the current components along *y*-axis is expected. Nevertheless, the *x* components of the currents flow in the same direction, resulting in a dipolar radiation along the *x*-axis. Given that the first self-resonance of the disc occurs at high frequencies, we expect a short dipole charge profile at the UHF-RFID band. Since the width of such dipole is comparable with the wavelength at the working frequency, the phase contributions of

each element cannot be neglected. Therefore, the radiation pattern of the disc can be approximated by the radiation pattern of an array of short dipoles excited in phase. In terms of far-field radiation, as a first order approximation it is possible to model the system as an array of two infinitely thin dipoles, excited in phase, and separated by a distance d. The effective distance d between the two dipoles is a function depending on the current density profile along the section of the metal layer, and is comprised between the physical dimensions of the disc: 38 mm (λ/10 at 885 MHz) and 120 mm (λ/2.8 at 885 MHz). Such dipole array is thus expected to present a maximum directivity value higher than the single dipole, and the radiation pattern is expected to present a maximum at $\theta = 0^{\circ}$ (direction normal to the disc plane). Moreover, a directional pattern is expected for the H-plane (yz), with a minimum directive gain at $\theta = 90^{\circ}$ due to the destructive interference between the two radiating elements. However, since the two elements of the array are in-phase excited and their distance is smaller than $\lambda/2$, the directive gain minimum value on the H-plane is not expected to reach zero. Far-field polarization is expected to be linear, with E-field oriented along the x-axis.

The simulated current pattern on the metal layer at the center frequency (885 MHz) is depicted in Figure 6.6b. As expected, each side of the disc exhibits a dipolar type current. The simulated radiation pattern (see Figure 6.8) confirms the behavior of the disc as an array of two short dipoles, with a maximum directive gain value $D_0 = 3.7$ dBi at $\theta = 0^{\circ}$. The minimum directive gain on the yz-plane is −1 dBi. Due to the width of the conductive path on the metal layer, the radiation efficiency is reasonably high, reaching the value of $\eta_{rad} = 23.2\%$ at 885 MHz. It is interesting to quantify the losses in each part of the disc. The simulation results indicate that 85% of the dissipated power is due to ohmic losses in the metal layer of the disc. Dielectric losses in the polycarbonate layer represent a 15% of the total losses. Based on the simulated radiation pattern, the antenna gain is $G_0 = -2.6$ dB. This means that, providing good impedance matching, it is possible to obtain a read range in the order of several meters. As an example, considering $EIRP = 4$ W, the read range is 7 m for ASICS with sensitivity

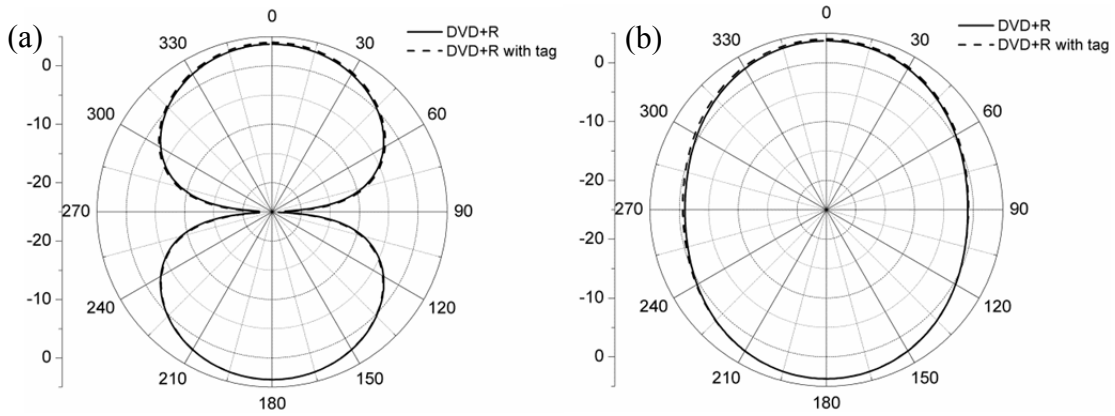

Figure 6.8. Radiation pattern at 885 MHz for DVD+R and DVD+R with tag (see section 6.2.3): (a) E-plane (xz-plane); (b) H-plane (yz-plane).

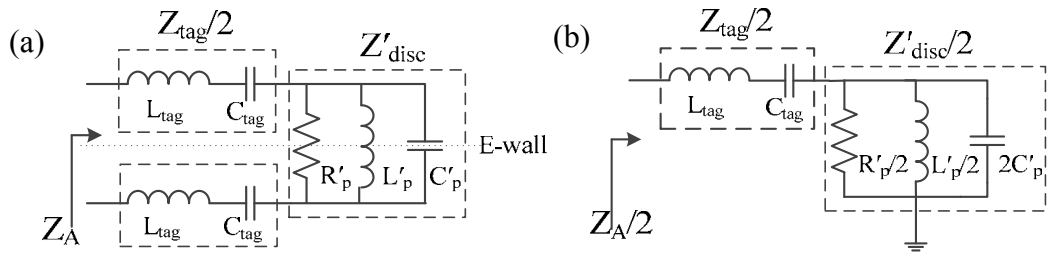

Figure 6.9. (a) Circuit model of the system composed by the DVD and the tag, (b) simplified model using electrical wall (*E*-wall) concept.

P_{th} = –15 dBm, and 10 m with sensitivity P_{th} = –18 dBm.

6.2.2 Tag design principles

In the previous section, the capability of a DVD to work as an efficient antenna at the UHF-RFID frequencies was demonstrated. In order to design an RFID tag capable of taking advantage of this potentiality, the coupling method problem has to be solved. In fact, coupling is necessary because the metal layer is not directly accessible in the DVD post-production stage, and a RFID tag can only be placed on top of the polycarbonate structural layer. The adopted solution is to produce an electric coupling between the tag and the disc by means of a series stepped-impedance resonator (SIR) synthetized through semi-lumped elements. The capacitance between the tag metal (top layer) and the disc metal (inner layer), C_{tag}, provides electric coupling. The series inductance, L_{tag}, realized through a thin line (e.g., 0.4 mm), forces a controllable series resonance, forming a virtual short circuit between the ASIC and the metal layer of the disc.

An equivalent circuit model for the whole structure can be obtained by means of a series connection of the disc (described in the previous section) and the tag circuit models, as shown in Figure 6.9a. Differential excitation and symmetry considerations, allows us to apply the electric wall concept (Figure 6.9b). Notice that, due to the series connection between the disc and the tag, the impedance seen from the ASIC is simply $Z_A = R_A + jX_A$, where $R_A = R_{tag} + R'_{disc}$ and $X_A = X_{tag} + X'_{disc}$. Although the disc can still be modeled by an RLC parallel resonator, the values vary due to the presence of the tag. In particular, a shorter effective current path on the metal disc results as a function of the capacitor length l_c. Thus, the new values of inductance L'_p and resistance R'_p are smaller compared to L_p and R_p. The resulting disc impedance is designated as $Z'_{disc} = R'_{disc} + jX'_{disc}$. The tag capacitance C_{tag} and inductance L_{tag} can be controlled by means of simple geometrical parameters (e.g., the area of the semi-lumped capacitor and the width of the semi-lumped inductor). By working in the vicinity of the LC series resonance, it is possible to control the tag series reactance X_{tag}, which can be either inductive or capacitive. Thus, the total reactance $X_A = X'_{disc} + X_{tag}$ can be adjusted in

order to match the capacitive reactance X_C of the RFID chip (ASIC). Since ohmic losses of the LC resonator are omitted in the model, the resistive part of the antenna system R_A is directly equal to R'_{disc}. Its value cannot be easily controlled for impedance matching, since it presents a very small variation as a function of the tag geometry. However, according to the simulation results, the value of R'_{disc} at UHF is in the range of 8-12 Ohms, thus providing a good matching level with many ASICs available on the market, without the need for an additional matching network.

It is important to note that the circuit proposed above is a simplified circuit model which allows an easy design of the tag in the UHF-RFID band. In order to describe the impedance behavior of the system in a wider band, it is necessary to take into account an additional capacitance introduced by the presence of the tag conductors, which is in the order of 100 fF and is placed in shunt with the impedance Z_A.

6.2.3 Layout synthesis and simulation

Based on the concepts illustrated in the previous section, the tag layout synthesis is presented here. Although it is not possible (without an additional mass balancing element) to achieve a perfect symmetry of the tag that guarantees that the barycenter is located at the center of the disc, the layout design has been focused on optimizing it. The chip, which introduces mass unbalance, has been chosen to be placed as near as possible to the rotation center of the disc, i.e., adjacently to the inner hole of the polycarbonate structure, in order to minimize the barycenter shift of the system. The electrical connection between the coupling capacitance C_{tag} (at the edge of the tag) and the ASIC (at the center of the tag) was designed in order to work as the tag inductance L_{tag}, resulting in a very simple final layout (Figure 6.10). The UHF-RFID chip used in the design is the *NXP UCODE G2XM*, with an input impedance of $Z_C = 16 - j148\ \Omega$ at 915 MHz, and a sensitivity of $P_{th} = -15$ dBm (See Table 1). However, the value of P_{th} for this ASIC has been experimentally measured over the UHF band [122], yielding results in the order of −13 dBm at the center frequency. The substrate used for the prototype is the *Rogers RO3010* (with thickness $h_s = 0.254$ mm, $\varepsilon_r = 10.2$, $\tan\delta = 0.0023$), which has a structural function only. In fact, the high permittivity of the material does not have a role, neither in size reduction, nor in increasing the tag performance. On the contrary, the required dimensions of the capacitive part of the tag slightly increase when using any substrate, rather than directly print or grow the metal layer on the polycarbonate surface. This is because adding a substrate on the polycarbonate layer decreases the capacitive coupling between the disc and the tag. An equivalent circuit model would describe the presence of the substrate as an additional capacitance in series with the capacitance between the disc and the tag. Actually, the *RO3010* substrate was chosen as a mechanical support for fabrication, being the only thin substrate available in our laboratory. Commercial versions of the tag might be

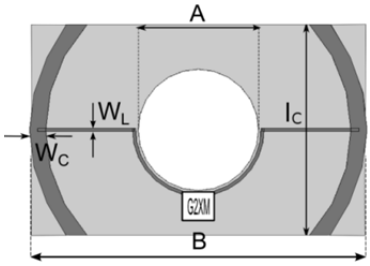

Figure 6.10. Final tag layout to be positioned over the central zone of the disc. The metal is represented in dark grey and *RO3010* substrate in light grey.

engineered without any substrate, e.g., by screen- printing the tag on the disc surface, in order to minimize the cost.

Once the layout strategy has been defined, the problem presents 3 degrees of freedom (l_C, W_C, W_L) in the geometry of the tag (Figure 6.10). Obviously, many different solutions exist in order to obtain the required reactance. As a starting point, the value of W_C was fixed at 2 mm, an arbitrary value that ensures a minimal overlapping of the tag within the DVD graphical label layer. A proper combination of l_C and W_L was then chosen in order to obtain the matching peak at the desired frequency (885 MHz). At this stage it is useful to consider that, as a first order approximation, the capacitor length l_C controls the capacitance value C_{tag}, and the line width W_L controls the inductance value L_{tag}. Final values for the geometrical parameters are $W_C = 2$ mm, $l_C = 16.5$ mm, $W_L = 0.4$ mm, $A = 15$ mm (corresponding to the diameter of the DVD inner hole) and $B = 42$ mm.

Simulation results, in terms of power reflection coefficient, are depicted in Figure 6.11a. As expected, good matching is achieved at 885 MHz ($|s_{11}|^2 = -13$ dB, corresponding to $\tau = 1 - |s_{11}|^2 = -0.2$ dB). Based on the simulated input impedance of the structure, a parameter extraction for the electrical model was performed, in order to demonstrate its validity. The extracted circuital values are $R'_p = 1500\ \Omega$, $L'_p = 19$ nH, $C'_p = 58$ fF, $L_{\text{tag}} = 20$ nH, $C_{\text{tag}} = 2$ pF. Very good agreement between electromagnetic and circuital impedance in the UHF-RFID band can be observed in Figure 6.11b.

The radiation pattern for the whole system is very similar to that of the DVD alone, as depicted in Figure 6.8, demonstrating that the tag is actually using the metal layer of the DVD as the main radiating element. The radiation efficiency of the system remains reasonably high, with a value of $\eta_{\text{rad}} = 22.8\%$ at 885 MHz, resulting in a maximum gain value of –2.4 dB. According to these results, it is possible to estimate a maximum theoretical read range of 5.6 m (considering $\tau = -0.2$ dB, $P_{\text{th}} = -13$ dBm and $EIRP = 4$W), on the basis of (3.1).

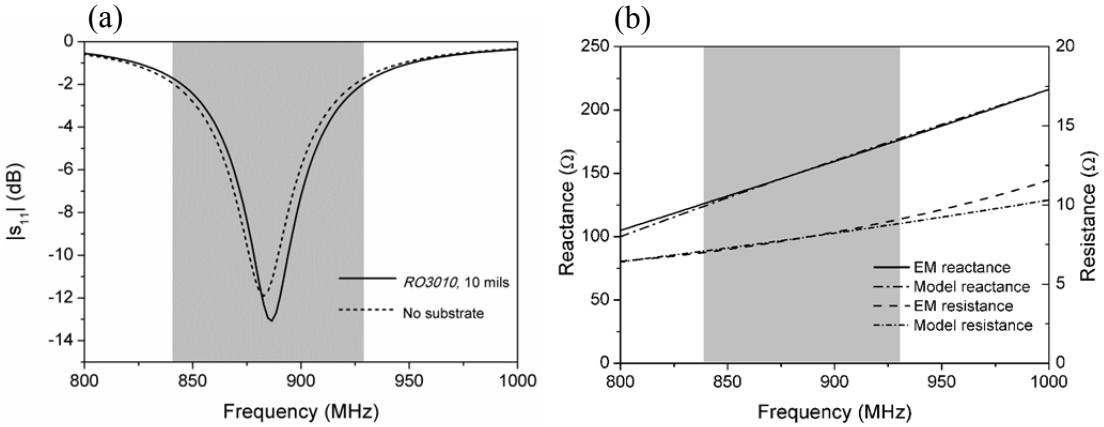

Figure 6.11. (a) Simulated amplitude of the power reflection coefficient of the tag described in Figure 6.10. (b) Comparison between the impedance of the circuit model and the one inferred from electromagnetic (EM) simulation (with *RO3010* substrate).

In order to compare the results, a simulation of the tag without the dielectric substrate was performed. The reflection coefficient amplitudes are very similar (Figure 6.11a), and the upward shift introduced by the substrate is only 3 MHz. The antenna gain for the tag without substrate is –2.7 dB, resulting in a theoretical read range of 5.4 m.

It is worth to mention that, due to the degrees of freedom in the problem, infinite solutions for C_{tag} and L_{tag} do exist. However, each solution produces a different impedance behavior over the frequency band. More precisely, the bandwidth of the tag is strictly related to the choice of the final solution. Since the tag can be modeled as a series LC resonator, bandwidth is maximized by minimizing the inductance value, which it implies a very wide inductive section, and maximizing the capacitance value, which implies a very large coupling area. In practical terms, this means that a tradeoff between geometrical layout issues and bandwidth performance must be chosen.

6.2.4 Fabrication and measurements

To validate the simulated results, the layout described in the previous section was fabricated by means of a PCB drilling machine (*LPKF-H100*). The measurements (not shown) present a frequency shift of the tag response, with a read range peak at 955 MHz. This effect has been attributed to the intrinsic indetermination of the electrical properties of the DVD materials at the UHF band, and to the simplifications made in the modeling of the disc. In fact, unlike most substrates used for tag implementation, DVD disc materials are not intended for microwave design. Therefore, manufactures neither report nor control their electrical properties. Moreover, as discussed in section 6.2.1, some geometrical parameters are not specified as well (e.g., the thickness of the reflecting

(a) (b)

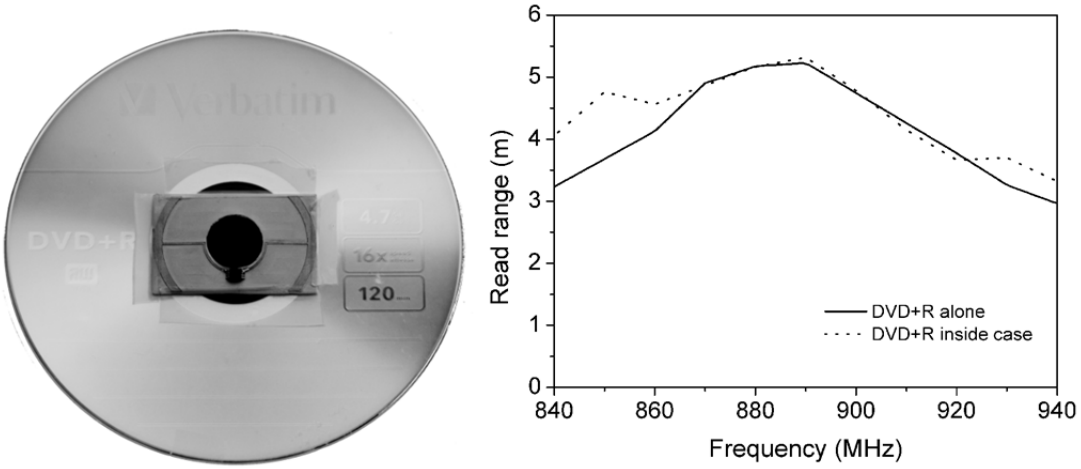

Figure 6.12. (a) Fabricated tag, mounted on a DVD+R disc, and (b) measured read range.

layer).

Based on the measured results, a second layout of the tag was synthetized and fabricated in order to correct the frequency shift. The matching position was adjusted by simply tailoring the length l_C of the tag capacitance. The corrected value of the geometrical parameter is $l_C = 26$ mm. The final tag, mounted on a DVD+R disc, is shown in Figure 6.12a. The measured read range of the new layout, depicted in Figure 6.12b, shows the curve correctly centered around 885 MHz, with a peak value of 5.2 m, which is very close to the 5.6 m predicted from the simulation. Furthermore, the results reveal that the read range is above 3 m in the whole UHF-RFID frequency band, confirming that the tag is capable of worldwide operation with very good performance.

A second read range measurement involved the DVD+R placed inside its standard plastic case. Comparing the curves (Figure 6.12b), it can be concluded that the presence of the box has small effect on the final read range.

It is worth to mention that, although the design was aimed at simplifying the mass balancing stage (e.g., minimize the required mass, simplify the calculation of its position), the presented tag was fabricated without the balancing element. This was partly due to fabrication issues, and partly because our tag is intended to be a prototype, since it uses a microwave substrate and a very large RFID chip packaging (SMD-TSSOP).

6.2.5 Conclusions

In this section, a first example of optical disc-based UHF-RFID tag has been presented. The tag was designed to be used when mounted on a DVD+R disc, or to be directly screen-printed over the disc surface. The tag prototype allowed to validate the potentiality of the new design approach described in the previous section. In fact, the

experimentally measured read range has a peak value of 5.2 m (very close to the 5.6 m predicted by electromagnetic simulation) and the read range is above 3 m within the UHF-RFID band, that is, one order of magnitude higher than the read ranges of conventional DVD tags reported in the literature [116, 117]. These results confirm the validity of the proposed circuit model of the optical disc, the coupling strategy between the ASIC and the radiating element, and the equivalent circuits of either element, which are at the basis of the design approach.

The potential of the presented methodology is clear on account of the RFID chip used in the design (the one available in our laboratory), that has a relatively low performance in terms of activation power (−13 dBm according to [122]), as compared to the latest commercially available ASICs (see Table 1). Therefore, it is possible to significantly improve the read range by considering the latest RFID chips available in the market.

6.3 Resistive scaling method

The promising performance of the optical disc-based tag presented in the previous section, along with the design simplicity and the possibility to manufacture the tag by means of serigraphy directly over the disc surface, encouraged us to carry on the study of this solution. An impedance matching analysis is especially useful to provide the design flexibility required to match the antenna to the various RFID ASICs available on the market. Indeed, as already mentioned, while the input reactance of the antenna can be easily matched by varying the tag geometry, its input resistance (in the range of 8-12 Ω) cannot be easily controlled, since it presents a very small variation as a function of tag geometry. For the case presented in the previous section, where the ASIC (*NXP UCODE G2XM*) resistance (16 Ω) matched relatively well to the antenna input resistance, the power reflection coefficient was acceptable (−13 dB at 885 MHz). However, depending on the ASIC input resistance, an impedance matching network may be needed. For instance, the more recent and sensitive *Alien Higgs 3* ASIC presents a higher input resistance, in the order of 25 Ω at 915 MHz, thus providing poor impedance matching when directly connected to the antenna.

An impedance matching analysis for the optical disc-based UHF-RFID tags is provided below, setting the basis of a design methodology which allows obtaining good performance for any ASIC and optical disc available on the market.

6.3.1 Analysis of the resistive scaling method

Let us assume the case of a generic impedance $Z = R + jX$ in shunt with a reactance X_p. Considering $Z' = R' + jX'$ to be the impedance resulting from the parallel combination of Z and X_p, the value of Z' can be easily inferred, yielding

$$Z' = \frac{R \cdot X_p^2}{R^2 + (X + X_p)^2} + j\frac{X_p \cdot \left[R^2 + X \cdot (X + X_p)\right]}{R^2 + (X + X_p)^2} \ . \tag{6.2}$$

Now, it is possible to imagine the real part of Z' to be equal to R times a scaling factor α, with $\alpha > 0$. That is:

$$R' = \alpha \cdot R \ . \tag{6.3}$$

This equality leads to a second order equation which solution provides the value of X_p as a function of R, X, and α:

$$\left(1 - \frac{1}{\alpha}\right) \cdot X_p^2 + 2X \cdot X_p + (X^2 + R^2) = 0 \, . \tag{6.4}$$

In order to have real solutions (pure reactive values), the discriminant Δ of (6.4) must be positive. This sets a limit on the maximum value of α, which is:

$$\alpha \le 1 + \left(\frac{X}{R}\right)^2 . \tag{6.5}$$

If (6.5) is satisfied, we have 2 real solutions for (6.4), given by:

$$X_{p1,2} = \frac{-\alpha X \pm \sqrt{\alpha\left[X^2 + (1-\alpha)R^2\right]}}{\alpha - 1} . \tag{6.6}$$

It can be demonstrated with algebra that for $\alpha < 1$ (resistance decrease), solution 1 is capacitive and solution 2 is inductive. Moreover, for $\alpha > 1$ (resistance increase) both solutions are inductive when $X < 0$, and capacitive when $X > 0$. The limiting case ($\alpha = 1$) is provided by an infinite reactance (whether positive or negative) or by the solution $X_p = -(X^2+R^2)/2X$.

It is also possible to demonstrate that the imaginary part of Z' can be written as:

$$X'_{1,2} = \mp\alpha \frac{\sqrt{\Delta}}{2} \tag{6.7}$$

showing that for a given value of α, the two solutions for X_p always give opposite values of X', which are capacitive for solution 1 and inductive for solution 2.

Now, given that the typical input impedance of an RFID ASIC is strongly capacitive, it is useful to find an approximate solution for (6.4) in the case of Z being strongly reactive. Under the assumptions:

$$X^2 \gg \left|1 - \alpha\right| R^2 \tag{6.8}$$

$$X^2 \gg R^2, \tag{6.9}$$

the solutions (6.6) of equation (6.4) can be simplified to

$$X_{p1,2} \approx \mp \frac{\sqrt{\alpha}}{1 \pm \sqrt{\alpha}} \cdot X \quad \text{for } X > 0 \tag{6.10}$$

$$X_{p1,2} \approx \pm \frac{\sqrt{\alpha}}{1 \mp \sqrt{\alpha}} \cdot X \quad \text{for } X < 0, \tag{6.11}$$

suggesting that the value of $X_{p1,2}$ can be easily calculated starting from X and α.

The imaginary part of Z' can be evaluated from (6.7) by using the conditions (6.8)-(6.9), leading to a very simple equation:

$$X'_{1,2} \approx \mp \sqrt{\alpha} \cdot X \quad \text{for } X > 0 \tag{6.12}$$

$$X'_{1,2} \approx \pm \sqrt{\alpha} \cdot X \quad \text{for } X < 0. \tag{6.13}$$

In this situation, the value of neither i) the required shunt reactance X_p and ii) the transformed load reactance X', no longer depends upon the load resistance R. Hence, a graphical representation of the approximated solutions as a function of α can be done (Figure 6.13). Note that, if (6.9) is satisfied, the approximation is always valid, i.e., (6.8) is also satisfied, for $0 < \alpha < 2$ (grey zone in the plot). Outside the grey region, the approximation may still be useful, but its accuracy gradually decreases as the value of α is increased.

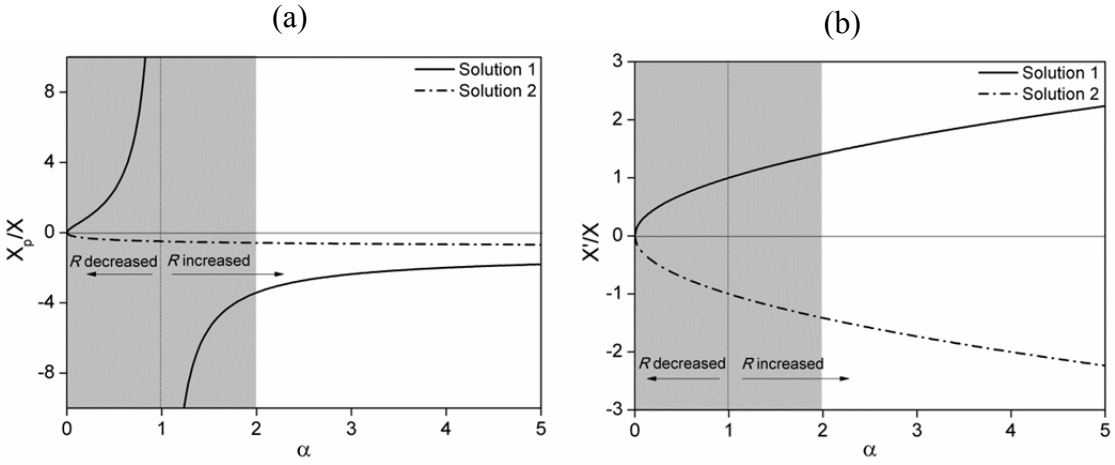

Figure 6.13. (a) Shunt reactance solutions for the reactive impedance approximation, and (b) transformed reactive values for the case $X < 0$. For $X > 0$, solution 1 and 2 are interchanged. The zone of validity is depicted in gray.

6.3.2 Bandwidth analysis for the transformed ASIC impedance

As to be expected, the introduction of the reactive element X_p in shunt with the ASIC modifies its susceptance slope, which is directly related to the maximum tag bandwidth achievable with a certain ASIC [31]. The transformed susceptance slope can be easily calculated taking advantage of the reactive impedance approximation, so that the solutions providing higher bandwidth can be found analytically. It will be demonstrated that solution 1 provides higher bandwidth than solution 2, for both $\alpha < 1$ and $\alpha > 1$, when the transformed ASIC is cascaded to an ideal antenna (i.e., the antenna which provides conjugate matching and exhibits the minimum susceptance slope [31] in its circuit model). The two cases will be analyzed separately, because the circuits involved are different.

Case $\alpha < 1$

As can be deduced from Figure 6.13a, capacitive (solution 1) and inductive (solution 2) solutions exist for the shunt reactance X_p when $\alpha < 1$ and $X < 0$. In the first case, the ASIC reactance is maintained capacitive, while in the second case it is changed to inductive (see Figure 6.13b). As a consequence, the ideal antenna matched to the transformed ASIC impedance would be modeled as a shunt RL and RC circuit, for the first and second case, respectively (Figure 6.14). The transformed susceptance slope of the ASIC in each case can be evaluated as

$$\frac{\partial B'_{C1}}{\partial \omega} = \frac{1}{\sqrt{\alpha}} C_c \text{ for solution 1} \tag{6.14}$$

$$\frac{\partial B'_{C2}}{\partial \omega} = \frac{2\sqrt{\alpha}+1}{\sqrt{\alpha}} C_c \text{ for solution 2}, \tag{6.15}$$

where C_C is the ASIC shunt capacitance, which also corresponds to the susceptance slope of the untransformed ASIC. Let us now calculate the susceptance slope of the whole tag, obtained cascading the transformed ASIC impedance to the ideal antenna circuit model. In this case, it is obtained that

$$\frac{\partial B'_{1}}{\partial \omega} = \frac{2}{\sqrt{\alpha}} C_c \text{ for solution 1} \tag{6.16}$$

$$\frac{\partial B'_{2}}{\partial \omega} = \frac{2(1+\sqrt{\alpha})}{\sqrt{\alpha}} C_c \text{ for solution 2}. \tag{6.17}$$

These results reveal that, in both cases, the susceptance slope is incremented as the ASIC resistance is scaled down, at the expense of the tag bandwidth. Nevertheless, the

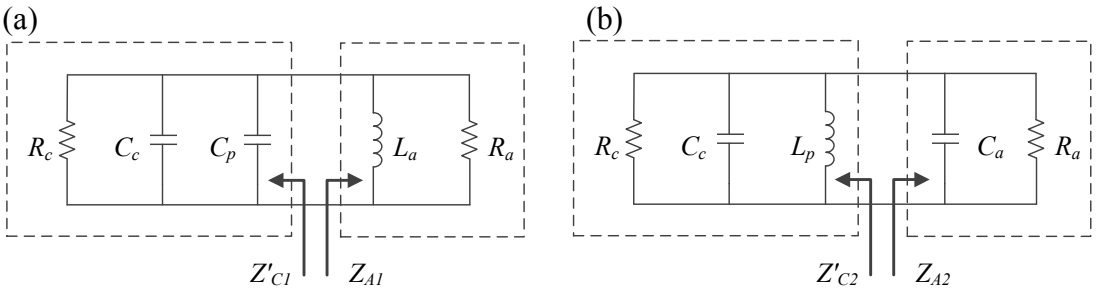

Figure 6.14. Circuit model of the transformed ASIC impedance matched to the tag antenna, for (a) solution 1 and (b) solution 2, in the case $\alpha < 1$.

capacitive solution (solution 1) provides better results, as can be deduced by comparing (6.16) with (6.17).

The tag half-power bandwidth associated to each solution can be calculated analytically, obtaining:

$$\Delta f_{-3dB}^{MAX} = \frac{1}{\pi R_c C_c}\sqrt{\alpha} \quad \text{for solution 1} \tag{6.18}$$

$$\Delta f_{-3dB}^{MAX} = \frac{1}{\pi R_c C_c}\frac{\sqrt{\alpha}}{1+\sqrt{\alpha}} \quad \text{for solution 2}. \tag{6.19}$$

Case $\alpha > 1$

In this case, provided that conditions (6.8)-(6.9) are satisfied, both solutions are inductive (see Figure 6.13a), and the transformed susceptance slopes of the ASIC are

$$\frac{\partial B'_{C1}}{\partial \omega} = \frac{2\sqrt{\alpha}-1}{\sqrt{\alpha}}C_c \quad \text{for solution 1} \tag{6.20}$$

$$\frac{\partial B'_{C2}}{\partial \omega} = \frac{2\sqrt{\alpha}+1}{\sqrt{\alpha}}C_c \quad \text{for solution 2}, \tag{6.21}$$

leading to the following values for the whole tag susceptance slopes:

$$\frac{\partial B'_1}{\partial \omega} = 2C_c \quad \text{for solution 1} \tag{6.22}$$

$$\frac{\partial B'_2}{\partial \omega} = \frac{2(1+\sqrt{\alpha})}{\sqrt{\alpha}}C_c \quad \text{for solution 2}. \tag{6.23}$$

Once again, solution 1 provides smaller susceptance slope in the final tag model. Moreover, solution 1 maintains the tag susceptance to the theoretical minimum (i.e., $2C_c$

[31]), independently from the value of α. On the other hand, solution 1 requires higher inductive values, resulting in larger tag areas dedicated to the matching network (with a consequent increase of ohmic losses due to the larger inductive paths).

The resulting tag half-power bandwidths are

$$\Delta f_{-3dB}^{MAX} = \frac{1}{\pi R_c C_c} \quad \text{for solution 1} \tag{6.24}$$

$$\Delta f_{-3dB}^{MAX} = \frac{1}{\pi R_c C_c} \frac{\sqrt{\alpha}}{1+\sqrt{\alpha}} \quad \text{for solution 2 .} \tag{6.25}$$

It is worth mentioning that, unlike solution 1, solution 2 does not present a singularity for $\alpha = 1$. Consequently, the same expressions can be used for both $\alpha < 1$ and $\alpha > 1$, as can be deduced comparing (6.15) with (6.21), (6.17) with (6.23), and (6.19) with (6.25).

6.3.3 Conclusions

In this section we demonstrated that the resistance scaling method provides a simple solution to the impedance matching problems involving a UHF-RFID ASIC. We will show in the next section that good impedance matching in optical disc-based tags can be obtained by using just one element (X_p), shunted to the ASIC.

Although the method was born in the context of optical disc-based tags, it may be extended to the more general context of UHF-RFID tag design, provided that conditions (6.8)-(6.9) are satisfied. In this case, a series element may be also required, and its value can be easily calculated on the basis of the transformed ASIC reactance expression (6.13). The method also allows easily controlling the matching level at resonance (i.e., the notch depth in the $|s_{11}|$ versus frequency), which directly depends on the ratio between the antenna and the transformed ASIC resistances. This can be very useful for the design of UHF-RFID tags since that, due to bandwidth considerations, a certain matching level could be preferred over conjugate matching [123, 124].

The resistance scaling method will be applied to the design of optical based-tags for DVDs and Blu-ray discs matched to the *Alien Higgs 3* ASIC, as detailed in the next sections.

6.4 UHF-RFID tag for DVDs matched to *Alien Higgs 3* ASIC

The tag presented in this section can be considered as an evolution of the DVD-based tag presented above. In fact, the lack of a matching network in the latter limited the choice of the ASIC to the ones presenting low values of input resistance R_C, given that the antenna input resistance R'_{disc} is low (8-12 Ω). In that case, the *NXP UCODE G2XM* ASIC was used, which has an input resistance R_C = 16 Ω at 915 MHz. However, newer and better performing RFID chips may present higher input resistance, so that specific matching strategies should be implemented. We will show here that the problem can be solved by introducing only a matching element (instead of two elements, as generally required in impedance matching problems), placed in shunt with the ASIC, since the series reactance provided by the LC resonator can be adjusted by varying the tag geometry.

The tag design strategy, regarding the coupling between the ASIC and the disc reflective layer, was maintained from the previous design (Section 6.2.2): a stepped-impedance resonator (SIR) capacitively couples the two elements (Figure 6.15, top). However, conjugate matching was obtained in this case by means of semi-lumped matching elements added in shunt to the ASIC (Figure 6.15, bottom). The required values of the matching reactances were determined by using the resistance scaling method, as detailed in the next section.

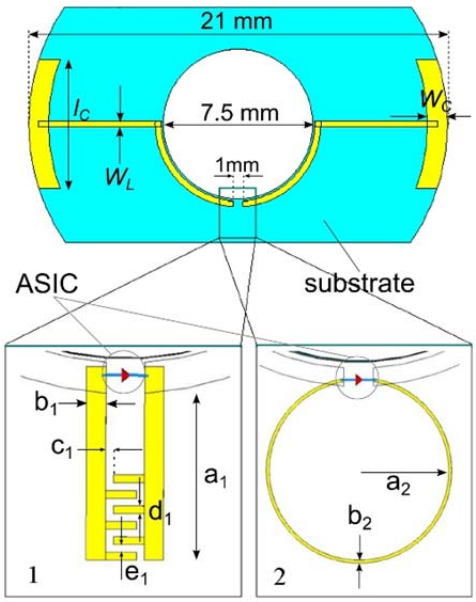

Figure 6.15. Proposed tag layout (on top). The matching elements are illustrated at bottom left (solution 1) and bottom right (solution 2).

6.4.1 Resistive scaling applied to *Alien Higgs 3*

Let us apply the previous method to obtain conjugate matching at 915 MHz between the *Alien Higgs 3* (SOT-323 packaged) ASIC and an antenna based on a DVD disc. As stated above, we can take advantage of the reactive impedance approximation by applying the transformation to the chip impedance Z_C, obtaining the transformed impedance Z'_C. To verify this, let us consider the input impedance of the ASIC at the center frequency, which is $Z_C = 25 - j190\ \Omega$. In this case, the load impedance is the antenna impedance Z_A, so that the resistance scaling factor providing conjugate matching can be easily calculated as $\alpha = R_A/R_C$. If the disc antenna resistance is assumed to be $R_A = 10\ \Omega$ (Section 6.2.3), a value of $\alpha = 0.4$ is obtained. As expected, conditions (6.8)-(6.9) are satisfied, as it can be proved by evaluating $X_C^2 = 3.6 \cdot 10^4\ \Omega^2 \gg |1-\alpha| \cdot R_C^2 = 3.75 \cdot 10^2\ \Omega^2$. Thus, since $X_C < 0$, the solutions for X_p can be calculated by using (6.11), obtaining $X_{p1} = -327\ \Omega$ and $X_{p2} = 74\ \Omega$. The transformed ASIC reactance can be inferred from (6.13), yielding $X'_{C1} = -120\ \Omega$ and $X'_{C2} = 120\ \Omega$. As a consequence, the required antenna reactance for each case is $X_{A1} = 120\ \Omega$ and $X_{A2} = -120\ \Omega$.

6.4.2 Tag design, synthesis and simulation

Let us now introduce the tag equivalent circuit model (Figure 6.16), which is a simplification of the model proposed for the previous tag (Figure 6.9). In fact, since its first resonance frequency occurs at 4.8 GHz, the RLC tank which models the disc impedance Z'_{disc} can be approximated to the series combination of the disc inductance L'_p and a resistance, which is directly the antenna resistance R_A. The tag (excluding the ASIC and the matching element) is still modeled as an LC series resonator in series with the disc impedance. On the left side of the model, the transformed chip impedance Z'_C was obtained as a shunt combination of the ASIC parallel model and the matching reactance X_p. The proposed model does not take into account the ohmic losses introduced by the matching network and by the sections L_{tag} and C_{tag}.

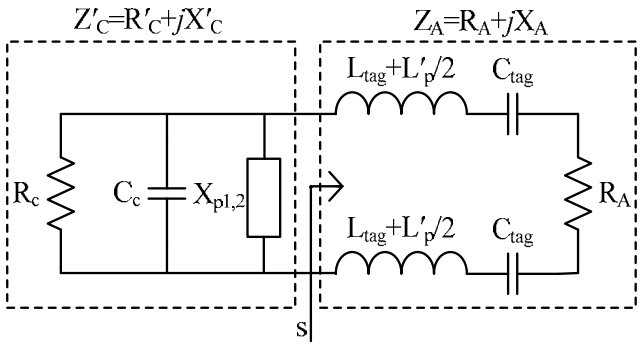

Figure 6.16. Simplified equivalent circuit model of the tag coupled to the disc.

6.4.2.1 Tag design process

The design process begins with the matching elements, which are implemented through semi-lumped components, a solution widely used in the design of UHF-RFID tags. The capacitive reactance, required for solution X_{p1}, was obtained by means of an interdigitated capacitor, whose parameters are number of fingers N, length a_1, width b_1 and e_1, spacing c_1 and d_1, whereas the inductive solution X_{p2} was provided by a loop inductor of radius a_2 and width b_2 (Figure 6.15). The final layout was obtained in each case by varying the geometrical parameters until the simulated reactance reached the required value (X_{p1} or X_{p2}). In order to get better accuracy, the simulated elements were placed at their final positions on the tag substrate (*Rogers RO3010*, $h_s = 0.254$ mm), which was placed on top of the disc. The tag LC series resonator was not included at this stage.

The next step is to determine, for each solution, the geometric parameters associated to the LC resonator. This was accomplished by simulating the resonator (coupled to the disc) without the matching network, and varying the capacitor area in order to adjust the antenna reactance to the required value (X_{A1} or X_{A2}). As it will be justified in the next paragraph, the value of the inductor width W_L (and consequently the value of L_{tag}) was fixed during the design process. This was set to $W_L = 0.6$ mm.

Finally, a simulation of the complete layout cascaded to the impedance Z_C is performed, in order to verify the impedance matching. At this stage it is useful to point out that, although the antenna resistance R_A (which can be inferred from the previous simulation) cannot be easily controlled by the tag geometry, a slight variation of its value occurs varying the LC resonator geometry. As a result, the minimum value of the power reflection coefficient is expected to present, for each solution, a deviation from the expected value. In case that poor impedance matching is obtained, the design of the matching element should be repeated taking into account a corrected value of α, which can be easily determined on the basis of the simulated value of R_A. Moreover, a small error in the matching element reactance X_p (geometrical tolerances might make difficult obtaining the exact required value) can introduce a frequency shift Δf (with respect to f_0) of the minimum power reflection coefficient, due to the deviation of X'_C from the expected value. An additional contribution to the frequency shift could be introduced by the non-zero frequency slope of the antenna conductance G_A, which exists because the antenna cannot be modeled as a pure parallel load. However, the total frequency shift can be corrected by simply tailoring the value of l_C in the final simulation, which adjusts the antenna reactance to the required value.

6.4.2.2 Tag bandwidth

Let us now analyze the final tag bandwidth associated to each solution (i.e., capacitive solution 1 and inductive solution 2). In Section 6.3.2, the maximum tag bandwidth associated to a certain ASIC was evaluated by considering an ideal antenna, modeled by a shunt RL or RC model. In this specific case, the antenna is modeled as a series RLC circuit, and therefore a dedicated analysis is required. For fabrication and measurement, the solution that provides broader bandwidth will be chosen.

First of all, we discuss the value of L_{tag}. Since the tag introduces a series resonance, bandwidth optimization suggests minimizing the inductance L_{tag}, thus adjusting the reactance by changing the value of C_{tag}. Moreover, it is difficult to efficiently control the value of L_{tag}, since it depends on the logarithm of the strip width W_L. On the contrary, the value of C_{tag} can be easily controlled since it linearly depends, in first approximation, on the capacitor area. Therefore, it is reasonable to adjust the tag reactance by simply varying the capacitor length l_C and the capacitor width W_C.

Let us compare solutions 1 and 2 from the bandwidth point of view. In Section 6.3.2 it was demonstrated that the transformed ASIC susceptance slope was lower for solution 1. However, it is necessary to sum the antenna susceptance slope to the previous expressions, in order to estimate the final tag bandwidth. To do this, it is firstly convenient to analyze the antenna reactance and its frequency slope, for each case, in the vicinity of ω_0. Based on the equivalent circuit model (Figure 6.16), these can be written as:

$$X_A\big|_{\omega_0} = (2L_{\text{tag}} + L'_p)\cdot\omega_s\left(\frac{\omega_0}{\omega_s} - \frac{\omega_s}{\omega_0}\right) \tag{6.26}$$

$$\left.\frac{\partial X_A}{\partial\omega}\right|_{\omega_0} = (2L_{\text{tag}} + L'_p)\left[1 + \left(\frac{\omega_s}{\omega_0}\right)^2\right], \tag{6.27}$$

where $\omega_s = \left[(L_{\text{tag}} + L'_p/2)C_{\text{tag}}\right]^{-1/2}$ is the tag series resonance angular frequency. Since an inductive antenna behavior is required for solution 1 and a capacitive behavior is required for solution 2, conditions $\omega_{s1} < \omega_0$ and $\omega_{s2} > \omega_0$ must be satisfied, and consequently $\omega_{s2} > \omega_{s1}$. Therefore, taking into account that L_{tag} is fixed in the design process and L'_p is weakly dependent on the tag geometry, a smaller value of (6.27) is obtained for solution 1. As a final step, let us write the expression of the susceptance slope of a generic load as a function of its impedance:

$$\left.\frac{\partial B_A}{\partial\omega}\right|_{\omega_0} = \frac{2X_A R_A}{|Z_A|^4}\cdot\left.\frac{\partial R_A}{\partial\omega}\right|_{\omega_0} + \frac{X_A{}^2 - R_A{}^2}{|Z_A|^4}\cdot\left.\frac{\partial X_A}{\partial\omega}\right|_{\omega_0}, \tag{6.28}$$

which can be approximated to:

$$\left.\frac{\partial B_A}{\partial \omega}\right|_{\omega_0} \approx \frac{1}{X_A^{\,2}} \cdot \left.\frac{\partial X_A}{\partial \omega}\right|_{\omega_0} \tag{6.29}$$

when $R_A << X_A$. Since $X_{A1} = -X_{A2}$ [as a consequence of (6.7)] and the antenna reactance slope is smaller for solution 1, susceptance slope (6.29) is also smaller for solution 1. Therefore it can be concluded that capacitive matching provides both smaller ASIC and antenna susceptance slopes, resulting in a greater bandwidth.

6.4.2.3 Simulation results

The EM simulations are performed by means of the *CST Microwave Studio* commercial software (the frequency domain solver is used). The disc was modeled as described at Section 6.2.1. The substrate used for the tag is the *Rogers RO3010* (with thickness $h_s = 0.254$ mm, $\varepsilon_r = 10.2$, $\tan\delta = 0.0023$), which has a structural function only. As it was demonstrated for the tag presented at the previous section, the high permittivity of the material does not have a role, neither in size reduction, nor in increasing the tag performance of optical-based tags.

The first simulations provided a possible set of solutions for the geometrical dimensions of the matching elements. The values were found to be $N = 6$, $a_1 = 5$ mm, $b_1 = 0.5$ mm, $c_1 = 0.2$ mm, $d_1 = 0.2$ mm, $e_1 = 0.2$ mm for the capacitive solution, and $a_2 = 3$ mm and $b_2 = 0.2$ mm for the inductive solution. The tag LC resonator geometry was then obtained for each solution, as described in the design process. The results are $l_{C1} = 13$ mm, $W_{C1} = 2$ mm and $l_{C2} = 3.1$ mm, $W_{C2} = 2$ mm. The values of the simulated antenna resistance are $R_{A1} = 9\ \Omega$ and $R_{A2} = 6\ \Omega$ at 915 MHz. Therefore, since $R'_C = 10\ \Omega$, the expected values of the power reflection coefficient at 915 MHz are −25 dB and −12 dB, respectively. Since both values provide very good performance in terms of read

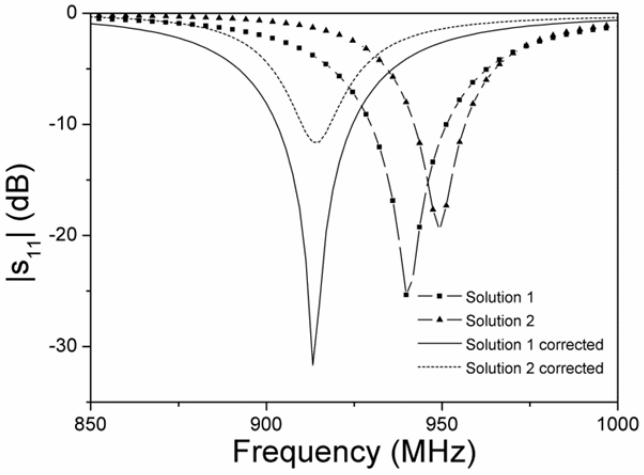

Figure 6.17. Simulated tag power reflection coefficient

range, the matching elements do not need to be corrected. The simulated power reflection coefficients of the complete tag are shown in Figure 6.17. The matching notches (−25 dB for solution 1 and −19 dB for solution 2) are clearly visible as expected, and the frequency shifts are $\Delta f_1 = 25$ MHz and $\Delta f_2 = 34$ MHz. In order to correct the shifts, a tailoring of the capacitor length l_C was performed as a final step. The resulting geometrical values are $l_{C1} = 14.4$ mm and $l_{C2} = 4.1$ mm. The final curves for $|s_{11}|$, centered at f_0, are also depicted in Figure 6.17. Good matching is achieved in both cases (−31 dB and −11 dB for cases 1 and 2, respectively) and the half-power bandwidths are $BW_1 = 65$ MHz and $BW_2 = 40$ MHz. Although bandwidths are smaller than the optimal values predicted in (6.18) and (6.19) (where an ideal network is cascaded to the transformed chip impedance), it is interesting to note that the ratio BW_1/BW_2 approaches the value obtained in the optimal case ($1+\alpha^{1/2} = 1.63$ for $\alpha = 0.4$).

Let us now compare the antenna gain of the tag for the two different solutions, since its value is strictly related to the tag read range. Simulated far-field (Figure 6.18) indicates that, while directivities are similar in both cases (4 dB approximately) an important difference in the radiation efficiency exists for the two cases, providing $\eta_{rad1} = 26\%$ and $\eta_{rad2} = 14\%$. There are mainly two reasons for this difference. First, the inductor is implemented through a thin line, which introduces more ohmic losses than an interdigitated capacitance does. Moreover, the second solution transforms the ASIC impedance, as seen from the antenna, from capacitive to inductive. This corresponds to changing the sign of the internal electric dipole existing around the ASIC, with respect to the external dipole created by the optical disc antenna (Figure 6.19). As can be seen in the figure, in the case of inductive matching the internal dipole is opposite in sign to the external dipole, causing a reduction of the radiation efficiency. The simulated antenna gains are $G_1 = -2$ dB and $G_2 = -4.3$ dB, corresponding to the expected read ranges $RR_1 = 9.3$ m and $RR_2 = 7.1$ m (considering $EIRP = 4$ W, $P_{th} = -17$ dBm), according to the read range equation (3.1).

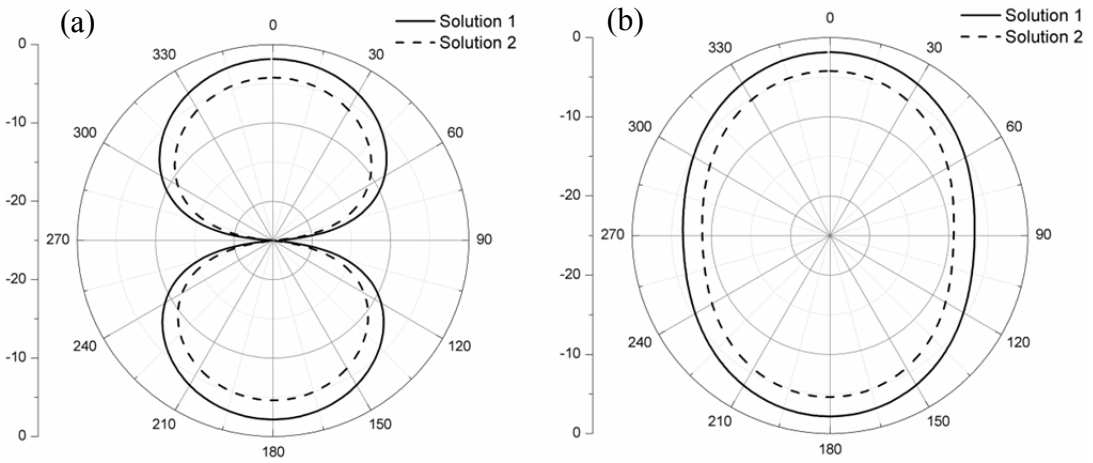

Figure 6.18. Simulated tag gain at 915 MHz in the (a) *E*-plane (*xz*-plane) and (b) *H*-plane (*yz*-plane).

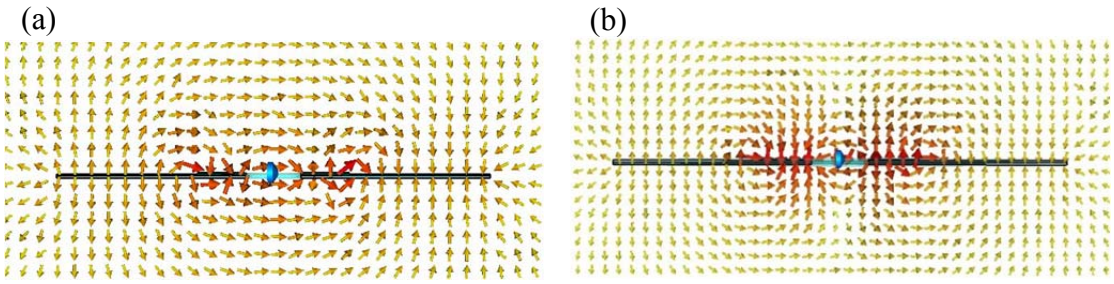

Figure 6.19. Electric field for (a) solution 1 and (b) solution 2. The cutting plane is the *xz*-plane.

6.4.3 Fabrication and measurements

To validate the simulated results, the layout associated to solution 1 (described in the previous section) was fabricated by means of a PCB milling machine (*LPKF-H100*). As explained above, solution 1 has been chosen because it provides wider bandwidth and higher antenna gain.

The measurements (not shown) present a frequency shift of the tag response, with a read range peak at 1 GHz approximately. This effect has been attributed to the intrinsic indetermination over the electrical properties of the DVD materials at the UHF band, and to the simplifications made in the modeling of the disc. In fact, unlike most substrates used for tag implementation, DVD disc materials are not intended for microwave design. Therefore, manufacturers neither report nor control their electrical properties. Moreover, some of the geometrical parameters (e.g., 0.2 mm spacing) of the capacitive matching element are very close to the fabrication tolerances of the PCB milling machine, introducing further error in the tag response.

Based on the measured results, a second prototype of the tag was synthetized and fabricated in order to correct the frequency shift. The matching position was easily adjusted by simply tailoring the length l_C of the tag capacitance. The corrected value of the geometrical parameter is $l_C = 22$ mm. The tag, mounted on a DVD+R disc, is depicted in Figure 6.20a. The read range measurement depicted in Figure 6.20b, shows a peak of 8.3 m at the center frequency, in good agreement with the simulated value. Based on the read range, the half-power bandwidth has been evaluated to be $BW = 50$ MHz.

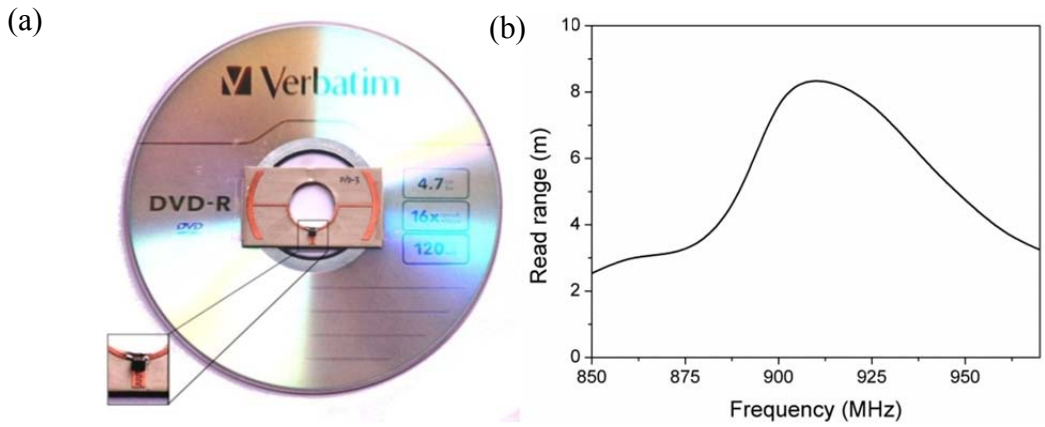

Figure 6.20. (a) The fabricated tag, mounted on a DVD-R disc. The matching network is depicted at bottom left. (b) Measured read range.

6.4.4 Conclusions

The analytical impedance matching method for optical disc-based UHF-RFID tags, presented at the previous section, has been applied in this section to the design of a DVD-based tag using the *Alien Higgs 3* ASIC, optimized to work in the North-American UHF-RFID band (902-928 MHz). The tag design process was presented, and the bandwidth limitations and radiation efficiencies associated to the different solutions were discussed. Based on that, the optimal solution was chosen for fabrication and measurement. The measurements agree with simulations, and measured read range reaches 8.3 meters at the center frequency (915 MHz), with a 50 MHz half-power bandwidth. Note that the obtained read range is an order of magnitude higher than the read ranges obtained with the tag designs described in the literature (see Section 6.1.2).

6.5 UHF-RFID tag for Blu-Ray discs

The design methodology presented in the previous section was then applied to the design of tags based on Blu-ray discs, which represent an important part of the actual optical disc production. The results, detailed below, confirm the validity of the optical disc-based tag approach and the design flexibility provided by the resistive scaling method.

Although there exist some important structural differences between DVD and Blu-ray discs (see Section 6.1.1), the electromagnetic modeling of the two discs is very similar: both can be modeled as a thin metal layer sandwiched between two polycarbonate layers. In the Blu-ray, the metal layer is located 1.1 mm below the disc surface, on top of the 0.1 mm hard layer (which is modeled as polycarbonate in the EM simulation), as

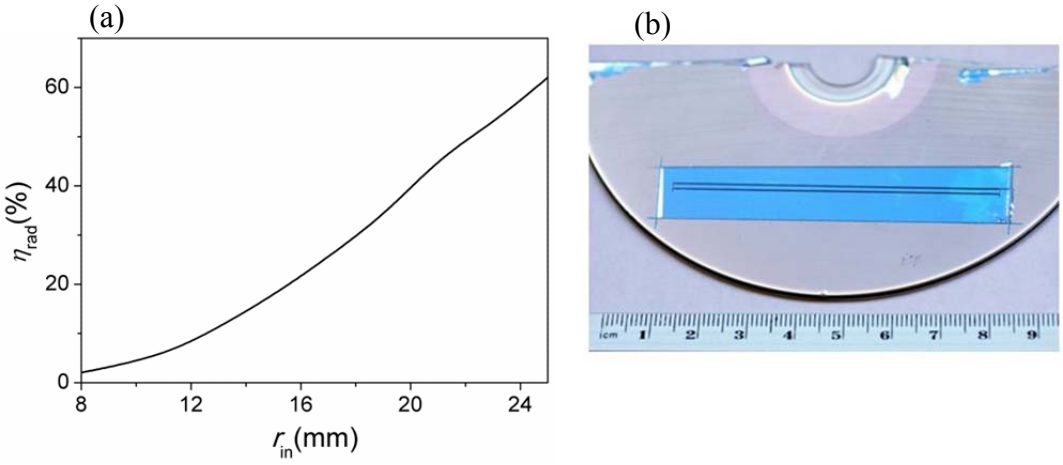

Figure 6.21. (a) Simulated radiation efficiency of the optical disc antenna, as a function of the inner radius of the metal film (the polycarbonate substrate was not considered), and (b) metal film resistance measurement path on the tested Blu-ray disc.

detailed in Figure 6.22. Additionally, the inner radius of the metal film is reduced from 19 mm (the value used for the DVD) to 12.5 mm for the considered Blu-ray disc. It is worth mentioning that, whereas the maximum internal radius of the metal layer is fixed to 24-25 mm (which is the beginning of the data area [125]), its minimum value is not fixed, and can vary upon the disc type and manufacturer. It was verified by simulations that, as the internal radius decreases, the radiation efficiency of the disc antenna also decreases significantly, as depicted in Figure 6.21a. This is the primary mechanism leading to a reduction of the performance when comparing the tag presented in this section with the tag detailed in the previous section. As in the previous case, the metal film square resistance is assumed to be $R_{\square} = 0.5\ \Omega$. It is worth mentioning that, a posteriori, the film square resistance was measured on the Blu-ray disc, as follows. A rectangular window (see Figure 6.21b) was opened on the lower side of the disc by removing the hard coating layer, so that the metal film was directly accessible. Then, with the aid of a cutter, a path of 1 mm width and 70 mm length was isolated from the rest of the film. The side-to-side resistance was successively measured by using a multimeter, which provided a value of $R = 53\ \Omega$. Taking into account that the path consisted of 70 squares connected in series, the square resistance was determined to be $R_{\square} = 0.76\ \Omega$, which is very near to the theoretical value used in the simulations. Later simulations revealed that a very small decrease (−0.4 dB) of the simulated tag gain arises when the theoretical value of the film square resistance (0.5 Ω) is substituted by the measured value (0.76 Ω) in the disc modeling.

6.5.1 Tag design, synthesis and simulation

Since the equivalent circuits of the Blu-ray and DVD discs are identical (except for the values of the circuit elements), the tag design flow follows the same scheme of the tag presented in the previous section. As in the previous design, the RFID ASIC used in

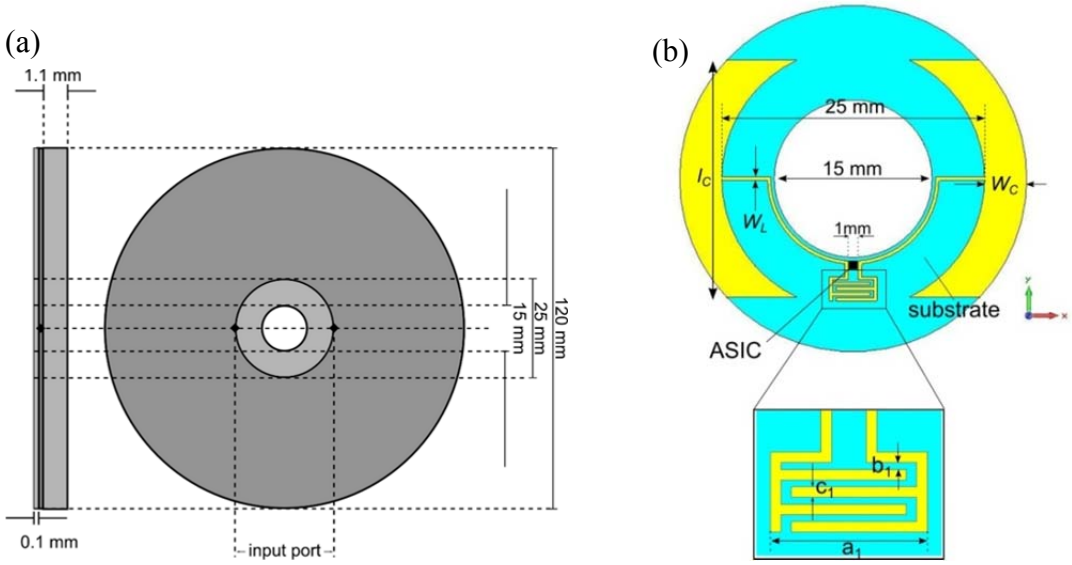

Figure 6.22. (a) Structure of the considered Blu-ray disc: lateral view (left), top view (right). Dark grey represents silver, light grey represents polycarbonate. Layer thicknesses are not drawn to scale. (b) Layout of the final tag. The close-up focuses on the matching element.

the design is the *Alien Higgs 3* with SOT-323 package, and the dielectric substrate is the *Rogers RO3010* (with thickness $h_s = 0.254$ mm, $\varepsilon_r = 10.2$, $\tan\delta = 0.0023$).

Based on the Blu-ray model described above (Figure 6.22a), a preliminary simulation was carried out in order to estimate the radiation properties of the standalone Blu-ray disc. The results showed a radiation pattern very similar to that of a DVD disc (Figure 6.8), with a directivity of $D_0 = 2.7$ dBi and the radiation maximum oriented along the z-axis. However, the radiation efficiency is sensibly lower, namely $\eta_{rad} = 10\%$ (versus 25% for the DVD), due to the smaller inner radius of the metal film. As a consequence, the simulated input resistance of the disc antenna (given by a successive simulation which included the LC resonator coupled to the disc) at resonance is $R_A = 5\ \Omega$, and therefore the scaling factor is $\alpha = R_C/R_A = 25/5 = 0.2$. The required value for the matching element reactance was then evaluated by using (6.11), obtaining $X_p = -154\ \Omega$ (for the reasons detailed in the previous section, the capacitive solution was implemented). The transformed ASIC impedance is $Z'_C = 5 - j85\ \Omega$, thus requiring an antenna impedance of $Z'_A = 5 + j85\ \Omega$. The topology of the matching capacitor and the LC resonator (Figure 6.22b) was then adjusted with the help of EM simulations, as detailed in the design process of the DVD tag (Section 6.4.2). The geometric parameters of the final layout (see Figure 6.22b) are $N = 4$, $a_1 = 4.5$ mm, $b_1 = 0.5$ mm, $c_1 = 0.3$ mm, $l_C = 22.6$ mm, $W_C = 4$ mm and $W_L = 0.3$ mm.

The simulated power reflection coefficient, before and after the final correction on the capacitor length l_C, is depicted in Figure 6.23a. Very good impedance matching (−25 dB) and half-power bandwidth (47 MHz) are exhibited, and the final response is centered

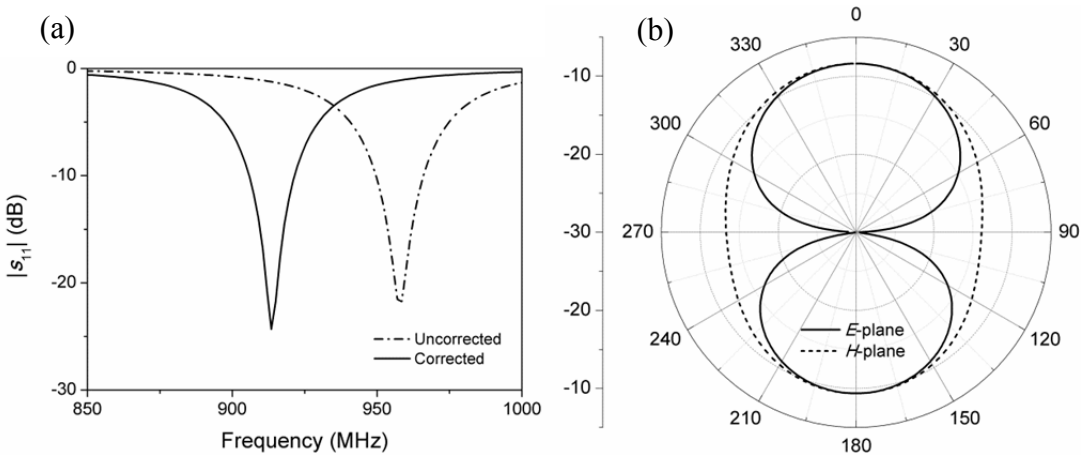

Figure 6.23. Simulated tag (a) power reflection coefficient and (b) radiation pattern (gain, expressed in dB) at 915 MHz in the *E*-plane (*xz*-plane) and *H*-plane (*yz*-plane).

approximately at the center of the North-American UHF-RFID band (915 MHz). Moreover, the tag radiation pattern suggested by EM simulation (Figure 6.23b) is in good agreement with the expected pattern of a disc antenna, already discussed for the previous disc-based tags, with a directivity of $D_0 = 4.2$ dB. The simulated radiation efficiency of the tag is $\eta_{rad} = 6\%$, which provides a maximum gain of $G_0 = -8.4$ dB. Therefore, the tag predicted read range (Figure 6.24b), evaluated on the basis of (3.1) and considering $EIRP = 4$ W and $P_{th} = -17$ dBm, reaches the value $RR = 4.5$ m at 915 MHz. Although this value is sensibly smaller as compared to the read range obtained by the DVD-based tag, it still represents an important improvement over the state of the art of optical disc tagging.

6.5.2 Fabrication and measurements

The tag described in the previous section was manufactured by means of a PCB drilling machine (*LPKF-H100*) and attached to a Blu-ray disc (Figure 6.24a).

The experimental read range, depicted in Figure 6.24b, exhibits a maximum value of 6.3 m at 914 MHz, and a half-power bandwidth of 40 MHz. Although the bandwidth is in good agreement with the simulated value (47 MHz), the experimental peak read range is higher (40%) than the value predicted by simulation. In order to justify this difference, it is worth mentioning that the disc electromagnetic modeling, described at the beginning of this section, is a first order approximation, since the exact composition and electric properties of the disc materials are not known accurately. Even though the square resistance of the metal film was confirmed experimentally (see the introduction of this section), the loss tangent of the disc substrate could not be measured, and its value is not declared by the disc manufacturers.

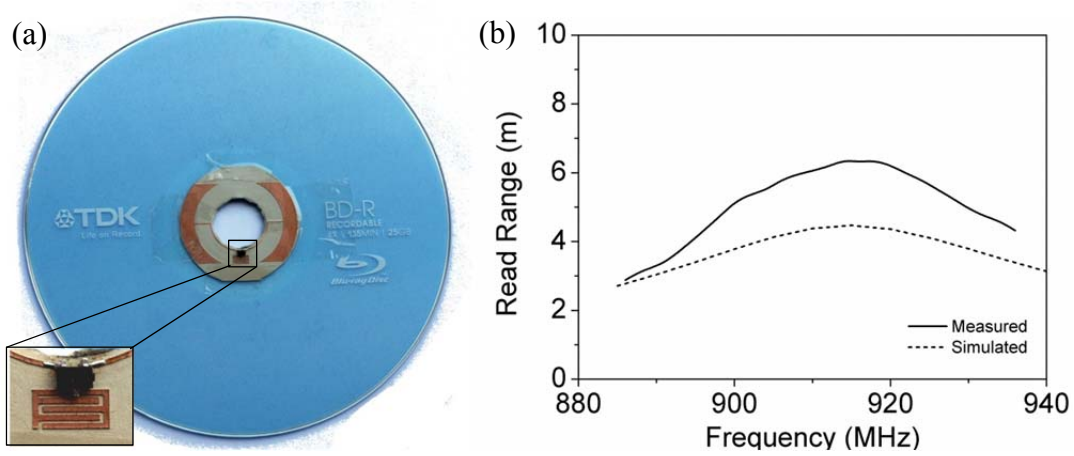

Figure 6.24. (a) The fabricated tag, mounted on a Blu-ray disc. The matching network is depicted at bottom left. (b) Measured read range (after correction).

6.5.3 Conclusions

In this section, an optical disc-based UHF-RFID tag mounted on a Blu-ray disc has been presented for the first time. As a first step, the physical structure of the disc was investigated, and a simplified electromagnetic model was generated in order to evaluate the radiation properties and the input impedance of the Blu-ray disc antenna by means of EM simulations. Then, as in the case of the DVD-based tag described at Section 6.4 the tag layout was designed by combining the general design principles of optical disc-based tags (Section 6.2.2) with the resistive scaling method, which allowed obtaining good impedance matching between the antenna and the RFID ASIC. A tag prototype was then fabricated and attached to the disc, and the read range was measured, showing a peak value of RR = 6.3 m and a half-power bandwidth of 40 MHz.

6.6 Reading of stacked optical discs

The read ranges of the optical disc-based tags presented in the previous sections, which are in the order of several meters, refer to the case of reading a single disc surrounded by air, or inserted in its plastic case (as demonstrated experimentally in Section 6.2.4, the disc plastic case does not significantly affect the tag response). However, in the real world, optical discs are often stored in a stack (e.g., on a pallet during shipping, on the retail shelves), which involves a large number of nearby tags interfering each other. In this situation, a modification of the tag behavior due to couplings has to be expected, since the distance between antennas is much smaller than the antenna dimensions. As suggested by previous research [126, 127], the behavior of

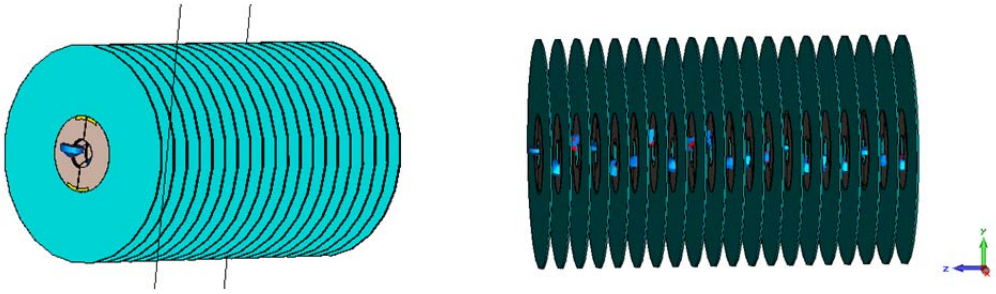

Figure 6.25. Lateral views of the simulated stack of tagged optical disc.

dense arrays of UHF-RFID tags may be substantially different from the behavior of the standalone tag. In fact, the antenna properties (e.g., radiation efficiency, radiation pattern), including its impedance, may be significantly affected by the mutual interference with nearby tags. Obviously, this is especially critical in the case of attaching the tags to metallic items, because these involve a much higher interaction with radio waves as compared to dielectric objects (e.g., plastics, textiles, paper). In particular, when dealing with stacks of tagged metallic items, special concern arises from the mutual shadowing between neighboring elements.

These considerations lead to conduct a preliminary investigation on the effects of stacking over optical-discs based tags. To this end, a 20 discs stack (Figure 6.25) was simulated by periodically repeating (along the *z*-direction) the structure of a single tagged disc, with a separation of 1 cm, a distance based on the thickness of the standard DVD case. In order to simplify the problem, the presence of the plastic case was not taken into account. The rotation angle of each disc was randomized, since in a real-world scenario the orientation of each disc is aleatory. The simulation consisted in exciting each disc individually, and evaluating the realized gain in the *z*-direction (and, consequently, the read range) of the structure in each case. The results (Figure 6.26) indicated that, although the mutual coupling between discs causes a degradation of the read range compared to a single disc, it is still possible to read stacked discs

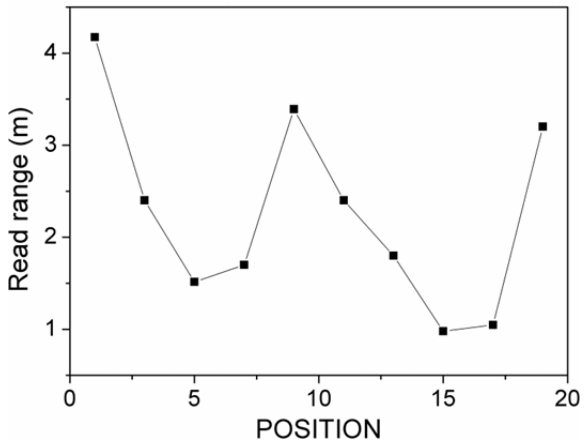

Figure 6.26. Simulated read range in the z-direction as a function of the disc position in the stack.

simultaneally. In the studied case, according to the simulation results, it was possible to read all the stacked DVDs from a distance of 80 cm (from the first element of the stack).

It is interesting to observe that the read range of stacked tags does not decay monotonically. This suggests that the stack may act as a propagating structure with unterminated ends, whose power reflections cause a stationary wave creating minima and maxima in fixed points of the structure. Also, the distance between minima (or maxima) is $\lambda_0/3$, which indicates that slow wave propagation through the piled discs occurs. In this regard, further investigation (including experimental confirmation) is needed, in order to understand and even control the behavior of the stack, thus improving the reliability of RFID tagging for this application.

7

A High-Gain Passive UHF-RFID Tag with Increased Read Range

In this chapter, some aspects regarding the performance limitations of passive UHF-RFID tags are briefly discussed. In particular, the maximum read range is explored in case the condition of size reduction, usually applied to the general-purpose commercial UHF-RFID tag design, is relaxed. In fact, whereas for many applications a tradeoff between tag dimensions and performance is necessary, there exist some applications where the read range optimization is a due, even at the expense of the tag dimensions. Such applications may include, for instance, inventory of boxes in a large warehouse, and pallet tagging, among others. In general, when a high read range is required and the dimensions of the tagged objects are relatively large, oversized (as compared to the usual sizes) tags with optimized read range might be preferred. The analysis suggested that, while maintaining a dipole type antenna, a significant improvement of the read range can be accomplished by extending the tag size to 1.25 wavelengths, and that further increases in dimensions worsen the tag performance due to the increasing number of blind spots.

As a proof of concept, a tag prototype is designed with the aid of the commercial software *CST Microwave Studio*, and manufactured. The experimental read range is presented, exhibiting good agreement with simulations, and compared to a high-end commercial general-purpose tag (*Alien Squiggle*).

7.1 Strategy to maximize the read range

The field radiated by an infinitely thin wire antenna of a given length l oriented along the z-axis can be calculated by integrating the radiation of the infinitesimal current element dI over the length of the antenna. As reported in many classical analysis of the problem [95]-[17], it is a good approximation to consider the current over the antenna as a perfect harmonic function of the position, with zeroes at both ends of the wire, thus neglecting the second order effects on the current distribution. The resulting expression for the directivity, as a function of the wire length l, can be written as [17]

$$D_0(l) = 2\frac{F(\theta,l)\big|_{MAX}}{\int_0^{\pi} F(\theta,l)\sin(\theta)d\theta}, \tag{7.1}$$

where $F(\theta,l)$ is a function proportional to the radiated power density, and can be expressed as

$$F(\theta,l) = \left[\frac{\cos\left(\beta\frac{l}{2}\right) - \cos\left(\beta\frac{l}{2}\cos(\theta)\right)}{\sin(\theta)}\right]^2, \tag{7.2}$$

where θ is the inclination angle and β is the free-space phase constant at the working frequency. A graphical representation of (7.1) for wire lengths up to 4 free-space wavelengths is depicted in Figure 7.1. It can be clearly seen from the graphic that the directivity increases monotonically with the antenna length up to approximately 1.25 wavelengths, where a peak value of $D_0 = 3.3$ (5.2 dBi) results. Above that length, the increase of the side lobes produces a sudden degradation of the directivity, leading to a minimum located at approximately 1.5 wavelengths. A further increase of the antenna length results in periodical directivity peaks and minima, whose levels tend to increase linearly with the antenna length. Nonetheless, the radiation pattern above the first peak

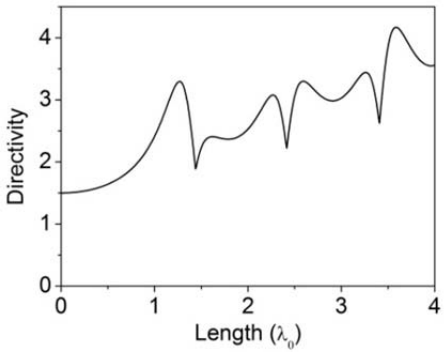

Figure 7.1. Directivity of a wire antenna as a function of its electrical length.

is characterized by a crescent number of lobes, and radiation zeros. Such kind of radiation pattern is not useful for a general-purpose RFID tag, since it produces undesired blind spots in the tag read range. It is also worth to mention that, above the first directivity peak, the following major peak occurs at 3.6 wavelengths, which implies tag lengths exceeding one meter.

For the above reasons, we found reasonable to design the tag to work at 1.25 wavelengths, corresponding to an overall length of $l = 410$ mm at the frequency $f_0 = 915$ MHz. The theoretical power radiation pattern, obtained from (7.1) and normalized to 5.2 dBi, is depicted in Figure 7.2. It is composed of a main lobe with a maximum at $\theta = 90º$, and two side lobes of magnitude −10 dB. The half-power beamwidth is 34º, and the null-to-null beamwidth is 74º. It is worth to mention that, for a non-zero radius wire, the effective antenna length may slightly differ from the theoretical value of 1.25 wavelengths.

Let us now quantify the maximum theoretical read range which can be obtained with this kind of tag. By using (3.1) with the values of $EIRP = 4$ W and a sensitivity of $P_{th} = -17$ dBm (e.g., Alien *Higgs-3* chip, SOT-323), and neglecting ohmic losses, the maximum predicted read range is $RR = 21$ m. Such value, which is only qualitative since losses have not been considered, is very promising since it doubles the maximum read range of general-purpose commercial UHF-RFID tags (e.g., the Alien *ALN-9640* "Squiggle" tag), which is of the order of 11-12 m.

It is worth mentioning that, according to the previous analysis, the read range is increased by making the tag more directive. Hence, due to its reduced beamwidth, the tag performance is more dependent upon its orientation with respect to the reader antenna. Although this is generally an undesired behavior in general-purpose UHF-RFID tags (where the tag orientation is not known a priori), it is not necessarily an issue

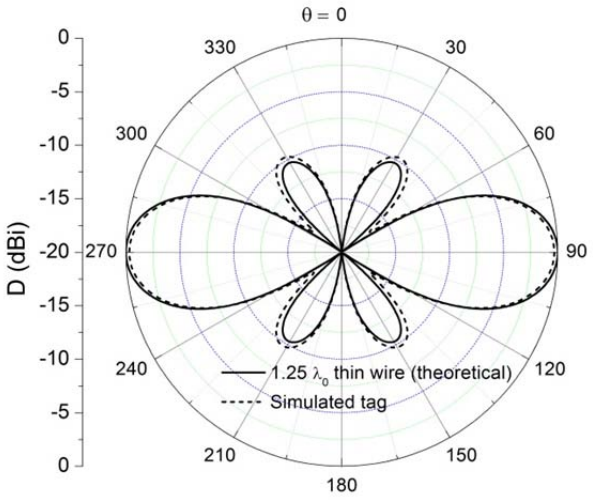

Figure 7.2. Directive gain in the *E*-plane, normalized to a directivity value of $D_0 = 5.2$ dBi.

for some applications requiring read range optimization (e.g., when the tag orientation is known). In this regard, it is useful to evaluate the half-read-range beamwidth of the tag, corresponding to the quarter-power beamwidth of the antenna [this is a consequence of the read range equation, (3.1)]. For the 1.25 wavelengths dipole antenna, the value is 46º, which is roughly half the value obtained with a half-wave dipole antenna (108º)

7.2 Tag design and simulation

For practical reasons, the presented tag prototype was chosen to use a copper wire to implement the 1.25 wavelengths antenna, so that the tag design described below refers to that case. However, since RFID tags are usually fabricated in planar technology (e.g., inlays), where the antenna is implemented by a thin metal strip, this latter case has also been considered, and will be described in a separate section.

7.2.1 Copper wire antenna

In this section we present the simulations of a UHF-RFID tag based on a 1.25 wavelength long wire antenna and the *Alien Higgs-3* RFID chip (SOT-323 packaged), designed to work in the 902-928 MHz band.

The first simulation involved a copper wire with circular cross section of diameter $a = 0.8$ mm. A 4 mm gap was opened at the center of the wire in order to connect the input port. The length of the wire was swept in the vicinity of 1.25 wavelengths, in order to determine the optimal length for the given wire diameter value a. It was found that the length $l = 400$ mm ($1.22\,\lambda$) provided the maximum directivity $D = 4.9$ dBi, which is very close to the theoretical value (5.2 dBi). The next step was to quantify the input impedance at the working frequency $f_0 = 915$ MHz (the center of the 902-928 MHz band), in order to design the impedance matching network between the chip and the antenna (see Figure 7.3). According to the simulation, the antenna presents a

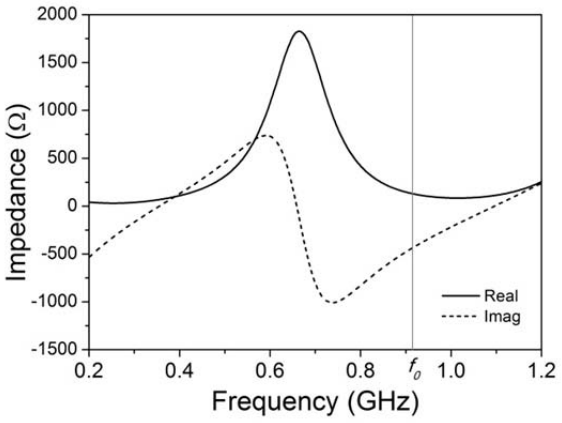

Figure 7.3. Simulated input impedance of the wire antenna.

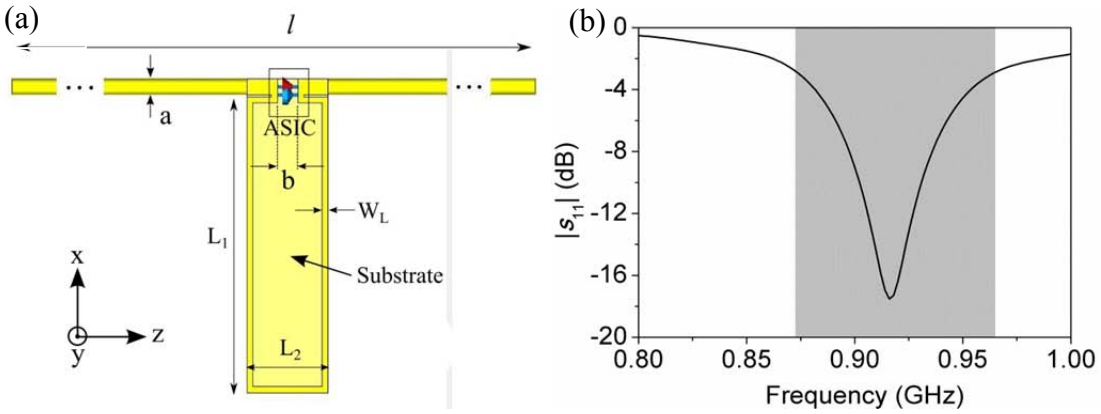

Figure 7.4. (a) Final tag layout, (b) simulated power reflection coefficient (half-power bandwidth in grey).

resistance $R_A = 130\ \Omega$ and a capacitive reactance $\chi_A = -440\ \Omega$ at f_0. It can be demonstrated, e.g., by using the resistance scaling technique described in Section 6.3, that a shunt inductance with value $L_p = 24$ nH transforms the chip impedance Z_c into the complex conjugate of the antenna impedance Z_A to a very good approximation, thus allowing to obtain a very good impedance (conjugate) matching without the need of a series element.

A second, and last, simulation comprises the wire antenna, the matching inductive element and the chip port exciting the system. The inductive element was implemented on a FR-4 substrate ($\varepsilon_r = 4.3$, $\tan\delta = 0.025$) with thickness $h = 1.5$ mm, which has also the function of carrying the soldering pads for the chip and the antenna. The final layout of the tag is shown in Figure 7.4a, and the values for the geometric parameters are $L_1 = 14.6$ mm, $L_2 = 4$ mm, $W_L = 0.2$ mm, $a = 0.8$ mm, $b = 1$ mm, $l = 400$ mm. The simulated power reflection coefficient between the chip and the antenna, depicted in Figure 7.4b, exhibits good impedance matching at the central frequency, and a half-power bandwidth of $BW = 90$ MHz.

Let us now examine the radiation properties of the tag, in order to predict the maximum read range. As can be seen in Figure 7.2, the simulated radiation pattern (normalized to $D_0 = 5.2$ dBi) of the tag is in good agreement with the theoretical pattern of a 1.25 wavelength long wire antenna, as calculated by using expression (7.1). The simulated directivity is 4.9 dBi, and the half power beamwidth is 33º. The effect of ohmic losses introduced by the conductors is taken into account in the simulation, resulting in a radiation efficiency of $\eta_{\text{rad}} = 92\%$, which leads to a realized gain of $G_0\,\tau = 4.4$ dB. Based on these results, the tag read range can be predicted by using (3.1), providing $RR = 19.4$ m.

7.2.2 Planar technology

It is interesting to explore the possibility of designing this kind of tag in planar technology, by means of standard fabrication techniques (e.g., inlay, screen printing, etc). In this case, the conductor has a rectangular section of width w and thickness t. The main concern about this implementation is the radiation efficiency, which is a function of the metal conductivity and its thickness. It is important to highlight that this kind of tag is focused on read range optimization, at the expense of its length, and this is worth only if the radiation efficiency remains sufficiently high (η_{rad} = 90% can be considered as a lower bound).

In order to quantify the effect of ohmic losses in the fully planar approach, we simulated (by means of *ADS Microwave Studio* commercial software) the antenna, with length l = 400 mm (1.22 λ), for different values of strip width w, thickness h and metal conductivity σ. A graphical representation of the simulated radiation efficiencies is depicted in Figure 7.5. The data reveal that it is possible to obtain high radiation efficiency even by using reduced conductivity materials, such as screen-printing conductive paint, with reasonable values of thickness (of the order of 20 μm) and conductor width (1 mm).

To maintain generality, the simulations did not take into account the presence of a dielectric substrate. This could be the case of direct screen printing of the tag over the item surface. Regarding the inlay implementation, the substrate should be chosen to be as thin as possible, and to present a low permittivity, in order to preserve the electrical length of the antenna and therefore its gain. Nevertheless, the characteristics of the tagged item (not considered in this study) are relevant for the determination of the optimum antenna dimensions.

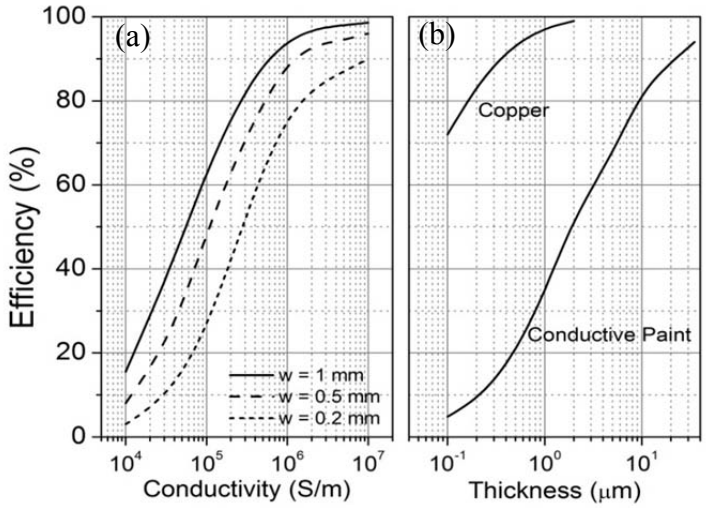

Figure 7.5. Simulated radiation efficiency of the planar tag (a) versus conductivity for h = 35 um and (b) versus conductor thickness for w = 1 mm. The conductive paint has a conductivity $\sigma = 10^6$ S/m [98, 99].

7.3 Fabrication and measurement

In order to validate the simulated results, the tag layout described in Section 7.2.1 was fabricated (Figure 7.6a) and its read range was measured. Due to the dimensions of the tag, the standard measurement process inside the TEM cell could not be carried out. Instead, the read range was measured in an outdoor environment, with the ground as a unique nearby scatterer, by means of a commercial *Motorola FX7400* UHF-RFID reader matched to a half-wave dipole antenna, obtaining a transmission *EIRP* = 1.5 W. The read range was measured in the 865-868 MHz (Europe) and 902-928 MHz (U.S. and others) bands available from the reader. The results, normalized to *EIRP* = 4W, and compared to the simulated read range curve, are depicted in Figure 7.6b. The data are in very good agreement in the 865-868 MHz band, where 14.4 m were obtained. On the other hand, the measured peak read range is 17.5 m in the 902-928 MHz band, which is 10% lower as compared to the simulated value. This discrepancy can be attributed to the fact that the actual chip sensitivity tends to be smaller [128]-[122] than the manufacturer nominal value. Indeed, each dB decrease in the chip sensitivity leads to 10% reduction of the read range, as suggested by (3.1). Nonetheless, when compared to one of the best performing available commercial tags in terms of read range, i.e., the *Alien ALN9640 "Squiggle"*, the tag presented in this work provides a measured read range in the 902-928 MHz band that represents an increase of almost 60% (Figure 7.6b). This improved read range has been achieved despite the fact that the nominal sensitivity (P_{th} = −18 dBm) of the unpackaged *Higgs-3* chip used in the *ALN-9640* inlay is better than the one of the SOT-323 version used in this work (−17 dBm).

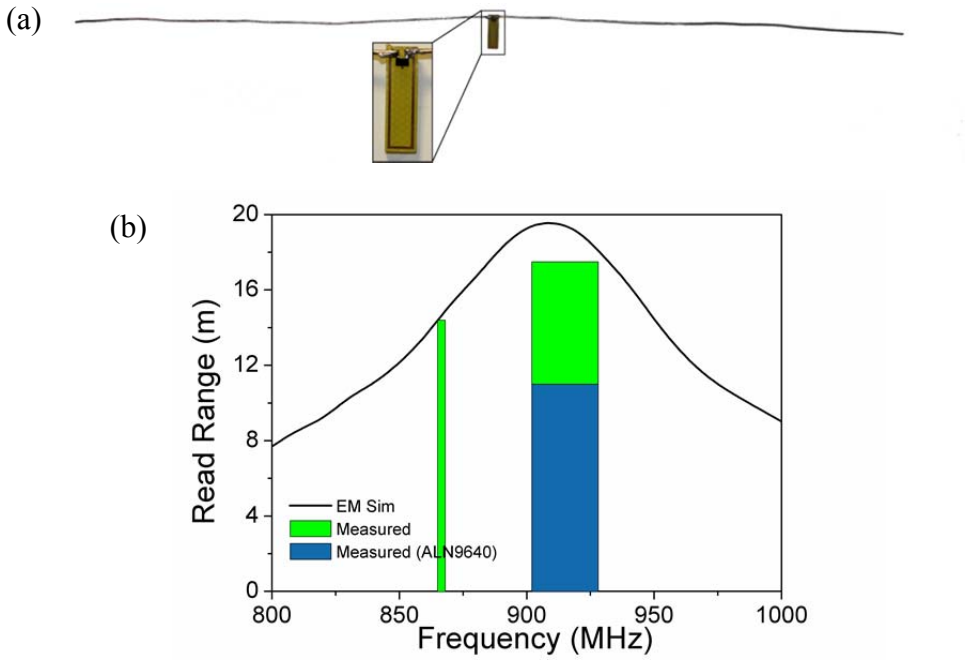

Figure 7.6. (a) Manufactured tag prototype, (b) simulated and measured read range.

It is also remarkable that the read range measured when the proposed tag is attached to a wooden pallet is 16.4 mm, pointing out the potential of these tags for such application.

7.4 Conclusions

The read range limitations of passive UHF-RFID tags based on electric dipole antennas have been studied in this chapter. A 1.25 wavelength long linear wire has been proposed as a tag antenna which maximizes the gain while maintaining acceptable dimensions and radiation pattern. Based on this result, a tag prototype has been designed by matching the antenna impedance to the *Alien Higgs-3* chip input impedance by means of a shunt inductance. The presented tag antenna dimensions are 400 mm x 0.8 mm, respectively, and a 4 mm × 14.6 mm rectangular substrate, holding the chip and the inductive matching network, is located at the center of the tag.

The measured read range exhibits a maximum value of 17.5 m at the 902-928 MHz band, representing an important improvement as compared to the best general-purpose commercial passive UHF-RFID tags. Moreover, several simulations predict that the tag can be implemented in planar technology (i.e., inlay) while maintaining high values of radiation efficiency.

8

Conclusions and Future Work

This thesis is enclosed in the context of antenna design for passive RFID tags working at the UHF frequency band. A significant part of the work is focused on exploring the benefits and limitations of metamaterial-inspired resonators as standalone radiating elements for UHF-RFID tags. To this end, an exhaustive analysis of their radiation properties was carried out, setting the basis for the design of tags meeting specific requirements. In this regard, the use of the split-ring resonator (SRR) working around its first resonance demonstrated its practical effectiveness in obtaining tags with very small size and reduced sensitivity to orientation. Also, complementary metamaterial-resonators have been proposed for the first time as antennas for tags operating at very small distance from metallic surfaces. Specially, a very low profile tag based on a complementary non-bianisotropic SRR (NB-CSRR) has been obtained, and its performance demonstrated competitiveness with state-of-the-art solutions. In addition, the analysis of the radiation properties of the SRR at the second resonance, carried out for the first time within this thesis, suggested that the particle compares with the popular half-wave dipole antenna, in terms of input impedance and radiation efficiency, though providing significant reduction of the maximum antenna dimension. Another important contribution provided in this thesis regards the RFID tagging of optical discs, which is a special case of item-level tagging of metallic objects. We proposed an innovative solution to the problem, by taking advantage of the metallic film of the disc and converting it into the main radiator of the tag. This approach allows one order of magnitude improvement in the tag performance in terms of read range, as compared to the state-of-the-art solutions.

The contents of the thesis have been divided into eight chapters (excluding the conclusions and future work), as follows. After discussing the motivation and objective of this work, in **Chapter 1**, a brief introduction to the RFID technology has been provided in **Chapter 2**.

In **Chapter 3**, an overview of passive UHF-RFID tags has been reported. In particular, the main tag antenna parameters have been introduced, followed by a general discussion over the design solutions and tips commonly employed in commercial tags. The most important performance indicators of passive tags, i.e., read range and bandwidth, have been discussed in detail. The rest of the chapter has been dedicated at providing a state of the art of passive UHF-RFID tag design. Firstly, the report has been focused on the use of metamaterial-inspired resonators in the tag design. To this end, the concepts of metamaterial and metamaterial-inspired resonator have also been introduced, and a brief overview of their application in the microwave community has been provided. Then, discussion over the state of the art has been directed to on-metal tags, with special attention to those solutions emphasizing the thickness reduction (low-profile on-metal tags).

The radiation properties of metamaterial-inspired resonators, specially focusing on the EC-SRR, the NB-SRR and their complementary counterparts (the CSRR and the NB-CSRR) have been analyzed in **Chapter 4**. Based on the evaluation of the electric and magnetic dipole moments generated around resonance, closed expressions for the radiation resistance, efficiency, quality factor and cross-polarization levels of the EC-SRR have been obtained. The analysis, validated by means of electromagnetic simulations, demonstrates the viability of the EC-SRR antenna for the design of miniaturized passive tags, and generated useful expressions that allow controlling the antenna characteristics by adjusting its geometry. In particular, it has been pointed out that, by increasing the separation between the external and internal rings, the radiation pattern of the EC-SRR could be made more uniform, thus reducing the sensitivity to orientation of the tags based on such antenna. The analysis has been then extended to study the radiation of the EC-SRR at the second resonance, also motivated by the absence of literature on the subject. It has been found that the radiation properties in this case are very similar to that of a half-wave dipole antenna, in terms of radiation resistance and efficiency, despite the lateral size of the SRR is halved. The radiation diagrams are similar, also because the cross-polarization values of the EC-SRR at the second resonance (−20 dB) have been found to be sensibly smaller than at the first resonance (−10 dB). Following on, the discussion has been focused on the radiation of complementary particles. Special attention was dedicated to the case of these particles radiating over a metal plane, with special concern about evaluating their performance degradation when the distance from the metal is reduced to very small values, as required in low-profile RFID tags. The analysis, based on electromagnetic simulations, suggested that, although a clear dependence of the behavior upon the distance from

metal exists, acceptable performance in the frame of passive tag design could be obtained at the second resonance, even for very small thickness (1.27 mm).

The validity of the above-mentioned analysis, along with the utility of the design tools arising from such analysis, has been corroborated in **Chapter 5**, where some practical examples have been provided. First, a passive UHF-RFID tag based on the SRR antenna has been designed, simulated and subjected to experimental validation. The design process has been detailed, revealing that good impedance matching could be obtained without the need of additional matching networks. In good agreement with theory and simulations, experimental data revealed that good performance in terms of read range (9.3 m) has been obtained, despite the very small tag size (30 mm x 30 mm). Moreover, the tag response has been adjusted to minimize the orientation sensitivity of the tag, obtaining a minimum read range of 4.2 m. Then, a low-profile on-metal tag based on the NB-CSRR antenna has been presented as an alternative to the state-of-the-art solutions, motivated by the encouraging conclusions of the analysis in the previous chapter. The tag design, aided by electromagnetic simulations, has been detailed. The measurement revealed a read range of 5.3 m, which is promising in relation to the NB-CSRR dimensions (45 mm x 45 mm) and the tag thickness (1.27 mm). However, it has been pointed out that the radiation efficiency of the antenna has been significantly degraded due to the presence of the high-permittivity dielectric substrate (*Rogers RO3010*), employed to contain the tag lateral dimensions to acceptable values. Therefore, an alternative solution avoiding the use of such substrates has been proposed. Specifically, a tag of the same size, based on a modified CSRR (i.e., the double slit CSRR, or 2-CSRR) antenna, suggested very encouraging results in terms of read range (between 7 and 10 m depending on the materials, according to the simulations). Finally, an SRR antenna working at the second resonance has been designed to operate in the 900 MHz ISM band, matched to a 50 Ω load, on the basis of the analysis carried out in the previous chapter. A prototype has been manufactured, and subjected to experimental validation, exhibiting good agreement with both theory and simulations. Despite the reduced lateral size ($\approx \lambda_0/5$), the antenna behavior in terms of input resistance, efficiency and bandwidth is similar to that of the commonly used half-wave dipole antenna, thus confirming the SRR antenna at the second resonance as a valuable alternative, especially when a reduction of the maximum antenna dimension is needed (at the expense of the area).

In **Chapter 6**, the problem of optical disc tagging has been treated, as a special case of item-level tagging of metallic objects. After an analysis of the disc structure, the state of the art of optical disc tagging has been reported. Then, the concept of optical-disc based tag has been introduced, detailing the working principle and discussing the benefits over the existing solutions. As a proof of concept, the approach has been first applied to design a tag for DVD discs, which required building a design methodology based on circuit modeling of the whole structure (i.e., the tag coupled to the disc). The experimental data validated the simulated results, and confirmed that significant

improvement could be obtained in terms of read range (5.2 m), compared to the existing solutions (less than a meter). The design method has been then improved to allow obtaining good impedance matching with any ASIC available on the market. To this end, an impedance matching method oriented to design simplicity has been developed on the basis of analytical approach. Such method, which considered the introduction of a matching capacitance in shunt with the RFID ASIC, has been then applied to the design of a tag for DVDs with a different, more advanced ASIC (*Alien Higgs 3*). Consequently, the tag read range was extended to 8.3 m, as confirmed by measurements. The method has been also applied to design a tag for Blu-Ray discs, with similar read range (6.3 m). Moreover, preliminary results also suggested that the proposed approach makes possible the reading of stacked discs.

Finally, in **Chapter 7**, the limitations of passive tags in terms of read range have been studied. To this end, the condition of size reduction imposed by the RFID design requirements of many applications, and characterizing most of the tags available on the market and in the literature, has been relaxed to some extent. After a discussion of the radiation pattern of linear wire antennas of different lengths, it has been concluded that a 1.25 wavelengths wire antenna provides a reasonable tradeoff between size and performance, and that further increase of the length causes degradation of the radiation pattern. Of course, being the tag length in the order of 40 cm, this solution is only suitable to identify relatively big objects (e.g., boxes, pallets). On the other hand, the performance improvements over standard tags are significant, and make the presented approach a possible choice for the applications demanding long reading distances. A tag prototype, implemented by using a copper wire of diameter 0.8 mm, exhibited a read range of 17.5 m in free space, thus demonstrating a great improvement over the typical general-purpose tags (40% higher compared to the *Alien "Squiggle"* high-end commercial tag).

As a **general conclusion**, the work developed within this thesis provided alternative solutions to the design of passive UHF-RFID tag antennas, responding to the challenging requirements of modern RFID tag design. The results, which contributed to the understanding of some unexplored radiating structures, have been disserted in specialized journals, international conferences, and generated a patent approved by the European Patent Office (see Patents).

Future Work

The encouraging results emerging from this thesis open the door to further exploration in the near future. Regarding the analysis of the radiation properties of metamaterial-inspired resonators, preliminary work showed that the two-turn spiral resonator (2-SR), operating between its first and second resonance, allows further reduction of the tag sensitivity to orientation, due to an increased value of cross polar radiation. However, a perfect balance between the radiation from the electric and magnetic moments, which would minimize the tag sensitivity to orientation, has not been accomplished yet. Though not producing an isotropic radiation pattern, this condition would allow obtaining a minimum read range equal to the 71% ($1/\sqrt{2}$) of the maximum read range (based on the theoretical analysis of orthogonal radiators in phase quadrature), thus representing an advance over the results obtained in this work.

The use of complementary metamaterial-inspired resonators for designing low-profile on-metal tags also inspired future research. In particular, the manufacturing of a tag prototype based on the 2-CSRR, which exhibited promising results in simulations, is still pending. Also, the size reduction of CSRR/NB-CSRR antennas at the second resonance without involving high-permittivity dielectrics should be explored. Specifically, removing half of the particle, by applying the proper boundary conditions to maintain unaltered the current distribution along the slot, is an interesting possibility.

Regarding the tagging of optical discs, the proposed method could be tested on different-sized discs. For example, preliminary simulations of the 80 mm MiniDVD suggest that, even if the antenna gain is lower as compared to the standard DVD, a read range of several meters (4-5 m) could be reached, thus still providing an interesting alternative to the state-of-the-art solutions. Moreover, further research is needed to understand, and eventually control, the signal propagation through a pile of stacked DVDs, in order to maximize the number of discs read simultaneously. This would make possible an effective and reliable tagging of optical discs in stores, libraries and video rental shops, as well as the tracking of packed discs through the supply chain.

References

[1] L. Brown, *Technical and Military Imperatives: A Radar History of World War 2*, CRC Press, 1999.

[2] J. R. Whitehead, *Super-regenerative receivers*, University Press, 1950.

[3] H. Stockman, "Communication by means of reflected power," *Proceedings of the IRE,* vol. 36, pp. 1196-1204, 1948.

[4] J. Landt, "The history of RFID," *IEEE Potentials,* vol. 24, pp. 8-11, 2005.

[5] R. Das and P. Harrop, "RFID forecasts, players and opportunities 2009–2019," *IDTechEx report,* 2009.

[6] P. Harrop and R. Das, "RFID Forecasts, Players and Opportunities 2014-2024," 2014.

[7] R. Das, "RFID Forecasts, Trends by Territory and Lessons," *IDTechEx report,* 2009.

[8] D. M. Dobkin, *The RF in RFID: UHF RFID in Practice*, Newnes, 2012.

[9] GS1, "Regulatory status for using RFID in the EPC Gen 2 band (860 to 960 MHz) of the UHF spectrum," 31 Octuber, 2014.

[10] D. M. Dobkin and S. M. Weigand, "Environmental effects on RFID tag antennas," in *IEEE MTT-S International Microwave Symposium Digest*, p. 4 pp., 2005.

[11] P. Nikitin, K. Rao, and S. Lam, "UHF RFID tag characterization: overview and state-of-the-art," in *Antenna Measurement Techniques Association Symposium (AMTA)*, 2012.

[12] E. Bergeret, J. Gaubert, P. Pannier, and J. M. Gaultier, "Modeling and design of CMOS UHF voltage multiplier for RFID in an EEPROM compatible process," *IEEE Transactions on Circuits and Systems Ii-Express Briefs,* vol. 54, pp. 833-837, Oct 2007.

[13] P. V. Nikitin and K. S. Rao, "Theory and measurement of backscattering from RFID tags," *IEEE Antennas and Propagation Magazine,* vol. 48, pp. 212-218, 2006.

[14] G. Marrocco, "The art of UHF RFID antenna design: impedance-matching and size-reduction techniques," *IEEE Antennas and Propagation Magazine,* vol. 50, pp. 66-79, 2008.

[15] L. J. Chu, "Physical Limitations of Omni-Directional Antennas," *Journal of Applied Physics,* vol. 19, pp. 1163-1175, 1948.

[16] H. A. Wheeler, "Fundamental Limitations of Small Antennas," *Proceedings of the Institute of Radio Engineers,* vol. 35, pp. 1479-1484, 1947.

[17] C. A. Balanis, *Antenna theory : analysis and design*, 3rd ed. Hoboken, NJ, John Wiley, 2005.

[18] L. Ukkonen, L. Sydanheimo, and M. Kivikoski, "Patch antenna with EBG ground plane and two-layer substrate for passive RFID of metallic objects," in *IEEE Antennas and Propagation Society International Symposium*, pp. 93-96, 2004.

[19] T. Björninen, K. E. Delzo, L. Ukkonen, A. Z. Elsherbeni, and L. Sydänheimo, "Long range metal mountable tag antenna for passive UHF RFID systems," in *IEEE International Conference on RFID-Technologies and Applications (RFID-TA)*, pp. 202-206, 2011.

[20] S. Uda and Y. Mushiake, *Yagi-Uda Antenna*, Research Institute of Electrical Communication, Tohoku University, 1954.

[21] D. D. Deavours, "Analysis and design of wideband passive UHF RFID tags using a circuit model," in *IEEE International Conference on RFID*, pp. 283-290, 2009.

[22] J. Choo, J. Ryoo, J. Hong, H. Jeon, C. Choi, and M. M. Tentzeris, "T-matching networks for the efficient matching of practical RFID tags," in *European Microwave Conference (EuMC)*, pp. 5-8, 2009.

[23] G. Zamora, S. Zuffanelli, F. Paredes, F. Martin, and J. Bonache, "Design and synthesis methodology for UHF-RFID tags based on the T-match Network," *IEEE Transactions on Microwave Theory and Techniques,* vol. 61, pp. 4090-4098, 2013.

[24] P. V. Nikitin and K. Rao, "Performance limitations of passive UHF RFID systems," in *IEEE Antennas and Propagation Society International Symposium*, 2006.

[25] K. S. Rao, P. V. Nikitin, and S. F. Lam, "Antenna design for UHF RFID tags: a review and a practical application," *IEEE Transactions on Antennas and Propagation,* vol. 53, pp. 3870-3876, 2005.

[26] W. A. Davis, T. Yang, E. D. Caswell, and W. L. Stutzman, "Fundamental limits on antenna size: a new limit," *IET Microwaves Antennas & Propagation,* vol. 5, pp. 1297-1302, Aug 19 2011.

[27] M. Gustafsson, C. Sohl, and G. Kristensson, "Illustrations of New Physical Bounds on Linearly Polarized Antennas," *IEEE Transactions on Antennas and Propagation,* vol. 57, pp. 1319-1327, May 2009.

[28] K. Mohammadpour-Aghdam, R. Faraji-Dana, G. A. Vandenbosch, S. Radiom, and G. G. Gielen, "Physical bound on Q factor for planar antennas," in *European Microwave Conference (EuMC)*, pp. 250-252, 2011.

[29] A. D. Yaghjian and S. R. Best, "Impedance, bandwidth, and Q of antennas," *IEEE Transactions on Antennas and Propagation,* vol. 53, pp. 1298-1324, Apr 2005.

[30] H. W. Bode, "Network analysis and feedback amplifier design," 1945.

[31] G. Zamora, F. Paredes, F. J. Herraiz-Martinez, F. Martin, and J. Bonache, "Bandwidth limitations of ultra high frequency-radio frequency identification tags," *IET Microwaves Antennas & Propagation,* vol. 7, pp. 788-794, Jul 16 2013.

[32] R. Marques, F. Martin, and M. Sorolla, *Metamaterials with Negative Parameters,*. Hoboken, N.J., Wiley-Interscience, 2008.

[33] G. V. Eleftheriades and K. G. Balmain, *Negative-refraction metamaterials. Fundamental Principles and Applications*, Wiley, 2005.

[34] N. Engheta and R. W. Ziolkowski, *Metamaterials: physics and engineering explorations*, John Wiley & Sons, 2006.

[35] C. Caloz and T. Itoh, *Electromagnetic Metamaterials: Transmission Line Theory and Microwave Applications: The Engineering Approach*, Wiley, 2006.

[36] F. Martín, *Artificial Transmission Lines for RF and Microwave Applications*, Wiley, 2015.

[37] V. G. Veselago, "The electrodynamics of substances with simultaneously negative values of ϵ and μ," *Physics-Uspekhi,* vol. 10, pp. 509-514, 1968.

[38] J. B. Pendry, A. J. Holden, D. J. Robbins, and W. J. Stewart, "Magnetism from conductors and enhanced nonlinear phenomena," *IEEE Transactions on Microwave Theory and Techniques,* vol. 47, pp. 2075-2084, Nov 1999.

[39] S. A. Schelkunoff and H. T. Friis, *Antennas: theory and practice* vol. 639, Wiley New York, 1952.

[40] W. N. Hardy and L. A. Whitehead, "Split-Ring Resonator for Use in Magnetic-Resonance from 200-2000 Mhz," *Review of Scientific Instruments,* vol. 52, pp. 213-216, 1981.

[41] D. R. Smith, W. J. Padilla, D. Vier, S. C. Nemat-Nasser, and S. Schultz, "Composite medium with simultaneously negative permeability and permittivity," *Physical Review Letters,* vol. 84, p. 4184, 2000.

[42] R. Marques, J. Martel, F. Mesa, and F. Medina, "Left-handed-media simulation and transmission of EM waves in subwavelength split-ring-resonator-loaded metallic waveguides," *Physical Review Letters,* vol. 89, Oct 2002.

[43] F. Falcone, F. Martin, R. Marques, J. Martel, J. Bonache, T. Lopetegi, M. A. G. Laso, and M. Sorolla, "Implementation of negative mu medium in coplanar waveguide technology," *Microwave and Optical Technology Letters,* vol. 5445, pp. 192-195, 2003.

[44] F. Martin, J. Bonache, F. Falcone, M. Sorolla, and R. Marques, "Split ring resonator-based left-handed coplanar waveguide," *Applied Physics Letters,* vol. 83, pp. 4652-4654, Dec 1 2003.

[45] J. Selga, M. Gil, F. Aznar, J. Bonache, and F. Martin, "Composite right-/left-handed coplanar waveguides loaded with split ring resonators and their application to high-pass filters," *IET Microwaves Antennas & Propagation,* vol. 4, pp. 822-827, 2010.

[46] F. Falcone, T. Lopetegi, J. D. Baena, R. Marqués, F. Martín, and M. Sorolla, "Effective negative-ϵ; stopband microstrip lines based on complementary split ring resonators," *IEEE Microwave and Wireless Components Letters,* vol. 14, pp. 280-282, 2004.

[47] M. Gil, J. Bonache, J. Garcia-Garcia, J. Martel, and F. Martin, "Composite right/left-handed metamaterial transmission lines based on complementary split-rings resonators and their applications to very wideband and compact filter design," *IEEE Transactions on Microwave Theory and Techniques,* vol. 55, pp. 1296-1304, 2007.

[48] M. Gil, J. Bonache, I. Gil, J. Garcia-Garcia, and F. Martin, "Artificial left-handed transmission lines for small size microwave components: Application to power dividers," in *European Microwave Conference (EuMC)*, pp. 1135-1138, 2006.

[49] J. Naqui, M. Durán-Sindreu, and F. Martín, "Novel sensors based on the symmetry properties of split ring resonators (SRRs)," *Sensors,* vol. 11, pp. 7545-7553, 2011.

[50] M. Puentes, C. Weiss, M. Schüssler, and R. Jakoby, "Sensor array based on split ring resonators for analysis of organic tissues," in *IEEE MTT-S International Microwave Symposium Digest*, pp. 1-4, 2011.

[51] I. Arnedo, J. Illescas, M. Flores, T. Lopetegi, M. A. G. Laso, F. Falcone, J. Bonache, J. Garcia-Garcia, F. Martin, J. A. Marcotegui, R. Marques, and M. Sorolla, "Forward and backward leaky wave radiation in split-ring-resonator-based metamaterials," *IET Microwaves Antennas & Propagation,* vol. 1, pp. 65-68, Feb 2007.

[52] S. Eggermont and I. Huynen, "Influence of number of split rings on the leaky radiation of a metamaterial transmission line based on complementary split ring resonators," *Microwave and Optical Technology Letters,* vol. 54, pp. 867-875, Apr 2012.

[53] G. Zamora, S. Zuffanelli, F. Paredes, F. J. Herraiz-Martínez, F. Martin, and J. Bonache, "Fundamental-Mode Leaky-Wave Antenna (LWA) Using Slotline and Split-Ring-Resonator (SRR)-Based Metamaterials," *IEEE Antennas and Wireless Propagation Letters,* vol. 12, pp. 1424-1427, 2013.

[54] K. B. Alici and E. Ozbay, "Electrically small split ring resonator antennas," *Journal of Applied Physics,* vol. 101, Apr 15 2007.

[55] J. J. Ma, X. Y. Cao, and T. Liu, "Design the size reduction patch antenna based on complementary split ring resonators," in *International Conference on Microwave and Millimeter Wave Technology*, 2010.

[56] R. W. Ziolkowski, P. Jin, and C. C. Lin, "Metamaterial-Inspired Engineering of Antennas," *Proceedings of the IEEE,* vol. 99, pp. 1720-1731, Oct 2011.

[57] F. J. Herraiz-Martinez, L. E. Garcia-Munoz, D. Gonzalez-Ovejero, V. Gonzalez-Posadas, and D. Segovia-Vargas, "Dual-Frequency Printed Dipole Loaded With Split Ring Resonators," *IEEE Antennas and Wireless Propagation Letters,* vol. 8, pp. 137-140, 2009.

[58] M. C. Tang and R. W. Ziolkowski, "A Study of Low-Profile, Broadside Radiation, Efficient, Electrically Small Antennas Based on Complementary Split Ring Resonators," *IEEE Transactions on Antennas and Propagation,* vol. 61, pp. 4419-4430, Sep 2013.

[59] X. Y. Cheng, D. E. Senior, J. J. Whalen, and Y. K. Yoon, "Electrically Small Tunable Split Ring Resonator Antenna," *IEEE Antennas and Propagation Society International Symposium,* 2010.

[60] J. Garcia-Garcia, F. Martin, J. D. Baena, R. Marques, and L. Jelinek, "On the resonances and polarizabilities of split ring resonators," *Journal of Applied Physics,* vol. 98, Aug 1 2005.

[61] M. Shamonin, E. Shamonina, V. Kalinin, and L. Solymar, "Resonant frequencies of a split-ring resonator: Analytical solutions and numerical simulations," *Microwave and Optical Technology Letters,* vol. 44, pp. 133-136, Jan 20 2005.

[62] R. Marqués, F. Medina, and R. Rafii-El-Idrissi, "Role of bianisotropy in negative permeability and left-handed metamaterials," *Physical Review B,* vol. 65, p. 144440, 2002.

[63] R. Marques, F. Mesa, J. Martel, and F. Medina, "Comparative analysis of edge- and broadside-coupled split ring resonators for metamaterial design - Theory

and experiments," *IEEE Transactions on Antennas and Propagation,* vol. 51, pp. 2572-2581, Oct 2003.

[64] B. Sauviac, C. R. Simovski, and S. A. Tretyakov, "Double split-ring resonators: Analytical modeling and numerical simulations," *Electromagnetics,* vol. 24, pp. 317-338, Jul 2004.

[65] M.-D. Chiou and S.-Y. Chen, "An electrically small planar antenna using complementary split-ring resonators," in *International Symposium on Antennas and Propagation (ISAP)*, pp. 1313-1316, 2012.

[66] S. H. Lim, Y. C. Oh, H. Lim, Y. S. Lee, and N. H. Myung, "Analysis and design of a UHF RFID tag antenna with a Split Ring Resonator," *IEEE International Workshop on Antenna Technology : Small Antennas and Novel Metamaterials,* pp. 398-401, 2008.

[67] B. D. Braaten, "A novel compact UHF RFID tag antenna designed with series connected open complementary split ring resonator (OCSRR) particles," *Antennas and Propagation, IEEE Transactions on,* vol. 58, pp. 3728-3733, 2010.

[68] B. D. Braaten and M. Aziz, "Using meander open complementary split ring resonator (MOCSRR) particles to design a compact UHF RFID tag antenna," *IEEE Antennas and Wireless Propagation Letters,* vol. 9, pp. 1037-1040, 2010.

[69] F. Paredes, G. Zamora, F. J. Herraiz-Martínez, F. Martín, and J. Bonache, "Dual-band uhf-rfid tags based on meander-line antennas loaded with spiral resonators," *IEEE Antennas and Wireless Propagation Letters,* vol. 10, pp. 768-771, 2011.

[70] B. D. Braaten, R. P. Scheeler, M. Reich, R. M. Nelson, C. Bauer-Reich, J. Glower, and G. J. Owen, "Compact metamaterial-based UHF RFID antennas: deformed omega and split-ring resonator structures," in *Applied Computational Electromagnetic Society*, 2010.

[71] F. Paredes, G. Z. González, J. Bonache, and F. Martin, "Dual-band impedance-matching networks based on split-ring resonators for applications in RF identification (RFID)," *IEEE Transactions on Microwave Theory and Techniques,* vol. 58, pp. 1159-1166, 2010.

[72] M. Polivka, A. Holub, M. Vyhnalik, and M. Svanda, "Impedance properties and radiation efficiency of electrically small double and triple split-ring antennas for UHF RFID applications," *Antennas and Wireless Propagation Letters, IEEE,* vol. 12, pp. 221-224, 2013.

[73] T.-H. Cheng, C.-H. Chiang, D.-W. Kung, and S.-Y. Chen, "A compact UHF RFID tag antenna using split-ring-resonator-loaded short dipole," in *Asia-Pacific Microwave Conference (APMC)*, pp. 453-455, 2014.

[74] P. Foster and R. Burberry, "Antenna problems in RFID systems," 1999.

[75] J. D. Griffin, G. D. Durgin, A. Haldi, and B. Kippelen, "RF tag antenna performance on various materials using radio link budgets," *IEEE Antennas and Wireless Propagation Letters,* vol. 5, pp. 247-250, 2006.

[76] S. R. Aroor and D. D. Deavours, "Evaluation of the state of passive UHF RFID: An experimental approach," *IEEE Systems Journal,* vol. 1, pp. 168-176, 2007.

[77] T. Bjorninen, L. Sydanheimo, L. Ukkonen, and Y. Rahmat-Samii, "Advances in antenna designs for UHF RFID tags mountable on conductive items," *IEEE Antennas and Propagation Magazine,* vol. 56, pp. 79-103, 2014.

[78] B. Yu, S. J. Kim, B. Jung, F. J. Harackiewicz, and B. Lee, "RFID tag antenna using two-shorted microstrip patches mountable on metallic objects," *Microwave and Optical Technology Letters,* vol. 49, pp. 414-416, 2007.

[79] T. V. Koskinen, H. Rajagopalan, and Y. Rahmat-Samii, "A thin multi-slotted dual patch UHF-band metal-mountable RFID tag antenna," *Microwave and Optical Technology Letters,* vol. 53, pp. 40-47, 2011.

[80] J. Zhang and Y. Long, "A Novel Metal-Mountable Electrically Small Antenna for RFID Tag Applications With Practical Guidelines for the Antenna Design," *IEEE Transactions on Antennas and Propagation,* vol. 62, pp. 5820-5829, 2014.

[81] J.-s. Kim, W.-K. Choi, and G.-Y. Choi, "Small proximity coupled ceramic patch antenna for UHF RFID tag mountable on metallic objects," *Progress In Electromagnetics Research C,* vol. 4, pp. 129-138, 2008.

[82] S. J. Kim, B. Yu, Y. S. Chung, F. J. Harackiewicz, and B. Lee, "Patch-type radio frequency identification tag antenna mountable on metallic platforms," *Microwave and Optical Technology Letters,* vol. 48, pp. 2446-2448, 2006.

[83] L. Ukkonen, D. Engel, L. Sydanheimo, and M. Kivikoski, "Planar wire-type inverted-F RFID tag antenna mountable on metallic objects," in *IEEE Antennas and Propagation Society International Symposium,*, pp. 101-104, 2004.

[84] H. Kwon and B. Lee, "Compact slotted planar inverted-F RFID tag mountable on metallic objects," *Electronics Letters,* vol. 41, pp. 1308-1310, 2005.

[85] W. Choi, H. W. Son, J.-H. Bae, G. Y. Choi, C. S. Pyo, and J.-S. Chae, "An RFID tag using a planar inverted-F antenna capable of being stuck to metallic objects," *ETRI journal,* vol. 28, pp. 216-218, 2006.

[86] B. Lee and B. Yu, "Compact structure of UHF band RFID tag antenna mountable on metallic objects," *Microwave and Optical Technology Letters,* vol. 50, pp. 232-234, 2008.

[87] H. D. Chen, Y. H. Tsao, and C. Y. Kuo, "Low-profile radio frequency identification tag antenna using a trapezoid patch mountable on metallic surfaces," *Microwave and Optical Technology Letters,* vol. 52, pp. 1697-1700, 2010.

[88] C. Cho, H. Choo, and I. Park, "Design of planar RFID tag antenna for metallic objects," *Electronics Letters,* vol. 44, pp. 175-177, 2008.

[89] T.-W. Koo, D. Kim, J.-I. Ryu, H.-M. Seo, J.-G. Yook, and J.-C. Kim, "Design of a label-typed UHF RFID tag antenna for metallic objects," *IEEE Antennas and Wireless Propagation Letters,* vol. 10, pp. 1010-1014, 2011.

[90] T. Björninen, V. Bhagavati, L. Sydänheimo, P. Kallio, and L. Ukkonen, "Small and flexible metal mountable passive UHF RFID tag on high-dielectric polymer-ceramic composite substrate," *IEEE Antennas and Wireless Propagation Letters,* vol. 11, pp. 1319-1322, 2012.

[91] T. Björninen, A. A. Babar, L. Ukkonen, L. Sydanheimo, A. Z. Elsherbeni, and J. Kallioinen, "Compact metal mountable UHF RFID tag on a Barium Titanate based substrate," *Progress In Electromagnetics Research C,* vol. 26, pp. 43-57, 2012.

[92] D.-U. Sim, D.-H. Kim, J.-I. Choi, and H.-D. Choi, "Design of novel dipole-type tag antennas using electromagnetic bandgap (EBG) surface for passive RFID applications," in *IEEE Antennas and Propagation Society International Symposium,*, pp. 1333-1336, 2007.

[93] B. Gao and M. M. Yuen, "Passive UHF RFID packaging with electromagnetic band gap (EBG) material for metallic objects tracking," *IEEE Transactions on Components, Packaging and Manufacturing Technology,* vol. 1, pp. 1140-1146, 2011.

[94] P. N. Murgatroyd, "Calculation of Proximity Losses in Multistranded Conductor Bunches," *IEE Proceedings-a-Science Measurement and Technology,* vol. 136, pp. 115-120, May 1989.
[95] S. J. Orfanidis, *Electromagnetic waves and antennas*. New Brunswick, NJ, Rutgers University, 2002.
[96] J. D. Jackson, *Classical electrodynamics* vol. 3. New York, Wiley, 1962.
[97] D. M. Pozar, *Microwave engineering*, John Wiley & Sons, 2009.
[98] P. V. Nikitin, S. Lam, and K. Rao, "Low cost silver ink RFID tag antennas," in *IEEE Antennas and Propagation Society International Symposium,*, pp. 353-356, 2005.
[99] P. Pongpaibool, "A study of cost-effective conductive ink for inkjet-printed RFID application," in *International Symposium on Antennas and Propagation (ISAP)*, Nagoys, pp. 1248-1251, 2012.
[100] D. M. Pozar, "New Results for Minimum Q, Maximum Gain, and Polarization Properties of Electrically Small Arbitrary Antennas," *European Conference on Antennas and Propagation,* pp. 1914-1917, 2009.
[101] J.-S. Hong and M. J. Lancaster, *Microstrip filters for RF/microwave applications*. New York, Wiley, 2001.
[102] R. Marqués, J. Baena, J. Martel, F. Medina, F. Falcone, M. Sorolla, and F. Martín, "Novel small resonant electromagnetic particles for metamaterial and filter design," *Proceedings ICEAA,* vol. 3, pp. 439-442, 2003.
[103] F. Falcone, T. Lopetegi, M. Laso, J. Baena, J. Bonache, M. Beruete, R. Marqués, F. Martin, and M. Sorolla, "Babinet principle applied to the design of metasurfaces and metamaterials," *Physical Review Letters,* vol. 93, p. 197401, 2004.
[104] H. G. Booker, "Slot aerials and their relation to complementary wire aerials (Babinet's principle)," *Journal of the Institution of Electrical Engineers-Part IIIA: Radiolocation,* vol. 93, pp. 620-626, 1946.
[105] G. A. Deschamps, "Impedance properties of complementary multiterminal planar structures," *IRE Transactions on Antennas and Propagation,* vol. 7, pp. 371-378, 1959.
[106] K. Lang, "Babinet's principle for a perfectly conducting screen with aperture covered by resistive sheet," *IEEE Transactions on Antennas and Propagation,* vol. 21, pp. 738-740, 1973.
[107] T. Senior, "Some extensions of Babinet's principle in electromagnetic theory," *IEEE Transactions on Antennas and Propagation,* vol. 25, pp. 417-420, 1977.
[108] R. Hansen, "Slot antenna in a resistive screen," *IEEE Transactions on Antennas and Propagation,* vol. 46, pp. 1028-1031, 1998.
[109] K. Yoshitomi, "Radiation from a slot in an impedance surface," *IEEE Transactions on Antennas and Propagation,* vol. 49, pp. 1370-1376, 2001.
[110] A. Vallecchi and G. B. Gentili, "Microstrip-fed slot antennas backed by a very thin cavity," *Microwave and Optical Technology Letters,* vol. 49, pp. 247-250, 2007.
[111] M. Polivka, A. Holub, M. Vyhnalik, and M. Svanda, "Impedance Properties and Radiation Efficiency of Electrically Small Double and Triple Split-Ring Antennas for UHF RFID Applications," *IEEE Antennas and Wireless Propagation Letters,* vol. 12, pp. 221-224, 2013.
[112] M. Y. Lai, R. L. Li, and M. M. Tentzeris, "Low-Profile Broadband RFID Tag antennas mountable on metallic objects," *IEEE Antennas and Propagation Society International Symposium,* 2010.

[113] *Johanson Technology*. Available: http://www.johansontechnology.com/datasheets/baluns/0900BL15C050.pdf

[114] F. R. Byers, "Care and Handling of CDs and DVDs—A Guide for Librarians and Archivists," *NIST Special Publication,* vol. 500, p. 252, 2003.

[115] R. C. Hansen and W. T. Pawlewicz, "Effective Conductivity and Microwave Reflectivity of Thin Metallic-Films," *IEEE Transactions on Microwave Theory and Techniques,* vol. 30, pp. 2064-2066, 1982.

[116] W. T. Luk and K. N. Yung, "Bending Dipole Design of Passive UHF RFID Tag Antenna for CD/DVD Discs," *Asia Pacific Microwave Conference (Apmc)* pp. 971-974, 2008.

[117] A. S. Andrenko, M. Kai, T. Maniwa, and T. Yamagajo, "Compact printed-on-CD UHF RFID tag antennas," *2007 IEEE Antennas and Propagation Society International Symposium,,* pp. 4976-4979, 2007.

[118] Y. Hanaoka, K. Hinode, K. Takeda, and D. Kodama, "Increase in electrical resistivity of copper and aluminum fine lines," *Materials Transactions,* vol. 43, pp. 1621-1623, Jul 2002.

[119] W. Zhang, S. H. Brongersma, O. Richard, B. Brijs, R. Palmans, L. Froyen, and K. Maex, "Influence of the electron mean free path on the resistivity of thin metal films," *Microelectronic Engineering,* vol. 76, pp. 146-152, Oct 2004.

[120] R. A. Matula, "Electrical-Resistivity of Copper, Gold, Palladium, and Silver," *Journal of Physical and Chemical Reference Data,* vol. 8, pp. 1147-1298, 1979.

[121] C. A. Grosvenor, R. T. Johnk, J. Baker-Jarvis, M. D. Janezic, and B. Riddle, "Time-Domain Free-Field Measurements of the Relative Permittivity of Building Materials," *IEEE Transactions on Instrumentation and Measurement,* vol. 58, pp. 2275-2282, Jul 2009.

[122] P. V. Nikitin, K. V. S. Rao, R. Martinez, and S. F. Lam, "Sensitivity and Impedance Measurements of UHF RFID Chips," *IEEE Transactions on Microwave Theory and Techniques,* vol. 57, pp. 1297-1302, May 2009.

[123] R. M. Fano, "Theoretical limitations on the broadband matching of arbitrary impedances," *Journal of the Franklin Institute,* vol. 249, pp. 57-83, 1950.

[124] D. F. Sievenpiper, D. C. Dawson, M. M. Jacob, T. Kanar, S. Kim, J. Long, and R. G. Quarfoth, "Experimental Validation of Performance Limits and Design Guidelines for Small Antennas," *IEEE Transactions on Antennas and Propagation,* vol. 60, pp. 8-19, Jan 2012.

[125] B.-r. D. Association, "White Paper Blu-ray Disc Format: 1. A Physical Format Specifications for BD-RE," 2006.

[126] F. Lu, X. Chen, and T. T. Ye, "Performance analysis of stacked RFID tags," in *IEEE International Conference on RFID*, pp. 330-337, 2009.

[127] S. M. Weigand and D. M. Dobkin, "Multiple RFID tag plane array effects," in *IEEE Antennas and Propagation Society International Symposium*, 2006.

[128] P. V. Nikitin and K. V. S. Rao, "Effect of Gen2 Protocol Parameters on RFID Tag Performance," *IEEE International Conference on RFID,* pp. 117-122, 2009.

Author list of publications

International Journals

1. F. Paredes, G. Zamora, S. Zuffanelli, F. J. Herraiz-Martínez, J. Bonache and F. Martín "Recent Advances in Multiband Printed Antennas Based on Metamaterial Loading," *Advances in Optoelectronics*, Article ID 968780, 2012.

2. F. Paredes, G. Zamora, S. Zuffanelli, F. J. Herraiz-Martinez, F. Martin, and J. Bonache, "Free-Space and on-Metal Dual-Band Tag for UHF-RFID Applications in Europe and USA," *Progress in Electromagnetics Research*, vol. 141, 577-590, August 2013.

3. S. Zuffanelli, G. Zamora, F. Paredes, F. Martín, and J. Bonache, "An approach for the design of passive UHF-RFID tags mounted on optical discs," *IEEE Transactons on Antennas and Propagation*, vol. 61(12), pp. 5860-5867, Dec. 2013.

4. G. Zamora, F. Paredes, S. Zuffanelli, F. Martín, and J. Bonache, "Design and Synthesis Methodology for UHF-RFID Tags Based on the T-match Network," *IEEE Transactions on Microwave Theory and Techniques*, vol 61(12), pp, 4090-4098, Dec. 2013.

5. G. Zamora, S. Zuffanelli, F. Paredes, F. Javier Herraiz-Martínez, F. Martín and J. Bonache, "Fundamental mode leaky-wave-antenna (LWA) using slotline and split-ring-resonator (SRR) based metamaterials," *IEEE Antennas and Wireless Propagation Letters*, vol. 12, pp. 1424-1427, 2013.

6. P. Aguilà, S. Zuffanelli, G. Zamora, F. Paredes, F. Martín and J. Bonache, "Front-to-back ratio improvement of printed antennas based on electrically small resonators for microwave presence detectors," *Electronics Letters*, vol.51, no.11, pp. 836-837, May 2015

7. S. Zuffanelli, G. Zamora, P. Aguila, F. Paredes, F. Martin and J. Bonache, "On the Radiation Properties of Split-Ring Resonators (SRRs) at the Second Resonance," *IEEE Transactions on Microwave Theory and Techniques*, vol. 63(7), pp. 2133-2141, May 2015.

8. S. Zuffanelli, G. Zamora, P. Aguila, F. Paredes, F. Martin and J. Bonache, "Analysis of the Split Ring Resonator (SRR) Antenna Applied to Passive UHF-

RFID Tag Design," *IEEE Transactions on Antennas and Propagation*, SUBMITTED in Feb. 2015.

9. S. Zuffanelli, G. Zamora, P. Aguila, F. Paredes, F. Martin and J. Bonache, "On-Metal UHF-RFID Passive Tags based on Non-Bianisotropic Complementary Split Ring Resonators," *IEEE Transactions on Antennas and Propagation*, SUBMITTED in Feb. 2015.

10. S. Zuffanelli, G. Zamora, P. Aguila, F. Paredes, F. Martin and J. Bonache, "A High-Gain Passive UHF-RFID Tag with Increased Read Range" *IEEE Antennas and Wireless Propagation Letters*, SUBMITTED in May. 2015.

International Conferences

1. S. Zuffanelli, G. Zamora, F. Paredes, P. Aguilà, F. Martín, and J. Bonache, "An Impedance Matching Method for Optical Disc-Based UHF-RFID Tags," *8th Annual IEEE International Conference on RFID*, Orlando (FL), USA, April, 8-10, 2014.

2. S. Zuffanelli, G. Zamora, F. Paredes, P. Aguilà, F. Martín and J. Bonache, "On-metal UHF-RFID tags based on non-bianisotropic complementary split ring resonators," *Meta '14, 5th International Conference on Metamaterials, Photonic Crystals and Plasmonics*, Singapore, 20-23 May, 2014. Invited.

3. S. Zuffanelli, P. Aguilà, F. Paredes, G. Zamora, F. Martín and J. Bonache, "Passive UHF-RFID tags for Blu-ray discs," *2014 International Symposium on Antennas and Propagation and USNC-URSI Radioscience Meeting (APS/URSI 2014)*, Memphis, Tennessee, 6-11 July 2014.

4. G. Zamora, P. Aguila, S. Zuffanelli, F. Paredes, F. Martin and J. Bonache, "Design of UHF-RFID tags based on the T-match network," *2014 International Symposium on Antennas and Propagation and USNC-URSI Radioscience Meeting (APS/URSI 2014)*, Memphis, Tennessee, 6-11 July 2014.

5. G. Zamora, S. Zuffanelli, F. Paredes, F. J. Herraiz-Martínez, F. Martín, J. Bonache, "Leaky-Wave Antenna (LWA) based on Slot Line and Non-Bianisotropic Split Ring Resonators (NB-SRRs) and Comparison with CPW Approach," *IEEE-APS Topical Conference on Antennas and Propagation in Wireless Communications*, Palm Beach, Aruba, 3-9 August 2014. Invited.

6. F. Paredes, P. Aguilà, S. Zuffanelli, G. Zamora, F. Martin and J. Bonache, "Quasi-isotropic electrically small antennas for UHF-RFID passive tags based on 2-turns spiral resonators," *IEEE AP-S Symposium on Antennas and Propagation and URSI CNC/USNC*, Vancouver, Canada, July 2015.

7. P. Aguilà, G. Zamora, S. Zuffanelli, F. Paredes, F. Martín and J. Bonache, "Design of printed antennas based on electrically small resonators for microwave applications," *IEEE International Symposium of Antennas and Propagation and North American Radio Science Meeting*, Vancouver, Canada, July 2015.

8. F. Paredes, S. Zuffanelli, P. Aguilà, G. Zamora, F. Martin and J. Bonache, "2-SR-Based Electrically Small Antenna for RFID Applications," *META'15, the 6th International Conference on Metamaterials, Photonic Crystals and Plasmonics*, New York, USA, August 2015.

9. P. Aguilà, S. Zuffanelli, G. Zamora, F. Paredes, F. Martín and J. Bonache, "Non-Bianisotropic Complementary Split Ring Resonator printed antenna with enhanced front-to-back ratio for microwave motion detectors," *XXX Simposium Nacional de la Unión Científica Internacional de Radio*, Pamplona, Spain, September 2015.

Patents

1 **Title:** *An optical disc with a wireless communication device, a wireless communication device and a method for its design and fabrication.*
Inventors: Jorge Bonache Albacete, Ferran Paredes Marco, Simone Zuffanelli, Ferran Martín Antolín and Gerard Zamora Gonzalez.
Applicants: Universitat Autònoma de Barcelona.
Application number: EP13382232.0 (EPO: european patent office).
1310982.2 (UK-PO: United Kingdom patent office).
P201330926 (OEPM: Oficina española de patentes y marcas).
Date of application: June 20, 2013.

2 **Title:** *Method for manufacturing a communication device to operate in near field and communication device thereof.*
Inventors: Jorge Bonache Albacete, Ferran Paredes Marco, Simone Zuffanelli, Ferran Martín Antolín and Gerard Zamora Gonzalez.
Applicants: Universitat Autònoma de Barcelona.
Application number: EP13382287.4 (EPO: European patent office).
1312367.4 (UK-PO: United Kingdom patent office).
P201331049 (OEPM :Oficina española de patentes y marcas).
Date of application: July 10, 2013.